UNIVERSITY OF Southampton

University of Southampton Research Repository
ePrints Soton

Copyright © and Moral Rights for this thesis are retained by the author and/or other copyright owners. A copy can be downloaded for personal non-commercial research or study, without prior permission or charge. This thesis cannot be reproduced or quoted extensively from without first obtaining permission in writing from the copyright holder/s. The content must not be changed in any way or sold commercially in any format or medium without the formal permission of the copyright holders.

When referring to this work, full bibliographic details including the author, title, awarding institution and date of the thesis must be given e.g.

AUTHOR (year of submission) "Full thesis title", University of Southampton, name of the University School or Department, PhD Thesis, pagination

http://eprints.soton.ac.uk

UNIVERSITY OF SOUTHAMPTON

FACULTY OF ENGINEERING SCIENCE AND MATHEMATICS

Optoelectronics Research Centre

Towards High Efficiency Microfluidic DNA Extension for Genomic Analysis

by

Timothy Robert Humphreys

Thesis for the degree of Doctor of Philosophy

July 2011

Abstract

Genomic analysis and DNA sequencing is a mature field with many established techniques. Developments in micro- and nanofabrication over the last decade or more have brought advances in a number of areas of chemical and biological analysis and genomics has been of particular interest. This thesis presents the development of two new techniques in microfluidic DNA manipulation that are directly applicable to the fabrication of next-generation genomic analysis devices.

A key area for any miniaturised device is the 'world-to-chip' connection. Even the most highly integrated micro total analysis systems require efficient sample loading and for sensitive detection as well as device reuse it is essential that molecules of interest are not lost in the world to chip transition. A new type of microfluidic interconnect is described in this work, which uses a shallow slope to make an in-plane connection between a microfluidic channel and a glass capillary. The microfluidic channel is fabricated in silicon capped with glass. The phenomenon of deep reactive-ion etch (DRIE) lag was applied to fabricate the slope and DRIE was also used to fabricate the microfluidic channels. The interconnect has been demonstrated to provide low loss loading of 48.5kbp DNA molecules from world to chip and is fabricated using standard silicon processing equipment.

The second new development reported in this thesis is the design, fabrication and characterisation of microfluidic DNA 'preconditioning' channels which are used to improve the efficiency of a downstream taper in the channel used for fluidic DNA extension. Extension of DNA in elongational flow has the potential to become a high-throughput genomic mapping technology. A common limitation to all systems previously demonstrated for stretching DNA with an elongational flow is that the stretching efficacy is strongly dependent upon the initial conformation of the DNA strand. The devices described in this thesis demonstrate an improvement in DNA preconditioning using non-contact microfluidic shearing flow in order to deliver extended molecules to a microfluidic channel in which optical interrogation of fluorescent markers takes place using a bespoke confocal spectroscopy system.

Table of Contents

Table of Figures

DECLARATION OF AUTHORSHIP

I, Timothy Robert Humphreys declare that the thesis entitled:

"Towards High Efficiency Microfluidic DNA Extension for Genomic Analysis"

and the work presented in the thesis are both my own, and have been generated by me as the result of my own original research. I confirm that:

- this work was done wholly or mainly while in candidature for a research degree at this University;
- where any part of this thesis has previously been submitted for a degree or any other qualification at this University or any other institution, this has been clearly stated;
- where I have consulted the published work of others, this is always clearly attributed;
- where I have quoted from the work of others, the source is always given. With the exception of such quotations, this thesis is entirely my own work;
- I have acknowledged all main sources of help;
- where the thesis is based on work done by myself jointly with others, I have made clear exactly what was done by others and what I have contributed myself;
- parts of this work have been published as:

Humphreys *et al.* (2009), "World-to-chip interconnects for efficient loading of genomic DNA into microfluidic channels." J. Micromech. Microeng. (10): 105024.

Signed: ……..

Date:…….

Acknowledgements

I gratefully acknowledge funding support from the Engineering and Physical Sciences Research Council (EPSRC, grant code EP/C011902/1) and the MC2 Access programme at Chalmers University of Technology which made the microfabrication possible.

My thanks go to all the staff at the Department of Microtechnology and Nanoscience (MC2) at Chalmers for making my time there so enjoyable and in particular to Ulf Södervall, Johan Andersson and Göran Petersson for their training, advice and support. The tireless work of Dave Saeger, Neil Sessions and Neal Fagan in running the temporary laboratory facilities in the time after the Mountbatten fire was critical to my work in that period and I am most grateful to them.

Thank you to my supervisor, Tracy Melvin and to other members of the Southampton academic community who provided technical and practical advice, notably Tom Brown, Christos Grivas and Julian Bailey who provided the electronic hardware definition which appears in appendix D.

My thanks to all the members of our research group who provided unlimited supplies of help, advice and most importantly, tea. Ben Husband, Nic Perney, Lucy Braddick, Matt Praeger and Daniel Friedrich deserve special mentions for giving good advice at the right times.

My thanks to Linda Humphreys for always being available to listen, Gareth Lewis for always being available to talk, to Kimberly McDougall for her invaluable support and finally to Karen Wilkinson for her encouragement in the final stages.

Definitions and Abbreviations

Acronym	Definition
APD	Avalanche Photodiode
API	Application-Programmer Interface
ARDE	Aspect Ratio Dependent Etching
ASE	Advanced Silicon Etch
BOE	Buffered Oxide Etch
BSA	Bovine Serum Albumin
CCD	Charge Coupled Device
CMOS	Complementary Metal-Oxide-Semiconductor
CMP	Chemical-Mechanical Polishing
De	Deborah number
DNA	Deoxyribonucleic Acid
dNTP	Deoxyribonucleotide Triphosphatase
DRIE	Deep Reactive-Ion Etching
dsDNA	double stranded DNA
EDTA	Ethylenediaminetetraacetic Acid
EMCCD	Electron-Multiplying Charge Coupled Device
ETFE	Ethylene Tetrafluoroethylene
FC	Fibre-optic Connector
FEA	Finite Element Analysis
FISH	Fluorescence In-Situ Hybridisation
FPGA	Field-Programmable Gate Array
FRET	Förster Resonance Energy Transfer
HeNe	Helium-Neon
HMDS	Hexamethyldisilazane
HPLC	High-Performance Liquid Chromatography
ICP	Inductively Coupled Plasma
IPA	Isopropyl Alcohol
Kb	Kilo-bases / Kilo-basepairs
Mb	Mega-bases / Mega-basepairs
MEMS	Micro-Electromechanical Systems
NA	Numerical Aperture

NIL	Nano-Imprint Lithography
NTC	No-Template Control
PC	Personal Computer
PCI	Peripheral Component Interface
PCR	Polymerase Chain Reaction
PDMS	Poly(dimethylsiloxane)
PECVD	Plasma-Enhanced Chemical Vapour Deposition
PEEK	Polyetheretherketone
PEG	Polyethylene Glycol
PMMA	Polymethylmethacrylate
PMT	Photomultiplier Tube
PNA	Peptide Nucleic Acid
qPCR	Quantitative Polymerase Chain Reaction
RCA	Radio Corporation of America
Re	Reynolds Number
RIE	Reactive-Ion Etching
RMS	Root Mean Square
SAW	Self Avoiding Walk
SBR	Signal to Background Ratio
SEM	Scanning Electron Microscope
SMD	Single Molecule Detection
SOI	Silicon On Insulator
SPAD	Single Photon Avalanche Diode
ssDNA	single stranded DNA
TE	Tris-EDTA Buffer
TTL	Transistor-Transistor Logic
USB	Universal Serial Bus
UV	Ultraviolet
VHDL	VHSIC Hardware Description Language
VHSIC	Very High Speed Integrated Circuit
Wi	Weissenberg number

Chapter 1 Introduction

1.1 Motivation and Project Aims

Work on deoxyribonucleic acid (DNA) spans more than a century and has expanded over the last fifty years since the structure of the molecule was described by Watson and Crick [1, 2]. In the 1970s the first complete genome sequence – of bacteriophage ΦX174 – was determined [3]. From this period to the present day there has been intense research interest in sequencing and analysis methods for dealing with large quantities of genetic material. The human genome contains approximately three billion base pairs [4] which equates to a total length of about a metre of DNA, coding for an estimated 20,000 to 25,000 genes [5]. Processing this amount of information is a time consuming process and in common with the Sanger method [3] many 'next-generation' methods [6] rely on polymerase enzymes which are limited to relatively short read-lengths and themselves introduce errors [7].

Emerging technologies for direct sequencing without the use of polymerases include scanning methods such as tip-enhanced Raman spectroscopy [8] and electrical reading with nanopores [9]. While the former is limited by low scanning speeds, nanopore sequencing shows great promise for rapid sequencing of long DNA strands. Both natural [10] and synthetically fabricated pores [11] are small enough to constrain a DNA strand to pass through with nucleotides in single file. As the strand passes through the pore, it can be interrogated in several ways. The ionic current through an α-hemolysin pore for example, shows a characteristic decrease when the pore is blocked by a DNA strand, although since several bases are present in the pore at a given time it is not possible to detect individual bases using this signal alone. Label-free modifications to this basic detection scheme include attaching an exonuclease enzyme to the pore to cleave nucleotides from the leading end of the DNA strand and thus cause them to pass through the pore singly and embedding tunnelling probes into the pore to measure the transverse electron current as the strand passes through. To date however, the small physical size of each nucleic acid base and the high transit rate of the DNA through the pore (~1

nucleotide per microsecond) has frustrated attempts to obtain single nucleic acid base resolution and identification [9].

There is no doubt that fast, label free and cost-effective sequencing of DNA would represent a significant step for genomic analysis, however, detailed sequence knowledge is not necessary in all applications. Early genomic mapping was achieved by labelling whole chromosomes using fluorescence *in-situ* hybridisation (FISH) [12] and more recently low resolution genomic analysis has been applied to detect chromosomal aberrations [13], for comparative genomic investigation [14] and for typing microbial organisms [15].

The megabase resolution of FISH was improved by the development of the technique on naked DNA strands rather than chromosomes, known as fibre-FISH, which gave a resolution of 1-300kbp [16]. Fibre-FISH relies on 'molecular combing' of DNA strands, meaning that they are attached by one end to a surface and uniformly extended across the surface by the action of a receding meniscus [17]. The uniform extension allows distances between labelled sites to be measured in space and the base-pair separations inferred [13].

A fibre-FISH sample takes time and skill to prepare and is not especially amenable to high throughput applications. Two key techniques are currently available for low resolution mapping: entropic confinement of DNA strands in nanochannels [18] and direct linear analysis (DLA) in microfluidic devices [19]. DNA may be driven into a nanochannel by means of an applied electric field and the uniformity of molecular extension is acceptable for genomic analysis [20]. In such devices, DNA is typically loaded to a microfluidic channel which is used to access a nanochannel array in such a way that the entire volume of fluid does not flow through the nanochannels. This means that DNA is loaded into the nanochannels at the discretion of the user and operation is not continuous which may limit throughput, although useful resolution of around 1.5kbp has been demonstrated [21].

Direct linear analysis is typically performed in a microfluidic device and involves elongating DNA by means of fluid interactions, primarily elongational flow [19, 22]. DNA strands flow through an optical detection region after elongation and the

position of fluorescently labelled probes that are hybridised to the strand is deduced from the variation in detected signal. This approach offers high throughput and sensitivity through continuous operation and the use of confocal spectroscopy, which offers proven resolution down to approximately 4kbp [23]. The fact that the DNA flows through an excitation volume removes the need for high (optical) resolution imaging of larger areas, as is the case with fibre-FISH and nanochannel arrays.

The performance of DNA stretching by elongational flow is highly dependent upon the molecular conformation when the strand enters the flow [22, 24, 25]. The focus of the work presented in this thesis is to improve the preconditioning of DNA strands in microfluidic shearing flow in order to improve the molecular extension caused by an elongational flow and thus improve the performance of a DLA system. In essence, the DNA strand must be arranged approximately linearly when it enters elongational flow in order to ensure effective extension. The design, fabrication and characterisation of microfluidic devices that demonstrate such improved preconditioning is described in this thesis. It is established that an improvement to stretching performance can be attained through the application of small effects of laminar flow during shear-preconditioning.

1.2 Summary of Main Achievements

Microfluidic devices were fabricated in silicon with a borosilicate capping layer and used in conjunction with a bespoke confocal optical detection system to measure single molecules of DNA. These devices comprise novel, in-plane interconnects providing access to a DNA preconditioning channel which is connected to an optical interrogation channel by a taper. The DNA molecules are partially straightened in the preconditioning channel prior to being stretching by the elongational flow in the taper and optically interrogated immediately after extension.

A new method for microfluidic preconditioning of DNA molecules in shearing flow has been demonstrated to provide a performance improvement for a simple funnel stretching system. This method uses channels which are physically much larger than the DNA strands they manipulate, which provides the possibility for low loss, high throughput devices.

A novel application of a known phenomenon of deep reactive-ion etching (DRIE) was used to fabricate microfluidic interconnects. This has been demonstrated to be effective in reducing loss of sample due to fouling in the loading of long polymers from world to chip. This high efficiency connection requires only common silicon processing equipment and requires no features in the borosilicate capping layer.

1.3 Thesis Structure

A review of the literature relating to the key technologies and methods for single molecule DNA manipulation and genomic analysis is provided in chapter 2. As outlined above, a wide variety of methods has been developed to read information from DNA molecules of sizes from a few bases to whole chromosomes and the appropriateness of a microfluidic solution for genomic analysis applications is evaluated in this context.

Chapter 3 provides a more detailed discussion of the behaviour of DNA in microfluidic systems and presents the theory and design behind the preconditioning channels. These form the basis of a device which manipulates long DNA strands on a length scale much smaller than the channel width and thus allows the performance of stretching by elongational flow to be improved.

An investigation into the application of the DRIE-lag phenomenon to form a sloped interconnect in order to improve the yield of DNA delivered from 'world-to-chip' is presented in chapter 4. This includes a discussion of alternative interconnect fabrication strategies that have been reported recently as well as some background on the nature of the DRIE process and etch lag effect. In light of this investigation an improved interconnect was designed and fabricated and this is described in chapter 5.

Chapter 6 details the experimental verification of the interconnect and preconditioning channel designs. Quantitative, real time polymerase chain reaction (qPCR) is used to measure the transit efficiency of 48.5kbp DNA strands passing through the fabricated microfluidic device. A confocal optical detection system was

built for the evaluation of the lengths of fluorescently labelled DNA strands within the microfluidic device. This system was used to compare several devices with different preconditioning channel designs. In each case a fixed funnel geometry is used to apply an elongational flow after the preconditioning stage and the extension of the DNA strands is measured immediately after the funnel using confocal detection of fluorescent dyes and single photon counting techniques.

Finally, chapter 7 discusses the conclusions that may be drawn from the results that have been presented in this thesis and offers some suggestions for future research opportunities.

Chapter 2 Literature Review – Extending DNA Molecules

This section presents a review of some key methods and technologies used for DNA extension. Practical methods for extending and probing single molecules of dsDNA have been developed within the last 20 years and range from experimentally simple surface techniques to the fine control available with microsphere-bound strands and optical tweezers. The central focus here is on the extension of 'free' molecules, i.e. without surface or microsphere attachment. Both nanofluidic and microfluidic methods for stretching free molecules are considered and their relative merits are assessed.

2.1 Introduction

DNA is an excellent model polymer because it is readily visualised with fluorescent labels [26], molecules of a wide range of known lengths and sequence are readily available and the general structure [2] is well defined having long been a matter of scientific interest. In addition to this, DNA is of crucial interest to biologists for the information it provides about the fundamental make up of an organism. To quote a recent review;

"Although the whole truth is by no means revealed by a DNA analysis, the information-to-effort ratio is so far unsurpassed by the identification and sequencing of other important biomolecules." [18]

DNA has been extensively studied from a wide variety of scientific viewpoints and a wealth of information is recorded in the literature. In this review, the central focus is on the behaviour of double stranded DNA (dsDNA) in miniaturised fluidic systems and the methods which are available to read genomic information from these molecules *in-vitro*. The complexity of genetic analysis means that there is a requirement for mapping and analysis at various levels of granularity. Staining chromosomes, fluorescence *in*-situ hybridisation (FISH), fibre-FISH, polymerase chain reaction (PCR), restriction mapping and sequencing have all played their part in building understanding over the last 35 years [3, 27-31]. The scale of these

techniques covers a corresponding range, from test tubes, to glass capillaries, microfluidics and nanofluidics.

For many applications, the highest level of detail, the base sequence itself, is not necessarily required. Typically for genomic analysis, a method is sought to uniformly straighten the DNA strand in order that relative distances between sites identified by fluorescent probes may be interpreted in terms of their position on the strand; a number of different methods of DNA stretching are discussed below.

2.2 Entropic DNA Stretching in Nanochannels

Although conceptually a simple method of polymer elongation, entropic confinement has only recently become accessible for DNA studies as nanofabrication methods have evolved. An overview of nanochannel fabrication methods is therefore provided here before the DNA extension performance of such devices is considered.

2.2.1 Nanochannel Fabrication Methods

The diffraction limit makes conventional photolithography of sub-500nm features challenging. Therefore to probe the behaviour of DNA in channels with characteristic sizes below the radius of gyration – or even below the persistence length (the distance over which a polymer behaves like an elastic rod) – alternative fabrication techniques are required. Approaches for nanochannel fabrication may be broadly split into moulding/stamping, bulk etching and sacrificial layer methods. Examples of each type of technique are given here.

Nanoimprint lithography (NIL) was demonstrated in 1995 as a method of mass producing sub-50nm structures [32]. As shown in figure 1, the process employs a re-useable master to imprint patterns into a thermoplastic polymer film. In this case the master was patterned using electron beam lithography which is a serial process (and thus more time consuming than conventional photolithography) but each master can be used many times; the patterned master was etched by reactive-ion etching (RIE). Polymethylmethacrylate (PMMA) was spun onto the silicon substrate to create a 55nm layer. During patterning, the mould and PMMA are heated above the glass transition temperature of the PMMA (105ºC [33]), the mould is compressed

against the sample and the temperature then lowered below the glass transition temperature. The compression pressure must be controlled to ensure pattern reproduction and avoid breakages to the master mould. In this initial demonstration of the technique the authors were able to produce sub-25nm features.

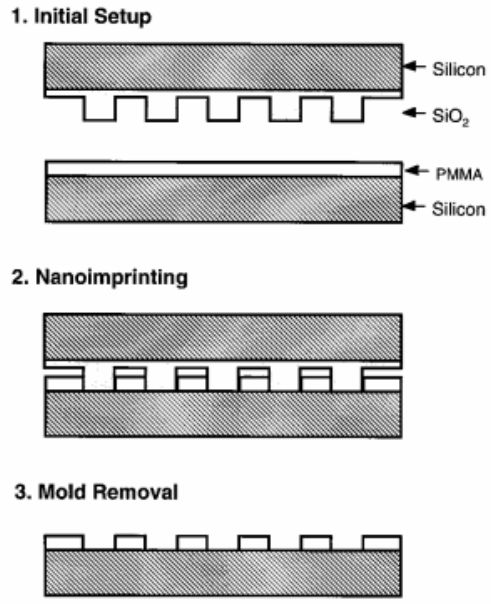

Figure 1, schematic of the nanoimprint lithography process: PMMA is heated above the glass transition temperature and compressed against a master mould, the PMMA is then cooled and the master removed leaving nanometre scale features [32].

An alternative technique based on sacrificial oxidation has been proposed to be capable of producing channels with widths down to 5nm [34]. The process is illustrated in figure 2; conventional photolithography is used to define the length and shape of the channel on a layer of amorphous silicon and the pattern is transferred by RIE. Silicon dioxide is then grown thermally to the required channel dimensions (b); different widths are available by altering the duration or temperature of the oxidation. A second amorphous silicon deposition is used to coat the wafer (c) and then chemical-mechanical polishing (CMP) is used to expose the oxide (d) for removal by buffered oxide etch (e). Finally the channels are sealed (f) with evaporated gold or plasma-enhanced chemical vapour deposition (PECVD) oxide. The authors report successful fabrication of a 10mm long, 25nm wide and 100nm deep channel and their process is CMOS (complementary metal-oxide-

semiconductor) compatible. The depth of the channels is determined by the initial thickness of amorphous silicon and the ingress of the capping layer.

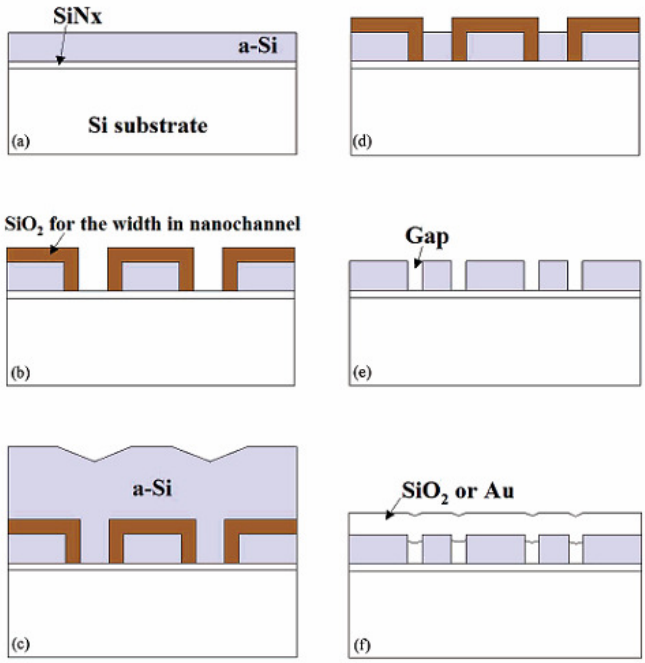

Figure 2, schematic process of nanochannel fabrication by growth of a sacrificial oxide layer [34]. A layer of amorphous silicon is deposited (a) and patterned by standard photolithography. Oxide is then grown to the required nanochannel width (b) and the gap backfilled with a second amorphous silicon deposition (c). The oxide is exposed by CMP (d) and removed with buffered oxide etch (e) leaving exposed nanochannels which can then be capped with oxide or gold (f).

For bulk nanomachining, reactive-ion etching (RIE) of silica can produce nanochannels with excellent feature definition. However, the surface roughness can be significant as shown in figure 3 which shows a microchannel interfacing with an array of nanochannels. This sample is fabricated with a single RIE to a depth of 100nm, the nanochannels are 90nm wide and the floor roughness is given as 10-20nm, attributed solely to the etching process [35]. Despite this roughness, glass may still often be a preferable material softer materials such as poly(dimethylsiloxane) (PDMS), particularly where strong confinement requires high mechanical integrity [36].

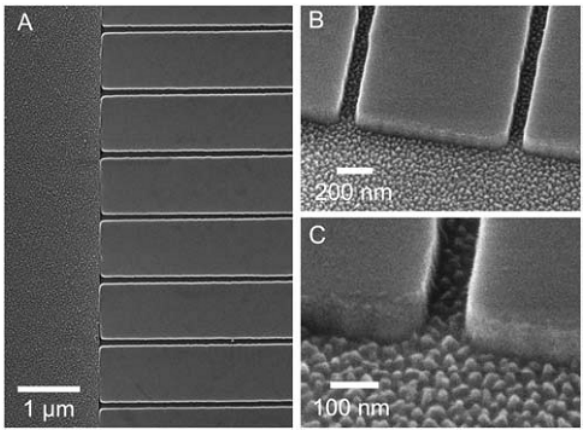

Figure 3, scanning electron microscope (SEM) of a microfluidic channel used as an interface to several nanochannels formed by RIE of fused silica [35]. The surface roughness is approximately 10% of the nanochannel dimensions.

Glass nanochannels with circular cross section have also been fabricated, using a polymeric fibre as a sacrificial template [37]. The electrospun heat depolymerizable polycarbonate (HDPC) fibres were removed by baking at 500ºC for 3h, producing nanochannels several micrometres in length. Optical detection of single molecules labelled with several fluorophores was demonstrated in these channels. For this measurement the channels were filled by capillary action. Although electrokinetic DNA loading should be possible, it may prove challenging to integrate the capillaries with larger fluid channels.

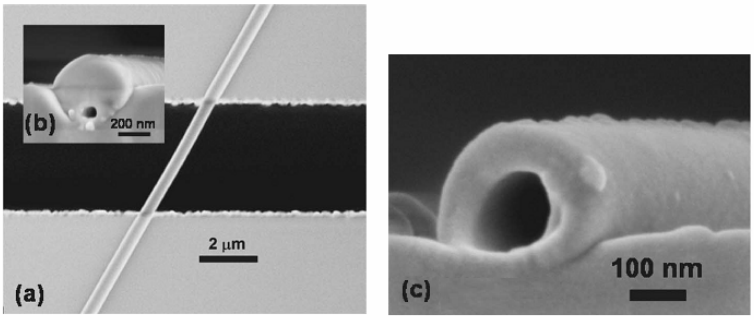

Figure 4, SEM micrographs of glass nanochannels formed around a sacrificial polymer fibre (adapted from [37]). (a) and (b) show 100nm inner diameter sputtered glass nanochannels grown over a 25µm-deep trench on a silicon substrate. (c) Shows a PECVD glass channel.

For fabrication methods that use bulk machining or stamping, the channels must be sealed with a capping layer. Capping of nanochannels at the wafer level requires either a clean planar surface in the case of glass bonding, or well defined processes to prevent clogging/non-uniform channel top-surfaces when sealing with an elastomer [38]. As an alternative, Cao et al. investigated the growth of a capping layer using tilted evaporation and sputter deposition of silicon dioxide. The growth of the capping layer is dependent upon the angle of tilt as well as the angular distribution of the deposited material. This means that additional material may be deposited on the sidewalls to reduce the channel size as the capping layer is grown.

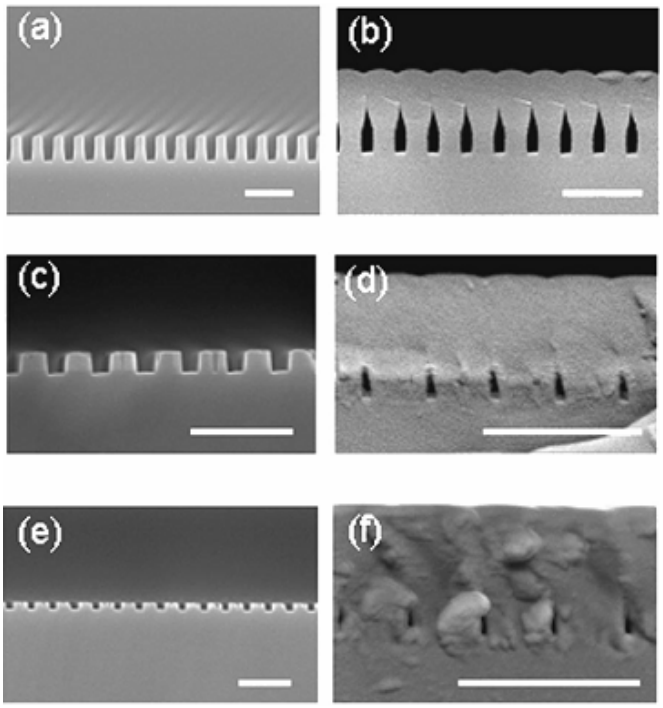

Figure 5, SEM images of nanochannels sealed by SiO_2 sputtering; scale bars 500nm [38]. The initial channel widths are: 85nm (a), 65nm (c) and 55nm (e); these channels are shown after growth of the capping layer in (b), (d) and (f) respectively. A channel width of less than 10nm was demonstrated as shown in (f).

Sputtering silicon dioxide also produces a transparent capping layer which is very thin and the team was able to demonstrate optical detection of single DNA molecules [38]. SEM images of these nanochannels in cross section are shown in figure 5, with different sizes produced by varying the initial width of the channels through 85nm (a), 65nm (c) and 55nm (e).

2.2.2 Conformation of DNA in Nanochannels

The behaviour of confined polymers was of interest to modellers long before nanofabrication techniques became commonplace. The three main arrangements are shown in figure 6; free in solution (top) the molecule adopts a random coil with a size determined by its radius of gyration, R_G. In a channel of characteristic size less than R_G (middle) the polymer may be modelled as a series of blobs as described by de Gennes [39]. When the characteristic length of the channel is less than the polymer's persistence length, P, it is modelled as reflecting from the channel walls with characteristic segment length λ as described by Odijk [40]. It should be noted that the transition from the de Gennes regime to the Odijk regime is gradual [41] but seems to occur when the channel width is around twice the persistence length [42]. As a guide, for λ-DNA in TE buffer (10mM tris-HCl, 0.1mM EDTA) at pH 8, P=50nm, R_G=0.5µm [43].

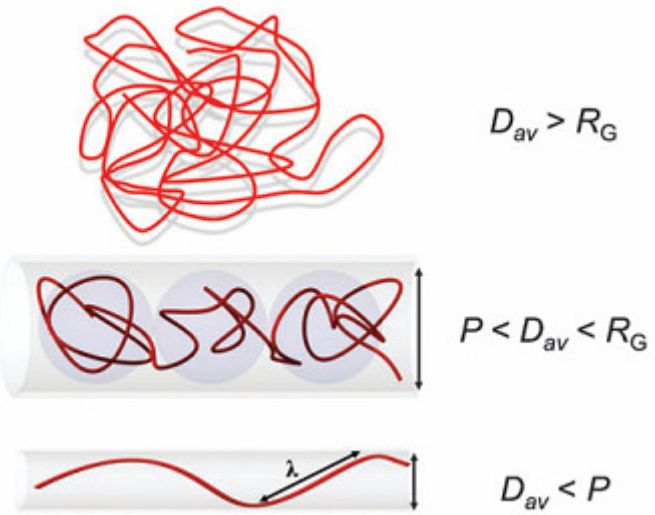

Figure 6, sketches of polymer conformation under increasing confinement [18], D_{av} represents the characteristic width of the channel, R_G the radius of gyration and P the persistence length. In free solution the random coil (top) is the most likely conformation, conformations adopted due to increasing confinement are modelled by the de Gennes regime (middle) and Odijk regime (bottom).

As the dynamic properties of DNA are somewhat dependent upon the suspending medium, it is possible to strengthen the confinement by changing the medium rather than the channel size. By adjusting the ionic strength of the buffer, DNA stretching to fractional extensions of greater than 0.5 was demonstrated in channels of 1µm by

100nm fabricated using conventional photolithographic processes. The persistence length of the DNA in the low ionic strength buffer was up to 122nm [20]. One drawback of this technique is that the low salt concentrations preclude the use of most DNA enzymes. The team therefore performed extensive preparation of the DNA samples with standard laboratory techniques prior to loading the DNA into the micro/nano fluidic device which itself was only used to stretch and hold the DNA for imaging. Figure 7 shows stretched DNA (white) after loading into the nanochannels, the location of one nanochannel is indicated by the blue lines. The electric field was switched off prior to imaging. The yellow traces are fluorescence intensity profiles which can be used to identify regions such as loops and folded ends which have a characteristic increased intensity.

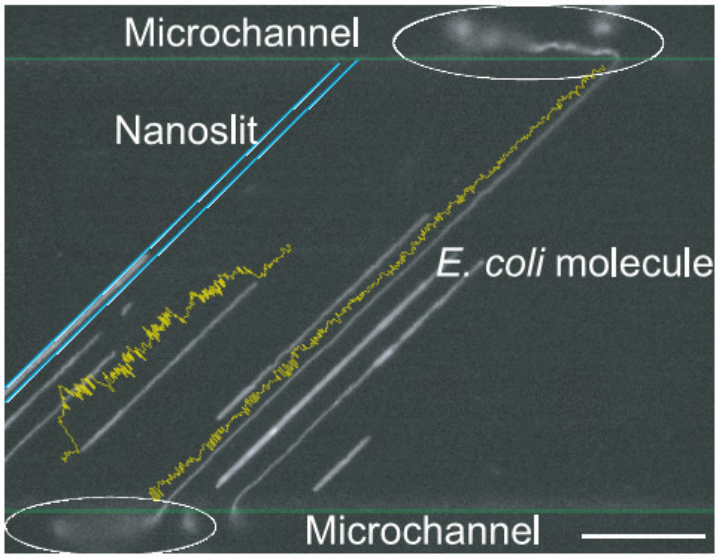

Figure 7, fluorescence image of DNA stretched by confinement in 100nm by 1µm channels; capillary action loads the DNA into the microchannels, an applied electrical field loads strands into the nanochannels. A large E. coli molecule can be seen to extend beyond the length of the nanochannel and the relaxed ends of the molecule within the microfluidic channel are highlighted by the ellipses. The scale bar represents 20µm [20].

As the relaxed dimensions of DNA strands (radius of gyration ~1µm [20]) are larger than the characteristic nanochannel dimensions they are highly unlikely to spontaneously enter the channels by diffusion. As the resistance to flow of a nanochannel is large, pressure driven flow is often impractical [18] and electrokinetic loading is commonly used [20, 35, 44]. The electric field may be

switched off after loading and thus the DNA observed in equilibrium, as is the case with figure 7.

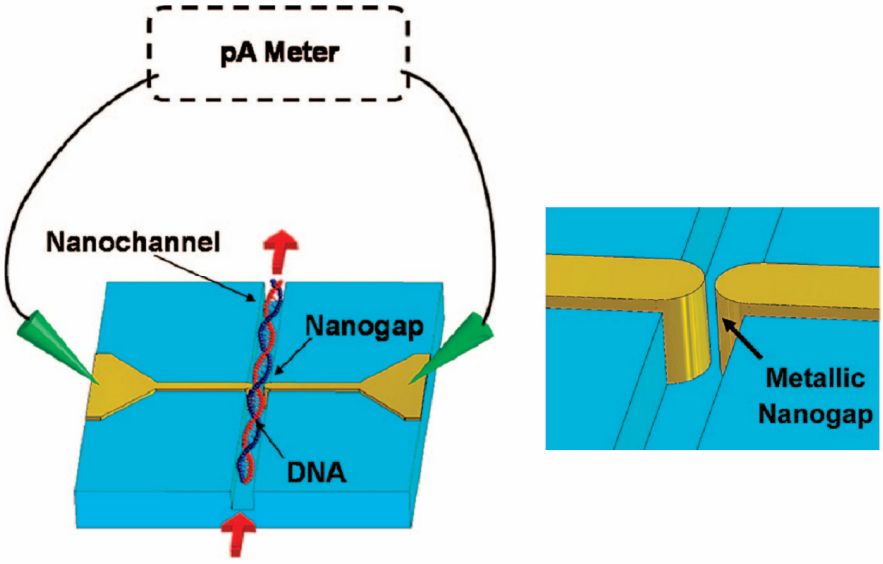

Figure 8, schematic of electrical DNA detection in a nanochannel using a metallic nanogap [45]; the DNA is insulating relative to the surrounding buffer and is detected by negative pulses in the current across the gap in the nanowire (right).

In addition to optical detection, electrical detection of DNA is possible in nanometre-scale devices. Although more commonly used in nanopores (e.g. [46]), electrical detection has also been demonstrated in nanochannel devices such as that illustrated by figure 8. For electrical probing of DNA a nanochannel is more convenient, since a nanopore relies on DNA entering the absorbing region by diffusion [46] whereas a channel device is more amenable to direct electrokinetic loading. The device in figure 8 is patterned by NIL and the channel realised by RIE; the pattern for the electrodes is transferred to a resist layer by NIL and metal deposited by evaporation with the final pattern realised by lift-off. Tilting the sample during the evaporation process shields parts of the channel from metal deposition; the nanowire is therefore not continuous but has a gap of several nanometres [45]. The authors fabricated several different gap sizes; an 18nm gap was too large to detect DNA, some detection was possible at 13nm and a 9nm gap (16nm height) showed clear signal pulses caused by DNA molecules proceeding through the gap.

A classic example of a genomic analysis technique is restriction mapping, in which genomic DNA is digested by restriction endonucleases and the resulting fragment lengths are analysed. Riehn et al. demonstrated restriction mapping in a quartz nanofluidic device using electrokinetic magnesium delivery to control the reaction [21]. The device is a typical arrangement of a nanochannel array accessed via a perpendicular microchannel at either end (see figure 3 (A) for an SEM image of a similar device). The input microfluidic channel contained a mixture of fluorescently labelled DNA and restriction enzymes in a buffer containing ethylenediaminetetraacetic acid (EDTA). EDTA is a chelator which binds to magnesium which is a cofactor for the restriction enzyme. The enzyme's action is thus inhibited; it binds to the DNA but does not digest it and the enzyme-DNA complex is loaded into the nanochannel. The outlet microfluidic channel contains an excess of magnesium ions which are loaded into the nanochannel array under electrokinetic control. Activation of the enzyme is thus constrained to take place in the nanochannels where the restriction digestion of stretched DNA may be observed.

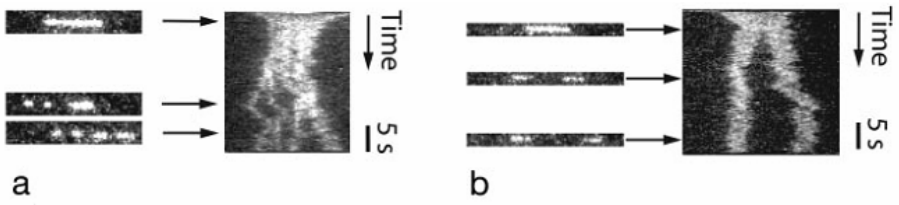

Figure 9, fluorescence images of restriction of λ-DNA in nanochannels of 100-200nm by the enzyme SmaI (a) and SacI (b) [21]. The time traces use one line per frame of data captured by CCD camera to produce a composite image.

The DNA is stained with an intercalator for optical detection; the low staining ratio (1 dye molecule per 20 base pairs) apparently does not inhibit the action of the enzyme. Figure 9 shows the restriction digestion of two DNA molecules, each by a different enzyme, with a composite image showing the variation over time. The different channel widths lead to an estimated DNA extension of 40% of contour length for figure 9 (a) and 30% for figure 9 (b). Although the stretching proportion is low, the nature of confinement in a nanochannel means it is independent of total molecular length and therefore the restriction fragments can be measured on the same length scale (i.e. same number of base pairs per pixel) as the intact molecule.

Nanochannels offer reproducible DNA extension that is independent of molecular length (above a known threshold) and via straightforward electrokinetic control deliver stationary molecules for imaging. Questions remain over the throughput available from these devices and in common with microfluidic devices, sample loading efficiency and the proportion of input molecules delivered intact are less widely reported.

2.3 Microfluidic DNA Stretching

Microfluidic DNA manipulation offers a possibility for high throughput and single DNA molecule detection. While detection of every DNA strand in a sample is an unnecessary goal for most practical applications, optimising the proportion of molecules detected is necessary for rare-molecule detection. Nanofluidic systems typically load a large number of molecules into a microfluidic channel which is aligned perpendicularly with an array of nanochannels. A sample of these input DNA molecules is loaded into the nanochannel array and thus the excellent stretching performance of the nanochannels is applied only to a subset of the total population of DNA strands. By contrast, the world-to-chip interface is more straightforward for a microfluidic system, which can therefore potentially sample a higher proportion of the input molecules. Genomic analysis techniques cover a wide range of resolutions and as such the best performance can usually be attained by choosing a strategy that is appropriate for the target problem. Where coarse-grained analysis is sufficient to identify a genomic variation of interest, it is appropriate to choose a system that gives satisfactory rather than optimum resolution if there are benefits in throughput, proportion of input strands analysed and device complexity.

Methods of microfluidic stretching may be broadly divided into those using tethered DNA molecules and those using free molecules (*i.e.* strands not tethered to beads or surfaces). Conjugating DNA to beads [47] or surfaces [48] provides a degree of control over individual molecules which allows flow-stretching dynamics to be investigated, as well as a means of producing DNA arrays. However the conjugation step increases experimental complexity which in turn reduces throughput. DNA stretching of free strands can be achieved using elongational or shear flow (or more commonly a mixture of both) in a cross slot [24], funnel [19], or a hydrodynamic

focusing device [49]. Further details of the behaviour of DNA in these flows are given in the chapter 3; some examples of devices applying such flows are presented below.

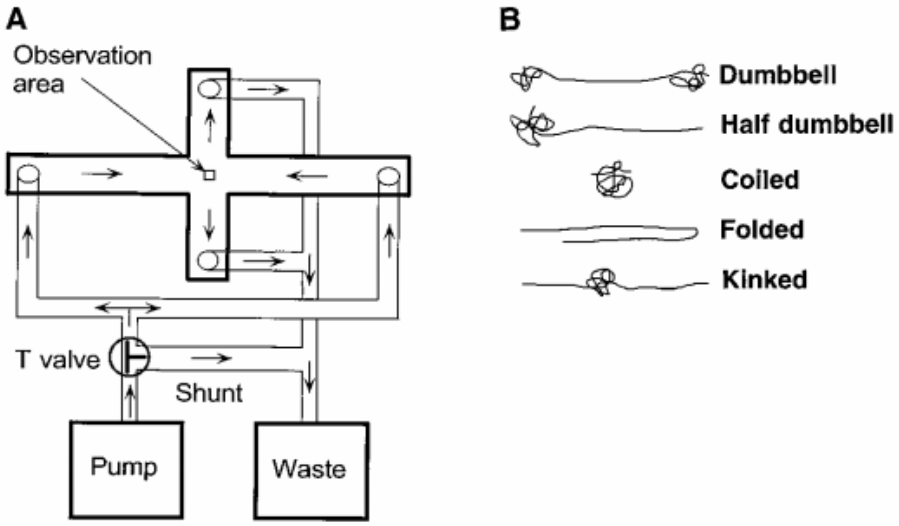

Figure 10, (A) schematic of a cross-slot microfluidic device for the generation of an elongational flow; the valve is used to switch on the flow as observation beings in order to capture the equilibrium state of the molecules in the observation region prior to stretching. (B) Illustrative sketches of commonly observed DNA conformations under elongational flow [24].

Figure 10 shows a schematic of a cross-slot device in which a sudden elongational flow is generated in the observation area by switching on the flow using a valve. Combined with a viscous solvent, this setup allows observation of the elongation of individual λ-DNA molecules from an initially relaxed state by video fluorescence microscopy. Although a continuous spectrum of DNA conformations was observed using this device [24], the authors report that some transient conformations are more common – these are shown in figure 10 (B). An extension of λ-DNA of up to 80% of contour length was demonstrated using this method, although stretching performance was strongly dependent on the initial conformation of each strand, with folded and coiled molecules stretching less readily.

Figure 11 shows the hydrodynamic focusing device used by Wong *et al.* to demonstrate stretching of T2 DNA (164kbp) to around 60% of its contour length [49]. As with the cross-slot device, an increased buffer viscosity was used to allow

observation of strands by fluorescence video microscopy. One significant benefit of stretching by hydrodynamic focusing is that the DNA solution is bounded on two sides by fluid rather than the channel walls, which relaxes the no-slip condition on the DNA solution. This leads to increased homogeneity of flow in the transverse direction and potentially provides more consistent DNA stretching, although there is still a strong dependence on the initial conformation.

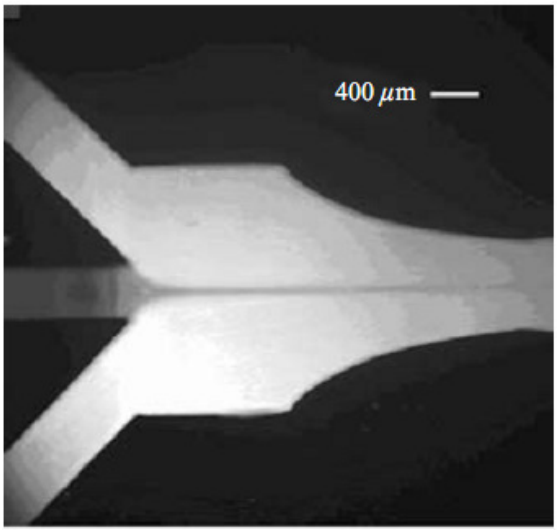

Figure 11, microscope image of a microfluidic channel used to study the effect of hydrodynamic focusing on DNA [49]. The DNA sample is injected via the central channel (flowing left to right) and focussed by the sheath flow from the side channels.

The layout of a funnel-based DNA stretching device reported by Chan *et al.* is illustrated in figure 12 [19]. The post array was included to precondition the DNA strands, although the authors found that the shearing flow present as a result of the device dimensions (channel height of 1μm) was the dominant factor in preconditioning and subsequently focussed their efforts on similar devices without posts [22]. The device pictured in figure 12 was reported to stretch 28% of all detected molecules (of λ-DNA) to the contour length of the unstained molecule [19]. The unstained contour length of λ-DNA is approximately 75% of the reported contour length of the molecule when saturated with intercalating dye. Chan *et al.* state that the peak at the contour length of the unstained molecule is a result of the sub-saturation staining ratio.

Preconditioning of DNA strands to prevent molecular folds impeding the stretching performance of elongational flows has been acknowledged as a critical step in microfluidic DNA extension [25]. However, comparatively little work has been done beyond applying a high shear rate that is present as a result of the device dimensions (e.g. [19]). To fully realise the benefits of genomic analysis in microfluidic systems more work is required in the area of preconditioning.

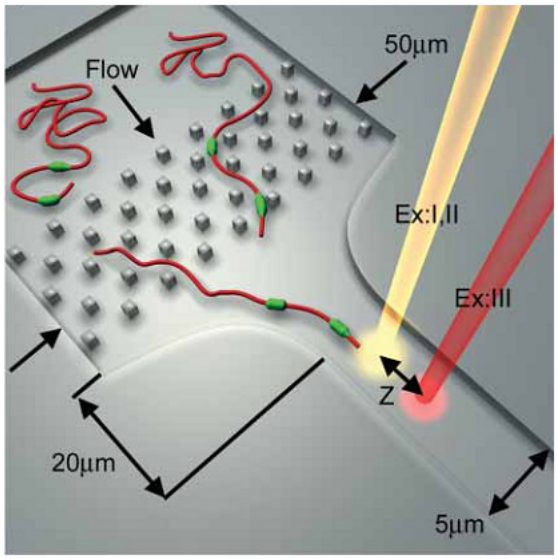

Figure 12, schematic of a microfluidic device which stretches DNA using fluid acceleration in a taper, the post array is designed to unravel the DNA strands prior to stretching and the strand length is deduced from the residence time in one laser spot and the speed of travel over the known distance (Z) to the second spot [19].

2.4 DNA Stretching on a Surface

In the mid 1990s, a technique called molecular combing was developed to stretch genomic DNA molecules over a surface. Briefly, a glass surface is treated with silane in order to facilitate the attachment of one end of a DNA strand. The surface may then be coated with protein to render it hydrophilic. A droplet of DNA in solution is spread over the surface and allowed to dry in air. As the meniscus at the air/water interface recedes across the glass, it stretches the DNA molecules and affixes them to the surface. This action only takes place at the interface and therefore long and short molecules are stretched by an equal proportion [17, 50].

Figure 13 shows the probability distributions of the observed molecular length for λ-DNA stretched on hydrophobic (A) and hydrophilic (B) glass surfaces. In both cases the DNA strands are intercalated with YOYO-1 prior to stretching. DNA stretched on the hydrophilic surface showed a peak extension around the unstained contour length of 16.5μm, while DNA stretched on the hydrophobic surface showed a peak near 22μm, the contour length of a λ-DNA molecule saturated with intercalator [51]. The performance of the method is dependent on the surface quality; in this case 70% of the molecules in a sample were stretched [17]. The uniformity of DNA extension provided by molecular combing makes it suitable for DNA mapping applications and it has been adopted as a refinement of the technique of fluorescence *in-situ* hybridisation (FISH) known as fibre FISH.

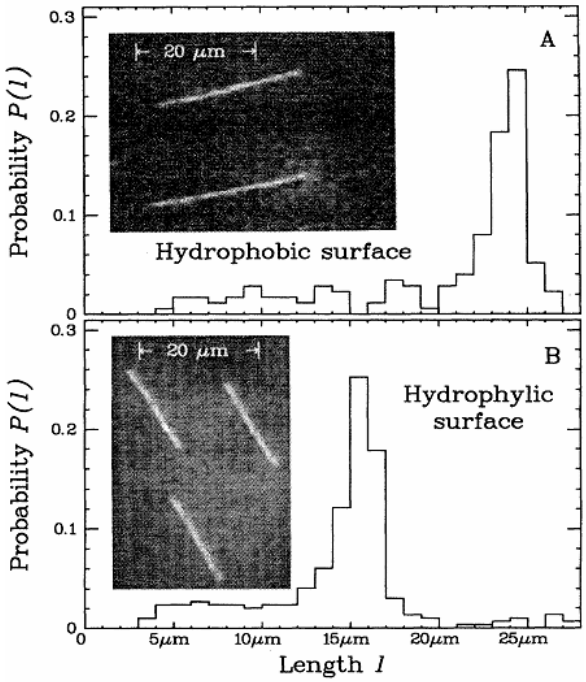

Figure 13, probability distributions of λ-DNA lengths when intercalated with YOYO-1 and stretched on a surface with a receding meniscus. The peaks are around the stained (A) and unstained (B) contour lengths for hydrophobic and hydrophilic surfaces respectively [50].

2.4.1 Fluorescence in-situ Hybridisation

Early optical genomic mapping had relatively coarse resolution and was performed by fluorescence *in-situ* hybridisation. In this procedure, whole chromosomes are

isolated from a cell and fluorescently stained for gene or chromosome identification. Sites of interest are highlighted with DNA hybridisation probes bearing fluorophores. An example is shown in figure 14, in which a fluorescently labelled DNA probe specific to chromosome 11 is used [52].

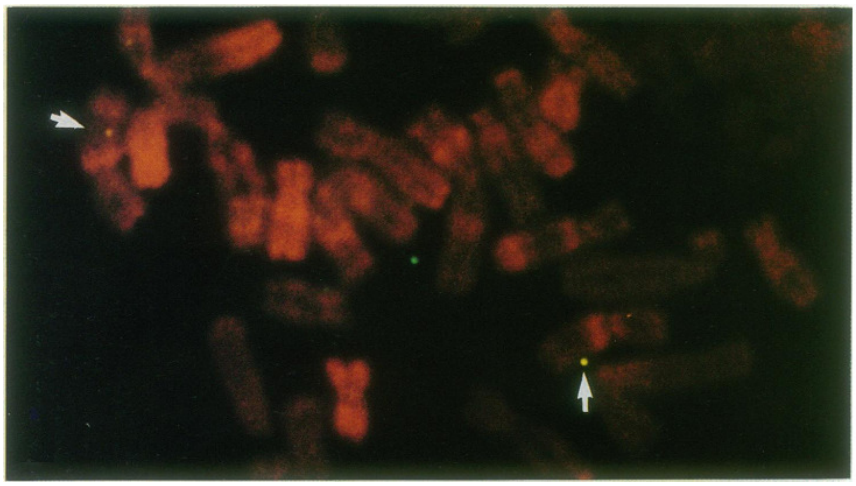

Figure 14, fluorescence image of FISH performed on metaphase chromosomes (stained with propidium iodide) with arrows indicating hybridisation signals on both copies of chromosome 11 [52].

In this example illustrating the state of the art in 1990, the probes are 1kb in length and metaphase chromosomes are used. The resolution of metaphase FISH was limited to probes spaced approximately 1Mb apart although a 10-fold increase in resolution is available using interphase chromatin [53]. In the quest for increasing resolution (approximate limits shown in table 1), the technique evolved into fibre-FISH in which individual DNA fibres are stretched and visualised (*cf.* [16, 28, 53-55]).

Technique	Resolution	Ref.
Metaphase FISH	1-3Mb	[28]
Interphase FISH	50kb – 1Mb	[55]
Fibre FISH	1-300kb	[16]

Table 1, resolution of common FISH techniques; chromosomes at different points in the cell are more or less tightly wound, fibre FISH is applied to single pieces of linearised DNA.

Although long DNA strands can be extracted from cells, they are prone to breakage either through shearing or when deposited on a microscope slide [54]. As the chance of this happening increases with the length of the strand there is an upper limit to the applicability of fibre FISH as shown in table 1. The method gives good visualisation of genomic changes such as deletions, translocations and duplications and the uniform stretching of each strand makes fibre FISH a good way to measure separations between probes associated to specific DNA sequences on the same strand.

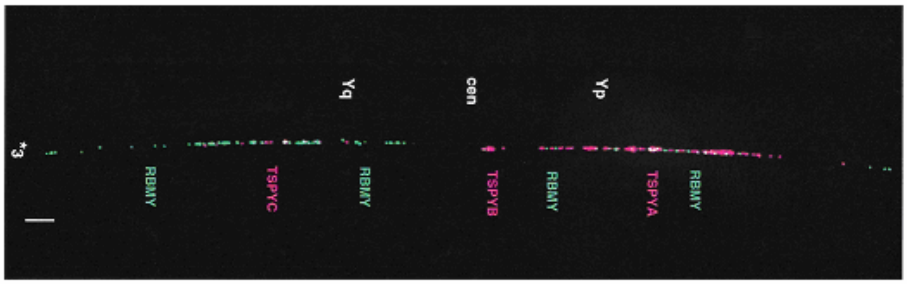

Figure 15, fluorescence image of DNA 'colour bar-coding' by fibre FISH indicating multicopy gene families (RBMY and TSPY) on the human Y-chromosome. The centromere (cen), long (Yq) and short (Yp) arms of the chromosome are labelled [56].

Figure 15 shows a single DNA molecule stretched on a surface and 'colour-bar coded' by fibre FISH. The human Y-chromosome has a large number of long and short repetitive sequences which makes it challenging to map. However, since fibre FISH can be applied to visualise the whole strand, it is possible to reveal the locations of repeat sequences as well as accurately sizing the separations. RBMY and TSPY, as seen in figure 15, are multicopy gene families which makes shotgun mapping [57] of the Y-chromosome more challenging but mapping by fibre FISH is still possible.

2.5 DNA Stretching with Optical/Mechanical Trapping

To explore the properties of a single piece of unstained DNA, the control available from optical trapping of a conjugated microsphere is unsurpassed. There are established methods for attaching dielectric and magnetic microspheres to both single [58] and double [59] stranded DNA. Typically one end is fixed, either by

grafting to a surface [60] or to a microsphere held in position (e.g. by pipette [61]), while the microsphere on the other end is pulled or twisted to stretch and/or coil the DNA [59, 62]. The force required to stretch and coil the DNA is inferred from fluctuations in the microsphere's position [59] or from the displacement of the laser beams in an optical trap [62].

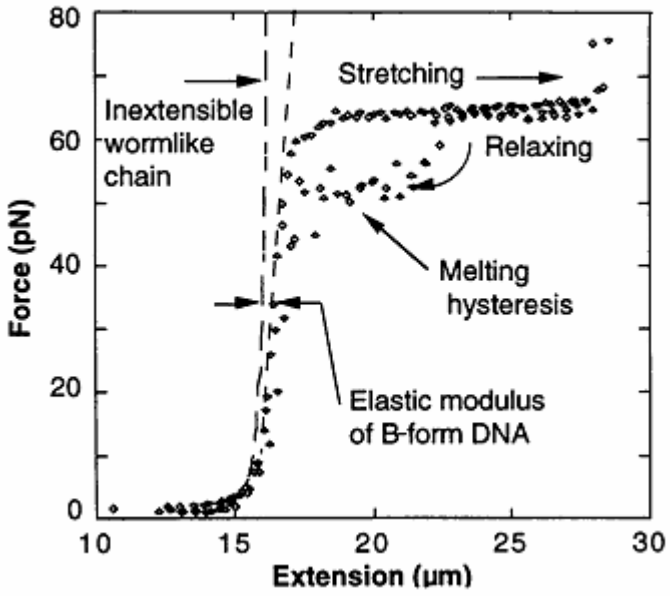

Figure 16, force-extension curve for double stranded DNA, produced by stretching λ-phage DNA at pH 8.0 (contour length 16.5μm) [62]. The wormlike chain model provides a good description of stretching below the overstretching transition that occurs around 65pN.

Stretching a molecule of double stranded DNA can take it through four distinct force-extension regimes: entropic elasticity, intrinsic elasticity, overstretching transition and finally the breaking of the covalent bonds [63]. Figure 16 shows the response of a single λ-DNA strand stretched by means of a latex bead attached to each end [62]. One bead is held stationary by a glass pipette while the other is held in an optical trap with position-sensitive photodetectors to measure displacement of the laser beam and infer the force. The contour length of λ-DNA is taken as 16.4μm and for an extension of up to 15μm (entopic elasticity region) force of less than 5pN is required. From 5-60pN the strand behaves elastically, while at around 65pN there is a sharp transition from B-form to S-form as the strand lengthens to approximately 1.7 times its contour length. This structural change is undesirable for experiments dependent upon intercalating fluorescent dyes or hybridising ssDNA probes and it is

the entropic unwinding region (where the wormlike chain model remains valid) that is of primary interest for such investigations.

B-form and S-form DNA are just two of the many different conformations of natural and synthetic DNA that have been observed [64]. B-form DNA is the most common conformation: a right-handed double helix characterised by an axial rise per nucleotide of 0.338nm and a turn angle per nucleotide of 36º, a major groove width of 1.17nm and a minor groove width of 0.57nm; the double helix achieves one complete turn over a distance of 10 base pairs [64]. At tensile forces above 65pN, a B-form DNA strand undergoes a cooperative transition to an overstretched S-form which is 1.7 times longer than its B-form contour length [61, 62]. The structure of S-form DNA is thought to be a double helix with reduced diameter and greatly increased base pair inclination and a 'flat-ribbon' ladder-like conformation [65, 66].

Studies such as that of figure 16 of DNA strands linked to beads or surfaces offer excellent control for making fine measurements and each molecule can be manipulated in a repeatable manner. However, for practical applications, simplicity and throughput considerations often make other methods necessary. Microfluidic extension of unmodified free DNA strands is dependent upon initial strand conformation [24, 25], but can reliably improve the average fractional extension of a sample (*cf.* [19]). The performance of the system as a whole must also be considered. Entropic confinement provides reproducible stretching that can be applied to a larger sample than is practicable with single-molecule methods that rely on trapping a conjugated microsphere, but it may still be unable to match the throughput of a larger microfluidic device.

2.6 Conclusions

A microfluidic platform offers several advantages for extension of free DNA molecules as a means to perform genomic analyses. Resolution of 4kbp is available with confocal optical detection of fluorescently labelled probes [23] and single molecule sensitivity has been demonstrated [67]. An elongational microfluidic flow can be generated by several methods which allow continuous device operation and thus offer the potential for high throughput [19, 24, 49]. The possibilities for high

throughput are enhanced by good world-to-chip connectivity which is generally more straightforward for a microfluidic device than it is for a nanofluidic device. The performance of an elongational flow for DNA extension of free strands is limited by the initial conformation of the molecules when entering the flow and thus a preconditioning step is vital to device performance [25]. A device with a high-efficiency world-to-chip connection and effective molecular preconditioning would therefore offer a significant advance in microfluidic genomic analysis.

Chapter 3 Design of Microfluidic Channels for the Extension of Free DNA Molecules

This chapter describes the design of the key elements of a microfluidic system for elongating long (*c*. 50kbp) DNA strands which are free in solution. The most reliable way to stretch a free DNA strand with only a fluidic interaction is to use an elongational flow. This may be generated in a variety of ways as discussed in chapter 2 (2.3), the simplest of which is a funnel in which the rapid reduction in channel size causes flow acceleration and lengthening of passing DNA strands. Used in isolation, the effectiveness of an elongational flow is limited by the initial conformation of the DNA strands as they enter it. Although in any microfluidic device the shearing effect of the laminar flow profile under pressure-driven flow will pre-stretch a DNA strand to some extent, the conformation of the strand as it enters the elongational flow is still a limiting factor [25] – this is shown schematically in figure 17.

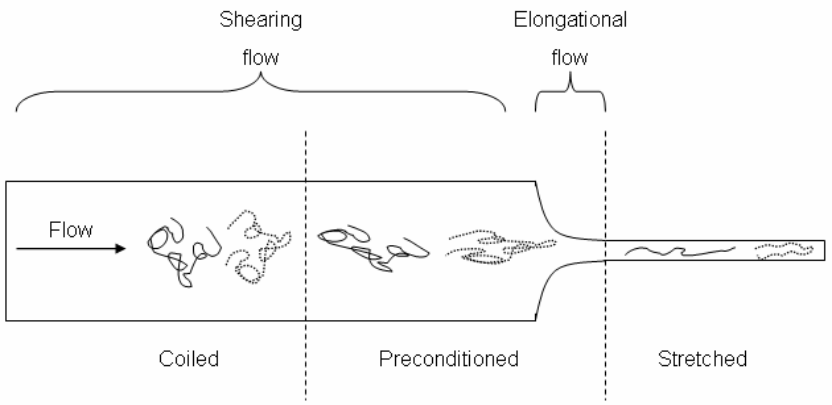

Figure 17, illustration of the key limitation of DNA preconditioning in a constant shear rate. The conformation immediately prior to stretching (labelled preconditioned) depends upon the initial conformation (coiled) and orientation, consequently after elongational flow (stretched) the overall extension may be limited by DNA conformation (dotted strand) rather than funnel stretching performance (solid strand).

The DNA strand represented by the dotted line and that represented by the solid line initially adopt a random coil conformation. The shearing effect of the parabolic

laminar flow profile stretches them both similarly, but because of the orientation of the coil and the relative positions of the ends of each strand, one is stretched to a linear conformation by the elongational flow (solid line) while the other is stretched in a folded conformation (dotted line).

The aim of the modelling work discussed in this chapter is to determine whether the preconditioning part of the scheme illustrated in figure 17 can be improved by altering the channel geometry, such that the overall system generates more reproducible DNA extension. A microfluidic solution to the DNA extension problem is pursued for reasons of throughput and potential for integration with other lab-on-a-chip components. There follows (in section 3.1) a review of literature that illustrates how the behaviour of DNA in a microfluidic system may be parameterised to allow predictions to be made about its behaviour in a microfluidic flow. Section 3.2 describes the methods that were used to model flows in various preconditioning channel geometries and section 3.3 describes the designs that were taken forward for later fabrication. Section 3.4 contains the modelling results that were obtained for the designs which were later fabricated.

3.1 Literature Review: Microfluidic DNA Deformation

In the cell, DNA exists in a variety of conformations – from supercoiled DNA packaged around histone and scaffold proteins to forming a chromosome, to relaxed, completely unwound sections – and different regions of the same strand may be in different states at the same time. In micro and nanofluidic devices however, the conformation of a DNA strand depends upon a number of factors including the local flow environment [68], the ionic strength of the buffer and channel dimensions [20], the size of the molecule and solution viscosity [69].

Any polymer chain in a good solvent (i.e. where interactions between the polymer and solvent molecules are energetically favourable) has the same universal features as a self avoiding walk (SAW) on a lattice [70]. In a non-flowing solvent therefore, a random coil is a good first approximation of the conformation of an individual molecule as this maximises its configurational entropy [71]. The size of a random coil is typically given as the route mean squared (RMS) distance of a chain segment

from the centre of mass of the molecule which is known as the radius of gyration (R_g). As an example, for λ-DNA saturated with the intercalating fluorescent dye TOTO-1, the radius of gyration is generally accepted as R_g=0.73μm [72].

3.1.1 Conformation of DNA Molecules in Laminar Flow

In a flowing solvent, a laminar flow profile is often sufficient to perturb the random coil conformation and cause entropic unwinding. A DNA molecule flowing in a capillary for example, shows conformational variation due to the interactions of different parts of each molecule with different parts of the flow field, appearing to expand and contract over time [73, 74]. Although clearly the laminar flow profile is continuous, it is conceptually useful to consider it as a series of discrete layers of different flow velocities. The behaviour of a long polymer such as DNA in such a flow is more interesting than that of a small molecule, since different parts of the DNA strand may be in different flow layers at the same time. The local movement of a section of a DNA strand is therefore dependent not only on the local flow conditions but also on the tensile force from adjacent length sections as well as on Brownian motion.

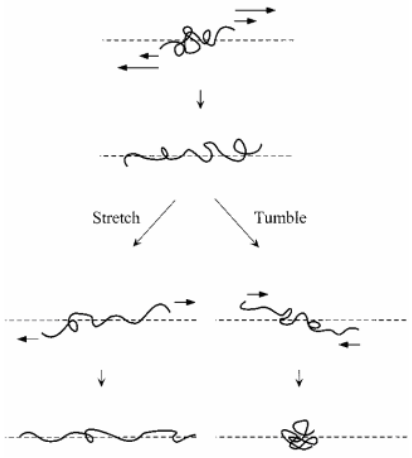

Figure 18, sketch of polymer behaviour in simple shear flow; a DNA molecule may be deformed from a random coil and subsequently stretch further or tumble and re-coil [68].

Although some typical DNA conformations such as a linear strand or a hairpin (folded strand) often occur in strongly deforming flows, the perturbations of Brownian motion are sufficient to move parts of a strand into different flow layers

with different velocities [75] and the conformation may not persist. For example, a perfectly straight molecule might be expected to be within a single flow layer and therefore each segment experiences the same fluid force propelling it axially. Diffusion of any part of the strand though, particularly the ends, can place a section of the molecule into a different flow layer which may cause a change in conformation or even end-over-end tumbling. This is shown in the case of simple shear by the illustration of figure 18; the fluid interaction is initially sufficient to straighten the DNA strand, but small fluctuations at either end of the strand are enough to cause it to either stretch further or tumble and relax into a random coil.

3.1.2 The Weissenberg and Deborah Numbers

In a microfluidic environment, a long polymer behaves very differently to a small molecule, as the local flow field can cause both stretching and tumbling as described above. Changes in conformation are dependent upon initial conformation as well as the flow to which the polymer is exposed. The local environment may expose a polymer molecule to different types of flow including shearing, elongational and rotational, with different magnitudes [68]. The strand will return to a random coil due to entropy and it does so with a characteristic relaxation time (τ_p) which is dependent upon solvent viscosity, polymer length and entropic confinement (e.g. in the case of narrow channels with width of the order of a persistence length, p). The effect of a particular flow field on a dilute solution of polymers is difficult to predict as the local environment for each one will be different. However, it is possible to characterise the flow in a device such that some general predictions may be made about average polymer behaviour.

Two dimensionless quantities are commonly used for this characterisation; the Weissenberg and Deborah numbers. These values combine the deformation time of the flow with the relaxation time of the polymer to allow predictions to be made about conformational change. The Weissenberg number is the product of the relaxation time, τp and the shear rate, $\dot{\gamma}$ (equation 1); the Deborah number (equation 2) is the product of the relaxation time and the strain rate parallel to flow, $\dot{\varepsilon}$. As the Weissenberg number approaches 1, the fluid forces become sufficient to cause

entropic unwinding and the polymer can stretch, although a stretched conformation may not be stable. Similarly a Deborah number of greater than 0.4 is sufficient to induce a coil-stretch transition [76].

$$Wi = \tau_p \dot{\gamma}$$

Equation 1

$$De = \dot{\varepsilon} \tau_p$$

Equation 2

3.1.3 Shear-Induced Migration of DNA in Microchannels

Another characteristic polymer behaviour in microchannel shearing flow is migration away from channel walls. It has been demonstrated both in theory [77] and in practice [78] that DNA in pressure driven flow in a microchannel migrates away from the channel walls. This effect is primarily due to hydrodynamic interactions between the molecule and the wall [79, 80] which cause a depletion region to develop at the edges of the channel. The thickness of this depletion region increases with shear rate [81], DNA size [78], DNA stretching [80] and concentration where solutions are non-dilute [82]. For the oscillatory flows that have been used to study this phenomenon there is an inverse relationship between oscillatory frequency and depletion layer thickness [78]. These factors are discussed with some specific examples below.

Chen *et al.* [77] present a Brownian dynamics simulation of DNA molecules in oscillatory pressure driven flow with some accompanying experimental results. By including hydrodynamic interactions between the polymer chain and channel walls they are able to model the migration of chains away from the walls which is found to increase as the Weissenberg number (Wi) increases. As a guide, their model suggests that the thickness of the depletion layer, L_d, is dependent on the equilibrium radius of gyration, R_g and Wi, giving $L_d/R_g \sim Wi^{2/3}$ for $Wi >> 1$. However the time for a fully developed concentration profile to appear scales as L_d^2/D, where D is the

diffusion coefficient. For λ-DNA in water saturated with the intercalating fluorescent dye TOTO-1, D=0.47μm^2/s, R_g=0.73μm, contour length, L=22μm [72].

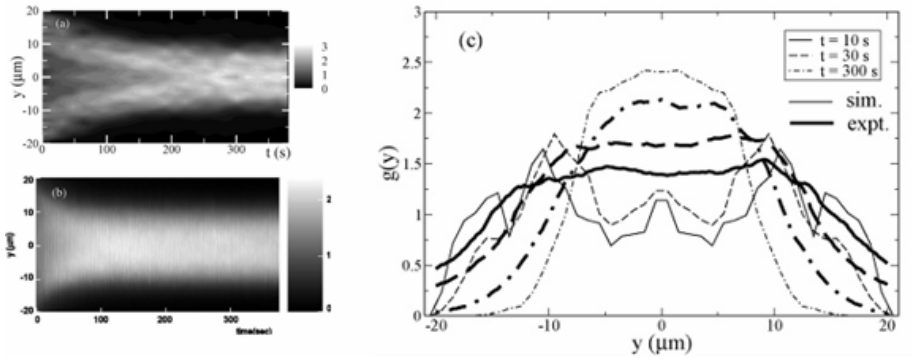

Figure 19, results showing shear-induced flow migration of DNA in microfluidic channels. (a) Simulation of chain distribution in a 40μm-side square channel with Wi=50, brighter regions showing higher concentration. (b) Experimental data for fluorescently labelled T2 DNA (164kbp) Wi=60 in a channel of the same size. (c) Chain density distribution for simulations (thin lines) and experiments (thick lines) [77].

Since the radius of gyration of a polymer scales as the square root of the number of monomers [70], this model predicts that L_d will be larger for longer molecules and higher shear rates. The results obtained by Chen et al. for a 40μm square channel are shown in figure 19, the increase in depletion layer thickness with time is clear for both simulation and experiment. Fluorescence smearing and concentration effects (often only single chains are simulated due to computational demands) are suggested by the authors as reasons for the smaller depletion regions observed experimentally, but it is clear that polymer chains cannot be expected to show a uniform cross-channel concentration distribution in steady flow.

The dependence of the time taken for the depletion layer to develop on the diffusion coefficient makes this a key parameter for successful modelling. Jendrejack *et al.* [83] showed that a non-free-draining model was necessary to observe polymer movement away from a wall in a microfluidic flow. The non-free-draining (Zimm [84]) model includes hydrodynamic interactions of solvent molecules within the coiled polymer chain that move with it and can be used to correctly model experimental data for diffusivity, giving a scaling relationship for diffusivity of $D \sim L^{-0.588}$ [83].

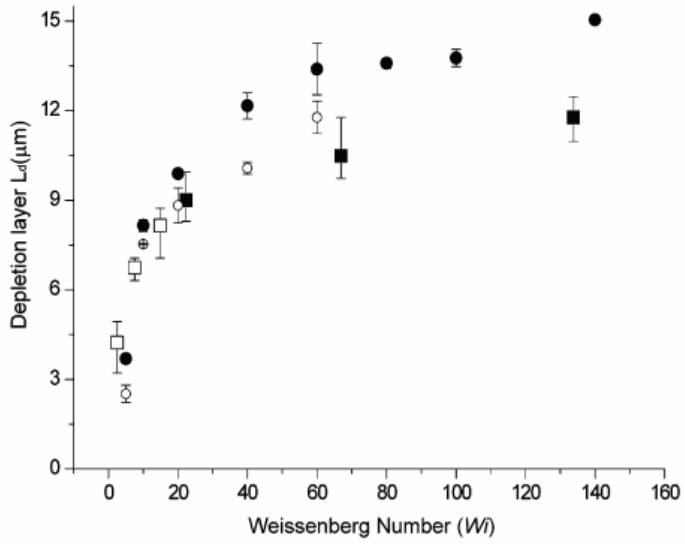

Figure 20, dependence of depletion layer width due to shear-induced flow migration on Weissenberg number, showing both experimental data (squares) and simulation data (circles). Results from T2 DNA (164kbp) shown as filled symbols, λ-DNA as open symbols; the channel dimensions were 40μm*40μm*8mm. Adapted from [78].

More detailed results illustrating the dependence of depletion layer thickness on Weissenberg number are shown in figure 20 [78]. The use of Wi allows comparison between different shear rates and DNA chain lengths. This graph shows that even at low Weissenberg numbers the depletion layer on one side of a channel may easily account for 10% of the total channel width, although the time taken for this layer to develop is long relative to typical flow times through microfluidic devices. At high Wi, the depletion layer could account for over 30% of the channel width, which is a significant confinement of the DNA in the central region of the channel. The confinement can be seen to be more pronounced for longer DNA molecules – the filled symbols represent T2-DNA which at 164kbp has a contour length more than three times that of λ-DNA.

3.1.4 DNA Extension in Elongational Flow

Although DNA may be stretched by shearing forces across a laminar flow gradient, more repeatable DNA stretching may be achieved using an elongational flow as the force on the molecule is typically greater and consistent in its direction along the

channel axis (whereas the direction of shear due to the laminar flow profile is different either side of the channel axis). A discussed in chapter 2 (section 2.3, page 17) there are several ways to generate an elongational flow; a simple funnel [22] is perhaps the easiest, while fluidic methods such as the cross slot [24] and hydrodynamic focusing [49] are also available. The variability of molecular residence time at the stagnation point of a cross slot device makes it less attractive for use in analytical applications, although for studying the effects of elongational flow such devices do offer a chance to observe the steady state molecular extension. The hydrodynamic focussing device of Wong *et al.* [49] creates a 'fluid funnel' to stretch the DNA. Applying different flow rates to the sheath fluid channels allows the DNA to be confined to a greater or lesser effect and gives control over the downstream position of the DNA within the device. Hydrodynamic focussing devices require little extra fabrication effort but do increase experimental complexity – producing stable and equal flow in the two side channels over long experimental times can be challenging.

3.1.5 Relating Shear and Elongational Flows to DNA Extension with the Weissenberg and Deborah Numbers

Figure 21 shows the mean fractional extension of a set of λ-DNA molecules exposed to a uniform shear flow in a 50μm gap between parallel glass plates as a function of different values of Wi (deforming effect of the shearing flow – labelled 'Shear') and De (deforming effect of the 'Elongational flow' – labelled as such) [68]. The data are time averaged for several individual strands: in shear flow, each strand does not assume a steady conformation but stretches and contracts as well as tumbling with time. The Weissenberg number for elongational flow in figure 21 is defined as the strain rate multiplied by the polymer relaxation time – this is more commonly referred to as the Deborah number as described in section 3.1.2.

In the case of elongational flow there is a sharp coil-stretch transition which is not seen in pure shear flow. The time dependent conformational variation in shear flow is mainly caused by tumbling. The strand does not necessarily tumble end-over-end in an elongated state; rather a small deviation from axial alignment of the stretched strand exposes it to a drag that allows it to recoil entropically. Results for higher

Weissenberg numbers (80<Wi<370) were produced by Duggal and Pasquali [85] using a glass plate and a roll to confine DNA to the observation region rather than two parallel plates as in [68]. They confirm the asymptotic growth towards a mean fractional extension of 0.5 for DNA strands in shearing flow.

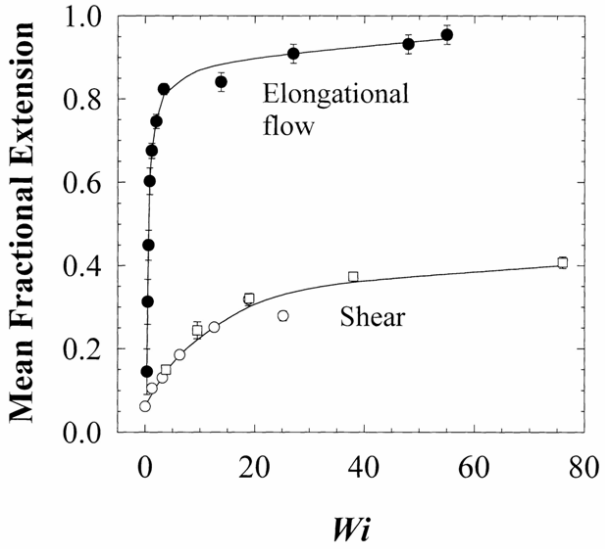

Figure 21, mean fractional extension of λ-DNA under shear and elongational flow; each point represents time averaged data for several individual DNA strands [68].

The channels described later in this chapter (in section 3.3) aim to pre-condition DNA molecules in shearing flow to reduce the proportion of folded strands in a sample and thus improve the stretching efficiency of a subsequent elongational flow. The results described above illustrate the capacity of shear flow to achieve this aim and also highlight the upper limit to its utility. The preconditioning channels presented below use varying-width rather than parallel-walled channels to allow Wi to be varied. The point of minimum Wi is normally at the channel axis, but where the width changes this point moves across the channel. This reduces the possibility of a molecule travelling the length of the channel at the point of maximum flow velocity and minimum Wi, thus increasing the chance that it will be subject to some deformation due to the shearing flow. The aim of the preconditioning channels is to produce a population of strands which have, on average, a greater fractional extension than those of the control case. Final stretching takes place in an elongational flow created be a taper downstream of the preconditioning channels. If

the preconditioning channels are effective, the proportion of fully stretched molecules downstream of the taper is predicted to increase.

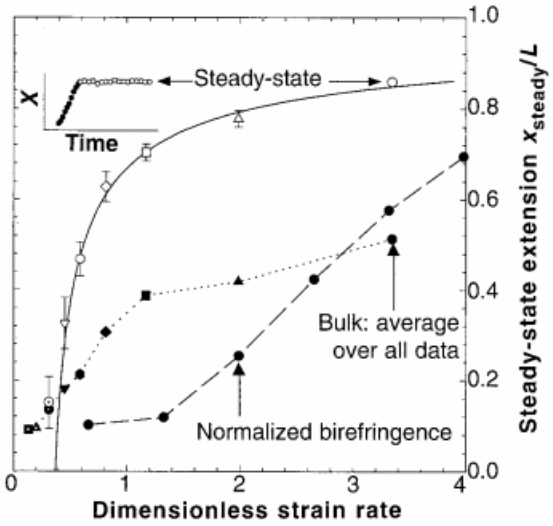

Figure 22, graph showing steady state extension of intercalated λ-DNA as a function of the Deborah number [76].

Clearly high values of De (Elongational Wi in figure 21) are capable of ensuring elongation of the DNA strand, but the key coil-stretch transition occurs at a relatively low value of De. A clearer presentation of the low De region was reported by Perkins *et al.* [76] and is reproduced here in figure 22, illustrating the critical value of De=0.5 for a coil-stretch transition [70]. This experiment used a cross-slot channel geometry (as illustrated in figure 10 (A) in chapter 2) which allowed the DNA to remain in the elongational flow for several seconds. A 'fully' stretched conformation therefore has time to develop and some molecular conformations were completely extended. However, folded strands took much longer to reach maximum extension (and frequently did not) whilst coiled strands rarely remained in the elongational flow for long enough to stretch significantly and their rate of extension was also lower, illustrating the value of a preconditioning step in molecular unravelling. For experiments in which the extensional flow is applied for a much shorter time, a higher value of De is necessary to generate a coil-stretch transition [70].

3.1.6 Conclusion

Various methods of microfluidic DNA deformation have been reported and the conditions required to ensure stretching of a single strand are well understood. For microfluidic extension of un-tethered strands, it is unlikely that every molecule can be fully extended, although preconditioning prior to an elongational flow can improve the average extension. The dimensionless Deborah and Weissenberg numbers may be used to characterise the strength of microfluidic flows in relation to molecular deformation and thus aid design of the critical elements of a microfluidic DNA extension system.

3.2 Methods for Modelling Microfluidic Channels

3.2.1 Comsol/Matlab Simulation

Finite element analysis (FEA) is an established method for finding numerical solutions to partial differential equations with applications in many areas of physics and engineering. Comsol Multiphysics (versions 3.5 and 4.0) was used to solve the Navier-Stokes equation for a variety of channel geometries. The Navier-Stokes equation (equation 3, [86]) characterises the three dimensional flow of a viscous Newtonian fluid, where ρ is the fluid density, V is the velocity vector, g is the gravitational force, P the applied pressure and μ the fluid viscosity.

$$\rho\left(\frac{d\vec{V}}{dt}+\vec{V}\left(\nabla\cdot\vec{V}\right)\right)=\rho g-\nabla P+\mu\nabla^{2}\vec{V}$$

Equation 3

The incompressibility condition for laminar flow is given in equation 4 and reduces the Navier-Stokes equation to the form shown in equation 5 ([86]).

$$\nabla\cdot V=0$$

Equation 4

$$\rho \frac{\mathrm{Dv}}{\mathrm{Dt}} = -\nabla P + \mu \nabla^2 \vec{V} + \rho g$$

Equation 5

The Reynolds number (Re) is the ratio of the inertial forces to the viscous forces and is used to give an idea of the characteristic flow in a fluid system. As written in equation 6, ρ is the fluid density, V is the velocity and μ is the viscosity; for a microfluidic system an approximate value of Re may be calculated by including a characteristic size, H [86].

$$\mathrm{Re} = \frac{\rho \frac{Dv}{Dt}}{\mu \nabla^2 \vec{V}} \approx \frac{\rho \vec{V} H}{\mu}$$

Equation 6

Microfluidic systems typically have a low Reynolds number (100>Re>0.001), which indicates that fluid flow is laminar unless turbulence is induced, which may be desirable for example to mix two fluid streams. For the channels described here, using water as a model fluid (μ=10^{-3}kgs^{-1}m^{-1}, ρ=1000kgm^{-3}, for 20ºC [87]) and characteristic channel size and velocity of 30µm and 0.01ms^{-1} respectively yields *Re*=0.3.

Default expressions are included in Comsol for the density and dynamic viscosity of water which was used as a representative fluid since the TRIS-EDTA buffer (10:1mM) in which the DNA was suspended during experiments is primarily composed of water. The temperature in all cases was set at 300K. For this study, the interest is in the effect of a microfluidic channel which is somewhat larger than the characteristic dimensions of the passing polymers. The narrowest part of any channel studied is 5µm, while the persistence length of a DNA strand in physiological buffer is approximately 50nm [88] with a radius of gyration of 0.73µm in the case of λ-DNA [72]. For this reason, while Comsol alone was sufficient to solve for and display the overall flow in the channel, it was also necessary to use the Comsol / Matlab interface to form some hypotheses about how a DNA strand might

behave in any given channel. The general approach was therefore to draw and solve a model for a channel (or part of a channel), then export that model to Matlab to interpolate the solution on the scale of the DNA strand. This two step approach allows the use of a mesh size which is small enough to accurately calculate the flow in the channel while still being large enough to be computationally feasible. Comsol interpolation of this mesh then allows the solution to be locally extended to the relevant length scale for DNA. Nevertheless the required computational load is high and modelling in three dimensions was not possible using a single desktop computer, as mesh studies revealed that the solutions for each channel did not converge. A mesh convergence study was also used to determine appropriate mesh parameters for the two dimensional model of each channel. Although numerically inaccurate, the three dimensional models showed similar variation in streamline position and Weissenberg number plots to their two dimensional equivalents at key locations in each channel geometry. For this reason, the two dimensional models are considered adequate for comparison between preconditioning channel designs.

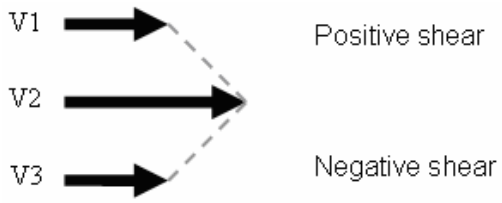

Figure 23, diagram to indicate the defined direction of positive and negative shear for Comsol modelling, drawn as the difference between three x-velocity vectors.

To compare the shearing flow either side of the peak flow velocity in a channel, the channel is first drawn and solved in a two dimensional Comsol fluid mechanics FEA; the solved model is then exported to Matlab for analysis. For comparison of different preconditioning channel designs, the Weissenberg number (equation 1) is calculated across a distance (50nm) approximating one persistence length at points along each channel. The points at which the Weissenberg number is calculated are determined from a streamline defined by specifying a start point at the centre of the channel inlet. This allows calculations to be made close to the peak flow velocity along the length of channels with non-parallel sidewalls. The Matlab/Comsol interface is used to calculate the coordinates of the streamline itself along with the

magnitude of the velocity vector at each point. Each channel is initially 30µm wide (y-direction) and the total length is 1424µm (x-direction). Preconditioning channels differ in several places in channel width (y-direction) but are all the overall length. To characterise the shear flow on a scale of interest for the deformation of DNA molecules, the velocity vectors on the central streamline are compared at each point with the vector 50nm to either side in the y-direction. The difference in the velocity vectors is used to calculate the shear rate at each point allowing the Weissenberg number to be plotted for each point on the streamline. The choice of a positive direction for shear is arbitrary and was defined as shown in figure 23.

3.2.2 Calculation of Wi and De

The Weissenberg number is calculated using Comsol script. A streamline is plotted and Wi at each point is calculated by taking the difference between the velocity vector on the streamline and at a point one persistence length (50nm) above it (*i.e.* V2-V1 in figure 23), then dividing by 50nm to give the shear rate. The shear rate is multiplied by the relaxation time to yield Wi. This assumes a linear velocity gradient which is a simplification commonly applied over entire channels (*cf.* [22]). In this analysis, points up to a maximum separation of 1µm (approximate radius of gyration of a coiled strand) could be considered, but taking points one persistence length apart accounts for the expectation that DNA molecules are partially extended due to the laminar flow in the connection. In a parallel walled channel, the flow is symmetrical about the central streamline so calculating Wi above and below the streamline simply gives equal and opposite results.

The strain rate parallel to the flow direction is given by the difference between the flow velocity at the exit and entrance to the funnel divided by the length of the funnel [22]. The strain rate is simply multiplied by the relaxation time to give the Deborah number. Using Comsol streamlines, it is possible to calculate a nominal De value for DNA strands entering the funnel at various points across the channel axis and following a streamline through the funnel, by dividing the relaxation time by the time taken to traverse the funnel.

3.2.3 Relaxation Time Estimation

The relaxation time of a polymer depends on its length and the viscosity of the solvent. For λ-DNA, various estimates have been made from mathematical models and experiments. The value of 94ms is used as a representative value of the relaxation time of λ-DNA in buffer and is taken from the linear correlation presented by Fang et al. [81] which is reproduced in figure 24. This is derived from their own data as well as that of three other studies [68, 76, 89].

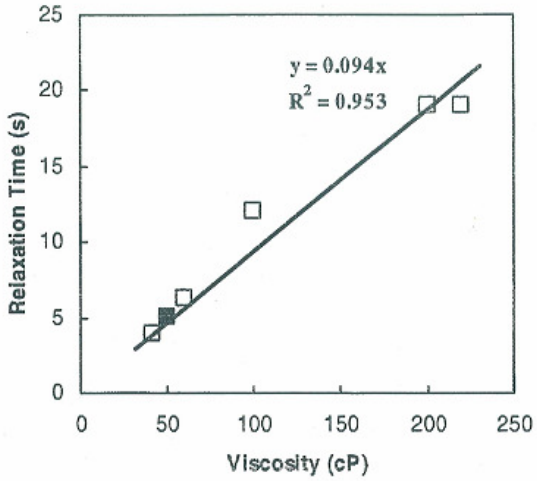

Figure 24, graph showing the relaxation time of λ-DNA as a function of solvent viscosity showing a linear relationship [81].

3.2.4 Shear-Induced Cross Stream Migration of DNA

The time taken to establish a depletion region as described in section 3.1.3 is much greater than the time the DNA is expected to spend in the preconditioning channels described below. However, the off-chip part of the fluidic system is also under laminar flow so the whole system must be taken into consideration. Measured from the centre to the edge of the channel in each case, for a typical pump rate of 12μL/hr and λ-DNA, Wi may be estimated for each part of the system as follows. Ethylene tetrafluoroethylene (ETFE) tubing (0.02" ID, 1/16" OD, Anachem) used for the connection to the DNA sample inlet valve Wi=0.03, capillary connecting plastic tube to chip (TSP075150, Polymicro, U.S.A.) Wi=8.80, preconditioning channel Wi=13.47, interrogation channel Wi=23.69. An estimation of the average time to flow through 10cm of the capillary (75μm inner diameter) at $12\mu Lh^{-1}$ gives 133 seconds. This would be sufficient for a significant development of the depletion layer judging by the results of Chen *et al.* [77] (figure 19), although the required time

for the layer to fully develop will be slightly increased due to the bigger difference between the channel size and DNA contour length [79]. With the various connections and changes in channel geometry in the experimental system, it is very difficult to make quantitative predictions about the concentration profile of DNA across the channel. All the same, it is necessary to bear in mind some of the more counter-intuitive phenomena of polymer behaviour such as this when forming hypotheses about polymer manipulation.

3.3 Channel Design

Microfluidic channel design focussed on the development of an improved method of DNA preconditioning in shearing flow prior to full extension by elongational flow. A single elongational flow element was used in the form of a funnel, the profile of which was based on an established design [19, 22]. Several preconditioning channel designs were produced, each based on a channel of 30µm-side square cross section. The preconditioning channels sit upstream of the funnel and the combination of shearing then elongational flow is used to extend passing DNA molecules.

From an early stage, designs focussed on a single fluid channel operating in continuous flow. Although cross-slot devices and deformation by hydrodynamic focussing offer more control over an elongation flow than a simple funnel, the focus of the work described here was to improve preconditioning using shearing flow upstream of the elongational flow element. The additional dependency on the residence time at the stagnation point of a cross-slot device or the stability of the sheath flow in a hydrodynamic focussing device was therefore undesirable.

A channel in which the flow was physically separated into several streams which later recombine was considered as a means of temporarily reducing the channel size to bring its characteristic length closer to that of the DNA strands used for testing. However, there is a potential for any improvements made to the strand conformation while in the sub-channels to be undone during a deceleration where the flow is recombined. Also, such a design inherently adds a second elongational flow (upstream of the final funnel) which would mask any effects generated primarily due to altering the shear rate.

The choice of channel size is limited by several factors. To improve preconditioning by shearing flow it is necessary to make somewhat subtle perturbations to the laminar flow environment in order to disrupt the molecular conformation on a length scale much smaller than that of the characteristic channel size. The relevant molecular length scale in this context is not the contour length, rather somewhere between limits defined by (a) the width of a folded molecule which can approach 1µm and (b) the persistence length of 50nm (see section 3.2.1). Modelling of the flow effects at these length scales allowed a suitable channel size to be chosen. Reducing the channel width to close to the contour length may be sufficient to reduce tumbling in one plane, but as the interrogation channel width is limited by integration with the off-chip optical system, a narrower preconditioning channel will have a less effective elongational flow in the tapered region. For a clear assessment of the efficacy of the sloped connection design, it was also desirable to have preconditioning channels of a size which integrates to the interconnect, the dimensions of which are, in part, defined by the connecting capillary.

Within the dimensional limitations described above and additionally the practical restriction that a geometry varying in one plane is easier to fabricate, channel designs with a periodically varying width were produced. The pitch of successive features was limited by the necessity to apply a continuous change to the molecular conformation, i.e. to perturb the conformation more frequently than the relaxation time would allow it to recoil. The shape of the sidewall features where the channel is wider is a somewhat arbitrary choice: similar effects may be observed with a rectangular profile. However, the presence of angular corners in the channel is undesirable as they create potential fouling sites and rectangular features also add to the dead volume within the chip; a curved sidewall is therefore preferred.

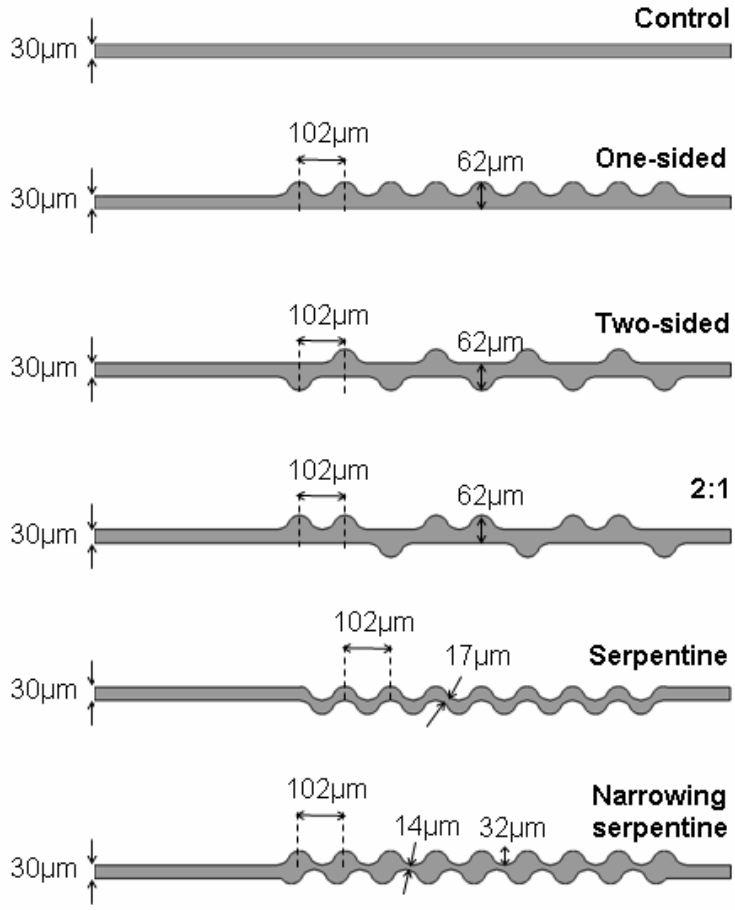

Figure 25, scale drawings of the preconditioning channel designs. Each channel is shown in plan view; these patterns are extruded to a uniform depth of 30µm. In the fabricated devices the parts of each channel with non-parallel sidewalls extend over a length of 10mm.

Diagrams of the different preconditioning channel designs that were fabricated are shown in figure 25; the basic channel is a 30µm side square channel, which constitutes the control case. Subsequent designs are based on selective in-plane widening of this initial channel. The flow in a microchannel with parallel sides is symmetrical about the channel axis. Periodic changes of the channel width break this symmetry and several hypotheses may be made about the effect this will have on passing DNA strands. For a folded strand on a streamline travelling approximately along the channel axis, the local shearing flow on the strand pulls whichever section is in the fastest flow at the channel centre ahead of the other parts of the molecule. Unless one end of the strand is in the fastest flow, this will tend to stretch the whole, folded strand but is unlikely to unfold the molecule unless it tumbles and recoils,

then stretches again from a more favourable initial conformation. Variations in the channel width alter the flow velocity profile and produce a variation in the shearing force that is applied to a passing molecule.

The one-sided channel provides a periodic flow variation due to the channel widening and narrowing with a pitch of 102μm. The effect of the flow variation is greater towards the top side (as drawn) than on the bottom. DNA strands tend to approximately follow streamlines as they pass through such structures. For a folded molecule travelling initially along the channel axis, there is greater variation in the fluid drag force on one side than the other if it occupies a space of the order 1μm. Over a single persistence length, the difference in shear towards either side of the channel is much less, but the shearing forces are greater than in the control case. The folded molecular conformation is predicted to be less stable in this situation than in the control channel. For a linear molecule however, the effect would be less significant as the chain would straddle less streamlines.

Although a molecule straddling the channel axis may be a special case, the increased shearing experienced over a persistence length either side of any given streamline is still greater than that in the control channel. It is also possible that the effect of shear-induced flow migration will concentrate the DNA strands towards the centre of the channel. Considering the shearing flow at the point of maximum velocity gives a nominal minimum values for Wi, as does measuring it over one persistence length. It is worth stating that the design aim is not to unfold a strand as it passes a single feature, rather to improve the overall 'pre-conditioning' effect of the shearing flow by exposing more molecules to a greater Wi.

In the one-sided channel, the changes in flow are more significant in one half of the channel than the other, for this reason the two-sided design was created with an equal number of widening regions on either side of the channel. Since laminar flow is reversible, any untangling of the DNA relies on a change being made to its conformation as it passes one channel feature, such that it enters the next feature in a new state. Although the time for a strand to pass between features is less than the relaxation time (see section 3.4.2), it is still possible that the net effect of several changes in channel width is zero due to the reversibility of laminar flow. For this

reason the 2:1 preconditioning channel was designed, such that molecules on any streamline would experience a periodic variation in local shear-flow but a conceptual strand on the central streamline wouldn't simply be pulled a little in one direction and then equally in the other direction.

The serpentine preconditioning channel was produced in two variations, one with a minimum width of 17µm, one with a minimum width of 14µm. These two designs also differ in the x-displacement between the points of maximum and minimum deviation in the y-direction. This pitch is 51µm in the serpentine design (minimum width 17µm) and 18µm in the narrowing-serpentine design. The former induces more pronounced changes in flow direction, while the latter design produces more frequent changes in direction. The minimum width of these channels is close to the contour length of unstained λ-DNA (assuming a length per base pair of 0.34nm [64]) which may be sufficient to reduce tumbling in the x-y plane. Tumbling is a problem for the stretching of DNA by an elongational flow funnel since molecules can reach the funnel entrance in a variety of conformations and orientations, of which only a linearised, roughly axially aligned strand is likely to be successfully elongated by the funnel.

In the fabricated devices, each of these preconditioning patterns is used to define a channel which is 1cm long and 30µm deep. In the one-sided channel therefore there are 98 wide regions spaced at a pitch of 102µm. 500µm downstream of the preconditioning features each channel tapers to a width of 5µm over a distance of 5µm thus generating an elongational flow which completes the DNA extension.

In order to evaluate these different preconditioning designs, simulations of the fluid flow are considered. To understand the fluid mechanics of each design, it is only necessary to simulate a portion of each channel which is also beneficial in reducing computational load.

3.4 Preconditioning Channel Simulation Results

Each preconditioning channel model is 1.4mm in overall length and 30µm wide at inlet and outlet. Expressions for the density and dynamic viscosity of water are

provided within Comsol and these are used with the temperature set at 300K. An inlet flow rate of 12µLh^{-1} is used to establish a representative flow. Each channel is modelled in three dimensions, but for the purpose of the comparative Weissenberg number analysis below only the flow on a central streamline is considered. The streamline starts at the centre of the channel inlet and remains at approximately the same depth while varying in y-position with the channel geometry.

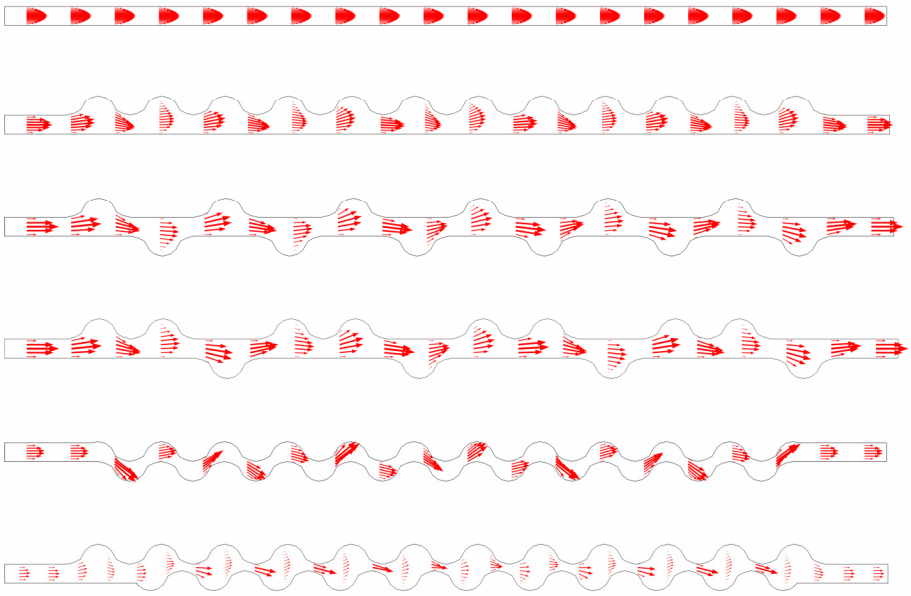

Figure 26, simulation results for the different preconditioning channel designs, the length of each arrow indicates the magnitude of the flow velocity vector at that point.

Figure 26 shows the characteristic velocity profile of each type of preconditioning channel; where the width of a channel changes the flow slows down and changes direction. Within the wider parts of the channels a skewed velocity profile is observed in which the flow velocity is no longer symmetrical about the centre of the channel. These changes of direction, flow speed and symmetry are the key elements in creating a flow environment which makes a folded polymer conformation less favourable.

3.4.1 Control preconditioning channel

The control chip is simply a 30µm-side square cross-section channel and is represented in simulation by a rectangle 30µm tall and 1.424mm long. The

unperturbed laminar flow has a characteristic parabolic velocity profile and is symmetrical about the channel axis. A streamline starting at the centre of the channel inlet will therefore end at the centre of the channel outlet as shown in figure 27.

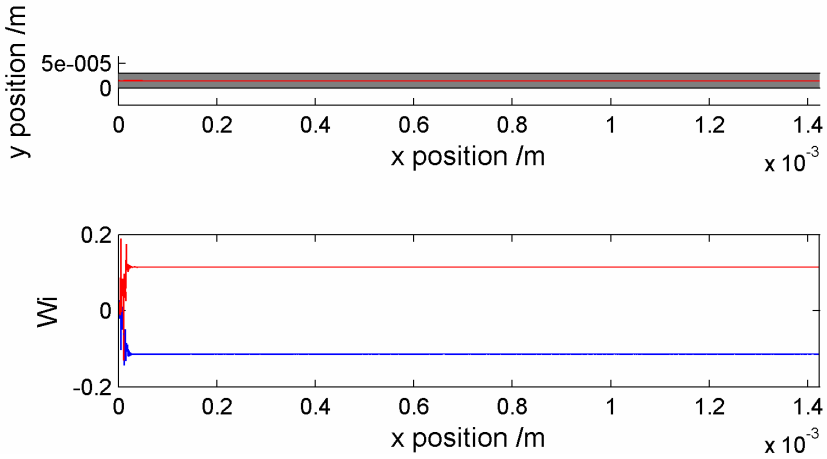

Figure 27, plot of control preconditioning channel design geometry showing central streamline and the Weissenberg number as a function of channel position. Aside from the numerical errors the value of Wi is constant either side of the streamline.

The shearing force one persistence length above and below the central streamline is measured from the model to allow calculation of the Weissenberg number for a λ-DNA molecule and this is plotted against the x-position in the channel. The input flow is uniform across the width of the channel but laminar flow is fully established within 50µm. The choice of one persistence length (50nm) provides an approximate minimum value of the strength of the shearing flow, since if any part of a DNA molecule is aligned normally to the streamline it must extend at least a persistence length in that direction. A maximum bound could also be considered by assuming a DNA strand would occupy a lateral space defined by its radius of gyration (0.73µm for λ-DNA) but it is the variation of Wi that is of key interest, rather than the absolute value. The flow is symmetrical about the central streamline and a streamline remaining in the same 'flow layer' as it traverses the channel has a constant value of Wi which is 0.11 in this simulation.

3.4.2 One-sided preconditioning channel

The one-sided preconditioning channel is based on the 30µm wide control channel but widens periodically to 62µm, with a pitch of 102µm. The streamlines in this case meander across the channel as seen in figure 28. Where the channel widens, the flow slows and the direction changes. This variation is reflected in a changing Weissenberg number which is plotted in figure 28 for points one persistence length (50nm) above (blue) and below (red) the central streamline.

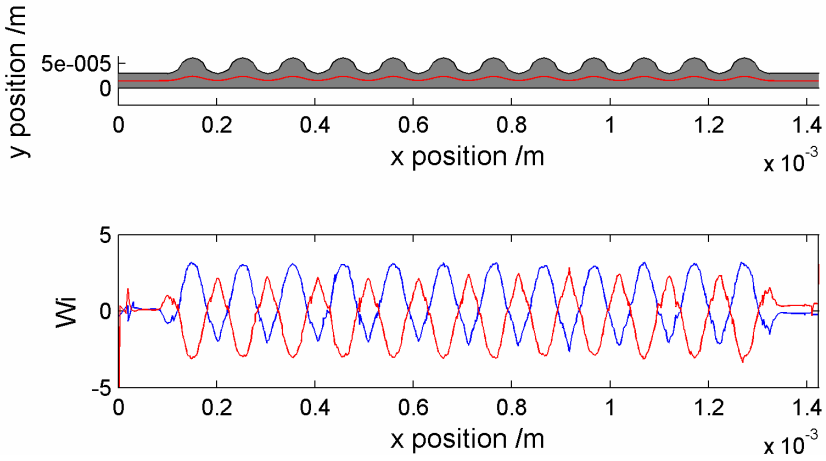

Figure 28, plot of Comsol geometry for one sided preconditioning channel design with streamline starting at the centre of the inlet and Weisseberg plot with shear measured one persistence length above and below each point on the streamline.

The peak value of Wi in the parallel-walled sections of this model is comparable to that of the control case (0.1). In the preconditioning section where the channel width varies, the Weissenberg number one persistence length above the central streamline varies between 3.05 and -1.96. The trace for one persistence length below centre is essentially the inverse of that for above. This indicates that a DNA strand travelling along the central streamline where the shearing flow is at a minimum will be exposed to a shearing force which is theoretically sufficient to cause entropic unwinding unless the molecule is fully extended and does not extend away from the streamline by even one persistence length at any point. It is proposed that the variation in Wi in the preconditioning section will make a folded conformation less stable as a molecule is more likely to change conformation when there is a change in the deforming strength of the flow conditions. Considering the two traces of the

Weissenberg graph of figure 28 individually, each one achieves a higher peak value of Wi in one direction than in the other. This differential is also potentially beneficial for extending a folded molecule travelling along a central streamline.

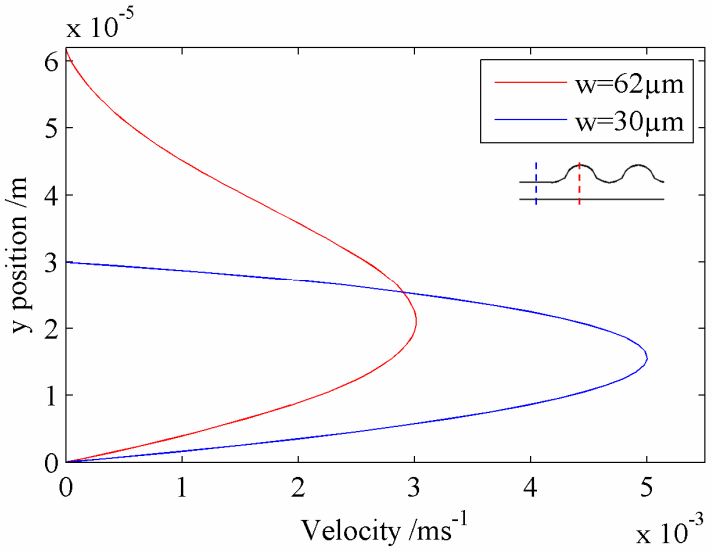

Figure 29, magnitude of the velocity vector as a function of transverse channel position for the one-sided preconditioning channel, showing the difference in flow at the widest and narrowest points as indicated by the inset.

The variation in the velocity profile across the channel is shown in figure 29 for a flow rate of $12\mu Lh^{-1}$; the blue trace shows the established laminar flow in the parallel-walled part of the channel where the width is fixed at 30µm. The red curve shows the profile at the widest point of the expansion where the channel width is 62µm. Where the channel is wider than 30µm, the channel walls are never parallel; making the velocity profile skewed. This is also proposed to make a folded conformation less stable as the parts of a molecule that extend across the channel width are potentially subjected to flows of different strengths. The location of the maximum flow speed is shifted across the channel by approximately 5µm; there is also a change in flow direction into and then out of the expansion. These changes in flow profile occur on a length scale that is smaller than the physical size of the channel, which enables the channel to produce an effect on passing DNA molecules that are smaller than its characteristic length.

The hypothesis is that straight strands are affected less by the flow, while folded strands are iteratively straightened by changes in the flow profile. In order for this to

work, it is necessary that the time a DNA strand takes to travel between features is less than the relaxation time of the molecule. The estimated λ-DNA relaxation time is 94ms and the pitch of the channel features is 102μm; this suggests that a DNA strand must be travelling at a minimum of 1.09×10^{-3} ms^{-1} in order to be perturbed frequently enough that it cannot recoil in between channel features. Considering figure 29 which illustrates the laminar flow parabola in the widest and narrowest regions of the preconditioning channel, a rough estimate suggests that across two-thirds of the width of the channel – whether in the parallel walled section or the expanded region – the flow is suitably fast. As the flow is shearing, there is also the likelihood of a depletion region close to the channel wall where DNA strands are less likely to travel, as described in section 3.1.3.

3.4.3 2:1 Preconditioning channel

Whereas in the one-sided channel design the features that cause the widening of the channel are all on the same side, for this design every third widening is on the opposite side of the channel. Although laminar flow is reversible, the relaxation time of a polymer means that any deformation is not necessarily reversible, therefore having repeating equal and opposite features is probably not an issue for DNA elongation. Nonetheless an asymmetric design is still of interest as folded molecules may be more easily straightened by changing the flow differently on each side of the channel. The peak value of Wi for the upper streamline in this simulation is 3.39 and the minimum is -3.34. The minimum at x=200μm has Wi=2.02.

On the scale of one persistence length, the flow strength varies approximately equally either side of the central streamline and the effect of each channel widening is similar to that of the one-sided channel. However, the differing velocity profile as illustrated in figure 29 is skewed twice as frequently toward one side of the channel. The Weisseberg number plot is aligned to the channel geometry to illustrate where the peaks in Wi are physically located; in this design Wi is at a maximum at the widest points of the channel.

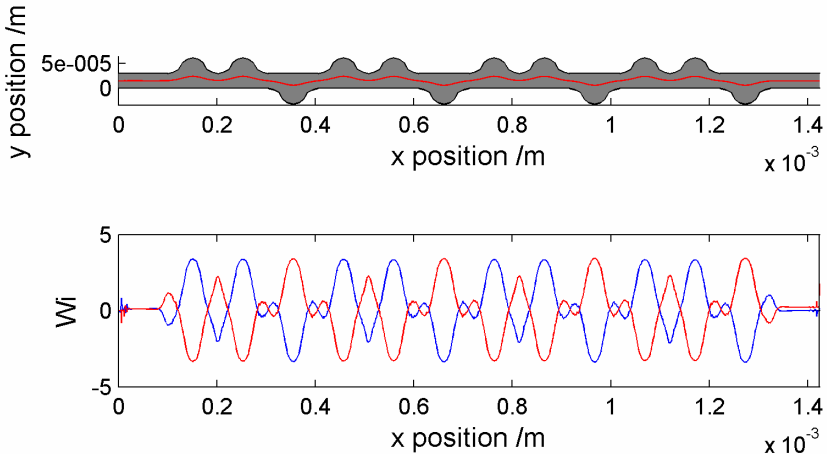

Figure 30, plot of the geometry defining the 2:1 preconditioning channel design showing the central streamline plot with corresponding Weissenberg number graph.

3.4.4 Serpentine preconditioning channel

Various types of serpentine channel are common in microfluidic systems and the frequent directional changes they produce are potentially of interest for DNA deformation. The channel is not fixed width which is why there are local minima in the Wi peaks; at the narrowest point the channel width is 17µm, with a value of Wi=16 and 9.5 at the widest points.

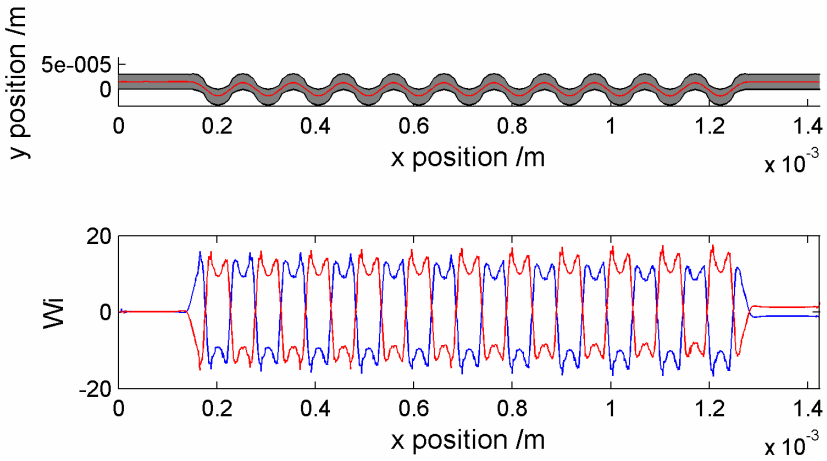

Figure 31, geometry of serpentine preconditioning channel as fabricated, with central streamline and accompanying Weissenberg number plot.

The direction of the shearing flow 50nm either side of the central streamline reverses with each change in the lateral flow direction and it is this alternating shear flow which is designed to promote the extension of folded molecules. In each case, the maximum value of Wi in the positive shear direction is separated from the point of minimum Wi by 20µm.

3.4.5 Narrowing-serpentine preconditioning channel

Using the serpentine design as a base but changing the offset between the curved features on either side, the design shown in figure 32 was also produced. The narrower regions in this channel (width 14µm) produce values of Wi around 7.3, the peaks occurring as the flow accelerates into the narrow regions. The maximum value of Wi seen on each streamline is followed almost immediately (3µm downstream) by the maximum in the opposite direction as the streamline exits the narrow section. The peaks on each streamline occur at the same pitch as the geometrical variation, with a maximum value every 102µm.

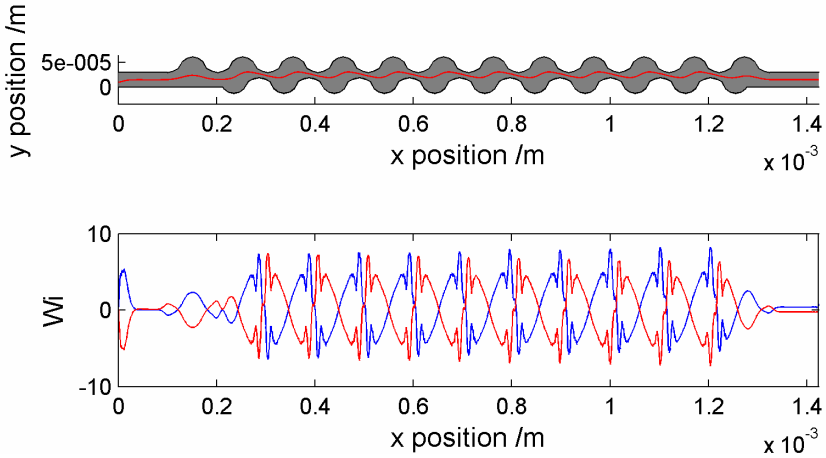

Figure 32, geometry plot of a variation on serpentine channel design showing the central streamline. The streamline passes close to the edge of the channel in the narrower sections, thus encountering regions of high Weissenberg number flow as shown in the lower graph.

3.4.6 Two-sided preconditioning channel

The two-sided channel is a symmetrical version of the one-sided channel with equally sized widening sections on alternating sides of the channel. In common with the one-sided design, the peak value of Wi is around 3.4 and the minimum value is

around -3.4. The direction of shearing flow alternates with the expansions on each side of the channel for measurements 50nm to either side of the streamline; the peak-to-trough pitch in each case is therefore 102µm

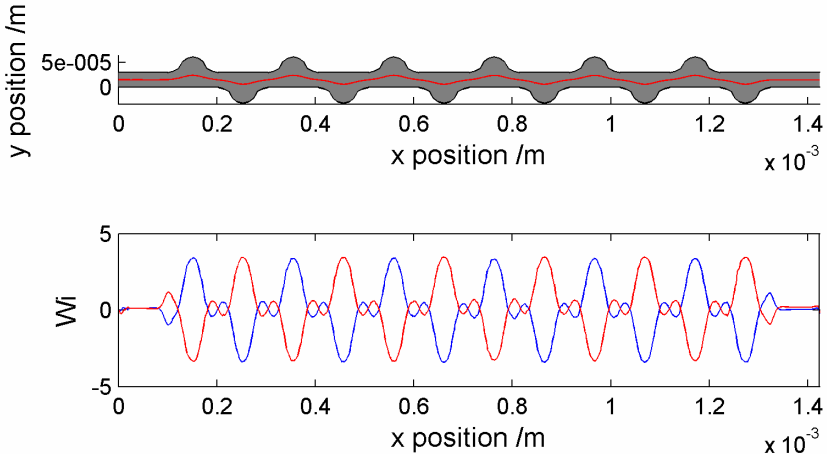

Figure 33, Comsol geometry plot showing central streamline and accompanying Weissenberg number plot for the two-sided preconditioning channel design.

3.4.7 Comparison of preconditioning channels

In the analysis presented above the shear rate is evaluated at each point along a streamline starting at the centre of the inlet of the channel, relative to points 50nm above and below. Although the value of the velocity vector at each point is found by mesh interpolation, the gradient is assumed to be linear over the 50nm between vectors. This same assumption is typically used over the whole width of a rectangular channel, but sacrifices less accuracy over this shorter distance.

The maximum values of Weissenberg number are shown in table 2. Although the narrowing-serpentine design has the narrowest regions of any channel (14µm) it does not exhibit the highest value of Wi. The more severe directional changes taken by the streamline in the serpentine channel give it a peak Wi more than double that of the narrowing design. The lowest values of Wi are observed at the central streamline of the control channel. The flow profile remains symmetrical about the axis of the control channel and the values of Wi either side of the streamline are therefore equal and opposite. For designs other than the control channel, the direction of shearing flow is reversed at several points along the streamline for points both 50nm above and below the streamline itself. This reversal is designed to 'pull' folded strands in

different directions and thus make folded conformations less stable in the preconditioning section. The peak values of Wi in the one-sided and two-sided preconditioning channels are very similar, as would be expected since the changes in channel geometry are similar. The same can be said of the 2:1 channel, although peak Wi 50nm above the streamline occurs twice as often in the positive shear direction.

Design	Max/min Wi 50nm above streamline	Max/min Wi 50nm below streamline
Control	0.11 / 0.11	-0.11 / -0.11
One-sided	3.20 / -2.64	3.08 / -3.37
Serpentine	15.96 / -16.68	17.6 / -15.09
Two-sided	3.42 / -3.41	3.47 / -3.36
Narrowing-Serpentine	8.24 / -6.45	7.39 / -7.30
2:1	3.39 / -3.38	3.43 / -3.33

Table 2, average Weissenberg number between central streamline and points 50nm above and below for each preconditioning channel design, calculated using $\tau_p = 0.094$s.

With the exception of the control channel, all of the preconditioning designs a peak Weissenberg number greater than 1 on the central streamline which makes a theoretical coil-stretch transition possible even at the point of minimum shear.

3.5 Elongational Flow Taper Simulation Results

Each of the preconditioning channels described above is designed to cause some elongation of passing DNA strands such that the average extension is greater than the control channel. To fully extend the DNA strands however, an elongational flow is also used. Downstream of each preconditioning channel is a taper which produces this elongational flow. The taper design is a simple $1/x^2$ profile as demonstrated by Chan et al. [19], the wide end is 30µm wide while the narrow end is 5µm, the depth

by design is 30µm throughout. The flow simulation of this design is shown in figure 34; the total extent of the funnel in the x-direction is 5µm.

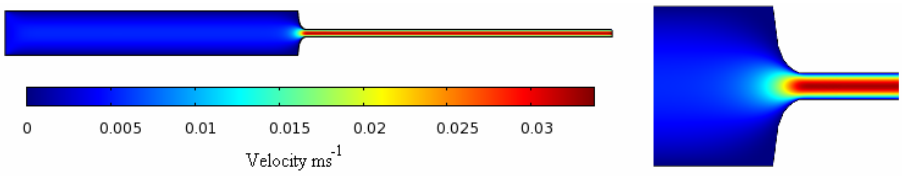

Figure 34, FEA simulation results for elongational flow in a taper showing the whole model and a close-up of the tapered region, inlet flow rate 12µLh^{-1}. The colour surface represents the velocity vector which peaks at 34mms^{-1} at the centre of the narrow part of the channel.

It is convenient to describe the effect of the funnel on a passing polymer using the Deborah number (De), as described in section 3.1.2. To calculate De from the model, streamline calculations are used because the observation that DNA strands tend to follow streamlines remains true where they traverse the funnel. Streamlines are plotted at intervals of 1µm up to 2µm from the channel sidewalls and De calculated for each streamline using the relaxation time of 0.094s [81]. The average fluid strain rate is calculated by dividing the change in velocity between the start and end of the funnel by the distance travelled along the streamline. A close-up view of the streamlines plotted for this analysis is shown in figure 35.

The variation in Deborah number across the width of the channel is shown in figure 36 for the 12µLh^{-1} flow rate used in the preconditioning channel simulations and also for some lower flow rates for comparison. Clearly in all cases the value is well above the theoretical value of ~0.5 required for a coil-stretch transition [70, 76]. As such, if the preconditioning channels provide more effective pre-shearing of the DNA strands, this should be evident in an increased average stretch downstream of the taper. For flow rates as low as 3µLh^{-1} the Deborah number for this funnel should be in double figures across the whole channel width. However, higher values of De are desirable because the flow deformation time is short relative to the relaxation time of the DNA. Although De=0.5 is sufficient to cause a coil stretch transition in an elongational flow [76], the deformation time is very short and thus a higher De increases the chance of stretching a molecule to its contour length.

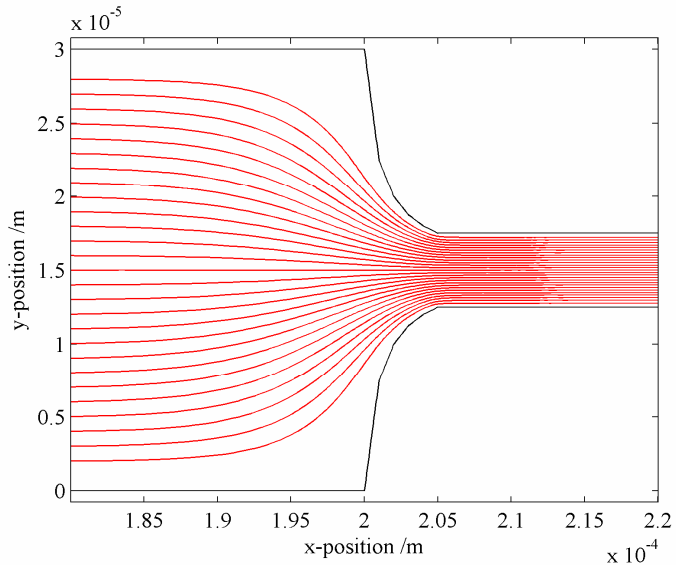

Figure 35, the elongational flow funnel model with streamlines showing the points at which the Deborah number is calculated.

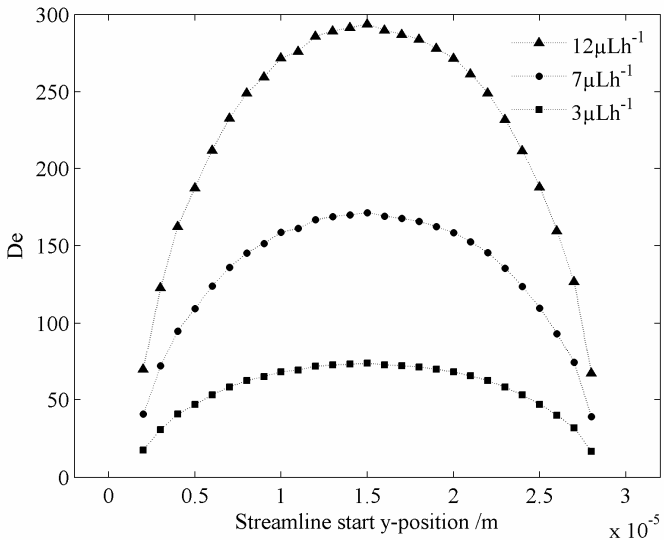

Figure 36, graph showing the Deborah number calculated for λ-DNA strands following streamlines through the funnel of figure 34. The streamlines are plotted up to 2μm from the channel walls.

3.6 Discussion

The central design philosophy of the DNA stretching devices is to load the DNA onto the chip with little disruption to the conformation beyond that caused simply by the device dimensions and subsequently to improve the linearity of the molecules in

a preconditioning channel before finally stretching them in a fluidic taper. The laminar flow in the capillary connecting pump to chip has two potential beneficial effects. Firstly the tendency of DNA strands under laminar flow to stretch and recoil/tumble means that a certain proportion of the strands will enter the device partially linearised. Secondly the capillary is long enough to allow shear-induced flow migration to begin to generate a depletion region at the fluid boundary. If this depletion region persists to some extent through the interconnect to the microchannel, the DNA will be exposed to a stronger elongational flow as seen in figure 36.

Pre-shearing of DNA molecules prior to stretching by elongational flow is known to improve overall stretching performance [25]. The preconditioning channels described in this chapter have been shown to generate higher values of the Weissenberg number than the comparable control channel. Strands on the central streamline represent the worst case for pre-shearing performance because the difference in flow velocity between adjacent streamlines is at a minimum. Channels with non-parallel sidewalls such as those described here expose a DNA strand on a central streamline to a varying shear rate which is periodically sufficient to cause a coil-stretch transition. This is true when measuring the shear rate over a single persistence length (50nm); the same calculation may be performed over a distance equal to the radius of gyration (0.73µm [72]) in which case the shear rate (and hence Wi) is greater.

The principle of the preconditioning channel designs is that variation in the channel width produces a skewed velocity gradient across the channel (as seen in figure 29). As a DNA strand travels along a streamline it is exposed to a shearing flow from the laminar flow gradient. Coiled regions of the molecule are exposed to a higher shear rate as they occupy a greater cross section of the channel. In a parallel-walled channel this is enough to cause straightening of the strand, although straightened strands often recoil or tumble and folded strands tend to stay folded. By varying the width of the channel with features on one side, the velocity differential between adjacent streamlines also varies more and is typically greater than the straight channel case. It is predicted that this greater differential will be more effective at unravelling folded regions of the DNA strand and that the higher shear rates will be

more effective in the general case. Thus the preconditioning channels will present a higher proportion of linearised DNA strands to the stretching funnel resulting in a higher average extension of the detected molecules.

Of the different preconditioning channel designs, the serpentine channel might reasonably be expected to perform the best as it offers the highest peak value of Wi, although it is not the narrowest channel. For fabrication, it is useful to have a selection of devices ranging from those offering a high value of Wi and strong directional changes such as the serpentine design, to those with lower values of Wi – provided the latter still promote a coil-stretch transition. All of the preconditioning devices presented above potentially offer some benefit over the control channel, both in terms of higher values of Wi and variation in the strength and direction of shearing flow.

Chapter 4 Characterisation of Deep Reactive-Ion Etching as a Method of Fabricating Microfluidic Devices with Sloped Interconnects

This chapter describes the investigation that was undertaken to develop the fabrication method used to produce microfluidic DNA extension devices. There were two aims to this investigation, firstly to verify that the proposed fabrication process could produce devices with the required characteristics of pressure tolerance and geometrical complexity and secondly to explore the possibility of producing a novel inlet/outlet connection that would improve the efficiency of DNA loading.

For the advantages of any miniaturised device to be realised it is essential that it has a reliable world-to-chip connection. For microfluidic devices, this typically means integrating a small-diameter tube which is connected to an off-chip fluid supply. A poor connection can lead to sample loss and potential contamination from dead volume where the tube meets the device and therefore many different strategies for improving this important area have been published; section 4.1.1 presents a review of those which are relevant to the study described in this thesis.

Loading long DNA molecules into microfluidic channels is more complex than loading small molecules because they are more susceptible to breakage and entanglement. For the devices produced in this study, it was desirable not only to ensure the DNA was loaded intact, but also to minimise conformational disruption so as to more completely test the preconditioning channels. In particular, for applications requiring rare-molecule detection and also for reuse of individual devices it is necessary to avoid damaging the DNA or allowing it to aggregate on the channel surfaces. Figure 37 shows a sketch of what an optimal connection between a capillary and a microfluidic device might look like. The fluid channel is perfectly matched to the inner diameter of a capillary tube and to the dimensions of the microfluidic channel so there is no dead volume and the walls in the transition region taper smoothly between the different size channels.

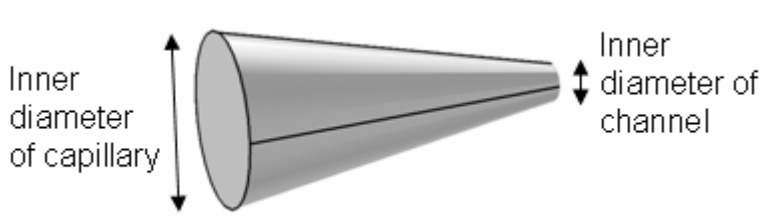

Figure 37, sketch of a hypothetical geometry of an optimal connection to a microfluidic device.

In practice such geometries are challenging to fabricate. In section 4.3 the results of an investigation into the possibility of using deep reactive-ion etching (DRIE) to fabricate a sloped, in-plane connection from a capillary to a silicon microfluidic device are presented. The method relies on the application of a known etching phenomenon called DRIE-lag, which causes narrow trenches to etch more slowly than wide trenches. Section 4.1.2 gives an explanation of the DRIE process and some of its characteristic features.

The use of DRIE and a silicon substrate is an attractive combination for microfluidics for a number of reasons. The designs presented in chapter 3 require a minimum feature size of 5µm and a high pressure tolerance to generate suitable conditions for DNA stretching, as well as a number of curved features. Accurate control of channel width is also a requirement as it is essential that a comparison can be made between different devices with small variations in their internal structure. DRIE provides excellent feature reproduction in silicon with minimal masking requirements and a borosilicate glass cap wafer can be attached by anodic bonding which provides excellent pressure tolerance [90] as well as being an optically transparent cover for fluorescence interrogation.

4.1 Literature Review: Fabrication of Microfluidic Interconnects

4.1.1 World-to-Chip Connection Strategies

The world-to-chip connection is a vital area of device construction which is frequently given much less consideration than other aspects of a design. Off-chip systems are typically facilitated by the wide variety of tubing and connectors originally produced for high-performance liquid chromatography (HPLC). In some

cases such components are suitable for the connection to the device itself, although this frequently consists of no more than sealing the end of a capillary against the top-surface of a chip. Various improvements can be made to the connection, depending on the fabrication technology and also whether permanent connections or replaceable parts are preferred. Other figures of merit include dead volume (where molecules can be lost/delayed), pressure tolerance, complexity (in assembly as well as extra fabrication steps) and ease of alignment.

For applications using electroosmotic pumping [91] or electrokinetic [92] loading, a simple well may be used to load the fluid into a device. For pressure-driven flows in silicon-Pyrex™ devices, the traditional approach is to machine a hole through the cap layer, often simply by drilling [93, 94] prior to bonding the two layers. This hole is aligned over the channel in the fluidic layer and the off-chip tubing typically butts-up to the hole.

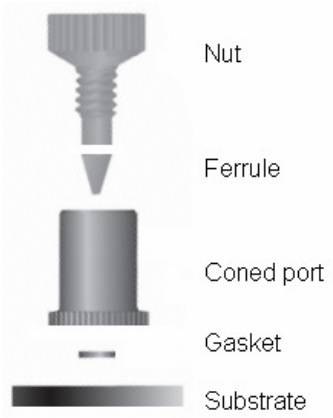

Figure 38, diagram of the components of an HPLC technology-derived connection port used to clamp tubing against the flat surface of a microfluidic device, from manufacturer's data sheet (N-333, Upchurch, U.S.A.).

Commercial products are available with high pressure tolerances fabricated in biocompatible polymers to make robust connections of this type. Such products typically consist of a socket with integrated o-ring sealing that is attached to the chip using epoxy resin. The connecting capillary is passed through the nut which screws into this socket and clamped in place with a ferrule, as shown in figure 38 (N333, Upchurch, U.S.A.). Although these connections can be made and broken freely, the footprint of the socket is relatively large and as such can constrain the design of the

microfluidic channels. They are also difficult to align and the dead volume means that some of the sample will come into contact with the outer surface of the chip potentially causing biofouling before the sample is even loaded.

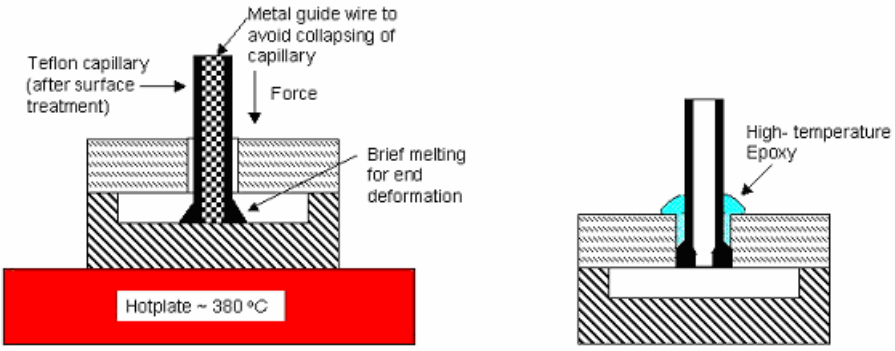

Figure 39, diagram of a microfluidic device connection scheme using a thermally deformable Teflon tube [93]. The connection can be reinforced with epoxy and external sleeves to improve robustness under handling.

Several variations of this basic through-wafer connection geometry have been proposed. As well as glass capillaries, Teflon tubing is a common interconnect component. Although Teflon tubes are generally larger they are easier to deform and this can be exploited when making a connection. An example of this is shown in figure 39 which is adapted from [93]; the tube is inserted through the Pyrex layer and heated to expand the end. When it is pulled back into the Pyrex it forms a sealed connection which can tolerate high pressures if secured with epoxy resin. The footprint of such a connection is much smaller than an external port but the tube must be attached permanently and the authors reported that some extra reinforcement was necessary to prevent damage to the tubing due to repeated flexing at the epoxy boundary.

An alternative geometry used to make a seal by deforming polymer tubing with an applied force and elevated temperature is shown in figure 40 [95]. As with all the techniques relying on tubing deformation the connection can often only be made once and the assembly is complex as well as requiring that all structures on the chip can withstand temperatures of 310ºC. In the case of figure 40, three glass wafers were used to fabricate a microfluidic channel, access hole and flanging recess. Thermoplastic tubing heated to just below its glass transition temperature could then

be deformed by means of an applied force to make a seal within the uppermost glass layer – the connecting tubing is subsequently inserted into the seal provided by the outer tubing and the connection is made.

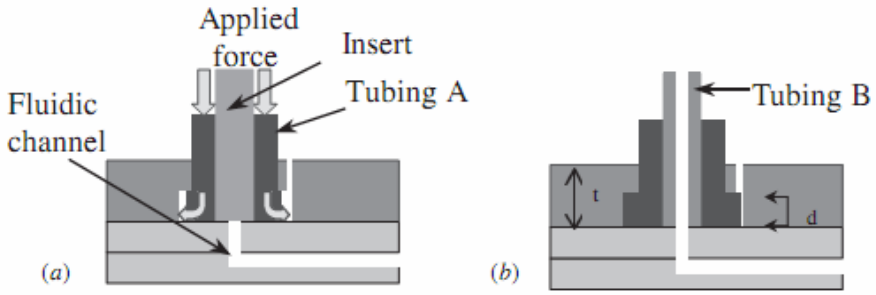

Figure 40, diagram of a process to make a sealed interconnect by deformation of polymer tubing [95]. This was demonstrated in a device formed of three layers of glass; the top layer contains a flanging recess and air vent (a). The tubing is deformed by pushing it against the middle glass layer and forms a seal around a connecting capillary (b).

Thermal deformation by freezing in liquid nitrogen has also been presented as a means of attaching polymer tubing to silicon devices, as Meng *et al*. demonstrated with polyetheretherketone (PEEK) tubing [96]. The tubing contracts under low temperature and is inserted into a micromachined recess in silicon; when it is brought back to room temperature it expands and forms a seal without the need for adhesive. Meng *et al*. used individual couplers fabricated in silicon and polyolefin to couple PEEK and fused silica tubing to silicon devices with high pressure tolerance.

Figure 41 shows the basic scheme of these connections, the coupler (in the middle of the diagram) is manufactured separately and a complementary recess is made on the device itself (bottom). This frees the device from the constraints of temperature tolerance placed on the tubing and coupler. The tubing and coupler are sealed together using low-temperature thermal deformation of the tubing and the coupler is then fixed to the receiver port with adhesive. This technique offers low dead volume self-aligning connections, but it is complex as a separate micromachining process is necessary to fabricate the couplers themselves.

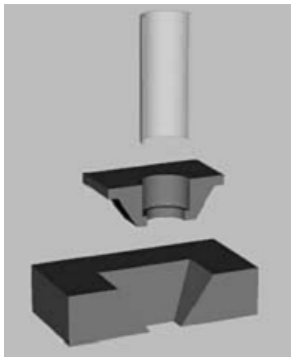

Figure 41, exploded view of a microfabricated capillary coupler, showing the capillary (top) with fluidic coupler (middle) that is attached to a self-aligning receiver port on a device (bottom) [96].

An alternative system of moulding a polymer to reduce dead volume is to use poly(dimethylsiloxane) (PDMS) to smooth the fluid path at the connection site [97]. This has been demonstrated for a side-on connection to a 120µm wide channel; the capillary is simply brought close to the channel, while a metal wire threaded through the capillary fits into the channel itself. PDMS is then cast around the capillary before the wire is withdrawn, leaving a smoothed connection path with a diameter defined by that of the wire.

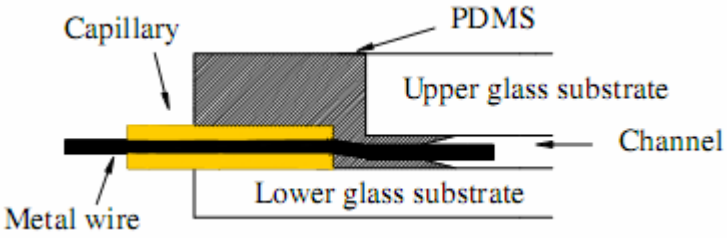

Figure 42, schematic diagram of a minimal dead volume connection to a microfluidic channel fabricated using PDMS casting [97].

This connection has potentially zero dead volume, although assembly could be challenging for smaller channels. It seems possible that some fragments of PDMS could be dragged into the capillary when the wire is removed. For a design with a tapered microfluidic channel this could potentially lead to a blockage, although for channels which are large enough throughout their length such debris can be pumped clear. For devices made entirely in PDMS, simply coring with a needle and pushing in a capillary may provide a suitable interconnect [98], although typically such connections have much lower pressure tolerances.

An excellent low dead volume connection that does not require any additional substrate layers is shown in figure 43 (from [99]). A capillary is inserted through a recess in the silicon layer which is matched to its outer diameter. A smaller opening at the bottom of the recess is matched to the inner diameter of the capillary. In this design, the smaller hole is machined in a second silicon wafer but it could conceivably be etched from the backside of the same wafer or used to connect to a channel etched in Pyrex.

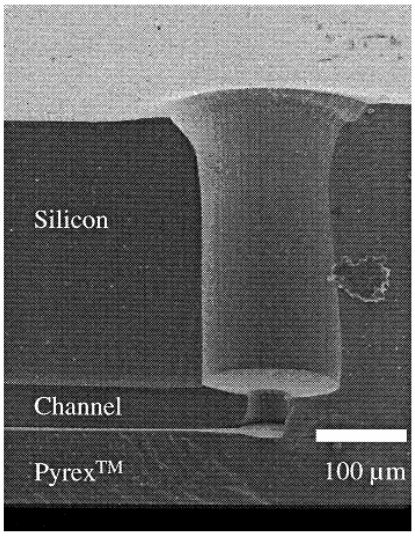

Figure 43, SEM micrograph of a low dead volume interconnect etched in silicon for connection to a microfluidic channel [99].

In general, interconnect design depends on the substrate material as well as the material of the connecting tubing. Deformable polymer tubing is convenient for reducing the dead volume in a connection, although polymer tubes generally have much larger diameters than those made of fused silica. More complex fabrication of course yields many options for interconnects with high pressure tolerance and low dead volume, although an extra wafer is often required. Even the most advanced interconnect designs frequently feature a 90º turn in the fluid path. Although this is not significant for many applications, it is a potential drawback for experiments on long polymers in solution, as the corner is a possible fouling site.

4.1.2 Deep Reactive-Ion Etching (DRIE)

DRIE is a popular technique for fabricating microfluidics and micro electro-mechanical systems (MEMS) devices in silicon because it offers high etch rates and highly anisotropic etch profiles with near-vertical sidewalls. The masking requirements are relatively simple; photoresist alone is often sufficient although an oxide layer can be used to protect the silicon and gives better pattern reproduction due to its favourable etch selectivity. The key to adapting reactive-ion etching into DRIE is the Bosch Process [100] which is described below along with some of the characteristic features it produces.

4.1.2.1 The Advanced Silicon Etch (ASE™/Bosch) Process

The Bosch Process is a method of adapting an isotropic etching process to produce anisotropic etching results. The process as implemented in the Surface Technology Systems (STS) inductively-coupled plasma (ICP) machine is shown in figure 44.

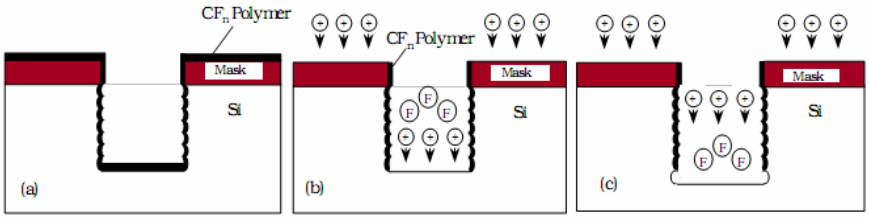

Figure 44, schematic of the STS ASE process. (a) Passivation stage; fluorocarbon polymer covers the surface. (b) Ion bombardment mechanically removes passivation layer from horizontal surfaces. (c) Silicon etched isotropically. These cycles can be applied repeatedly to make a trench with near-vertical sidewalls [101].

A plasma is generated from process gasses which alternate between an SF_6/O_2 mixture and C_4F_8. In figure 44 (a), the gas is C_4F_8 and the plasma forms a polymer coating on the wafer surface, including the sidewalls of the trench. In (b) and (c) the process gas is SF_6, with typically 10% O_2. Ions from the plasma are accelerated by the platen electrode (see figure 45) and bombard the horizontal surfaces of the wafer, removing the polymer coating there. When the polymer is removed, isotropic etching of the silicon takes place at the bottom of the trench. This last step is short and repeated application of all three steps can therefore etch a trench with a vertical sidewall profile. The balance of timing between the etching and deposition cycles is

critical to the process; changing the relative lengths of the cycles causes the trench sidewalls to taper, while reducing the length of both cycles reduces the etch rate but improves sidewall smoothness.

Figure 45 shows a schematic diagram of the key parts of an ICP DRIE machine [101]. The process gas (SF_6+O_2/C_4F_8) is introduced through the inlet at the top and a plasma is generated within the radio-frequency (RF) coil. The pressure in the chamber is controlled through the pumping port and wafers are generally introduced via an isolated loading chamber to allow the pressure in the machine to remain stable. The wafer is cooled from the back side by helium gas (<80ºC during processing [102, 103], to protect the photoresist) and sits on a platform which is raised up to the plasma during processing. The platen electrode is used to accelerate ions towards the wafer during the etching cycle. The etching performance depends on the interplay between several critical parameters. The inlet gas mixture, process pressure, coil power and frequency, platen power and absolute and relative lengths of the etching and deposition cycles all have a significant effect on the etching results.

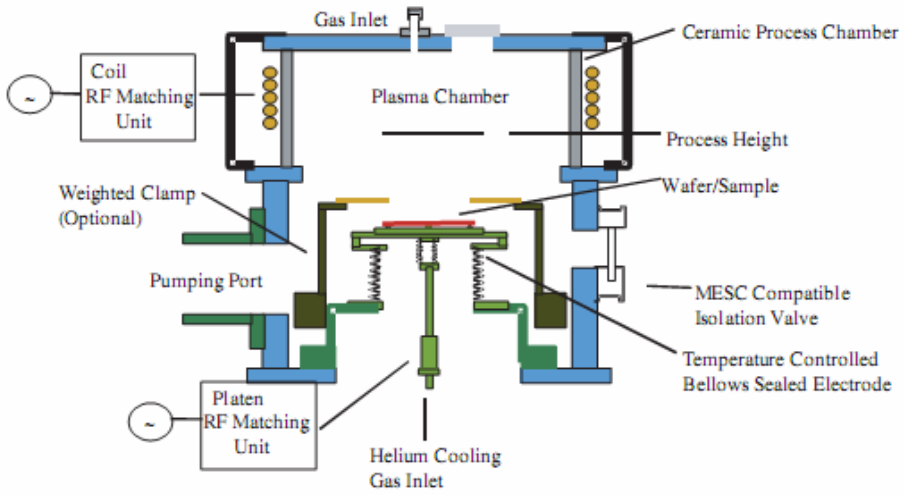

Figure 45, diagram showing the principal parts of an STS inductively-coupled plasma deep reactive-ion etching system [101].

The fact that varying degrees of anisotropy – from isotropic etching to vertical etching – are available from the same machine makes it convenient to use DRIE for a variety of non-standard etch processes. The wall tapering effect of cycle length can easily be adapted for slope fabrication [104], while alternating

isotropic/anisotropic steps can be used to fabricate more complex out-of-plane geometric profiles [105]. The availability of high etch rates combined with vertical sidewall profiles makes DRIE an attractive choice for through-wafer etching. As well as allowing connections between wafers in layered microfluidic designs [106] this has been used to directly fabricate devices such as arrays of microneedles for transdermal fluid injection/extraction [107, 108].

4.1.2.2 DRIE-lag and Aspect Ratio Dependent Etching

In general DRIE produces good etch uniformity across a wafer [101], but it does have some characteristic features that can complicate processing. For example, mask apertures with a smaller diameter etch more slowly during DRIE than those with a large diameter. The same is true for trenches of all shapes, with the critical dimension being the shortest length of the mask opening [109]. This is a manifestation of the more general phenomenon of aspect ratio dependent etching (ARDE) in which the etch rate in a trench is observed to decrease as the aspect ratio (depth/width) increases. The graphs below illustrate two facts about DRIE-lag; that the effect is most significant for trenches with a width <10µm (figure 46) and that the aspect ratio (length/width) of the mask aperture is not a critical factor (figure 47). In each case the etch time is fixed for all features and the depth of each trench is measured by cleaving the wafer and imaging by scanning electron microscope (SEM) [109]. These results are appropriate to the depths considered in the experimental sections, but for clarity ARDE is particularly significant from depth:width ratios beyond 4:1 [110].

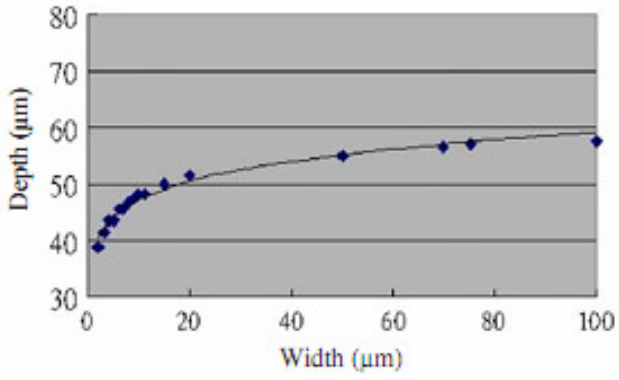

Figure 46, DRIE-lag as a function of trench width in silicon etched by ICP [19].

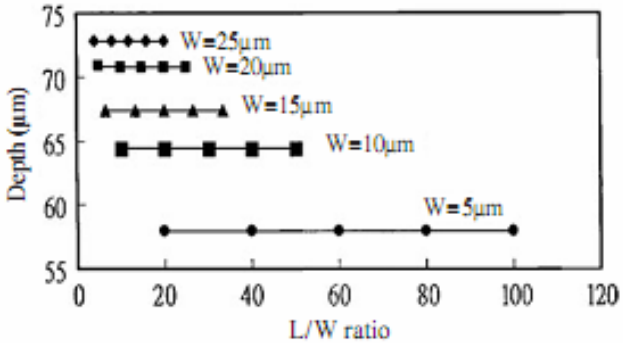

Figure 47, graph showing the etch depth as a function of the length/width aspect ratio of a silicon trench after DRIE. This aspect ratio is not a significant factor for the DRIE-lag phenomenon [19].

For trenches of width 1μm and larger, the ARDE effect may be explained by any of four mechanisms [111]; Knudsen transport of neutrals, ion shadowing, neutral shadowing and differential charging of insulating microstructures. Differential charging (similar to that illustrated in figure 48 below) can occur due to an insulating mask material, but as silicon is a relatively good conductor the ion angular distribution (IAD) is considered to be the most important factor in ARDE [112]. The IAD is significant because the removal of the passivation layer from the bottom of a trench during the etch phase happens due to ion bombardment. The ions in the plasma are accelerated towards the sample by the platen electrode and they reach the surface with a certain angular distribution. Part of this distribution is shadowed in a narrow trench which inhibits removal of the passivation layer causing a reduced etch rate which can eventually drop to zero. For this reason, ARDE can be observed to be more sensitive to SF_6 flow rate than to platen power [103] – over typical operational ranges, the platen power is always sufficient to impart enough energy for the ions to remove polymer from the trench base. However low platen power can reduce the rate at which the polymer is removed and contribute to ARDE or even cause pinch off [102]. Increasing the coil power can also cause increased ARDE because the ion-shadowing effect is greater in a narrow trench, thus as the coil power increases, the ion-flux in a wider trench increases by a greater proportion than it does in a narrow trench [113].

4.1.2.3 Trench Footing

Trench footing is primarily of concern for users of silicon-on-insulator (SOI) wafers where etching through the silicon to the buried insulator layer (typically silicon

dioxide) is a common process. As shown in figure 48 it is possible for charge build-up at the trench base to cause notching at the interface of the two materials. The origin of the charge build-up is the difference in anisotropy between the directionality of electrons and that of ions – the ions are highly directional (approximately normal to the sample) while the electrons approach the surface with a wide range of incident angles [111]. This causes negative charging on the upper surface which deflects the ions as they transit the trench and causes a build up of positive charge at the trench base. Stopping the etch process at exactly the correct time to ensure the buried oxide layer has been reached and undercutting is avoided is particularly challenging, not least as the silicon etch rate may vary with trench depth and parameter ramping. The operating frequency of the RF coil that generates the plasma in an ICP machine is typically 13.56MHz, reducing this to 380kHz is sufficient to reduce notching in many cases [101]. This change is not suitable for all processes however, as it broadens the energy range of the ions in the plasma. Low energy ions have lower directionality which slows down the removal of the passivation layer – an unnecessary complication for silicon-only wafers.

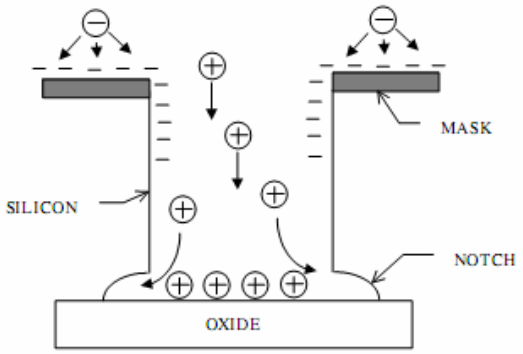

Figure 48, diagram showing charge build up in an SOI wafer which leads to notching at the foot of the trench [101].

4.1.2.4 Edge scalloping

The isotropic nature of the etch cycle in DRIE can lead to a high degree of roughness on the trench sidewalls. In processes where the parameters are fixed, the balance required to obtain vertical sidewalls and a sufficiently high etch rate often leads to some degree of edge scalloping. Although decreasing the time of both cycles can reduce scalloping at the expense of etch rate, this often leads to further problems

such as bottom grassing and pinch-off (see section 0) when trenches reach high aspect ratios. To achieve high aspect ratios with smooth sidewalls it is necessary to change the process parameters as the etching depth increases.

Figure 49 shows the difference between a process with fixed parameters (A) and one where the parameters are changed (B) with etching time/depth [114]. Using this system, the Chabloz *et al.* were able to produce trenches with an aspect ratio of up to 40:1 and a sidewall roughness of <8nm. The balance between the rate of deposition of the passivating polymer layer and its removal by ion-bombardment is the key factor in this process. A lower ion bombardment energy (lower electrode power) and a thicker polymer layer (increased deposition cycle time) are used to reduce scalloping at the top of the trench. As depth increases this would cause the trench to pinch-off due to inadequate removal of the passivation layer from the floor. The platen power and the etch cycle length are therefore increased at greater depths to increase the energy of the bombarding ions and therefore improve polymer removal.

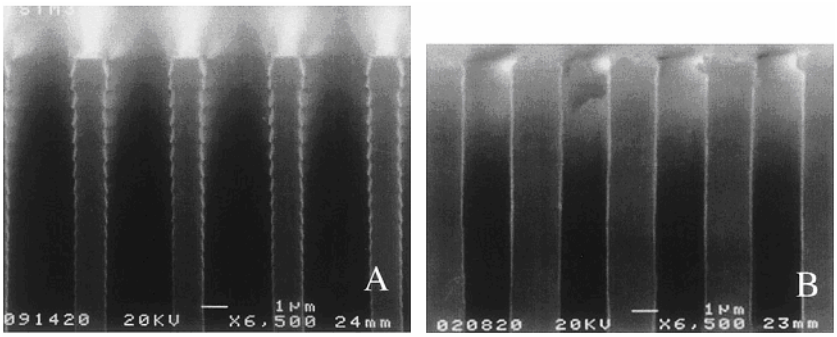

Figure 49, SEM images of edge scalloping in deep silicon etching by DRIE [114]. (A) Process with fixed parameters suitable for etching the whole trench. (B) Optimised process to minimise edge-scalloping, changing the RF coil power, pressure and cycle times as the etch depth increases.

4.1.2.5 Grassing

If the balance of the etching conditions is not correct, in addition to poor profile control it is possible that 'bottom grass' will be deposited in a trench as illustrated in figure 50 [115]. The 'grass' is a build up of the passivation polymer in cases where it is inadequately removed during the etching phase. This build-up can also lead to the trench 'pinching-off' in which case the desired depth will not be reached and

deposited polymer will remain in the trench after processing. Although the polymer is easy to remove in subsequent processing (e.g. O_2 plasma photoresist removal) the bottom of the trench will still be rough due to the uneven etching.

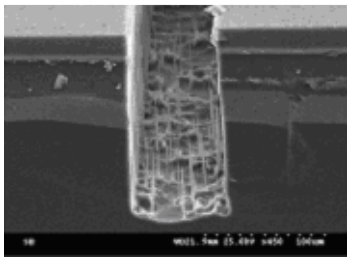

Figure 50, SEM image of bottom grass formation resulting from polymer deposition at the trench base during DRIE of silicon [115].

4.1.2.6 Pattern Density (Microloading) and Cross-Wafer Uniformity

The uniformity of the DRIE etching process across a 100mm wafer is of the order of 5% [116], the main non-uniformity stems from a higher concentration of fluorine radicals at the edge of the wafer where the silicon load is less [117]. The term 'microloading' is variously used to refer to cross-wafer uniformity and as an alternative term for DRIE-lag. Here the latter terminology is not used, but local pattern density can lead to variations in the etch rate across a wafer, i.e. where there are more open areas the etch rate can be lower due to a reduced local concentration of fluorine radicals.

The different features of DRIE described above can be limitations, but they can also be exploited. Some development is normally required to find the correct process for each application, but the rich variety of etching behaviour gives a great flexibility in the structures that can be produced from a single process.

4.1.3 Applications of Specific Effects of DRIE

The notching phenomenon in SOI wafer processing using DRIE has been used to release devices such that they are free to move without the need for hazardous hydrofluoric acid (HF) etching. Typically the silicon is etched down the oxide layer and the oxide is removed by etching in hydrofluoric acid (HF) thus undercutting the

device. For some structures such as thin beams, the notching effect is sufficient to perform this undercutting in the silicon layer thus removing a process step [118]. Large areas around a freestanding structure can also be removed by using a similar process to etch arrays of holes surrounded by a perimeter trench. The notching effect undercuts the array and causes it to fall onto the insulating layer. Once isolated from the bulk silicon the charging effect is even greater which causes increased ion scattering and therefore localised isotropic etching. As such, the array of holes is entirely etched away leaving the device – a resonator formed from a beam and shuttle mass in the case of [118] – with a large space around it. The size of the holes is determined by the need to avoid DRIE-lag excessively retarding the etch rate and small gaps between the holes reduce the time required to undercut the sacrificial structure and thus the time to remove it.

DRIE-lag has been used to produce a number of sloped and curved surfaces. Typically an array of different width trenches is etched anisotropically to produce the desired curvature in the bulk of the wafer and the walls dividing the trenches are subsequently removed by isotropic etching (RIE or chemical etching). As an example, an out-of-plane curved electrode used as an actuator was fabricated by this method [119]. A similar process using two isotropic etch steps has also been demonstrated [120], in which a slope is defined by RIE-lag through a mask of increasing trench diameter. The slope is then smoothed and further etched by RIE after the masking layer is removed. This process was able to produce curved structures with a surface roughness of 25nm peak-to-valley. An alternative method of removing the walls left by an anisotropic DRIE-lag process step is sacrificial oxidation. If the walls are thin (~1µm) they can be completely removed by thermal oxidation and HF etch [121]. This method has the advantage of retaining sidewall angles in portions of a device where sacrificial walls are not present.

4.1.4 Alternative Methods for Fabrication of Out-of-Plane Slopes

In considering the fabrication of an in-plane connection with a slope connecting a capillary to a microfluidic channel, there are other methods available to produce the slope. A common approach is to use a wet etch in KOH which produces a slope of 54.7º in <100> silicon. This would introduce an extra process into a design where

the critical features (microfluidic channels themselves) are to be fabricated by DRIE, as KOH etching has more complex masking requirements (a silicon nitride layer on both sides of the wafer). Another option is to use a greyscale mask to produce a sloping layer of photoresist [122]. As the resist is removed by the etching process, the slope in the resist is reproduced in the substrate. Although greyscale photomasks are more expensive to produce, the main limitation of this technique is that the total depth over which a slope can be created is dependent upon the thickness of the resist layer. Another photolithographic solution for slope formation initially in resist is diffraction gradient lithography – using a diffraction pattern to differentially expose sections of resist. Again this is limited by resist thickness but the technique finds applications in nanofluidics [123].

4.1.5 Anodic Bonding

For devices fabricated in silicon, anodic bonding of a glass wafer is commonly used for packaging devices and sealing microfluidic channels [124-127]. The choice of glass depends on matching the coefficient of thermal expansion with silicon (*cf.* [125]). At elevated temperatures sodium impurities in the glass become mobile and under a large electric field they migrate towards the anode leaving oxygen ions at the interface which bond to the silicon atoms in the device wafer.

4.1.6 Conclusion

World-to-chip fluid delivery strategies presented in the literature generally employ a connection through the top layer of the device, perpendicular to the microfluidic channels. Various strategies have been presented for pressure-tolerant, low dead volume interconnects, but connections offering low loss delivery of long biopolymers such as DNA are less commonly reported. A smooth, in-plane fluid connection may offer efficient DNA loading/unloading which is essential for practical applications in genomic analysis. DRIE of silicon is an established technology which offers many benefits for microfluidics including facile reproduction of curved patterns and pressure-tolerant devices with favourable optical properties through the use of anodic bonding of borosilicate wafers. By exploiting some known properties of DRIE it is possible to produce out-of-plane slopes in

silicon devices and this may offer a method to produce a novel interconnect for efficient microfluidic DNA loading.

4.2 Materials and Methods

4.2.1 Silicon and Pyrex Substrates

Undoped <100> silicon single side polished six inch diameter 500µm thickness silicon wafers were used for all silicon processing. Pyrex wafers, 1000µm thickness and double-side polished, were purchased from Si-Mat, Germany. For wafers with an oxide masking layer stock silicon wafers of the same type with a 500nm thermally grown silicon dioxide layer were used. The oxide was thinned by a calibrated etch in hydrofluoric acid (HF) and the thickness confirmed by ellipsometry against a standard. An additional timed HF etch was used to completely remove the oxide from the exposed areas after photolithography.

4.2.2 Photolithography

Photolithography masks were purchased from Qudos (U.K.) and Uppsala University (Sweden). Hexamethyldisilazane was used as a photoresist adhesion promoter for both of the resists considered, AZ1512 and AZ4562 (Clariant, Singapore), which are both positive resists. Final parameters for the photolithography process are given in the results section but the outline was fixed. After spinning (RC8, Suss MicroTec, Germany) a layer of HMDS, the photoresist was spun then 'soft baked' on a hotplate at 100ºC for 1-5 minutes depending on resist type and thickness. The wafer was then aligned on a Suss MicroTec mask aligner and exposed to UV at 6mWcm^{-2} before developing in either Microposit MF312 mixed 1:1 with deionised water or neat Microposit MF222. A rinse in deionised water was used to arrest the development and the wafer was dried under nitrogen prior to inspection. Successfully patterned wafers were finally 'hard baked' at 120ºC to improve photoresist adhesion.

4.2.3 Silicon Etching

DRIE was performed in a Surface Technology Systems Multiplex ICP device (STS, now SPTS, U.K.). Final process parameters are given in the results section but all anisotropic etching was based on two standard protocols for 'fast' and 'slow' etching. The slow process is based on a 7 second etch cycle and a 5 second deposition cycle, both with a coil power of 800W. For etching, flow rates of 130sccm SF_6 and 13sccm O_2 are used with a platen power of 8W. During deposition there is a flow of 85sccm C_4F_8 with a platen power of 0W. The fast process has etching and deposition cycles of 12 and 7 seconds respectively, both with a coil power of 600W. The gas flow rates are the same as the slow process, while the platen power is 10W for etching and 0W for deposition. For both processes the final cycle is always an etch cycle and the pressure is maintained at 15mT. For isotropic etching, investigations were based on a standard protocol with a gas flow of 130sccm SF_6, 13sccm O_2 together with a coil power of 600W and a platen power of 0W. The pressure was 15mT, although this was later increased to ensure wall removal.

4.2.4 Other Processes

Anodic bonding was performed in an SB6 bonder (Suss MicroTec, Germany) at atmospheric pressure for 2 hours at -500V. A DISCO (model DAD3350, DISCO, Japan) dicing saw was used to dice wafers after processing. Two SEMs were used for inspection and sample measurement, a JSM-6301F (JEOL, Japan) and a LEO 1455 VP (LEO, U.K.). For quick inspections such as estimating the etch rate midway through processing, a Tencor (U.S.A.) AS500 surface profiler was used. Although this was suitable for depth measurements in open areas such as the capillary trench, the stylus was too wide to fit into narrow trenches, particularly as the depth/width aspect ratio increased. Photoresist removal was performed in oxygen plasma (PVA Tepla, U.S.A.) at 1kV for up to 10 minutes as required.

4.3 DRIE Calibration Processing Results

The central focus of the fabrication results presented in this chapter is the development of a DRIE-lag process to generate out-of-plane slopes in silicon. This places several requirements on key process steps. The photolithography process had

to be capable of reproducing features with a line width of two or three micrometres in a resist layer capable of withstanding thirty minutes or more of a DRIE process. An anisotropic DRIE process was required to produce high aspect ratio walls and an isotropic process capable of quickly removing those walls was also developed.

4.3.1 Photolithography

A choice of two standard photoresists was available, AZ1512 and AZ4562. The thicknesses produced by a 30 second spin at 3000rpm are given by the manufacturer as 1.5µm and 7µm respectively, the selectivity was estimated as 1:65 vs. silicon for both under DRIE. Reproducing mask features with a width of less than ~3µm proved to be much more challenging with the thicker resist. However, a deep (130µm) etch is required to form the channel that houses the capillary, which could potentially remove all of the resist when using AZ1512. AZ4562 was therefore the resist of choice, although this meant that the trenches which would exhibit the most DRIE-lag – the 1 and 2µm widths – would often not be etched due to incomplete photoresist removal during photolithography. For the purposes of slope formation in microfluidics however, the ability to etch 1 and 2µm trenches is not critical. Nevertheless a higher spin speed was used to moderate the thickness of the resist layer and aid in the accuracy of mask feature reproduction.

The final parameters used for photolithography were;

- HMDS prime 30 second spin, 1000rpm
- Spin AZ4562, 4000rpm 30 seconds (for a 6µm layer)
- Soft bake on hotplate, 100ºC for 5 minutes
- Exposure, 20 seconds at 6mWcm^{-2}
- Development, 2 minutes in 1:1 (volume/volume) MF312/deinonised water
- Hard bake, 120ºC for 1 hour

Figure 51 shows the end of one of the connecting channels from a prototype device after photolithography for layer 2. The photolithography process was refined only until it was adequate for producing 2-3µm features. For deep etches such as this, it is often preferable to use a silicon dioxide masking layer as the selectivity is superior

to that of photoresist. This is particularly useful at the edge of a trench for example, where the photoresist profile is often not vertical and the mask is effectively thinner which can result in trench widening. Initially, some wafers were processed with a 500nm or thinner silicon dioxide layer. This however, made definition of the wall thicknesses more difficult since the oxide etches isotropically in buffered hydrofluoric acid which causes some undercutting of the photoresist mask. The final wall size etched into the substrate was therefore a combination of the size on the mask and the thickness of the oxide layer (as well as the isotropy of the wet etch). As mentioned previously, trenches of 2µm and less are of limited utility for the application of interest and therefore a thick photoresist mask was preferred to the extra complication of the oxide mask.

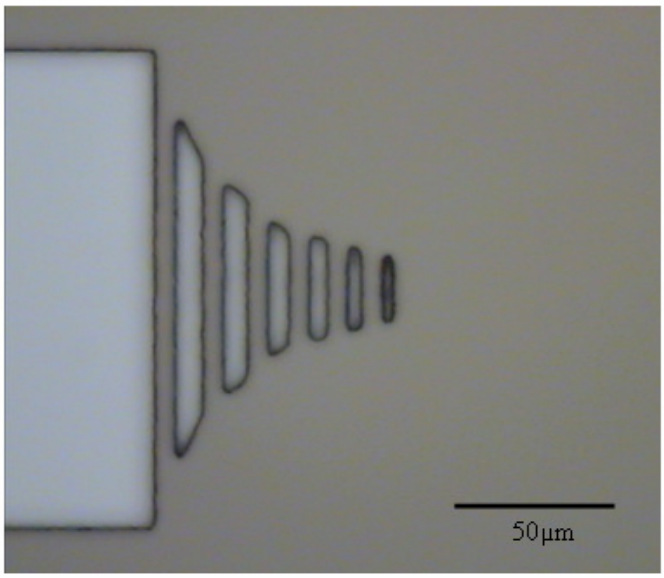

Figure 51, microscope image of prototype interconnect with capillary trench (left) and narrow trenches to form a slope, shown after photolithography. The grey area is photoresist (6µm thickness); the blue area is bare silicon. This sample was produced using a 20 second exposure and 2 minute development.

4.3.2 DRIE of Silicon

As described in section 4.2.3, silicon etching was based on established protocols for 'fast' and 'slow' etching; results from each of these processes are presented below. These methods were tailored to produce sacrificial walls between deep trenches which could be easily removed using a subsequent isotropic etch.

All etching processes were tested against a standard set of mask patterns, a full description of which is available in Appendix A. The basic pattern for demonstration of DRIE-lag was a series of trenches of fixed length with width 1-10µm. The spacing between these trenches (and hence width of the sacrificial walls) was fixed for each calibration pattern, but different patterns produced walls in a range of widths from 2-8µm. Larger trenches were also produced with widths in the range 25-150µm, which not only widened the range over which DRIE-lag could be measured, but also provided useful information about etching of the walls in relatively open areas of the wafer. The depths achieved with each etch process were evaluated by cleaving the silicon wafer after scoring with a diamond pen and imaging in cross-section in an SEM.

4.3.2.1 Slow anisotropic etch process

The central consideration with this etching process was to generate a sidewall profile that was close to vertical with low roughness, allowing high aspect ratio, thin walls to be produced. The sidewall roughness is a function of scalloping (see section 4.1.2.4) and thus is a critical factor for fabricating thin walls with high aspect ratio. These results are for the slow etch described in the Materials and Methods section which is designed to have a high quality at the expense of etch rate, for convenience the key parameters for this process are reproduced in table 3.

Parameter	Etch Cycle	Passivation Cycle
Length (s)	7	5
Coil power (W)	800	800
Platen power (W)	8	0
Gas flow rate (sccm)	SF_6, O_2, 130, 13	C_4F_8, 85
Pressure (mT)	15	15

Table 3, process parameters for standard slow anisotropic etch process.

Figure 52 shows a cleaved cross section of the standard slope calibration pattern taken in the SEM. The pattern consists of ten trenches of fixed length, each 1µm wider than the previous, from 1 to 10µm, separated by walls of a fixed size. Similar

patterns are used that have a different fixed value of trench length. The wall width in this case is 8µm and the pattern length was 500µm. The DRIE-lag effect can be seen here as etch depth decreases from larger to smaller trenches (right to left). At this magnification the quality of the sidewalls is difficult to discern. It is clear however that all trenches 'pinch-off' due to excessive polymer deposition as a result of the long passivation cycle (relative to the etching cycle). The polymer removal rate is lower at the bottom of a deep trench due to ion-shadowing, hence at some aspect ratio removal will be incomplete during the etch cycle and from this point polymer residue will build up with each DRIE cycle. Eventually enough polymer is deposited to prevent further etching and the trench can be seen to pinch-off.

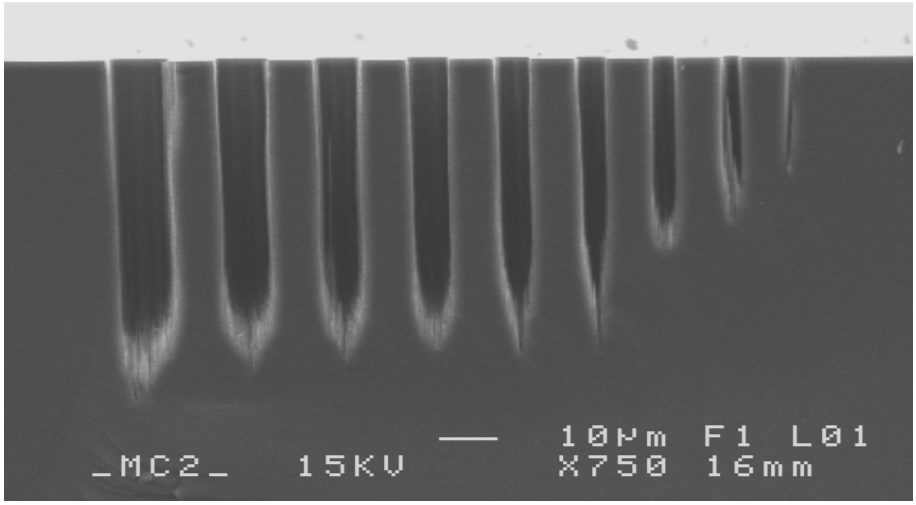

Figure 52, SEM image showing a cross section of the slope calibration pattern. Trench widths of 10-2µm are produced, the 1µm trench was not successfully reproduced during photolithography. Walls 8µm wide; pattern length 500µm, etch cycle 7s, deposition cycle 5s.

The effect of the balance of cycle times between etching and deposition is further illustrated by figure 53, where the polymer grassing on the bottom of larger trenches is clearly evident. It is apparent that this build-up of polymer begins around the trench perimeter which causes the bottom of the trench to adopt a curved profile which will obviously be present even if the polymer grass is subsequently removed.

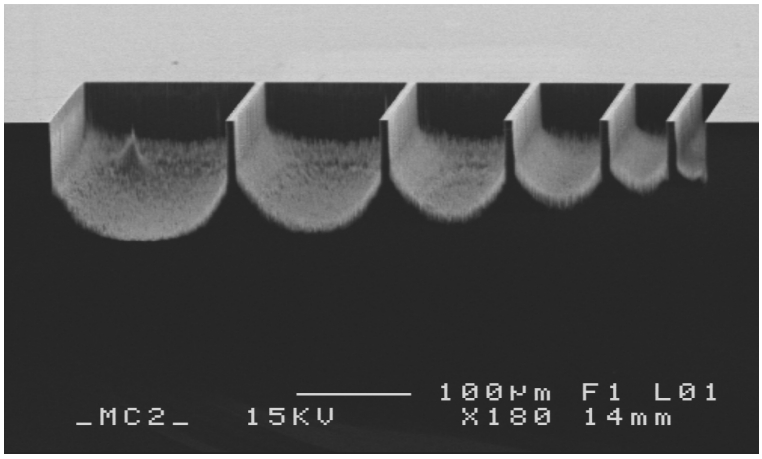

Figure 53, SEM image of etching results in wide trenches (25-150µm) using the slow etching process (etch cycle 7s, deposition cycle 5s). The build-up of polymer affects the trench profile and eventually causes pinch-off.

4.3.2.2 Fast anisotropic etch process

For etching to depth of around 150µm, as is required for the capillary housing, the standard fast etch process performed well, the key parameters for this process are reproduced in table 4. The etch rate was 4µmmin^{-1} in open areas and although the sidewall profile was not as good as that of the slow etch recipe it was acceptable in most cases (peak-to-valley scallop roughness approximately 1µm).

Parameter	Etch Cycle	Passivation Cycle
Length (s)	12	7
Coil power (W)	600	600
Platen power (W)	10	0
Gas flow rate (sccm)	SF_6, O_2, 130, 13	C_4F_8, 85
Pressure (mT)	15	15

Table 4, process parameters for standard fast anisotropic etch process.

A version of the standard slope calibration pattern of described in section 4.3.2.1 (trench widths 10, 9, 8, 7, 6, 5, 4, 3, 2 and 1µm, length 500µm) with 2µm walls was included in the mask design to explore the limits of achievable wall aspect ratio. An SEM of this design etched with the fast recipe is shown in figure 54; the tallest surviving wall has an aspect ratio greater than 40:1, although clearly this result is

likely to be difficult to reproduce as the wall to the right of it has been etched away entirely. The slope on the right hand side of the pattern suggests that the last wall was initially present and hence this isn't simply a lithography error, although the lack of a significant ridge at the base of the trench suggests that the wall was destroyed some time before the end of the etch process.

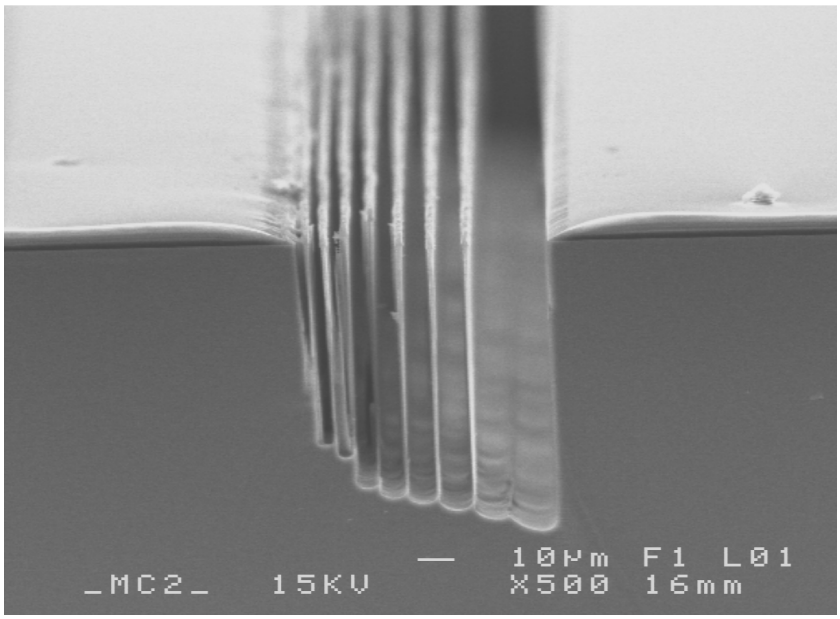

Figure 54, SEM image of trenches of 10µm width and less separated by 2µm walls etched using the fast DRIE process (etch cycle 12s, deposition cycle 7s). The tallest surviving wall has an aspect ratio greater than 40:1.

Figure 55 shows a cross-section through a pattern of 500µm long trenches separated by 8µm walls, etched with the 'fast' process. The sidewall profile is not vertical and some walls taper significantly towards the bottom. The visible trenches are 10-2µm wide by design (from left to right) although the trench on the right hand end has a measured mask opening of 3.5µm rather than 2µm. This is probably a photolithography error; it is likely that the trench is actually the result of merging of the adjacent 1 and 2µm mask patterns. This would be consistent with the DRIE-lag effect seen in this micrograph since the resulting 3.5µm trench reaches an etch depth in between that seen in the 3 and 4µm trenches. Some aspects of photoresist performance may be evaluated from figure 55. The thin walls generally show some undercutting of the resist and although the resist profile is not vertical it has remained thick enough to protect the features of the duration of the process.

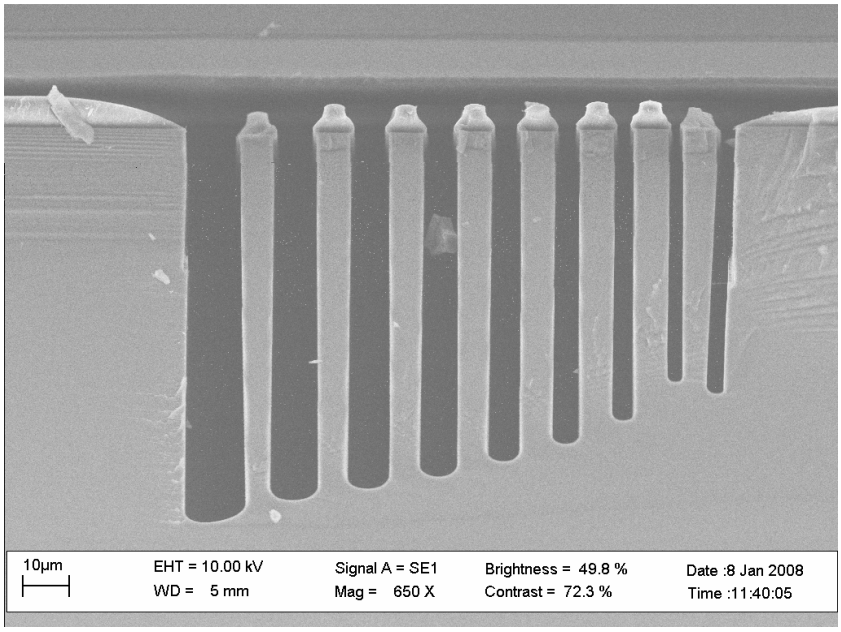

Figure 55, SEM image of trenches of length 500µm, width 10-3µm etched with the fast process (etch cycle 12s, deposition cycle 7s). The rightmost trench is likely formed from a merging of the 1 and 2µm trenches defined on the mask due to inadequate photolithography.

Measurements were taken from micrographs such as that shown in figure 55 from patterns at various locations across the wafer and the results combined to characterise the DRIE-lag effect over the whole wafer. Calibration patterns with different wall widths were used, but all data comes from patterns of fixed, 500µm length. The results of this analysis are shown in figure 56 and are in good agreement with similar work in literature (*cf.* [109]). DRIE-lag is apparent across the whole range of trench widths studied, although it is clearly most significant in trenches less than 25µm wide.

The DRIE-lag effect is dominated by the smallest dimension of a mask opening and this may be illustrated from the SEM data by plotting the observed etch rate against trench length for a fixed width as in figure 57. Several representative widths were chosen and they all show a consistent etch rate across the patterns of lengths 500µm to 2mm. Difficulties in cleaving the wafer accurately enough mean that insufficient data was collected from the 150µm length patterns for inclusion in this analysis.

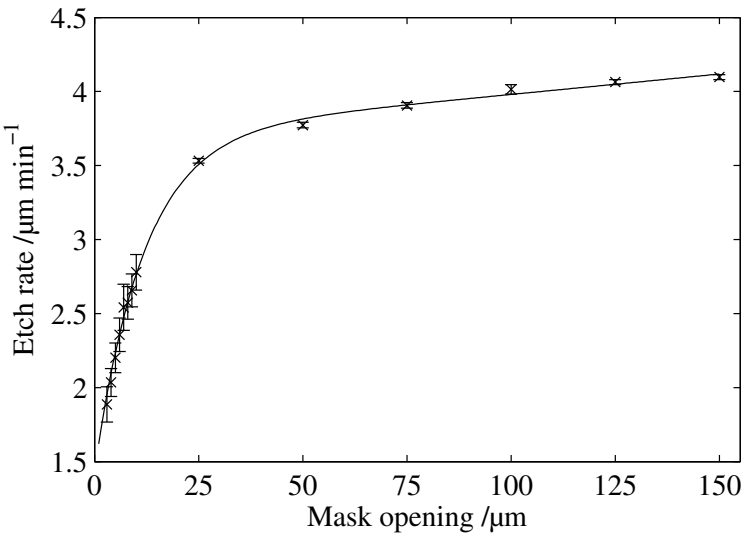

Figure 56, mean DRIE etch rate of the 'fast etch' (etch cycle 12s, deposition cycle 7s) process as a function of the smallest dimension of the mask opening. Total etch depth was 150μm in open areas, error bars show the standard error; the line is a guide for the eye.

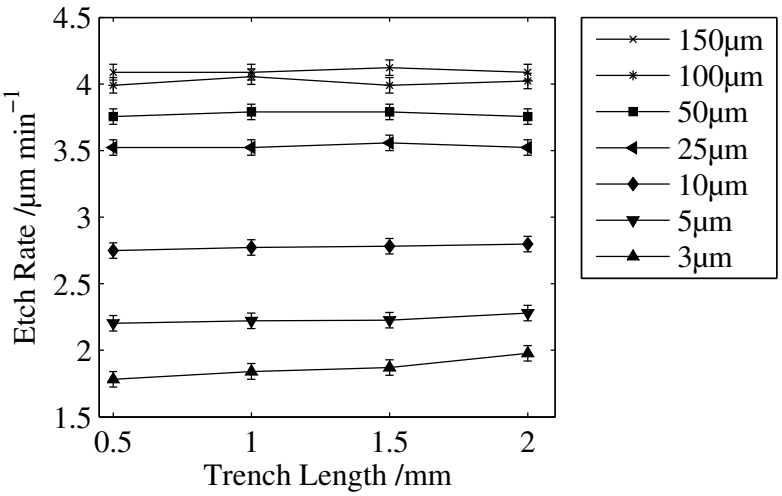

Figure 57, DRIE etch rate (fast process) as a function of trench length for several representative trench widths; the width is the dominant factor. The wafer was etched to a depth of 150μm in open areas.

4.3.3 Isotropic etch processes

An isotropic, or near isotropic etching process is required to remove the walls between the trenches in order for any slope that can be formed by DRIE-lag to be useful for microfluidic applications. The processes presented here are variations on

a process that gives an isotropic etch at the wafer surface, the parameters for which are reproduced in table 5. The processes described in this section change one or more of these parameters. None of the variations provides truly isotropic etching but the name is used to distinguish them from the near-vertical processes described above.

Parameter	Etch Cycle
Coil power (W)	600
Platen power (W)	0
Gas flow rate (sccm)	SF_6, O_2, 130, 13
Pressure (mT)	15

Table 5, process parameters for standard isotropic etch process.

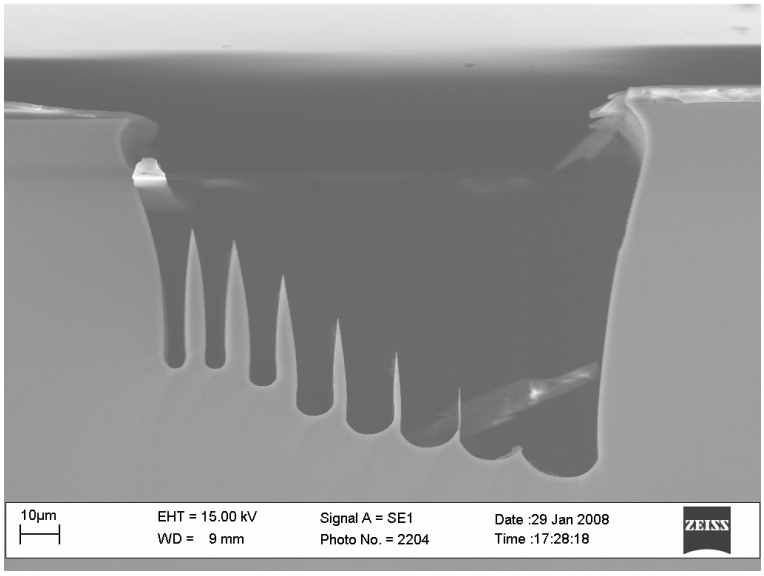

Figure 58, SEM image showing the effect of etching for 10 minutes at 15mT, 10W platen power to remove walls of initial width 8µm from 500µm long trenches.

Figure 58 shows the effect of a ten minute etch using only SF_6 with 10% O_2 and a platen power of 10W for 10 minutes. For an isotropic etch at the wafer surface the platen power would typically be 0W but this was increased to promoted ion transport into the deep trenches. The walls in the figure were originally 8µm in width and

represent the widest walls in the calibration mask design and therefore the hardest to remove. Clearly this etch was suitable for removing walls with slightly wider trenches (8, 9, 10µm) to either side, however the walls between the narrowest trenches remained problematic. The tapering towards the top of the partially removed walls (for example the leftmost wall in figure 58) shows that the etch rate at the top of the wafer is greater than the etch rate at the bottom of the trench. This is to be expected, as the ion angular distribution makes isotropic etching at the trench base challenging.

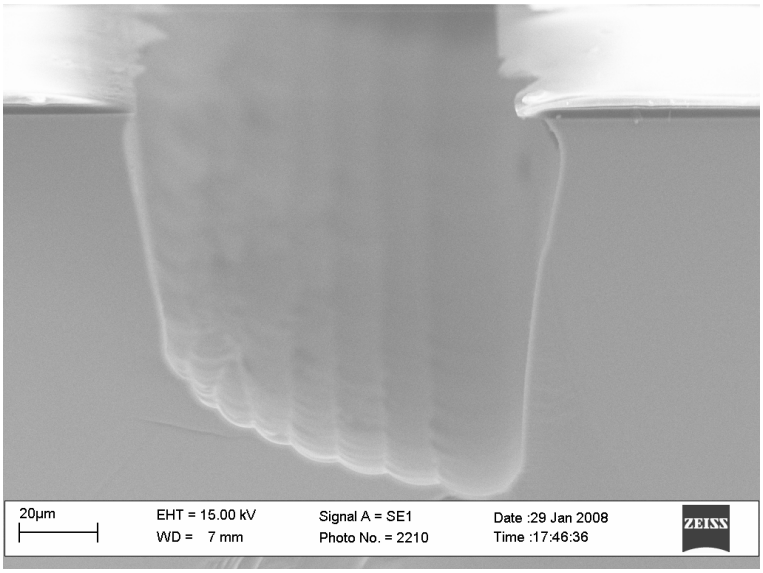

Figure 59, SEM image of a slope produced from a sample initially containing 500µm long trenches of width <10µm separated by 4µm walls. The walls were removed by etching for 10 minutes at 15mT with a 10W platen power.

For the removal of 4µm and narrower walls, the 10W platen power, 15mT process was adequate; figure 59 shows a sample initially formed from narrow trenches (1-10µm) separated by 4µm walls. The walls have been completely cleared leaving an open slope with a peak to valley roughness of 1.5µm and an end-to-end angle of 22º from the horizontal. The only limitation of this process is that the etching time of 10 minutes is quite long. As the isotropic part of the process exists only to remove the walls, it is preferable to keep it short to avoid unwanted etching of the channel sides or damage to the slope in areas where the walls are removed more readily.

A sample produced with the fast anisotropic etch process was used to investigate the effect of a shorter, 5.5 minute isotropic etch performed at 30mT with a Platen power of 0W. Figure 60 shows an example of the effect of this etch process on a slope with repeated trench widths, *i.e.* (from left to right) trench widths of 10, 10, 9, 9, 8, 8 … 2, 2µm, separated by 8µm walls. The higher process pressure in this case had the desired effect of increasing the etch rate at the base of the trenches. This is useful because the bottom of the wall was previously the last part to be removed and a longer, 10 minute isotropic etch was required for complete removal. Such a long etch increases the depth of the entire slope, which has makes accurate process design more complex and increases the difficulty of producing a slope because a slope can be levelled over time due to the higher etch rate closer to the upper wafer surface. By inducing a higher etch rate at the trench base, it is possible to reduce the time spent under isotropic etching conditions.

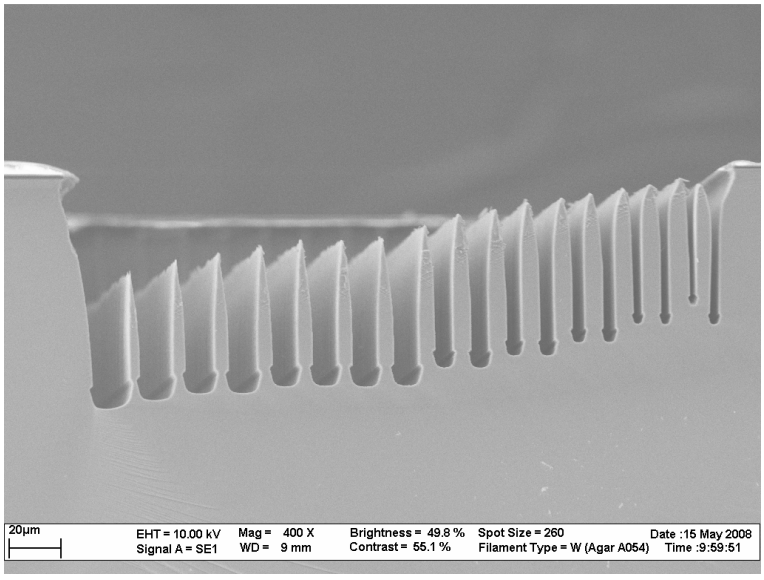

Figure 60, SEM image of trenches separated by 8µm walls which have been etched 'isotropically' for 5.5 minutes with a platen power of 0W at 30mT.

Figure 61 shows the lateral etch rate measured from SEM micrographs looking down onto the wafer surface. The increase in trench length from the mask specification is measured at both the top and bottom of the trench and an average of the two measurements is used to calculate the etch rate. In general, samples were cleaved with a view to measuring variation in the depth etched and wall size, hence most samples were unsuitable for measuring the lateral etch rate cause by an isotropic

process. The nature of the rectangular mask patterns and the fact that the walls are removed at some point during the etch further complicates this measurement, but it serves as a guide for subsequent design.

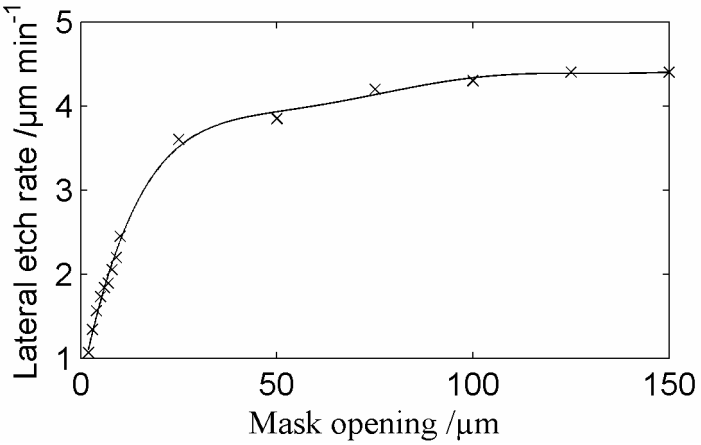

Figure 61, etch rate in the (lateral) plane of the wafer as a function of mask opening for 'isotropic' etching with platen power of 0W at 30mT.

For the larger (width > 25µm) trenches, removal of the adjacent walls was straightforward and any conditions that were suitable for removing walls between sub-10µm trenches were also suitable for removing walls between larger trenches. For many applications, simply using narrower walls would be adequate since these are easily removed with a variety of short etches under isotropic conditions. Increasing the process pressure to 40mT for the isotropic etch was found to cause instability in the plasma and no further improvements were found for the isotropic etch process alone. However, aside from the flexibility offered by wider walls with respect to slope profile, they are also more robust for deep anisotropic etching. A process was therefore devised to allow the continued use of the 8µm walls.

4.3.3.1 Modifications to the anisotropic etch process

Two aspects of the etching behaviour described above are complimentary to each other for the purpose of removing the walls. Firstly, etching with the fast process a tapering of the walls was observed such that the bottom is narrower than the top in deep etches. Secondly, in isotropic etching there is always preferential etching at the top of a wall, although increasing the process pressure can cause an increase in the etch rate at the wall base as well. Combining these factors, a process was designed

to increase the tapering and thus allow the generation of a wall profile that is better matched to the expected rate of removal.

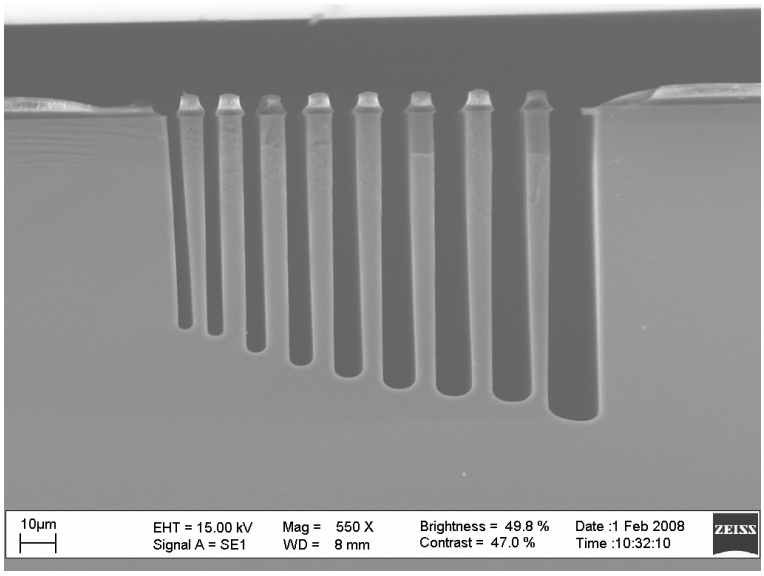

Figure 62, SEM image of trenches of 10µm width and less with fixed length of 0.5mm etched with the fast programme with the etching cycle extended to 14 seconds, passivation cycle 7 seconds.

Figure 62 shows a calibration pattern with 8µm walls etched with similar parameters to the fast recipe described above, the only difference being that the etch cycle was extended from 12 seconds to 14. Increased tapering was visible in most of the walls fabricated on this wafer and a ten minute isotropic etch at 30mT removed a large proportion of the walls. Observation of patterns after anisotropic etching found that the base of the walls was still several micrometres wide in most cases and a further change to this process was therefore investigated, increasing the etch cycle time to 16 seconds. An example of a pattern etched with these new parameters (16 second etch cycle, passivation cycle length remains 7 seconds) is shown in figure 63.

The 16 second etch cycle process also has the beneficial side-effect of increasing the etch rate by an average of $0.7\mu m min^{-1}$ over the standard etch for trenches with width 10µm and less. The performance of each of the three processes is compared in figure 64 which also highlights that DRIE-lag can be assumed to be approximately linear over the size range of interest.

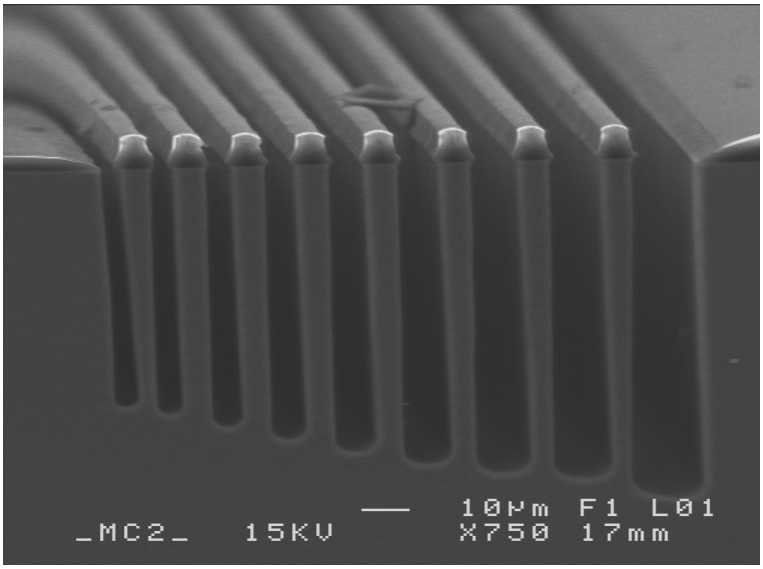

Figure 63, SEM image of trenches of 10µm width and less with fixed length of 1mm etched with the fast programme with the etching cycle extended to 16 seconds, passivation cycle 7 seconds.

The wall tapering was measured for samples from the original process as well from the two modified processes. Only patterns with 8µm walls were considered for this analysis as they can be more accurately measured from the digital images and are not removed by the process as can be the case with thinner walls. Other than its width and length, the defining feature of each wall is the width of the adjacent trenches, one of which is generally one micrometre bigger than the other; therefore the wall tapering is plotted against the average width of the two adjacent trenches in figure 65. In the case of the standard slow etch recipe (not plotted), the tapering causes the walls to widen towards the bottom by an average of 0.03±0.01µm per µm etched vertically. This tapering is overcome by the pinch-off effect when the etching process is overcome by polymer deposition.

The tapering effect on the vertical walls is generally stronger in those bounded by wider trenches, probably because the ion angular distribution means that ions further from the surface normal can reach the trench base in a wider trench. The tapering can be seen to increase proportionally in each case as the etch cycle is lengthened. These data may be further condensed by using the change in wall width to calculate an average taper angle which gives a good correlation with the length of the etch cycle for a fixed passivation cycle length (over the small range studied) as shown in figure 66.

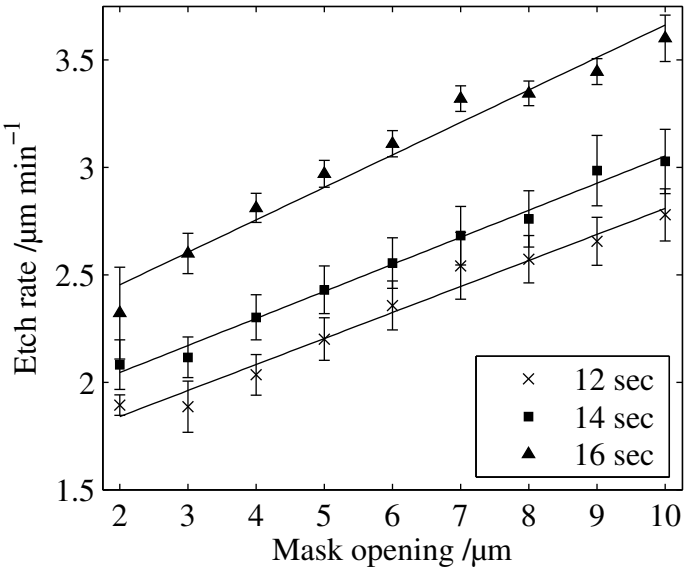

Figure 64, average etch rate as a function of smallest dimension of mask opening. Legend indicates length of etch cycle, passivation cycle fixed at 7 seconds; error bars show the standard error.

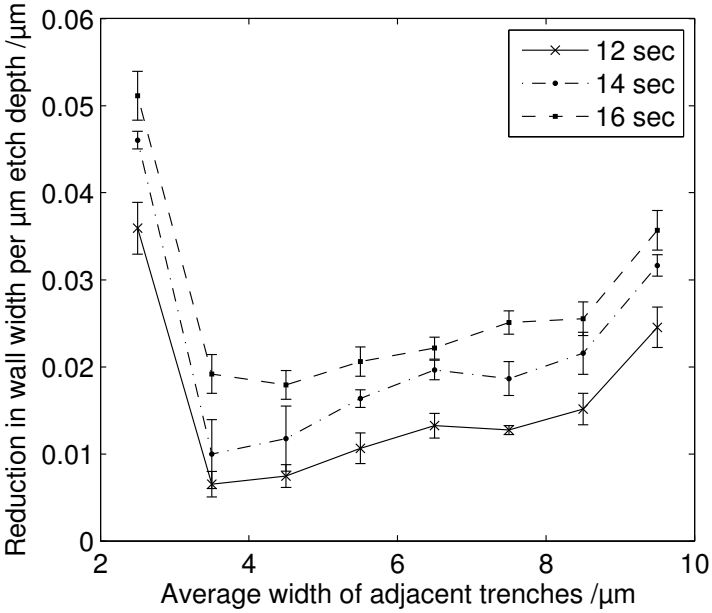

Figure 65, wall tapering rate as a function of the width of the trenches on either side of the wall, averaged over a deep etch for the standard process (12s etch cycle) and the two variations with increased etch cycle length – error bars show the standard error.

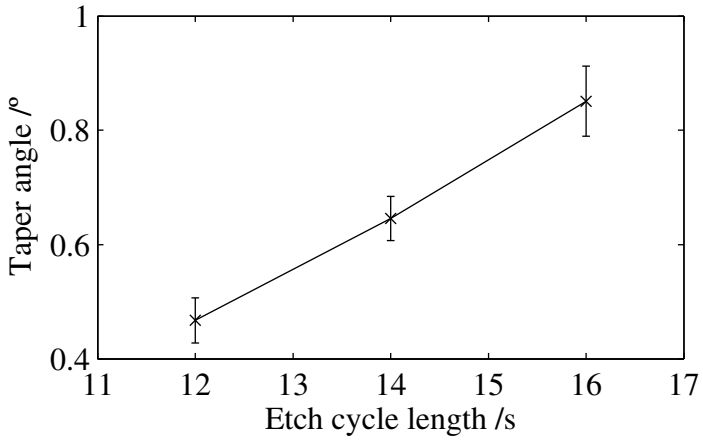

Figure 66, wall taper angle for each variation on the fast etch programme as a function of the etch cycle length, error bars show standard error.

For the largest trenches (25-100µm), the wall tapering sometimes proved great enough that the walls were lost before the end of the anisotropic processing. An example of this is shown in figure 67: the walls bounding the 25, 50 and 75µm trenches remain intact, while the walls bounding the 100, 125 and 150µm trenches have been almost entirely removed. The fact that the depth differential in such trenches is small makes the loss of a wall less critical for overall slope formation. Clearly larger walls are an option if trenches of this width are critical to a given design.

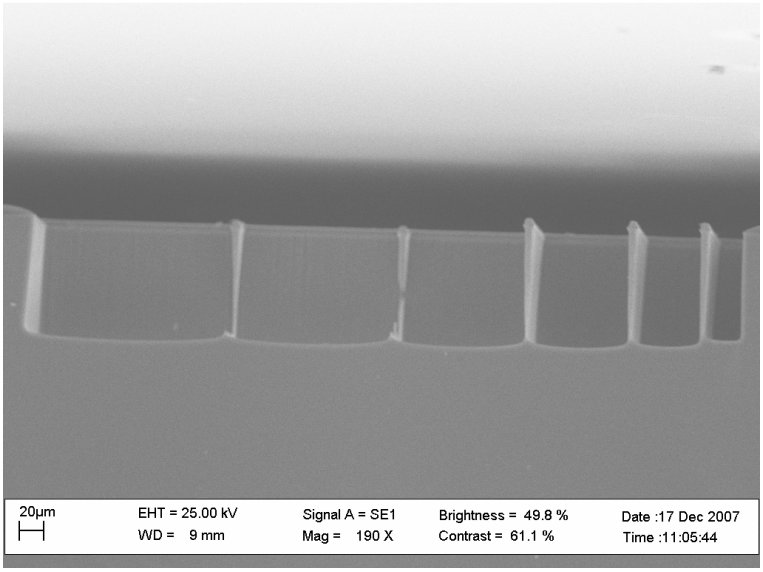

Figure 67, SEM image of trenches of width 150µm (left), 125µm, 100µm, 75µm, 50µm and 25µm (right) etched with the fast programme with the extended 16 second etch cycle (7 second deposition cycle). Where one adjacent trench is greater than 100µm in width the walls have not survived the process.

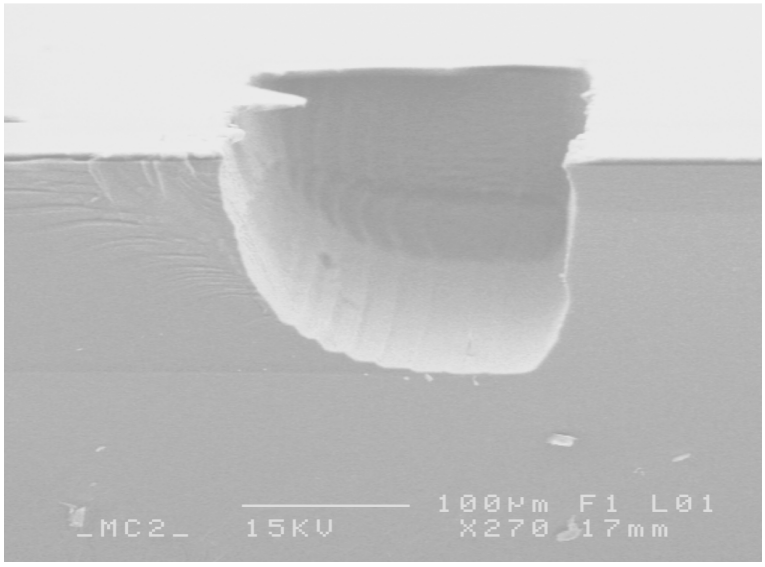

Figure 68, SEM image of a sample initially containing 8µm walls with trenches of width 1-10µm (left to right), length 500µm, etched with the fast programme with revised 16 second etch cycle. The walls were subsequently removed with an isotropic etch of 6 minutes at 30mT, exposing the slope.

Testing the efficacy of the isotropic etch with revised parameters (see section 4.3.3.2) for removing the tapered 8µm walls gave excellent results as illustrated by figure 68. The slope produced by DRIE-lag remains intact, the walls have been completely removed and some smoothing of the surface due to the isotropic etching has also taken place.

4.3.3.2 Final calibration process parameters

The best process parameters found in the calibration processing are as follows, of course these only serve as a guide and a new batch is likely to experience some difference in etch rates but they served well as a basis for subsequent designs.

- AZ4562 photoresist (after priming with HMDS) spin 4000rpm 30 seconds
- Exposure of 20 seconds
- Development of photoresist, 2 minutes in MF222
- Anisotropic etch (19.5 minutes for slope formation)
  - Etch cycle: 16 seconds, 130sccm SF_6, 13sccm O2, Platen power 10W, coil power 600W
  - Passivation cycle: 7 seconds, 85sccm C_4F_8, Platen power 0W, coil power 600W

- Isotropic etch (6 minutes for wall removal)
  - 130sccm SF_6, 13sccm O_2, Platen power 0W, coil power 600W, pressure 30mT
- Anodic bonding: 2 hours, -500V, atmospheric pressure

4.3.4 Prototype Device Channels

Two interconnect regions of prototype channels were successfully cleaved for imaging and are shown below. They consist of a 150µm wide channel to house a capillary (left side of image) tapering in-plane to 20µm, which would connect to a channel etched in a subsequent process (and would appear on the right of the image). Walls divide the tapered region into narrow trenches in order to produce a slope at the channel base. As these channels taper to 20µm in-plane width, producing samples such as these for SEM is challenging and an image of the slope with the walls removed could not be produced. The lack of walls in the finished samples can be observed to some extent by optical microscopy and confirmed by the fact that water was later pumped through several devices.

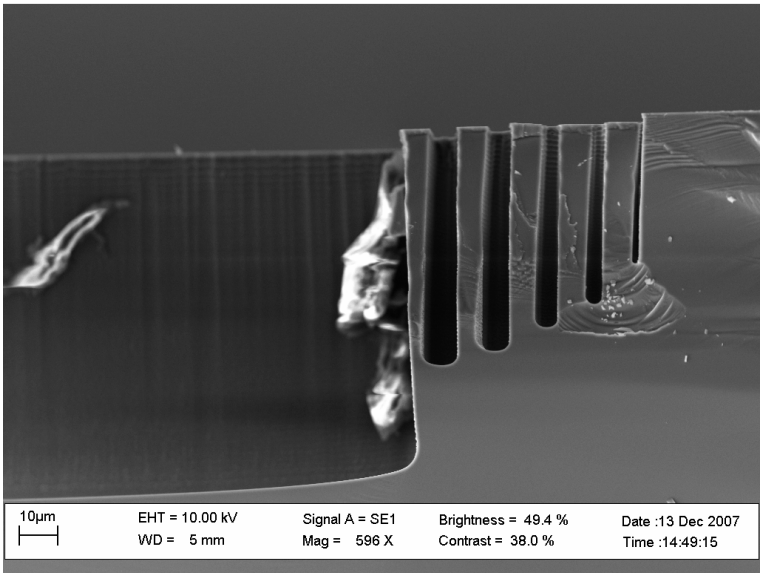

Figure 69, SEM image of a sloped channel for capillary connection to a microfluidic device, etched with 16s etch cycle, 7s deposition cycle. The capillary would sit in the deep trench to the left. An isotropic etch process would be used to remove the walls from the slope before a microfluidic channel was etched to a shallower depth to the right of the sloped region.

In figure 69, the results of the anisotropic etch can be seen to form a slope within the channel. Figure 70 shows the equivalent control channel with no DRIE-lag trenches. There is some sloping of the channel floor in the tapered region as the effective feature width is reduced, but because the area is not divided up into individual, low-width features, the DRIE-lag is much less pronounced than that in figure 69.

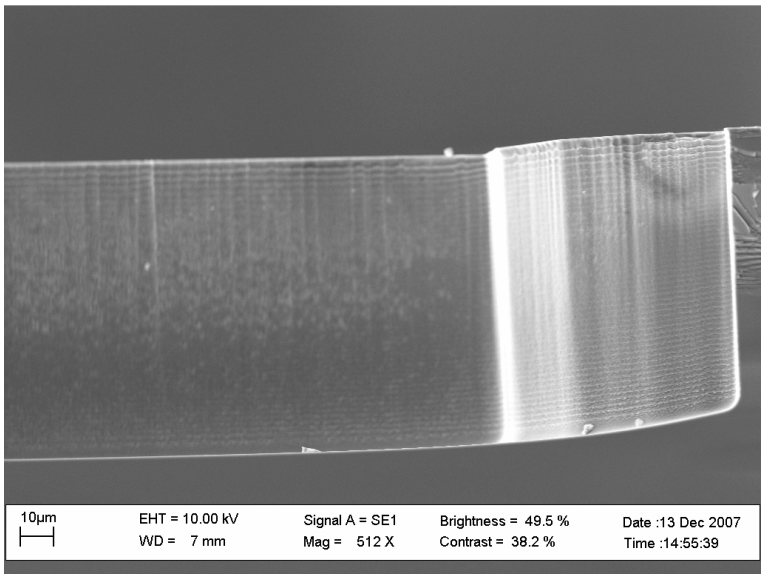

Figure 70, SEM image of the control channel for the capillary connection etched with 16s etch cycle, 7s deposition cycle. The capillary sits in the trench seen here (initial width 150µm); the analysis channel is later etched to a shallower depth to the right of the tapered region.

Figure 69 and figure 70 show the proof of concept for a sloped connection region fabricated within a microfluidic channel, connecting a deep capillary housing trench to a shallower microfluidic channel. The DRIE-lag characterisation data presented in this chapter may be used to design a variety of channels with significant out-of-plane curvature.

4.4 Discussion

A novel process was demonstrated for the fabrication of a sloped in-plane capillary connection to a microfluidic channel. This process relies on well-defined anisotropic and isotropic etch processes and protocols for each of these were developed. DRIE of silicon is an established technology in the fabrication of microfluidic devices. The adaptation of this technology for producing a world-to-chip connection allows a

simple, coherent process to be used throughout later device fabrication. Characterisation of the DRIE-lag effect for trenches of 2-150µm width to an appropriate depth (150µm maximum) provides the basis for a more refined slope design and a tailored world-to-chip connection. Generating more data points around the lengths more sensitive to DRIE-lag means that the data collected can be safely interpolated for subsequent designs. Up to the depth of interest a single set of DRIE parameters were found to be suitable. Although parameter ramping could potentially improve sidewall roughness and further accentuate wall tapering this was not critical to a successful process. The DRIE-lag effect actually generates very shallow slopes which are desirable for loading long polymers into microfluidic devices.

A method of removing walls of up to 8µm width was developed. For applications requiring a slope closer to the top surface of the wafer, narrower walls offer the possibility of a smoother surface. Wider walls however, are more robust where a deeper etch is required and tapering these walls facilitates their later removal. While a single wall size per mask is preferable such that the isotropic etch affects all slopes similarly, this range of options does add some flexibility for slope design. Wall removal between longer trenches is easier to confirm by microscopy without the need to cleave the sample and use the SEM. Over lengths of approximately 20µm, the photoresist masking the wall typically remains intact even when the wall itself is etched away. Observed from above the wafer surface, this makes it very difficult to confirm that the wall has been cleared and if the photoresist is stripped then a further isotropic etch is not possible as other structures will be damaged. For walls more than 100µm long the photoresist tends not to remain intact once the wall is removed and a simple inspection makes clear whether the length of isotropic etch was sufficient.

Although etching a recess into the glass wafer potentially removes some small regions of dead volume around the capillary tip this was considered an unnecessary complication during silicon process development. Consequently the glass wafer can be conveniently attached with no alignment. The 1000µm thick borosilicate wafers bonded readily to silicon in all cases. The bonder contains a facility to apply some force to the top wafer and to use much higher voltages than the -500V which proved to be sufficient but neither of these measures was necessary. In fabrication, the only

drawback to the borosilicate wafers is in dicing. The total thickness of the bonded wafers is 1.5mm and dicing of these samples was very slow.

Photoresist alone was found to be an adequate masking material although a relatively thick layer is required to protect the surface for deeper etches. A photolithography process was developed to allow reproduction of features down to 2µm linewidth with a 6µm photoresist layer.

Several devices were produced in this characterisation work in order to prove the anodic bonding and assembly stages. These last steps were successful and the processes described in this chapter therefore formed the basis of the device fabrication described in chapter 5.

Chapter 5 Fabrication of Microfluidic Devices for DNA Extension

5.1 Introduction

In this section the fabrication of microfluidic devices for the extension of DNA molecules is discussed. These devices feature a sloped world-to-chip connection to integrate a glass capillary that is introduced in the plane of the chip, as well as a variety of DNA manipulation channel geometries. The layout common to all devices is illustrated in figure 71. The connecting capillary is housed in a deep trench (not shown), which interfaces to the DNA manipulation channels *via* a slope to match the depth and a taper to match the width. Extension of DNA strands is performed in two stages; by shear flow in the preconditioning region and by elongational flow in a funnel. The extended strands are detected optically as they pass through the interrogation channel as described in chapter 6.

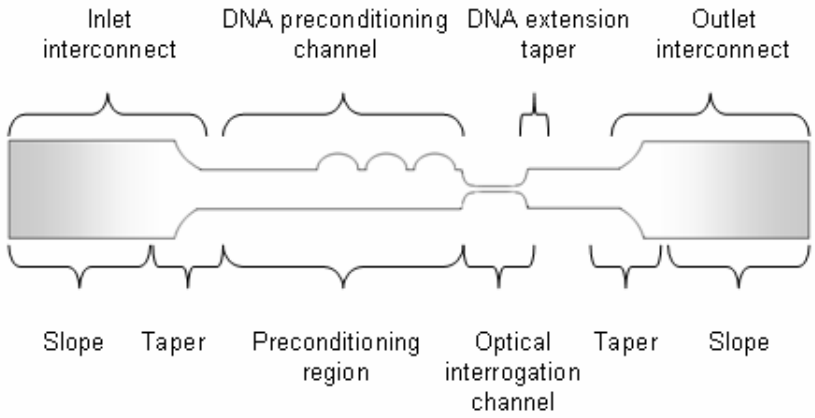

Figure 71, sketch of the main features present in each of the microfluidic devices: the slopes connect the capillary housing to the shallower features, an in plane taper is also present in the interconnect to match the channel width to the DNA manipulation channels. DNA is stretched by the preconditioning region and the funnel and is presented for optical interrogation in the narrow channel.

The interconnect design is detailed in section 5.3 and is fabricated by an extension of the DRIE-lag process described in chapter 4. The fabrication substrate is silicon with a borosilicate cap layer; all fluidic features are etched in the silicon layer and

DNA manipulation channels are based on the designs described in chapter 3. The photolithography mask design is described in section 5.4 which includes an explanation of the features used to produce the sloped connection, as well as the layout of the devices on each wafer.

Some refinement of the DRIE-lag characterisation presented in chapter 4 was necessary for the improved interconnect design and results from this development are presented in section 5.6.1, with a summary of the final fabrication process in section 5.6.2. Three dimensional finite element analysis (FEA) of the interconnect was undertaken to allow quantitative comparison of the sloped channel with the control interconnect which features a step change in depth between the capillary trench and DNA preconditioning channel. The results of this analysis are presented in section 5.7. A model of the connection as fabricated based on dimensions from SEM micrographs is also included, to verify that imperfections in the fabrication process do not fundamentally alter the interconnect characteristics.

5.2 Materials and Methods

All materials and methods were as described in chapter 4 section 4.2, with the exception of the borosilicate cap wafer. The 1mm thick wafers used in the initial characterisation were chosen for strength but the devices proved to be robust under general handling. A thinner glass layer (300µm thickness, six inch diameter borosilicate, University Wafer, U.S.A.) was chosen to allow the use of shorter working distance objective lenses. These wafers did not bond so readily as those described in chapter 4 and the bonding voltage was therefore increased to -1kV. Anodic bonding took up to 2.5 hours to complete for six inch wafers of 300µm thickness.

5.3 Slope Design

The aim of the prototype slope design in the calibration mask set described in chapter 4 was to have one region where the channel was simultaneously tapering in the plane of the wafer and sloping out of plane. This limits the length of the slope and complicates the fabrication (specifically wall removal in the DRIE-lag process)

and hence for device fabrication some refinements were made to the design. In the new design, each essential channel feature is considered separately; the out-of-plane slope now comes before the in-plane taper. The capillary still sits in a deep trench but now abuts a step in the channel floor. This reduces the dead volume which exists around the capillary walls as the fluid leaves the capillary and enters the silicon channel, as well as reducing the change in fluid cross-section. The step leads directly onto the slope which connects the deeper capillary trench to the shallower DNA manipulation channels, as illustrated in figure 72.

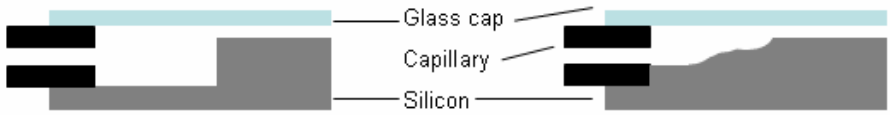

Figure 72, sketch showing the layout the new interconnect design (right) and the control case (left). The step and slope in the new design reduce dead volume and smooth the fluid path.

The slope itself is fabricated using the DRIE-lag method that was described in chapter 4 (sections 4.2 and 4.3), but the process is repeated with a second mask thus forming a longer slope in two stages (see figure 73). Briefly, a series of trenches of reducing width is etched into a silicon wafer, creating a slope in the bulk of the substrate spanned by a series of thin walls. The walls between the trenches are then removed leaving a deep trench to house a capillary and a slope up to an intermediate depth. A second etch of narrow trenches produces a second slope abutted to the first connecting the intermediate depth to the desired depth of the DNA preconditioning channels.

To design this revised connection, a simple model was produced in Matlab. The DRIE-lag process depends on trench width (smallest dimension) and etch rate of the DRIE process in use. The model contains data from the prototype fabrication (for each different etch process that was investigated) and together with Matlab one-dimensional interpolation, estimates an etch rate for a given trench size, etch process and time. A proposed series of trenches can be entered into the model as a vector and used to generate a plot of the etch depth for a given mask design.

To create a slope connecting a deep trench suitable for housing the capillary (75µm inner diameter, 125µm outer diameter) to an analysis channel of a suitable size, a two step fabrication process is required. The DRIE-lag technique is capable of producing a slope with a low gradient, which is well-suited to the gentle loading of biological samples to microfluidic devices, but it is necessary to produce two connected slopes to make the required change in depth. Figure 73 shows the output of the Matlab model for two connected slopes produced by two masking steps. The etch depth is plotted as if etched into a 500µm thick wafer to give an idea of the device structure.

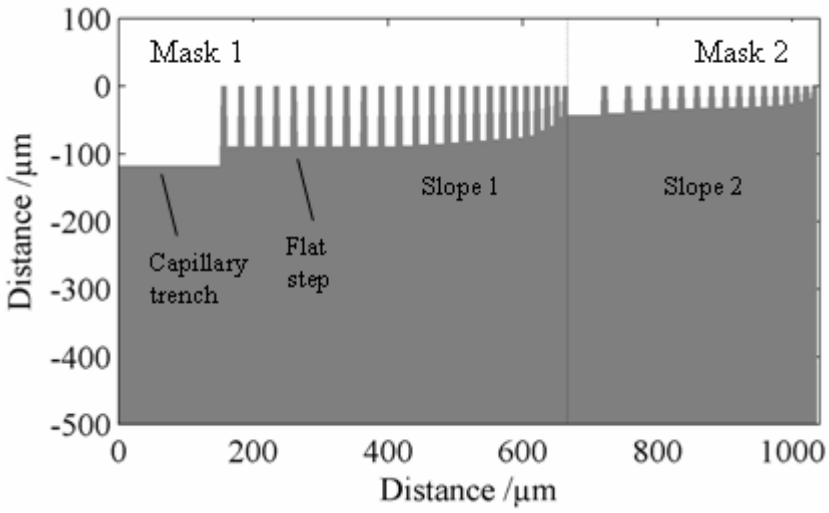

Figure 73, diagram of the revised slope design. Interpolation of characterisation data are used to calculate the etch rate for each trench which is displayed as the depth reached in a fixed-time etch of a 500µm silicon wafer.

In this design, 8µm walls are used to separate each trench. The process forms a deep trench (final depth 130µm) to house the capillary which ends in a step that will abut the end of the capillary wall when the final device is assembled. The capillary-housing trench is necessarily slightly larger than the capillary itself and thus fluid flowing from the capillary into the trench would normally slow down as the width of the fluid path increased. In this case, the step height is equal to the capillary wall thickness (25µm) and thus the change in effective channel width is reduced. The step also ensures reproducibility when attaching the capillary; it will always be secured at the beginning of the slope. The step itself is produced by ten 16µm wide trenches. This provides a short distance to allow transient flow effects from the edge

of the capillary to dissipate. After the step, the first part of the slope is fabricated by trenches from 15 to 3µm, getting narrower in decrements of 1µm. In mask 2, trenches of 50, 25 and 20µm are used to achieve an etch depth that will connect the two slopes. The bulk of the depth reduction in the second slope is then accomplished by the same series of 15 to 3µm trenches as was used in mask 1. A plan view of these trench designs is shown in figure 74. Interpolation of data obtained in the process characterisation is also used to estimate a lateral etch rate and hence the capillary channel in the mask is slightly narrower (109µm) than the capillary itself (125µm). The capillary trench is only larger than the capillary after the etching process is complete.

5.4 Device Mask Design

The mask design used to fabricate the revised interconnect is shown in figure 74, with the layout of the capillary trench, step and slope. The capillary sits in a 6.5mm long trench which is slightly tapered to make capillary insertion easier during chip assembly. The epoxy resin (Repositionable Epoxy, B&Q, U.K.) used to secure the capillary (TSP075150, Composite Metal Services, U.K.) was found to flow approximately 5mm into the channel.

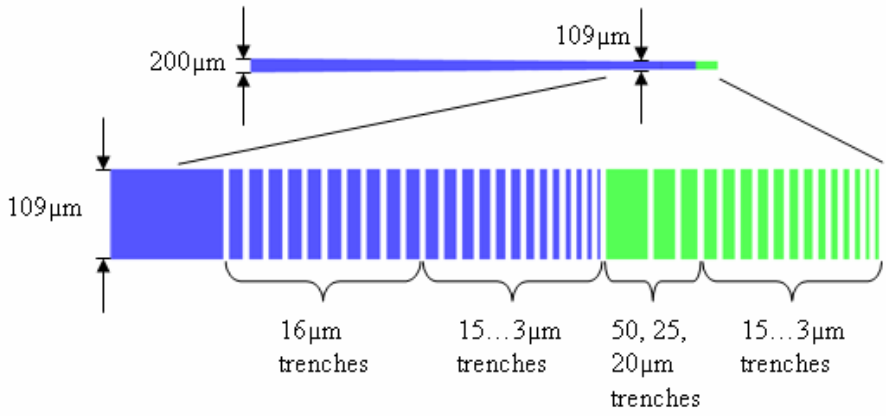

Figure 74, mask design for two step slope fabrication. The longer etch of layer 1 (blue) provides a deep channel to house the capillary which tapers out to make capillary insertion easier. The 16µm trenches form a step, while the trenches of decreasing width (15, 14, 13 … 3µm) form a slope. Layer 2 (green) produces the second part of the slope; the 50µm trench is etched to the same depth as the 3µm trench of mask 1; the 15, 14, 13 … 3µm trenches produce a slope to a final depth of 30µm to connect to the DNA preconditioning channels. The length (across the channel) of the small trenches is 109µm throughout.

The layout for a single device is shown in figure 75: the connection at either end is the same and in between is one of the 30µm wide preconditioning channels followed by an in-plane taper to a 5µm wide interrogation channel. A name for each design was added to the DNA manipulation channel layer which aids in chip identification after the devices are diced and assembled. Chip-level alignment marks allow the mask alignment to be checked while the channels are inspected prior to exposure. The chip-level alignment marks are copies of the wafer-level marks which are shown in Appendix A, figure 152. The wafer level alignment marks themselves are unchanged from the calibration mask set.

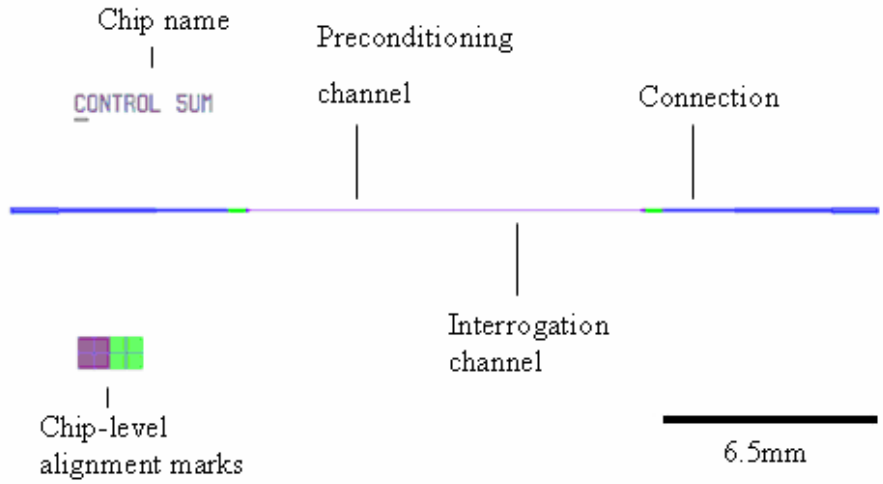

Figure 75, layout of a single chip showing all three masking layers; two to produce the connection (blue and green) and a third to produce the analysis channels (purple). The chip name is etched in the final layer which assists identification during assembly.

Each chip is the same size and the different preconditioning channel designs and sloped/control interconnects can be tiled together as shown in figure 76. Each six-inch diameter silicon wafer contained 36 chips. The first mask includes small marks for alignment of the dicing saw; the dashed lines in figure 76 indicate where the wafer will be diced. The alignment marks for dicing are not visible at this zoom level, but there is a small cross present at each intersection of the dashed lines. Chips to the left and right of those shown are exactly adjacent such that the inlet capillary housing of one runs into the outlet capillary housing of the next. When diced, the chips are separated and the end of each capillary housing is opened.

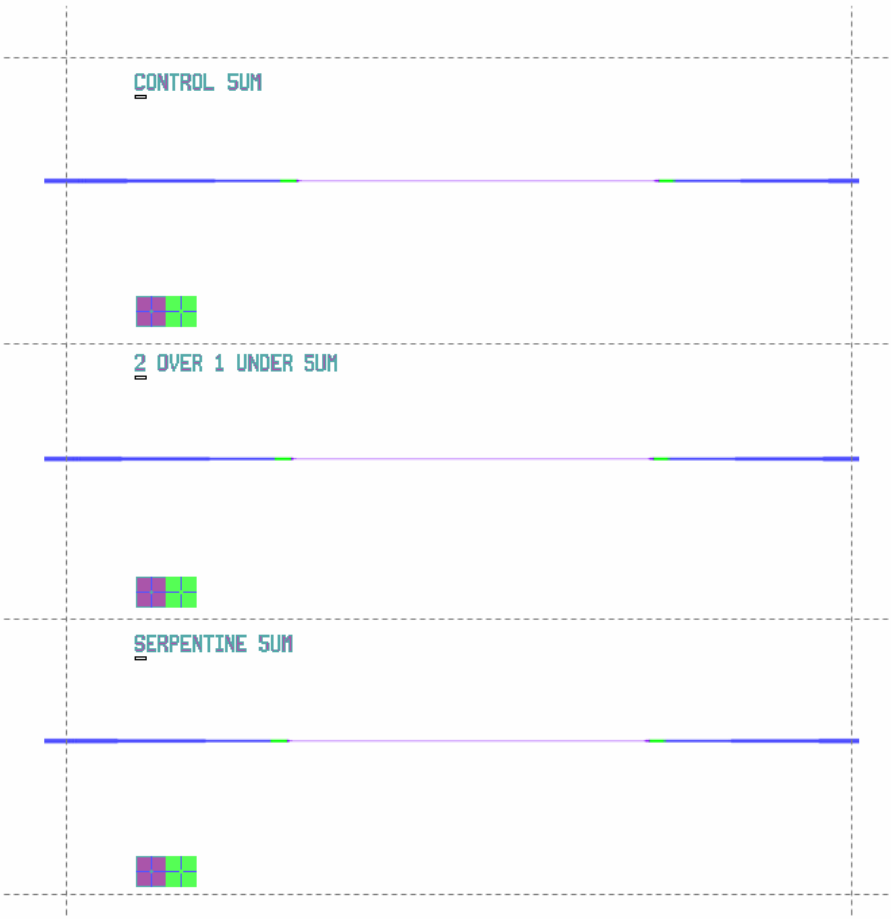

Figure 76, the layout of three adjacent devices. Patterns such as this are tiled across the wafer – devices to the left and right are directly adjacent such that the outlet capillary trench for one device runs into the inlet capillary trench for another. Dashed lines indicate where the wafer will be diced; the vertical lines cross the capillary connection channels thus opening the end of the channel to allow access.

5.5 Device Fabrication Process

The interconnect fabrication steps – comprising the first two mask layers – are shown in figure 77 which consists of the predicted and achieved results for each process step. The process parameters used for this fabrication are those defined in chapter 4, section 4.3.3.2. Figure 77 (A) Shows the predicted result from the anisotropic etch using mask 1, consisting of a channel of 115µm deep and then sequentially narrower trenches with inter-trench walls over a distance of 470µm. (B) Shows the predicted result of the subsequent isotropic etch – a channel of 130µm deep and wide, followed by a step (25µm high consistent with the capillary wall) and

then a sloping channel. (C) The second mask and isotropic etch again produce a series of trenches of decreasing width with inter-trench walls. (D) Shows the interconnect following the final isotropic etch. (E) Shows an SEM micrograph of the fabricated structure following the first anisotropic etch step. The small amounts of debris on the wafer are the result of the cleaving process and may be silicon fragments or residual photoresist. (F) Shows the slope from (E) following isotropic etch. (G) Is an SEM image showing the anisotropically etched trenches of decreasing width produced with the second mask and the isotropically etched channel produced with the first mask, while (H) shows the sloped connection channel following the second isotropic etch. The vertical misalignment between the two parts of the slope seen in figure 77 (H) is discussed in section 5.6.1 and modelled in section 5.7.

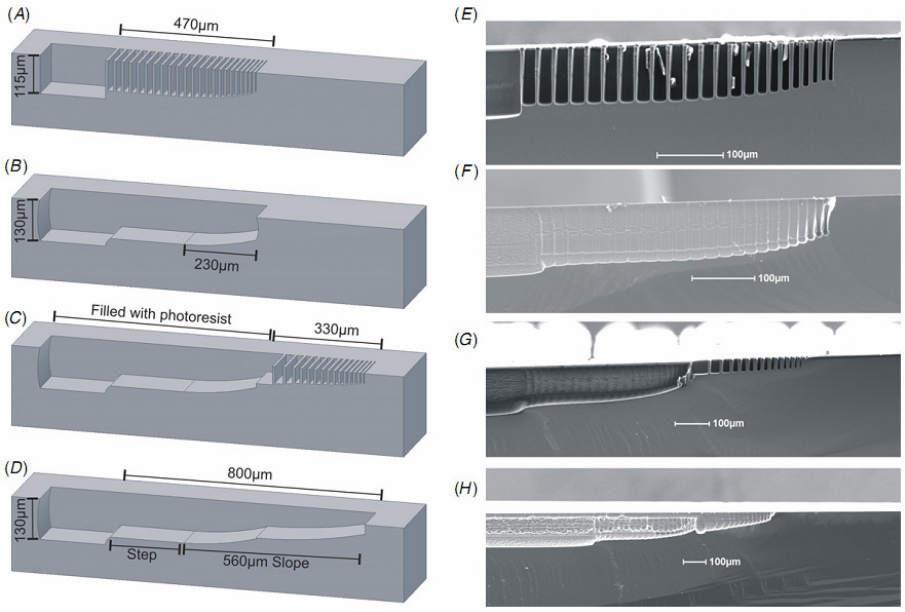

Figure 77, scale diagram of the fabrication steps of the revised connection (A)–(D) and SEM micrographs of cleaved device wafers at each fabrication step (E)–(H).

The final masking layer is applied after the sloped interconnects have been fabricated and adds the DNA manipulation channels between the two connections. There is thus a smooth and continuous change in the depth of the channel, from the 130µm deep section required to house the capillary, to the 30µm deep section required for the manipulation channels. The width of the interconnect region is constant; an in-plane taper is included with the DNA manipulation channels to reduce the width to

30µm. Once the etching is complete the wafer is cleaned and prepared for bonding. A diagram highlighting the key elements of the final device is shown in figure 78; the diagram is to scale although the DNA manipulation channel is much shorter than that of the actual devices to allow the whole design to be visualised and only a part of the capillary trench is shown.

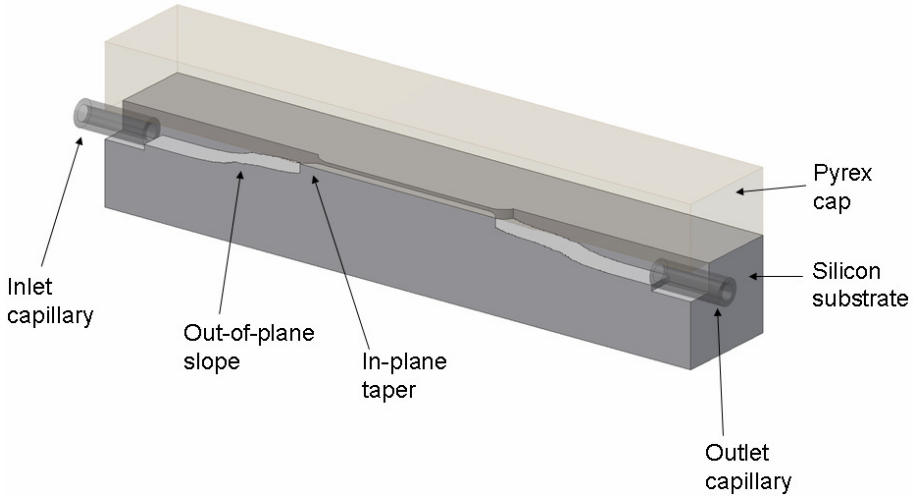

Figure 78, cut-away diagram of the finished microfluidic DNA stretching device. The processed silicon is attached to a borosilicate cover wafer by anodic bonding. The inlet and outlet capillaries are then threaded into their trenches until flush with the steps and secured with epoxy. This diagram is to scale except for the length of the DNA manipulation channel and the lengths of the capillary housings.

5.6 Device Fabrication Results

5.6.1 DRIE and Photolithography

The two-step slope fabrication process required some further calibration measurements, although it is usually necessary to make some etch rate measurements before processing a new batch in any case. These measurements were taken from the trenches used to form the interconnect as shown in figure 74. As with previous calibration measurements, etched wafers were cleaved and imaged by SEM and the digital images measured to ascertain the etch rate. The final process consists of three photolithography masks with associated etching stages. Mask 1 produces the deep capillary housing, step and the first part of the interconnect slope; mask 2 produces the second part of the interconnect slope. Mask 3 produces the DNA manipulation

channels, in each case comprising a preconditioning channel of approximately 30µm width connected by an in-plane taper to an optical interrogation channel of 5µm width. The change in depth from the capillary housing to the DNA manipulation channels is achieved using masks 1 and 2; the change in width is accomplished with a taper in mask 3 where the interconnect meets the DNA manipulation channels.

The anisotropic etch rates for mask 1 and mask 2, measuring micrographs such as figure 77 (E) and (G) respectively, are shown in figure 79. The total depth etched using mask 1 (130µm in wide trenches) is greater than that etched with mask 2 and the average etch rate is greater for mask 2. The fact that the average etch rate is higher for a shallower etch indicates that the etch rate is greater when etching at the wafer surface than at the bottom of a deep trench. Knowledge of this difference is vital to ensure that the two parts of the slope align to each other in the out-of-plane direction, as the target depth for mask 2 is less than that for mask 1.

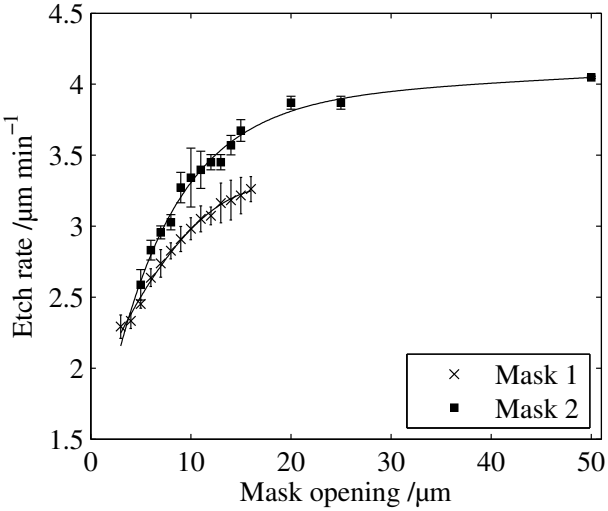

Figure 79, anisotropic etch rates for the two mask layers as a function of the mask opening – since etch rate decreases with aspect ratio, the deeper etch of mask 1 (to 115µm in open areas) has a lower average etch rate than the shallower etch of mask 2. The DRIE process used 16 second etch cycles and 7 second passivation cycles.

The same is true of the isotropic etch rates as shown in figure 80. It should be noted that the isotropic etch rate is generally higher than the anisotropic rate since there is no passivation cycle. The effect of estimating the etch rate for the second mask based on the depth reached with the first mask can be seen in figure 77 (G) and (H).

The second part of the slope in these calibration samples is etched too deeply and therefore does not align vertically with the first part. The final device wafers were produced with the application of the data shown in figure 79 and figure 80 and thus are not expected to contain the vertical misalignment of figure 77 (H). However, the slope was modelled both with and without the vertical misalignment, in order to assess the effect its presence would have on the flow characteristics of the interconnect region; no significant adverse effects were found.

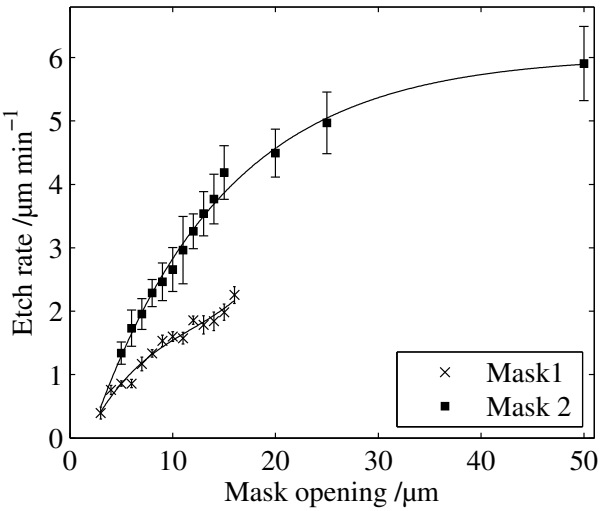

Figure 80, isotropic etch rate as a function of mask opening size for each layer in the revised connection slope fabrication process; the average rate is again lower for the deeper etch of mask 1. The isotropic etch process is performed at 30mT.

The most serious potential problem of a vertical misalignment is not over-etching of the shallower part of the slope, but rather over (or under) etching of the DNA manipulation channels in the third masking layer. This would cause a step change in channel depth at the point where it is shallowest which would create a potential fouling site for DNA. The devices fabricated in light of the etch rate data from mask 2 described here typically did not show additional fouling at this site suggesting the vertical alignment is adequate.

Five silicon device wafers were produced and bonded to borosilicate cap wafers (300µm thickness) and inspection after dicing suggested a yield of around 80%. The main causes of failed devices during silicon processing were inadequate alignment

and problems with photolithography. As the shallow channels for DNA manipulation and observation are the most critical these are etched last to ensure they are not affected by subsequent processing. However, this does cause some complications in the photolithography for the final masking layer as there are deep trenches (for the interconnects) present in the wafer. Spinning an even layer of photoresist over a deep trench is challenging and the trenches themselves must be filled with resist. To improve the resist coverage in this step, some manual spreading was added to the spinning process. Resist is normally dispensed onto the centre of the slowly rotating wafer where it covers a diameter of around 3 inches with the effect that some trenches are not covered until high-rpm spinning begins. By spreading the resist while it is dispensed, it has time to fill the deep trenches and better coverage is achieved at edges of the wafer. This proved to be adequate for device fabrication but could be improved, perhaps by spray coating the resist.

The optical interrogation channel is etched in the same step as the preconditioning channels and the length of the etch process is defined by the preconditioning channel target depth of 30µm. The width of the interrogation channel is 5µm and it is therefore subject to greater DRIE-lag than the 30µm wide preconditioning channels. Using the data presented above the final depth of the interrogation channel is estimated as 20µm for a process producing preconditioning channels of 30µm depth.

5.6.2 Final Process Parameters

The final process flow is illustrated by the diagrams below. The values given were typical for production of the device wafers, although each was slightly different depending on inspection of the wafer after development, during etching and during bonding. Other than the timing of each step, the etching and photolithography conditions were exactly as described in chapter 4, section 4.3.3.2.

Six inch <100> silicon wafer, double side polished, 500µm thick, spin HMDS primer, 1000rpm 30 seconds.

Spin AZ4562 4000rpm (shown in red); 30 seconds for a 6µm layer. Softbake on hotplate at 100ºC for 5 minutes.

Expose mask 1 for 25 seconds, develop for 2.5 minutes. Hardbake in oven at 120ºC for 1 hour.

Anisotropic DRIE of mask 1; 29 minutes, 16 second etch cycle, 7 second deposition cycle. Depth at deepest point 115µm.

Isotropic DRIE, 9 minutes.

Strip photoresist in oxygen plasma at 1kV for 10 minutes, prime (HMDS, 1000rpm 30 seconds), manually spread resist prior to spinning at 4000rpm for 30 seconds for a 6µm layer. Softbake on hotplate at 100ºC for 5 minutes.

Expose mask 2 for 30 seconds, develop for 3 minutes. Hardbake in oven at 120ºC for 1 hour.

Anisotropic DRIE, 9 minutes: 16 second etch cycle, 7 second deposition.

Isotropic DRIE, 6 minutes.

Strip photoresist in oxygen plasma at 1kV for 10 minutes, prime (HMDS, 1000rpm 30 seconds), manually spread photoresist prior to spinning at 4000rpm for 30 seconds for a 6µm layer. Softbake on hotplate at 100ºC for 5 minutes.

Expose mask 3 for 30 seconds, develop for 2.5 minutes. Hardbake in oven at 120ºC for 1 hour.

Anisotropic DRIE, 6 minutes, 16 second etch cycle, 7 second deposition cycle. Strip photoresist in oxygen plasma at 1kV for 10 minutes, inspect to ensure complete removal.

Anodic bonding of silicon wafer (grey) to six inch, 300µm thick double side polished borosilicate wafer (blue) at 1kV for 2.5 hours.

After wafer dicing, capillaries are fixed in place with epoxy resin.

5.6.3 Device assembly

Figure 81 shows the device after assembly. The capillary (Polymicro, U.S.A.) is fused silica with a polyimide coating, the thickness of which is given by the manufacturer as 12µm. In order to minimise the depth of the channel which houses

the capillary, it is designed for the diameter of the uncoated capillary. The coating at the end of the capillary was removed by ashing in a flame and the glass subsequently cleaned with acetone and isopropyl alcohol (IPA). The inside of the capillary is also cleaned by pumping through an excess of ethanol, followed by air to dry the inner surfaces. Particles present inside the capillary could block the channel and in some cases were found to be visible through a fluorescence microscope and thus could introduce error to fluorescence measurements if they were not removed. The uncoated capillary is fragile and is reinforced by a covering of epoxy resin when the device is affixed to the microscope slide (see figure 81). The capillary is prone to breakage at the point at which it exits the chip unless supported in this way. Where the polyimide-coated capillary protrudes from the epoxy it is flexible and robust, no breakage occurred at this point under normal handling conditions.

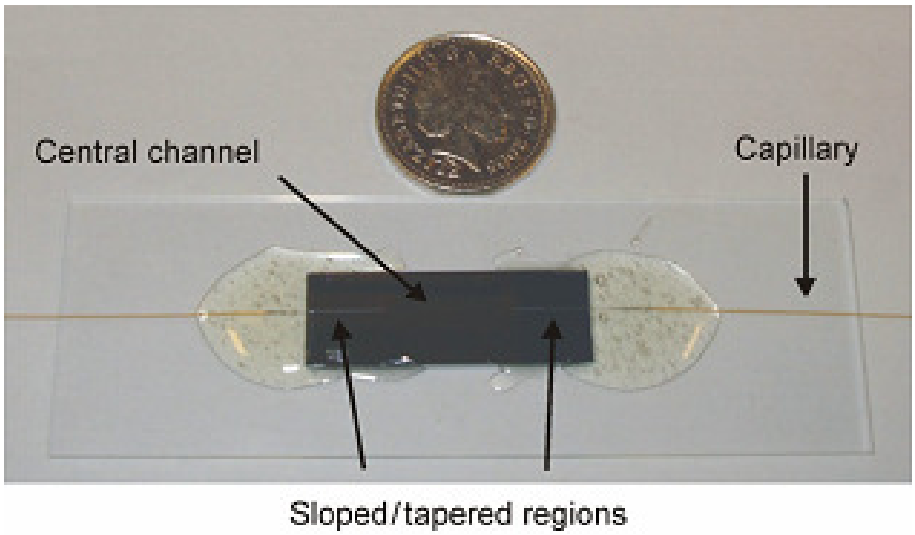

Figure 81, photograph of the final assembled microfluidic device. Securing it to a microscope slide with epoxy also reinforces the connection at the point where the capillary enters the chip and is most vulnerable to breakage. A five pence piece is used to highlight the scale of the device.

The 'central channel' region in figure 81 contains the DNA manipulation channels – a preconditioning section followed by a taper to a narrower optical interrogation channel. The 'sloped/tapered regions' contain the interconnects – each a capillary housing trench of 130µm-square, with a smooth reduction in channel dimensions from to 30µm-square.

5.7 Modelling Results

Three-dimensional Comsol models of fluid flow were developed for the control interconnect, the world-to-chip connection as designed and the worst case fabricated connection with vertical misalignment as shown in figure 77 (H). The latter model is shown in figure 82, with a streamline originating at the central point of the flow in the capillary. Flow velocity data along the streamline is interpolated with the Matlab/Comsol interface in order to calculate the fluid acceleration to identify areas that could affect a passing DNA strand and thus evaluate the connections. It was possible to perform this analysis in three dimensions as it is more coarse-grained than that used to estimate the Weissenberg number in chapter 3, with the distance between points on the streamline of the order micrometres rather than nanometres. A mesh convergence check also revealed that the solution converged most readily in the region of interest around the flow acceleration through the connecting slope.

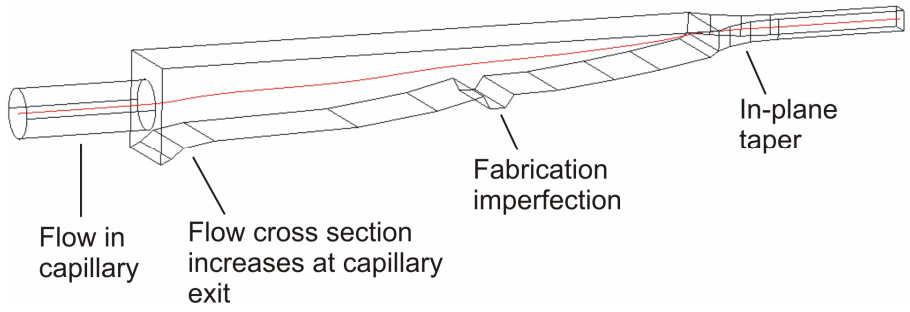

Figure 82, 3D model of the connection slope as fabricated based on dimensions from figure 77 (H). The red line is a streamline originating at the axis of the inlet capillary.

The maximum acceleration along the streamline, together with the maximum values in the vertical and horizontal directions is shown in table 6. The in-plane acceleration for the sloped channel as designed (ii) is greater than the out-of-plane acceleration; hence the force applied to each DNA molecule is dependent on the in-plane design of the channels, not on the connection itself. This is also true for the model based on fabrication data (iii). The control connection channel (i) is larger overall and therefore has a lower resistance to flow and requires a lower pressure to generate the target velocity in the 30µm-side square channel which would be the start of the preconditioning channel in the actual device. Comparing all three models, the maximum axial flow accelerations are similar, as are the maximum in-

plane transverse accelerations; these are primarily a function of the in-plane taper which is the same in each case. For the new slope design, the out-of-plane acceleration is an order of magnitude less than the control channel. The maximum flow acceleration at any point on the streamline is also reduced by 48% in the sloped connection design relative to the control case. These factors indicate that the sloped connection will have a lesser effect on passing DNA molecules.

Model	(i) Step profile between input and microfluidic channels	(ii) Designed device	(iii) Fabricated device
Input pressure (Pa)	30.8	36.1	35.7
Maximum axial flow acceleration (ms^{-2})	1.494	1.649	1.402
Maximum in-plane transverse acceleration (ms^{-2})	0.025	0.062	0.054
Maximum out-of-plane transverse acceleration (ms^{-2})	0.294	0.010	0.015
Maximum magnitude of acceleration vector on typical streamline (ms^{-2})	2.693	1.5994	1.284
Dead volume (pL)	185.5	108	158

Table 6, calculated flow acceleration and estimated dead volume for three microfluidic connection configurations. In all cases the maximum velocity in the analysis channel is set at $0.01ms^{-1}$ by adjusting the input pressure. The overall length of each model is 1.3mm.

A crude estimate of the dead volume in the connection was made from each model by plotting a large number of equidistantly spaced streamlines (typically 100) originating from the inlet. This reveals the areas of swept volume and areas where flow may stagnate. The total volume of the areas considered to be dead volume was calculated as shown in table 6. The sloped connection by design (ii) would therefore represent a 42% reduction in dead volume in the connection although in practice this is dependent upon fabrication accuracy. The estimate for the slope as fabricated represents a worst case estimate (a reduction of 15%) since the device wafers were

fabricated in light of the etch rate behaviour revealed by these samples. The figures provided here represent a simplistic geometric estimate intended only to give an idea of the proportional improvement that might be expected from the sloped connection design.

5.8 Discussion

The process characterised in chapter 4 was extended to a produce a long slope by means of a repetition of the method with a second masking layer. This allowed a gentle slope to be fabricated connecting a 30µm deep microfluidic channel to a 130µm deep trench which houses a connecting capillary of outer diameter 125µm. The two processes produce a 25µm step matched to the capillary wall thickness and a 560µm long slope reducing the depth of the channel by 75µm, an average gradient of 7.6º. The characterisation data was augmented with details of the etch rates relevant to the depths required for each part of the slope to allow out-of-plane alignment of each section. The misalignment observed between the two parts of the slope (shown in the SEM micrograph of figure 77 (H)) is approximately 20µm in size but is smaller in the devices used for the experiments described in chapter 6 due to the application of this new data. The step that was added to the design (*cf.* figure 73) improved consistency of capillary location and reduced the dead volume in the connection. The dead volume was further reduced by making accurate allowance for widening of the capillary housing during isotropic etching. Changing the channel dimensions with a separate of the out-of-plane slope and in-plane taper reduces the flow acceleration that is applied to passing DNA molecules which prevents the flow effects in the connection from dominating those in the preconditioning channels. Reducing the thickness of the borosilicate cap wafer reduced the time required to dice the wafers although the thinner wafers required more time at a higher voltage to bond completely.

No features were etched in the borosilicate cap wafer, which makes bonding convenient as no alignment is required, however further optimisation of the reduction in dead volume could come from etching the borosilicate layer. The dead volume in the connection design is primarily around the end of the capillary due to the thickness of the capillary glass. The step in the silicon layer eliminates a part of

this, but a similar step fabricated in the borosilicate wafer would further reduce the dead volume.

Inspections during fabrication and experience with device assembly found that a robust interconnect had been produced that allowed reproducible capillary location and was faithful to the original design. FEA modelling of the interconnect shows that it produces favourable flow characteristics for DNA loading. The modelling also suggests that small misalignments in the vertical direction are tolerable. DNA manipulation channels with features that curve in the plane of the wafer were straightforward to fabricate using DRIE. The testing of the finished devices is described in chapter 6.

Chapter 6 Evaluation of DNA Preconditioning Channels and Interconnects

In chapter 5, the fabrication of a microfluidic DNA stretching device was described; in this chapter the characterisation and testing of the device is detailed. Each device consists of a silicon layer with microfluidic channels and a glass capping layer. The microfluidic channels contain several elements: a world-to-chip connection region at the inlet and outlet which integrates a glass capillary; a preconditioning channel in which shearing flow partially straightens passing DNA strands; a tapered region connecting the preconditioning channel to a smaller optical interrogation channel. The two key aspects that must be tested are the world-to-chip connection performance and the preconditioning channel performance.

The interconnects are fabricated in the plane of the microfluidic channels and consist of a deep trench which contains a capillary that is held in place with epoxy resin. The deep capillary trench is connected to the shallower microfluidic channels by means of a sloping channel which gradually reduces the overall depth; this design is tested against a control device in which there is a step change in depth between the capillary trench and microfluidic channel, as shown in figure 72. The microfluidic DNA stretching channels each contain a preconditioning channel connected via an in-plane taper to a narrower interrogation channel. In each case the interrogation channel is the same size and the taper has the same profile; only the preconditioning channel varies between devices.

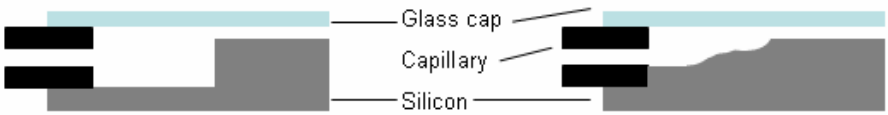

Figure 83, sketch showing the layout of the assembled connections, the control device (left) and sloped connection (right) for improved DNA loading.

The world-to-chip connection is designed for minimal loss of DNA at the chip interface. The obvious way to test this is to load a known quantity of DNA and measure the proportion of the sample that is successfully transported through the

system. The challenge in this approach is that the device is designed to handle low concentrations of DNA for single molecule detection. At low concentrations, techniques for measuring DNA such as the absorbance of ultraviolet light at 260nm [128] or backbone staining combined with comparison of fluorescence intensity against a standard curve, proved insufficiently sensitive. For these reasons, quantitative polymerase chain reaction (qPCR) [129] was chosen as the method of comparing the concentrations of DNA samples. The sloped interconnect is compared with: (i) a device with a vertical step change in depth between the capillary trench and DNA preconditioning channel table 6 and (ii) a simple capillary. This second test is designed to asses whether DNA is lost elsewhere in the off-chip pumping and sample injection system.

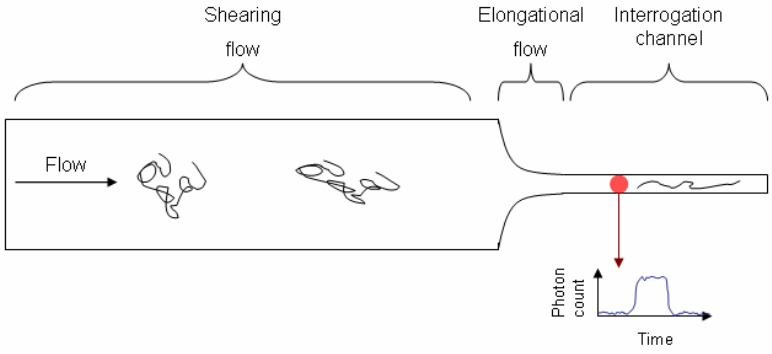

Figure 84, sketch illustrating the detection mechanism for SMD. Passing DNA molecules are extended by the elongational flow in the tapered microfluidic channel and subsequently pass through an optically defined detection volume. Emitted fluorescence is detected by a photon counter and pulses in the photon count are used to identify and measure single molecules.

The DNA preconditioning channels as described in chapter 3 are designed to linearise passing DNA strands to some extent prior to stretching in elongational flow. The DNA extension performance of each chip is determined by using fluorescence spectroscopy to observe single molecules of dsDNA passing through an optically defined observation volume downstream of the elongation funnel as illustrated in figure 84. The residence time in the observation volume is used to estimate the extension of each strand and results are presented comparing parallel-walled control channels with other preconditioning geometries.

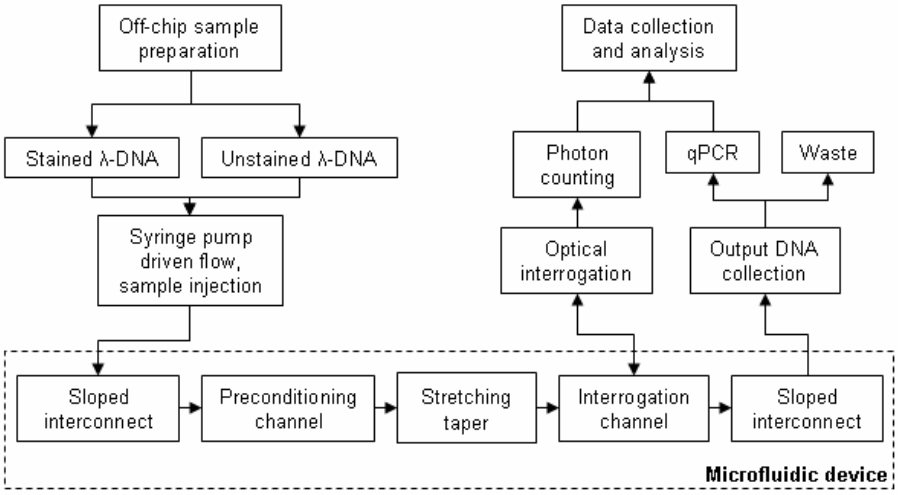

Figure 85, elements of the experimental system which are described in detail in this chapter. This system is used for two distinct experiments; measuring the loss of unstained DNA transiting the system using unstained DNA and qPCR and measuring the DNA extension by optical interrogation and photon counting.

The key parts of the experimental system described in this chapter are shown diagrammatically in figure 85. For the experiments testing the world-to-chip connection efficiency, unstained λ-DNA is used and the output collected for measurement by qPCR. For the measurements of DNA extension, fluorescently stained λ-DNA is used and optically interrogated as it passes through the microfluidic device; the output solution is collected for disposal. Each type of experiment uses a microfluidic device with the same basic elements, with pressure-driven flow provided by a syringe pump in all cases. Sections 6.1, 6.2 and 6.3 contain some background on the techniques that are employed in these experiments. This includes a description of the qPCR method and a discussion of the key optical considerations and comparable results for measurement of DNA extension in microdevices.

6.1 Quantitative Polymerase Chain Reaction (qPCR)

The central aim of the connection design discussed in chapter 3 and chapter 4 is to improve the efficiency of DNA transit through a microfluidic device. The performance of the new connection design must be evaluated for the low

concentrations of DNA that it will operate on. A dilute input solution of DNA is required for single strand detection in microfluidic devices in order that a maximum of one molecule can be expected to occupy the detection volume at any one time. In order to measure the efficacy of the new connection design, it is therefore necessary to test it with a similarly dilute input sample. This sample is further diluted during the experiment due to dispersion [130, 131] into the buffer solution and because collection of the eluent commences before the DNA molecules are expected to transit through the device and continues for a small volume after the DNA is expected to have eluted. For this reason quantitative polymerase chain reaction (qPCR) was chosen as the means of measuring the quantity of DNA in the input and output samples and thus estimating the transit efficiency [129].

PCR was invented in the 1980s by Kary Mullis [132], for which he won a share of the 1993 Nobel Prize for Chemistry. It is a thermal cycling process in which the extension of DNA primer strands hybridised to a template by DNA polymerase enzymes is used to exponentially amplify a specific target DNA sequence. A temperature graph for one PCR cycle is shown in figure 86a. The PCR solution contains DNA polymerase, deoxyribonucleotide triphosphatases (dNTPs), forward and reverse primers and an initial quantity of the target strand. Heating to around 95ºC denatures the target DNA strands (D); the solution is then cooled to 50-60ºC, determined by the melting temperature of the primers which anneal to the target strands (A) at this stage. The solution is then heated to 72ºC and the polymerase enzyme extends the primers (E) in the 5' to 3' direction [133] to create a copy of a section of the target strand.

$$P = T(1+E)^n$$

Equation 7

In this way it is theoretically possible to double the amount of target DNA in every cycle. The length of the first amplified strand is determined by the time of the extension cycle and the rate of extension by the polymerase, but because this new strand will be extended in the other direction in the second cycle, each strand that is subsequently produced has its length determined by the separation of the primers. In

practice the amplification is not perfectly efficient; until one or more of the reaction components becomes limiting, the amount of product in a cycle is given by equation 7, where *P* is product measured after *n* cycles, *T* is the starting quantity of template and *E* is the efficiency (percentage copied per cycle, range 0-1) [134].

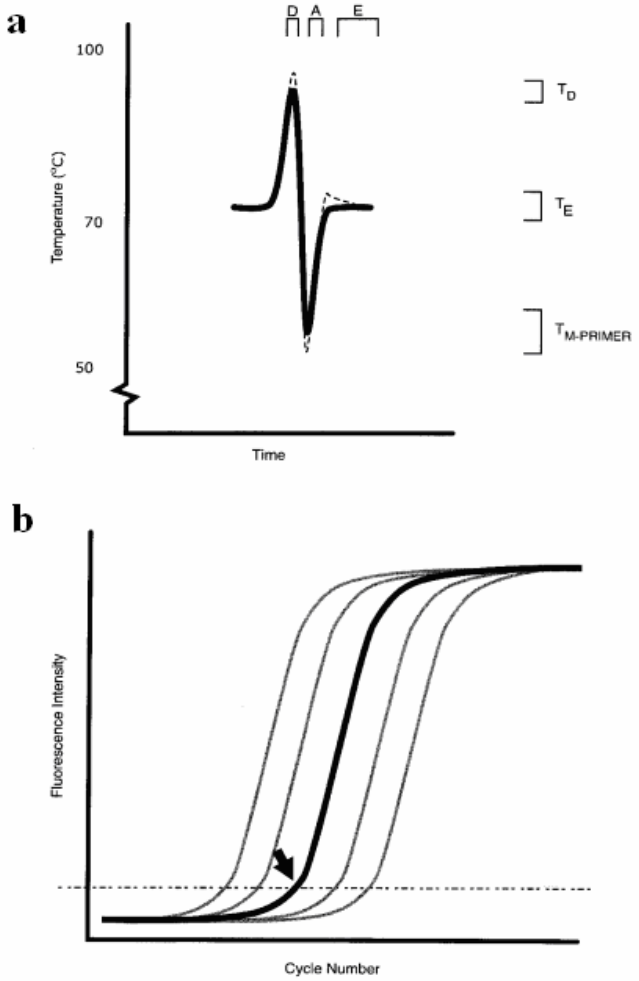

Figure 86, illustrative graphs of the PCR process. (A) Temperature profile for one cycle of PCR; (B) typical growth of fluorescence intensity during qPCR [129].

The use of dyes such as SYBR Green I that bind to double stranded DNA allows the DNA concentration to be monitored in real time [135] by measuring the fluorescence intensity at the end of each extension cycle. The fluorescence intensity of SYBR Green I is 100 times higher when bound to DNA than it is free in solution (Lightcycler product literature, Roche, Switzerland) and the binding structure is thought to be a mixture of groove binding and intercalation [136, 137]. Although the

dye does bind to single stranded DNA, the fluorescence of this complex is ~11 fold lower than when bound to double stranded DNA [137]. Typical growth of the fluorescence intensity is illustrated by figure 86B; samples with a higher initial concentration of target molecules are the first to exhibit an increase in intensity, when enough product has accumulated the exponential progress of the reaction may be observed in the growth of the fluorescence signal. A plateau is reached when one of the reaction components becomes limiting, the level of which can be independent of the initial concentration of template [134]. Interpolation of the cycle number plot to find the point at which the measured intensity crosses a threshold [138] or the point at which the growth in intensity reaches a maximum [139] allows the initial concentration of target molecules to be calculated from an accompanying standard curve produced from a serial dilution. qPCR is susceptible to errors from a variety of sources and is sensitive to operator inconsistency [140] and producing a standard curve with every experiment improves the accuracy of the final measurement.

6.2 Single Molecule Detection of DNA in Solution

There are several excellent reviews on broader aspects of single molecule detection (SMD), covering fluorescent spectroscopy of single bio-molecules [141], optical aspects [142], systems combining visualisation and manipulation of single DNA molecules [143], more generic optical detection of single molecules [144], SMD in living cells [145] and single molecule biophysics [146]. Here the focus is on SMD of DNA in a flowing solution, which imposes timing constraints (each strand must be measured as it passes through a detection region) and requires that detection is possible through some transparent enclosing structure (such as a glass capillary) rather than having the DNA exposed on a surface. Although detection of single DNA molecules is required, it can be argued that this is not true SMD since the light emitted from many fluorophores is used to detect each DNA strand. The single molecule referred to throughout this chapter is a single, double-stranded DNA (dsDNA) strand rather than a single fluorescent molecule.

6.2.1 Photon Detectors

Optical SMD relies on high efficiency collection and detection of emitted photons as well as a low noise background. The main options for photodetectors are a

photomultiplier tube (PMT) or a semiconductor device such as a single-photon avalanche diode (SPAD) as these provide a quick enough response time (<50ns) for photon counting. Although sensitive cameras such as EMCCDs (electron multiplying charge coupled devices) are capable of single molecule detection, the overhead of shifting data electronically in a pixel array introduces a time delay which is undesirable for measurement applications where the target molecule is fast-moving.

A PMT typically has a narrower spectral response than a SPAD, which has better performance over the visible range as well as a higher quantum efficiency [147]. A SPAD is a specialisation of an avalanche photodiode (APD), which itself is a reverse biased p-n junction semiconductor device with high gain. In an APD, a bias voltage just below the breakdown voltage is applied to the junction in which incident photons can trigger an avalanche breakdown which produces a linear amplification of the original signal.

A SPAD provides a macroscopic current pulse of fixed size which is synchronous with photon arrival time. A reverse bias above the breakdown voltage is applied to the junction and the electric field across the depletion layer is large but no free carriers are present. A carrier (such as a single photoelectron) injected into the electric field is accelerated and can create a secondary electron-hole pair, starting an avalanche process. The avalanche current is proportional to the difference between the bias voltage and the breakdown voltage and thus each pulse is the same size. A quenching circuit is used to quench the avalanche current by reducing the bias voltage to at or below the breakdown voltage. When the bias voltage is reset another photon can be detected and it is this response that causes a dead-time for the detector [148]. The rising edge of the avalanche current pulse can be used to time the arrival of a photon with picosecond time resolution [149] and it is the time resolution which makes the SPAD a particularly attractive option for many applications. The spectral range of a commercially available SPAD is illustrated by figure 87. In the 1980s, Cova et al. [149, 150] demonstrated SPAD timing resolution down to 20ps; the same group later developed the active quenching circuit [151] which reduces the dead time between avalanche pulses and thereby increases the count rates which can be measured.

6.2.2 Confocal Spectroscopy

The technique of confocal spectroscopy (*i.e.* extracting information from a single fixed volume element *cf.* [152]) is ideally suited to the problem of detecting single DNA strands in flowing solution. With the sensitivity of the detectors described above, the challenge of SMD is to maximise the signal to background ratio (SBR) in order to make detection of the target molecule possible. By making the detection volume as small as possible, the noise background may be reduced with no loss of signal from the target molecule. A small observation volume may be obtained by focusing a laser beam to a narrow waist (typically a diffraction-limited spot is used) to restrict the volume in which a fluorescent dye may be excited and by using an aperture (such as a pinhole) reject out-of-focus light. In this way the beam width limits the detection volume perpendicular to the optical axis, while the aperture limits its axial extension [153]. A typical detection volume is therefore in the femtolitre range.

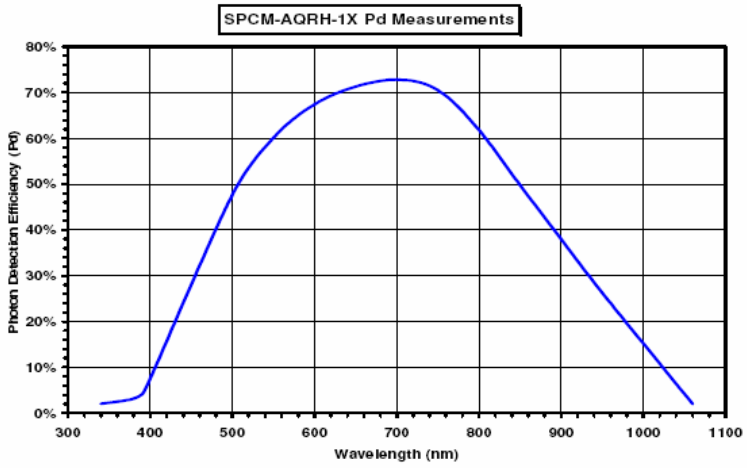

Figure 87, typical photon detection efficiency of a SPAD taken from the manufacturer's datasheet (SPCM-AQRH-1X, Perkin Elmer, U.S.A.).

A diagram of the typical elements of an epi-illuminated confocal spectroscopy system is shown in figure 88. The excitation laser beam is reflected towards a microscope objective by the dichroic D1. The same objective collects the emitted light from fluorescent molecules in the observation volume. The emission is focussed onto a pinhole, ph, to reject out-of-focus light before entering the detector (APD). In this case a second dichroic, D2, is used to separate the emission from two

sources (such as a donor and acceptor in FRET) and filters F_a and F_d are used to improve spectral resolution. Similar assemblies have been used for SMD of DNA in capillaries, [154] and microchannels fabricated in polymer [155] and glass [156].

6.2.3 Integrated Detection Optics

Although typically at the cost of increased fabrication complexity, integrating optical elements within a microfluidic device can substantially reduce the cost of a detection system while maintaining single molecule sensitivity. Krogmeier *et al.* used a custom fabricated lens, mirror and filter block attached directly to a microfluidic device etched in fused silica to form a fixed-position detection system. The photon detector and free space fibre launch optics were the only off-chip optical elements. Although a high concentration of DNA ($5ng\mu L^{-1}$) was used in the input solution, they were able to demonstrate single molecule detection [157].

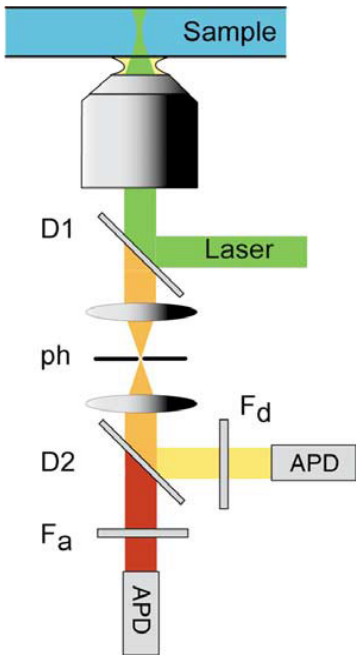

Figure 88, typical elements in a confocal spectroscopy system: excitation light from a laser is coupled into the system via a dichroic mirror D1 and focused through a high NA objective, the fluorescence is collected through the same objective and focused through a pinhole, ph. A further dichroic, D2, may be used to separate light emitted from multiple fluorophores which is spectrally filtered (Fa, Fd) prior to detection. Figure adapted from [146].

Other integrated optics approaches typically include one or more buried optical fibres (e.g. [158]) to improve the efficiency with which excitation light is delivered and emitted light collected. An elegant, though technically challenging solution is to integrate the detector itself into the microfluidic device which allows fluorescence detection with no collection optics, as was demonstrated by Chabinyc et al. [147]. This group integrated a microfabricated silicon photodiode and polymeric emission filter aligned orthogonally with a buried optical fibre in a poly(dimethylsiloxane) (PDMS) microfluidic device. This assembly was suitable for detection of the fluorescence from Fluorescein down to a concentration of $10^{-1}\mu M$ and was demonstrated for protein detection (but not used for DNA detection).

6.3 Microfluidic Extension of Free DNA Strands

Stretching DNA strands that are free in solution, without relying on attachment to either a surface or a handle such as a microsphere, can reduce experimental complexity and thus enhance throughput. Molecular extension is usually achieved by means of an elongational flow generated either by a funnel [19] or dynamically in a cross-slot [76] or hydrodynamic focussing device [49]. In this section some key results are summarised in order to place the experimental results of section 6.7 in context.

The system produced by Chan *et al*. [19] to investigate stretching and mapping of single DNA molecules featured an array of posts as a preconditioning step designed to linearise DNA strands prior to stretching in a funnel as shown in figure 89A. DNA strands were stained along their entire length with TOTO-3 and two sites of interest were labelled with fluorescently tagged (with tetramethylrhodamine) peptide nucleic acid (PNA) probes. The optical detection system consisted of three detection spots in two locations. Two spots were produced at the same wavelength (633nm) to excite the TOTO-3, these were separated by a known distance *Z* as depicted in figure 89A. The flow speed of each strand was deduced from the time taken to travel this distance. The remaining detection spot at 532nm was used to excite the tetramethylrhodamine attached to the PNA probes and thus identify their position on the DNA strand. The signal from each dye was separated by spectral filtering and

coupled into optical fibres for transmission to single photon avalanche diodes (figure 89B).

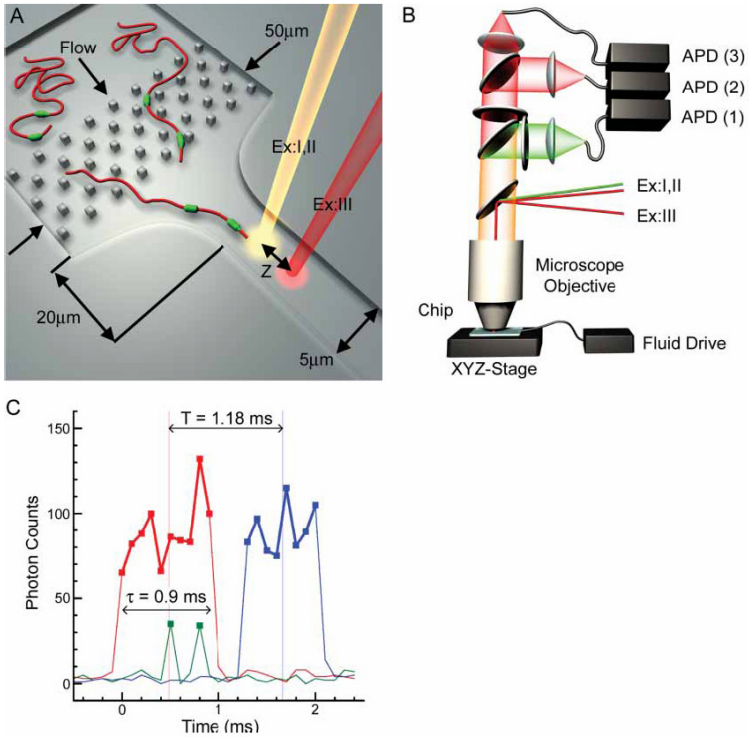

Figure 89, confocal spectroscopy setup for DNA detection, adapted from [19]. (A) Schematic, (B) optical setup, (C) example raw data; the blue and red traces are from the intercalating dye on the λ-DNA as it passes through each excitation spot, the green trace is from PNA probes.

Sample photon counting traces produced by this system are shown in figure 89C. The TOTO-3 stained backbone shows up in each 633nm spot (red and blue traces) and the PNA probes are identified by peaks in the green trace. The time delay between the centre of the red and blue bursts is used to measure the speed of each passing DNA strand and the residence time in either spot may then be used to calculate the length. The system has subsequently been further applied in DNA stretching, sizing and mapping [22, 159].

The results shown in figure 90 were obtained from the Chan *et al*. device with an input DNA concentration of 120pgµL^{-1}; 28% of detected molecules were found to have a length of 16.25-17.25µm and were considered to be fully stretched. The contour length of λ-DNA saturated with TOTO-1 has been measured as 22µm [51]. The stretching observed in figure 90 however peaks closer to the unstained contour

length of 16.5µm; the authors suggest that their sub-saturation staining density (reported as varying between 1:5 and 1:10 dye molecules:base pairs, saturation being 1:4 [26]) explains this difference [19]. They also estimate that the 'stem and flowers' configuration, wherein the ends of a DNA strand are less stretched than the centre, could not account for more than 0.9µm of the difference due to the successful detection of a second fluorescent tag located close to one end of the strand.

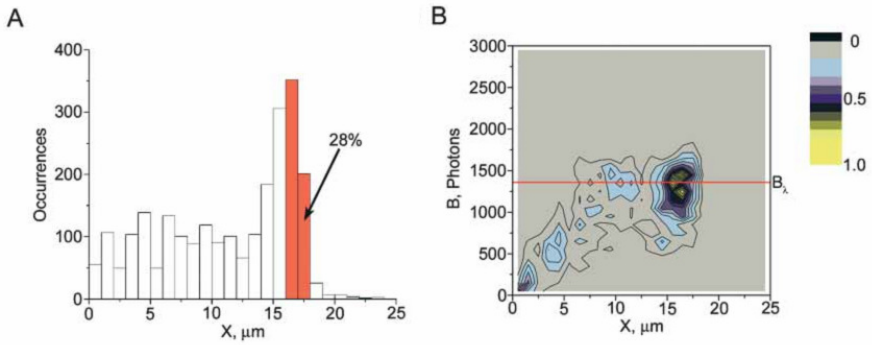

Figure 90, length characteristics of TOTO-3 stained λ-DNA detected by confocal spectroscopy, represented as (A) a histogram of number of occurrences as a function of the total extent of the molecule, *X* and (B) a comet plot of the burst size as a function of total extension with the frequency of occurrence indicated by the colourbar, reproduced from [19]. The number of photons per molecule, B, includes a correction for faster moving molecules emitting less photons to allow the data to be combined.

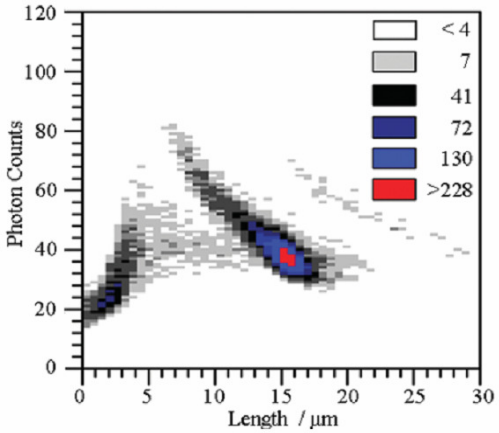

Figure 91, two-dimensional histogram of mean photon counts per molecule as a function of the nominal length of λ-DNA stained with POPO-3, (z-contrast is on a logarithmic scale) reproduced from [157].

Figure 91 shows the results for a device using both a focusing sheath flow and a tapering microfluidic channel to stretch POPO-3 labelled λ-DNA stained at a dye molecule to base pair ratio of 1:5 with an input concentration of $5ng\mu L^{-1}$ [157]. Again the peak is seen close to the unstained contour length. The points with length greater than the unstained contour length were assumed to be due to multiple DNA strands simultaneously occupying the detection volume. Similar 'comet' plots have also been observed for longer, 185.1kb DNA strands [22, 159].

6.4 Materials and Methods for Interconnect Testing and qPCR

World-to-chip interconnects were tested by injecting a known quantity of λ-DNA into the system and measuring the proportion of that quantity that was successfully transported through the system. As the devices are designed for use with low concentrations of DNA, a low concentration input solution was used for this experiment and hence measurement of the concentration was performed by qPCR.

For each experiment, a chip was primed and connected to the pumping/sample injection system. The unstained λ-DNA was prepared to a known concentration prior to use – a serial dilution was prepared and a sample taken from this series was used as input to the chip. The input sample was pumped through the chip over a period of a few hours and the output collected. The input, output and serial dilution were then measured by qPCR. A standard curve produced from the serial dilution was used to estimate the concentration of the input and output λ-DNA samples and the transport efficiency of the device could thus be calculated.

6.4.1 Device Preparation and Experimental Setup for Interconnect Testing

As indicated by the shaded boxes in figure 92, this section details the preparation of the microfluidic devices and DNA samples used to test the world-to-chip connection. Each new device required priming with liquid and connecting to the pumping / sample injection system. In order to avoid bubbles forming and blocking the microfluidic channels, each chip was initially primed with ethanol. Some bubble formation was occasionally observed during the priming stage, however bubbles were able to pass through the narrow channels and flush out of the system due to the

lower surface tension of the ethanol-air interface. Once a chip is primed, it is still necessary to avoid introducing air to the connecting capillary but this is more readily achieved than avoiding bubble formation in the chip itself. After priming the chip was flushed with a continuous flow of aqueous buffer (10mM Tris-HCl, 1.9µM bovine serum albumin (BSA)) for 24 hours.

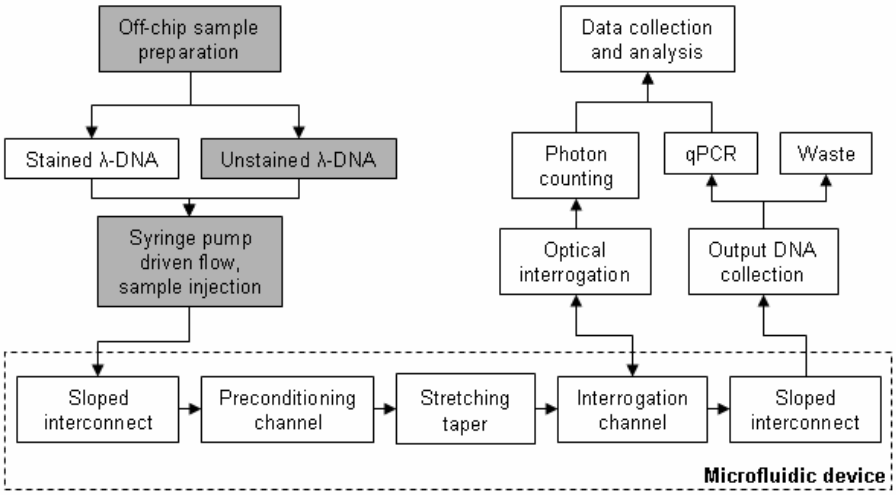

Figure 92, diagram showing the key parts of the experimental system used for testing the microfluidic devices, in this section the off-chip preparations and sample injection are described.

All DNA samples were suspended in 10mM Tris-HCl buffer pH 7.9, with 1.9µM BSA to prevent non-specific adsorption to interior surfaces [160]. λ-DNA exists as a single piece of double stranded DNA which has a twelve base overhang at either end. These complementary "sticky ends" can cause the molecule to adopt a circular conformation. For this reason, λ-DNA (GenBank # J02459, Promega, U.K.) was 'heat-snapped' prior to use according to the supplier's instructions; heating to 65ºC for 5 minutes and cooling on ice; after which it was stored at 4ºC. This ensures the 12-mer complementary overhangs are separated and the molecules are in a linear conformation.

The experimental setup for flowing DNA samples through microfluidic chips to test the interconnect is shown in figure 93. Pressure driven flow was provided by a syringe pump (KDS100, KD Scientific, U.S.A.) using a 1mL glass syringe (Hamilton, Switzerland) at a flow rate of 0.04mlhr^{-1} via a six-port sample injector

(Rheodyne 7010, Anachem, U.K.). This ensures accurate injection of a fixed input volume as defined by the sample loop (100µL, Upchurch, U.S.A.) and prevents the introduction of air bubbles. It also allows continuous operation of the chip at a fixed flow rate, as the flow is freely switched to include/exclude the sample loop but never needs to be stopped. Ethylene tetrafluoroethylene (ETFE) tubing (0.02" ID, 1/16" OD, Anachem) is used to connect the syringe to the sample injector and the sample injector to the capillary via a zero dead volume fitting (Upchurch P770, Anachem, U.K.). The capillary was 10cm in length, 75µm inner diameter, 150µm outer diameter (TSP075150, Composite Metal Services, U.K.).

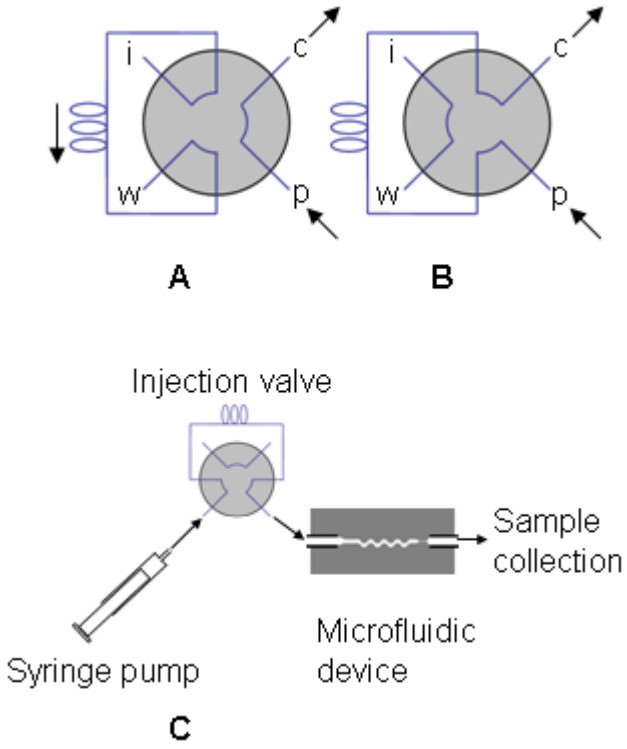

Figure 93, six port valve operation and experimental setup for interconnect testing. The valve has two ports to connect the sample loop and one each to connect the syringe needle (i), waste outlet (w), syringe pump (p) and output to the chip (c). In the loading position (A) the sample loop is bypassed and buffer flows directly from the syringe pump to the chip such that the sample loop may be loaded via the injection port. In the injection position (B), flow through the loop loads a sample plug into the device, which is then collected from the chip outlet (C) for measurement.

For each experiment, 100µL of unstained λ-DNA (48.5kbp, 16.5µm contour length) at a concentration of 1ngmL^{-1}, prepared from the same master stock, was pumped through the chip. A fivefold excess of sample was injected into the sample loop to ensure it was completely filled and the sample was not diluted by residual buffer in the loop. Output collection commenced concurrently with sample injection and a total volume of 500µL was collected to allow for the swept volume of the system and sample plug dispersion. The total output volume was verified with a pipette and the expected maximum concentration is 200pg/ml. The output was collected in a microcentrifuge tube; to prevent evaporation and environmental contamination the tube lid was pierced and the capillary fed through the hole. The tube was also covered with Parafilm and qPCR was performed immediately after sample collection as described in section 6.4.2.

6.4.1.1 Sample dispersion

In order to measure the proportion of DNA that successfully transits the system it is necessary to ensure that a sufficient volume of fluid is collected at the outlet. Prior to experimental confirmation of a suitable volume, the sample plug dispersion was approximated using the Taylor-Aris dispersion model [130, 131] in which the dispersion coefficient may be calculated by equation 8. Here D is the coefficient of molecular diffusion, R is the tube radius and U is the mean velocity; D=0.47±0.03 µm^2/s for intercalated λ-DNA [72].

$$D^* = D + \frac{R^2 U^2}{48 D}$$

Equation 8

The dispersion length may be estimated using $\sqrt{D^* t}$ [87], where t is the time for the plug to flow through the tube. To approximate the dispersion of the sample plug throughout the system a piecewise calculation is made as follows. The parts of the system to be considered are: the sample loop on the injection valve, the inlet glass capillary, the microfluidic channels (simplified as two parts; 30µm width preconditioning section and 5µm width interrogation channel) and the outlet capillary.

Firstly, D^* is calculated for each section for a fixed volumetric flow rate (12µLh^{-1}). Next, $\sqrt{D^*t}$ is calculated for sample loop to find the extension of the sample plug as it passes through; t is calculated from the average flow velocity found by dividing the flow rate (in m^{3}s^{-1}) by the sample loop cross-section (in m^2) and the known length of the sample loop. The volume of the sample plug is recalculated from its revised length (length of sample loop $+\sqrt{D^*t}$) to ensure that t is correctly calculated in subsequent steps. The process is repeated for each element, moving downstream through the system, in each case approximating the flow time using the increased volume that stems from plug dispersion in the previous element. The results of this approximation are shown in table 7 for an initial plug volume of 100µL. Taylor-Aris dispersion is derived for particles not polymers, but the intention is simply to give a first idea of the minimum quantity of sample that must be collected experimentally.

Element of system	**Plug vol. after element (µL)**
Sample loop	138
Inlet capillary	144
30µm channel	146
5µm channel	147
Outlet capillary	153

Table 7, piecewise Taylor-Aris sample plug dispersion calculation showing the estimated plug volume after flow through each element of the fluidic system.

6.4.2 qPCR Primer design

Sections 6.4.2 and 6.4.3 give the experimental details of the method of λ-DNA concentration estimation by qPCR that was used in assessing the transport efficiency of the world-to-chip connections. This is the final experimental step for interconnect testing as illustrated in figure 94. As described in section 6.4.1, unstained λ-DNA is prepared as a serial dilution and a sample is injected into the microfluidic device. Fluid is collected at the device outlet until the input sample has had time to elute in its entirety. Immediately after the outlet collection is complete, qPCR is performed

on an input sample, output sample and serial dilution. This allows the input and output samples to be compared to a standard curve in order to deduce their concentrations. From this information the transport efficiency of the microfluidic device can be calculated.

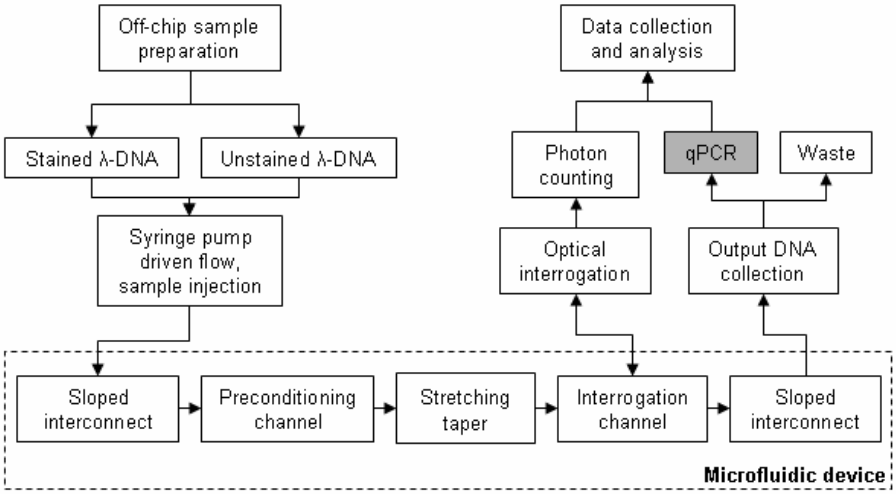

Figure 94, diagram showing the key parts of the experimental system used for testing the microfluidic devices, in this section the design of the qPCR experiment is described.

The PCR primers themselves were designed using the Primer3Plus program [161], a web interface to a software tool which supplies default values for the parameters associated with each primer and primer pair. Most of these parameters were accepted at the default value, although primer length was limited to 18-22 bases with a target product length of 400-600 bases. The melting temperature of the primers (T_m) was specified as 52-58ºC and the GC content as 40-60%, after discussion with the suppliers and in line with established general primer design guidelines [162]. Optimisation to avoid stable secondary structures (e.g. hairpins, self dimers, cross dimers) was performed by the software. The primers were designed for the λ-DNA sequence GenBank®/EMBL accession Number J02459, which has a total length of 48502 base pairs (bp). The sequences are given in table 8 and they generate a 522bp product; the error rate of the polymerase enzyme itself makes longer amplicons undesirable [163], but a larger amplicon shows up more quickly in real-time PCR because the signal is proportional to the quantity of dsDNA. Primers were supplied by ATDBio Ltd (U.K.).

Sequence	Start position (bases)	Length (bases)	T_m (ºC)	GC content (%)
5' gccacctgttactggtcgat 3'	28902	20	60.0	55
5' acggtggaaacgatacttgc 3'	29423	20	60.0	50

Table 8, primer sequences and key characteristics for qPCR experiments.

6.4.3 qPCR protocol

qPCR was performed in a LightCycler 1.5 (Roche, Switzerland) in glass capillaries. PCR mixtures were prepared in sterile eppendorf tubes prior to loading into LightCycler capillaries. A brief centrifuge pulse on the loaded capillaries ensured that the solution reached the base of the capillaries and was not divided by air bubbles. The eppendorf tubes, pipettes tube racks and buffer solution were sterilised in an autoclave and also under UV during sterilisation of the PCR cabinet in which solutions were prepared. Each tube was prepared to a final volume of 25µL and contained:

- 3µL template
- 12.5µL qPCR mix with SYBR green (AB-1158, Thermo Scientific, U.K.)
- 5.5µL BSA (38µM stock)
- 2µL forward primer, (10µM stock)
- 2µL reverse primer (10µM stock)

The temperature cycling was preceded by heat activation of the polymerase at 95ºC for 15 minutes. Each cycle then consists of denaturation at 94ºC for 15s, primer annealing at 50ºC for 30s and extension at 72ºC for 45s. The manufacturer gives the extension rate of the DNA polymerase as ~1000bp/min, but recommends an extension cycle of more than 30 seconds for amplicons exceeding 300bp. The concentration of unknown samples was calculated using the LightCycler software and the standard curve method [29]. A standard curve was produced in every measurement to minimise the effect of possible day to day variations such as reagent aging and pipette calibration changes.

6.5 Materials and Methods for Confocal Spectroscopy

The confocal spectroscopy experiments that were performed to test the effectiveness of the preconditioning channels required careful preparation of microfluidic devices, input DNA samples, excitation and collection optics and data collection hardware and software. Each of these elements is described in detail in this section.

6.5.1 Device Preparation and DNA Staining for Confocal Spectroscopy

As illustrated in figure 95, before attachment to the experimental system and alignment with the optical setup, each device went through some preparatory stages and the fluorescently labelled λ-DNA sample was prepared.

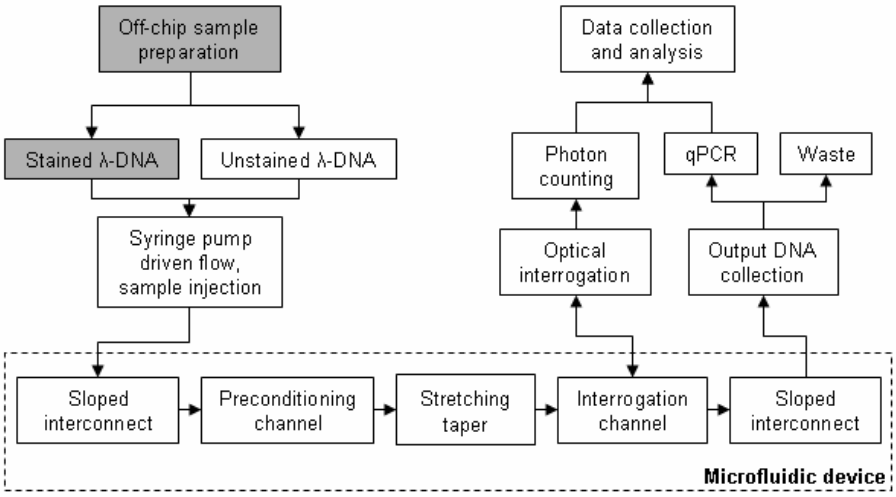

Figure 95, diagram showing the key parts of the experimental system used for testing the microfluidic devices, in this section the off-chip preparation of fluorescently labelled DNA is described.

Prior to use, the internal surfaces of each device were coated with polyethylene glycol (PEG) to prevent adsorption of both DNA strands in normal operation and dye molecules during alignment of the chip to the optical system. Although the presence of bovine serum albumin (BSA) in the buffer was previously sufficient in interconnect testing experiments to prevent significant loss of DNA, for single molecule detection it was undesirable to have additional small molecules in the buffer. The PEG coating also prevented adsorption of the alignment dye to the channel surfaces. The PEG coating protocol was: prime with ethanol, clean with a

1:1:5 ratio of $HCl:H_2O_2:H_2O$, flush with deionised water and incubate with 4% PEG in toluene for 1 hour, after which devices were flushed overnight with buffer solution.

Ethylenediaminetetraacetic acid (EDTA) was added to the buffer used for DNA solutions, which inhibits enzymatic activity and thus prevents degradation of the DNA. The working concentration was 10:1mM TRIS-Cl:EDTA which is hereafter referred to as TE buffer; although this is a common buffer for DNA experiments, EDTA was not previously added to avoid unwanted interactions with the polymerase enzyme during qPCR. The TE buffer was prepared to pH 7.9 and sterilised in an autoclave.

DNA stains were chosen to match the available excitation sources and the most efficient operation range of the SPAD detector. TOTO-3 (642/660nm, Invitrogen, U.K.) and POPO-3 (534/570nm, Invitrogen) 1mM stock were used according to the same protocol [164] to stain λ-DNA at a ratio of one dye molecule to five base pairs. Briefly, 1µL dye stock was diluted with 99µL sterile TE buffer and DNA stock was diluted to a total volume of 900µL. These two samples were mixed by pipette giving a final dye concentration of $1.2x10^{-7}$M and λ-DNA concentration of $400ngmL^{-1}$ in a total volume of 1mL. This solution was incubated for one hour in the dark at room temperature before being stored at 4ºC for up to a week. No consideration was given to unbound dye molecules as dimeric cyanine dyes are virtually non-fluorescent in solution, with 190-1400 fold enhancement when bound to dsDNA [26, 165]. Dilute input DNA concentrations of $100pgmL^{-1}$ were used. This gives an average of 1.9 molecules in the detection channel at any one time (channel volume 1nL) which reduces the probability that two strands will enter the detection volume at the same time.

6.5.2 Optical Apparatus for Confocal Spectroscopy

Optical interrogation of fluorescently stained DNA takes place as it passes through the interrogation channel within the microfluidic device. This section describes the optical setup that was used to excite the dye on the DNA and collect the resulting fluorescence. Excitation light was provided by a laser diode (5mW, 635nm,

Thorlabs, U.S.A.). The beam was spectrally filtered (HQ620/60, Chroma, U.S.A.) and focussed through a 10x microscope objective lens (NA 0.25, Nikon) onto the exposed end of a single mode optical fibre (SM600, Thorlabs). The other end of the fibre was attached to a collimator (CFC-11-B, Thorlabs) which was clamped to an x-y translator as shown in figure 96. A dichroic mirror (Q660LP, Chroma, U.S.A.) reflected the excitation light into a 10x microscope objective lens (RMS10X, Thorlabs) which focussed the beam to a waist inside the microfluidic channel. The waist size and Rayleigh length of the beam determined the excitation volume which was matched to the detection channel dimensions (see section 6.5.8). The objective was connected to the cube by a lens tube and a focusing ring which provided fine focus. The cube served as the mounting point for the other elements and was itself attached to a vertically mounted rack and pinion stage which allowed the whole assembly to be distanced from the stage holding the microfluidic device as required.

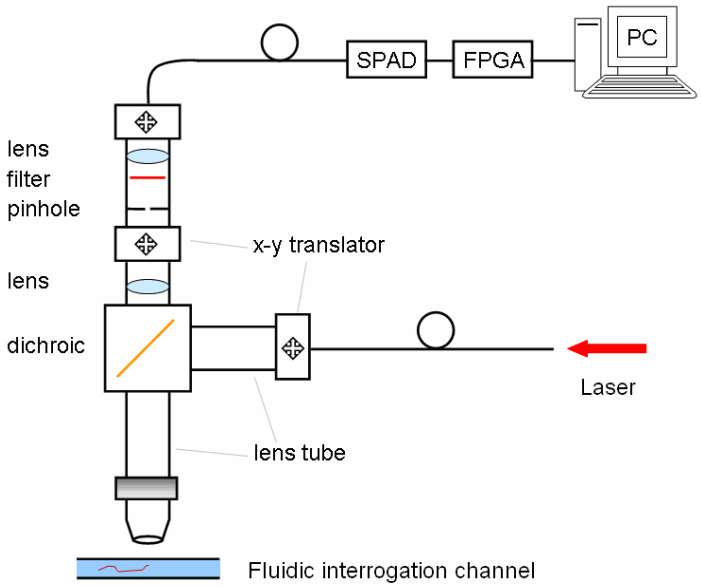

Figure 96, diagram of the key elements of the confocal spectroscopy system. The laser is fibre-coupled to a system of lens tubes which is mounted to a vertical translation stage which provides coarse focus. The collected light is fibre-coupled to a single photon avalanche diode (SPAD) which outputs an electronic pulse for each photon detected. These pulses are counted in hardware (FPGA, field-programmable gate array) and the count is periodically transmitted to the PC over a USB link.

Emitted light from the TOTO-3 fluorescent dye (peak emission 660nm) which intercalates the DNA was collected from the solid angle defined by the numerical aperture of the objective. Light at this wavelength passes through the dichroic and was bandpass filtered (692/40, Semrock, U.S.A.) to reduce noise caused by Rayleigh scattering. The tube lens was positioned after the filter and focussed the emitted light onto a multimode optical fibre (100µm core) which was directly coupled to the SPAD (SPCM-AQRH-1FC, Perkin Elmer, U.S.A.) via an FC connector. The fibre itself was opaquely shielded to ensure no stray photons were collected.

The availability of a 5mW, 635nm excitation source made TOTO-3 an attractive option despite its low quantum yield of 0.06 (according to manufacturer's data sheet, Invitrogen, U.S.A.). Although the 543nm HeNe available provided less power, the quantum yield of 0.46 (manufacturer's data sheet, Invitrogen, U.S.A.) available from POPO-3 provides a viable alternative. A similar setup was used for experiments in which the λ-DNA was stained with POPO-3. In this case the excitation source was a 0.5mW, 543nm HeNe (Thorlabs) and no excitation filter was used. A different dichroic mirror (Q565LP, Chroma) and emission filter (HQ610/75, Chroma) were introduced for the POPO-3 excitation (534nm peak) and emission (570nm peak) spectra. The pinhole was omitted from these experiments and a single tube lens (N_A 0.12, Edmund Optics) was used to couple the emitted light to the collection fibre.

$$d \leq \frac{M}{NA}\frac{2.5\lambda}{\pi}$$

Equation 9

The pinhole is a key element in confocal optics as it rejects out of focus light and thus greatly reduces background noise. Optimal pinhole size selection was determined using the formula shown in equation 9, where *M*, is the magnification of the microscope, *NA*, the numerical aperture of the tube lens and *λ,* the wavelength [166].

6.5.3 Optical Alignment Method

Two methods were developed to align the experimental apparatus; firstly to align the optical elements of the system with each other and secondly to position the optical detection volume within the microfluidic interrogation channel. The former is described here the latter in section 6.5.4.

Two plane mirrors were used to align the beam from the diode laser to the fibre-launch objective. The fibre was secured adjacent to the objective by an FC connector mounted on an xyz-translation stage which was used to manoeuvre the fibre aperture to the beam waist by measuring the power at the distal end using a power meter (Newport, U.S.A.). The free end of the fibre was then attached to the collimator which was adjusted in x and y such that the beam met the centre of the dichroic mirror. The angle of the dichroic was then adjusted such that the reflected beam was aligned vertically in the lens tube and the clear aperture of the objective lens was filled.

To align the collection path, a plane mirror was positioned under the objective at the beam waist by finding the maximum power of the reflected light. The tube lens and pinhole were subsequently aligned by eye using the xy translator before the position was optimised using the power meter. The collection fibre launch lens (uppermost in figure 96) was then added to the system and aligned such that the reflected spot could be seen to pass through the FC connector, at which point the emission filter was added to the lens tube. Finally the collection fibre was connected between the lens tube and the SPAD detector and the position of the launch lens and fibre aperture optimised using the SPAD output. Alternative data acquisition software was produced for this purpose, as described in section 6.5.7, which displayed the photon count rate on the PC updated at ~1 second intervals with a time-averaged value.

6.5.4 Alignment of Beam Waist to Detection Channel

Initial alignment of the excitation beam waist to the detection channel in the microfluidic device was accomplished using the reflected signal strength. Figure 97 shows the variation in the reflected signal as the chip is raised through the beam

waist. A small peak is encountered from the top surface of the borosilicate cap layer and a second larger peak from the silicon surface. This initial vertical alignment was produced by moving the chip in 25µm increments and may be refined by reducing the step size; 5µm steps were the minimum used in this initial alignment.

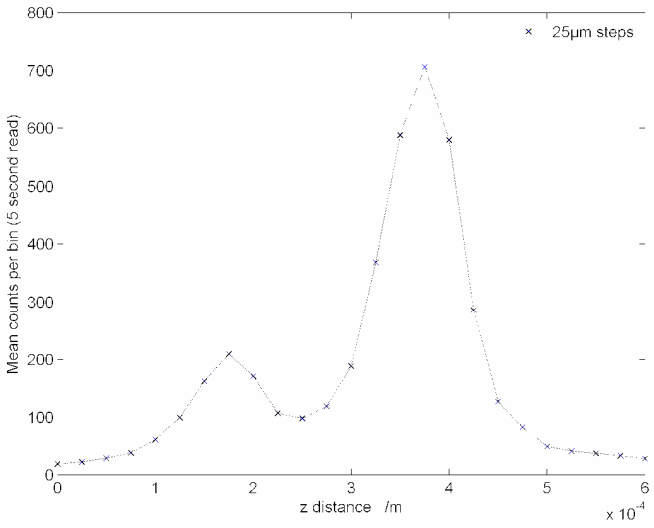

Figure 97, vertical reflection map of the chip showing peaks in the reflected confocal signal at the top surface of the borosilcate cap (left) and the borosilicate/silicon interface (right).

Having aligned the beam waist to the glass/silicon interface, a similar process may be used to align the chip in the x-y plane. Figure 98 shows the reflected signal from 5µm steps across the detection channel which is itself 5µm wide and this alignment was subsequently refined using 1µm steps to find the minimum of the reflected signal. In this case the beam waist is moving from the glass/silicon interface where the chip is bonded to the glass/liquid interface of the microfluidic channel and thus the reflected signal is expected to decrease as alignment improves.

This alignment is sufficient to position the beam waist approximately into the microfluidic channel while it is full of buffer. Fluorescent dye is then loaded into the channel and the peak fluorescence signal is used to determine the optimum position of the beam waist.

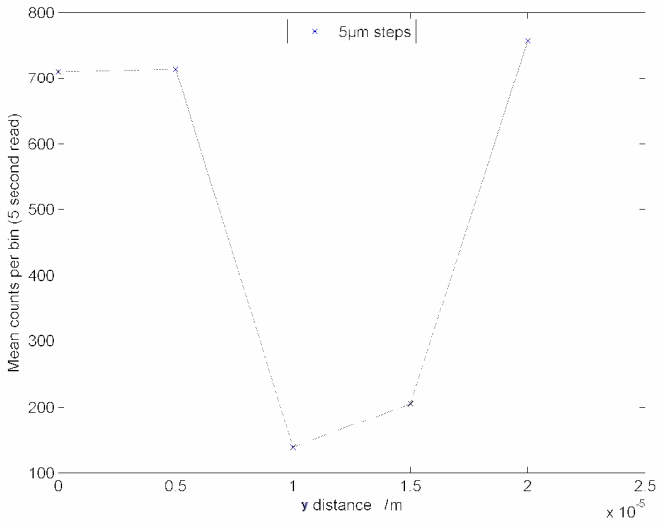

Figure 98, reflected photon count rate as a function of the transverse beam position across the microfluidic channel; the beam waist is vertically located at borosilicate/silicon interface. Moving the beam across the microfluidic channel a dip in the reflected signal indicates alignment.

6.5.5 Precision Alignment of Beam Waist and Interrogation Channel

The final alignment of the optical detection volume to the microfluidic channel is performed by filling the channel with a solution of fluorescent dye. Precision alignment must be performed with all optical elements – including the emission filter – in place. Although the change in reflected signal from the buffer-filled channel allows reasonable alignment in this situation thanks to the sensitivity of the detector, greater sensitivity can be achieved with a fluorescent signal that passes through the emission filter by design.

$$\log \frac{I_0}{I} = \varepsilon cd = optical\ density$$

Equation 10

If the dye concentration were too high, absorbance of the excitation light by dye molecules at the top of the channel would prevent the whole channel from being illuminated. This would lead to incorrect alignment in which the excitation volume was positioned too close to the top of the channel. Using the Beer-Lambert law

(equation 10 [167]) the absorbance of the dyes in the channel may be checked in order to establish whether the whole depth is effectively illuminated.

In this form of the law, d is the thickness of the sample, ε, decadic molar extinction coefficient (in $M^{-1}cm^{-1}$), c, concentration (in moles per litre), I, incident light intensity, $I=I_0$ at the boundary of the sample. For the Cy5.5 used for alignment of the 633nm laser excitation volume to the microfluidic channel the following estimates are used: ε = 100,000 $M^{-1}cm^{-1}$ @635nm [168], d = 0.001cm (20µm channel depth), c= $8.86x10^{-6}$ (10µg/ml Cy5.5, MW 1128.4). This gives an estimate of the optical density of OD = $1.772x10^{-3}$ for the channel filled with Cy5.5, indicating that the whole channel depth is effectively illuminated.

Small translations away from optimal alignment should quickly show a large decrease in fluorescence count (which is observed to be the case in practice) because the excitation volume is matched to the channel dimensions. As with the reflected signal, the fluorescence alignment signal is monitored by observing the average photon count per second detected by the SPAD. This value is displayed on the PC monitor via the software programme described in section 6.5.7. Once the beam waist is aligned to the channel the fluorescent dye is flushed out with an excess of buffer.

6.5.6 Pulse Counting Hardware

The fluorescence signal is interpreted by means of a photon counting system consisting of a single-photon avalanche detector (SPAD) and a hardware electronic pulse counter. The SPAD produces a short electronic pulse for each photon it detects and the hardware counter counts those pulses. The total photon count per 0.1ms is stored in hardware and transmitted periodically to a personal computer (PC) via a universal serial bus (USB) connection. This system allows the emitted optical signal to be collected and stored for later analysis as indicated in figure 99.

The SPAD itself outputs an 18ns TTL (transistor-transistor logic) pulse (minimum 2.5V) for each detected photon and is capable of count rates as high as 25 million photons per second. There is a ‘dead time’ of 30ns after each detection event which

ultimately is what limits the count rate. For the experiments described in this chapter it is not necessary to analyse these pulses in real time, hence the output of the photon detector may be recorded to a PC for later analysis.

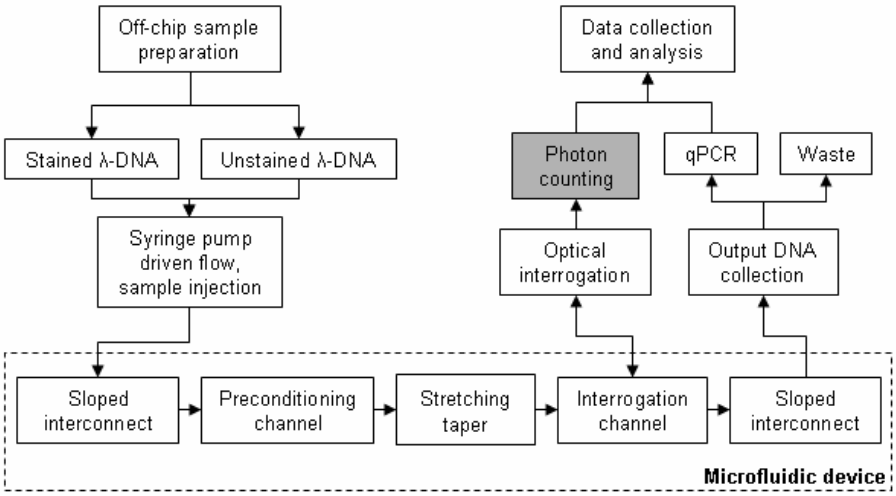

Figure 99, diagram showing the key parts of the experimental system used for testing the microfluidic devices, in this section the photon counting hardware is described.

The collection of this data presents two challenges: (a) the TTL pulse must be converted for transmission over some established communication protocol such USB or peripheral component interface (PCI) and (b) the time of arrival of each pulse must be logged. Although PCI offers a higher data rate, using an FPGA to perform hardware time-binning reduces the required data rate to the point where USB transfer is a viable solution. An off-the-shelf FPGA/USB system is also a highly cost-effective and flexible method of performing data acquisition.

For the proposed DNA detection to be evaluated here, it is possible to associate many fluorophores to the same molecule by using an intercalating dye, which gives a relatively large signal compared to true single molecule detection (i.e. of a single fluorophore). To identify a passing DNA strand therefore, the expected signal is an increase in count rate – significantly above background – with duration dependent on the length of the strand. In the case of λ-DNA (with intercalated contour length 16-22μm) such a signal could last for up to $22 \times 10^{-6}/v$ seconds, where v is the flow speed

of the passing strand in ms^{-1}. Hence at the design flow rate a fully extended intercalated λ-DNA would produce a signal of the order 2.2ms.

In practice, all applications with SPADs perform some time-division of detected photons since a maximum of one photon may be detected in the time period defined by the dead time of the module. Clearly nanosecond time resolution is something of an over-specification for measuring millisecond signal pulses. To reduce the amount of data that needs to be transmitted to and stored on the PC, a custom hardware solution was produced to count the TTL pulses into 0.1ms time bins. Hence a single number can be sent once per bin length to record the number of TTL pulses (photons) observed in that time. The data rate is thus reduced to a point where USB may be used for communication with the PC. The time-binning is performed in hardware on a Spartan 3E FPGA (Xylinx, CA, U.S.A.) connected via a Basys 2 development board (Digilent, WA, U.S.A.). The FPGA programme is generated from a VHDL (hardware description language) implementation; the bin length is set by the VHDL which must be re-synthesised (and the FPGA re-programmed) in order to change the hardware bin length. The VHDL was produced by a colleague (Julian Bailey), the system design and software components were the work of the author.

6.5.7 Software for Data Collection and Analysis

Two pieces of software were written to process the data produced from the photon counter during confocal spectroscopy experiments. The first programme, described in section 6.5.7.1 is a USB communication utility that periodically reads photon count data from the FPGA and either writes it to disk on a PC or prints a live feed of the count rate to the monitor. The second programme (section 6.5.7.2) is essentially an offline pulse detection routine that is used to analyse the raw count data after the experiment is complete. It identifies the peaks in the photon count which indicate potential DNA detection events and gives measurements of the pulse lengths which are used to estimate the length of individual DNA strands.

6.5.7.1 USB Communication Software

The FPGA counts the pulses in each binning period (set to 0.1ms) and stores the count in a register. The contents of this register are read via the USB port on the Basys 2 board by a C-programme (data capture programme attached in Appendix C) using the Digilent port communications utility application-programmer interface API (Digilent, WA, U.S.A.). This API allows USB communication facilitated by the Atmel AT90USB162 integrated circuit (IC) on the development board to appear as a direct read of a register within the FPGA. The C-programme streams the count values to a binary file, writing one 16-bit value for each bin.

Address	Contents	Value
0x00	Data Valid	00 or FF
0x01	Data1 (low byte)	00 -> FF
0x02	Data1 (high byte)	00 -> FF
0x03	Data2 (low byte)	00 -> FF
0x04	Data2 (high byte)	00 -> FF
0x05	Data3 (low byte)	00 -> FF
0x06	Data4 (high byte)	00 -> FF
…	…	…
0xFE	Data127 (high byte)	00 -> FF

Figure 100, layout of the FPGA register set, all 256 8-bit registers are read in each read cycle.

The logical register layout is shown in figure 100. The communications utility allows 256 registers to be maintained on the chip which may then be read by the PC software. Each USB packet transferred may read or write any number of these registers. The time to transfer the extra data when reading many registers is negligible compared to the packet transfer time and hence it is more efficient to make fewer reads of more registers than more reads of fewer registers. The PC software repeatedly reads all 255 registers and checks the value of the control value 'data valid'. If the FPGA has written new data to the data bytes then data valid will take the value FF and the software will write all the data bytes to disk before writing 00 to data valid to allow the FPGA to refill the buffer. This approach is faster than

reading the control signal and data separately because one less USB packet is required for each write cycle. Typically, photon count data are recorded over several hours and signal pulses from DNA strands passing through the observation region will occur infrequently. Searching of the data for DNA detection events is therefore performed separately.

For DNA stretching experiments the data read from the FPGA was streamed directly to disk for subsequent analysis, however for alignment both of the chip to the optical system and of the optical system itself, an alternative data acquisition programme was written. The alternative acquisition software prints the average value from each set of 80 packets to the PC monitor. As each data packet contains a buffer with 12.7ms of data (0.1ms time division, 127 16-bit values per packet), this results in an updated value approximately once per second. The signal from the SPAD detector may therefore be monitored directly for low-power detection applications. Also the confocal optical system combined with a tracer dye in the microfluidic channel allows accurate alignment of the chip to the detection optics.

6.5.7.2 DNA Detection Software

A separate C-programme (see Appendix C for source code) was produced to find signal pulses which could be interpreted as passing DNA strands. This programme applies a correction to the count rate due to the photon detection efficiency, measured count rate and wavelength, based on data supplied by the SPAD manufacturer. The background signal is analysed to set two threshold values which are used for detecting and measuring signal pulses. Threshold 1 is set approximately at the noise level and threshold 2 at least twice the level of threshold 1, as shown in figure 101. The data are searched for pulses which cross threshold 2 and the width of each detected pulse is measured at threshold 1. This method allows the full width of each pulse to be measured, without erroneously detecting small spikes in the noise background.

The programme outputs two text files, one with a more verbose description of each data pulse for manual inspection and one containing an m*2 matrix where each row

contains the length and total number of photons of one pulse. This second file is used as the input to data processing and display scripts written in Matlab.

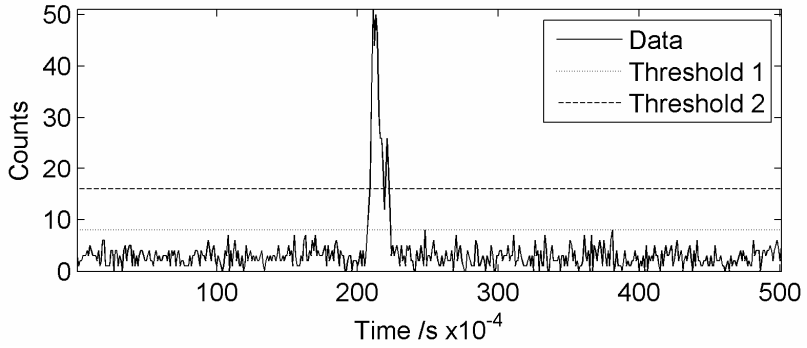

Figure 101, illustration of the method use for automated pulse detection. Set a signal threshold (1), use double that level (threshold 2) to find signal pulses in the data then measure the pulse width at the signal threshold (2). This ensures the full width of the pulse is measured and that the detection software is not distracted by noise fluctuations.

The data recorded in the verbose output is shown in for a typical pulse in figure 102. The timestamp gives the time from the start of the file. The pre- and post-amble are useful for detecting erroneous signals – they can show for example where two adjacent data pulses appear to overlap and thus can help to identify where two strands have passed through the detection region very close together in time or cases where two short pulses could potentially be due to the same DNA molecule. The number of bins containing signal are used to assign the pulse length and the total number of counts in those bins gives the total number of photons seen in that pulse.

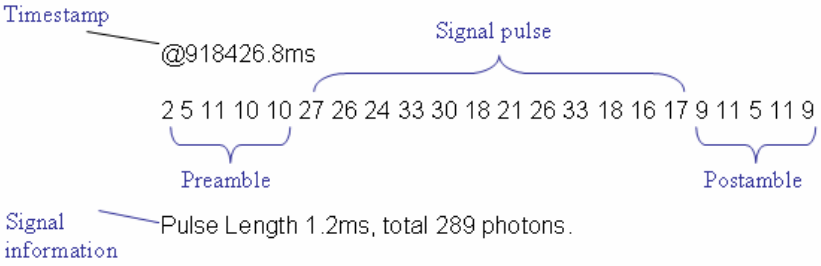

Figure 102, typical signal pulse output recorded to file by the automated pulse detection software for one DNA detection event.

6.5.8 Spot Transit Time

The pulse length as described above includes an error originating from the time a DNA strand takes to cross the detection volume. The residence time of a DNA strand in the detection volume begins when the leading end of the strand enters the spot and finishes when the trailing end exits the spot. The actual strand length should be measured from, for example, when the leading end of the strand enters the spot to when the trailing end enters the spot. The residence time is therefore composed of the time between each end of the strand entering the detection volume, plus the time for the trailing end of the strand to cross the detection volume.

$$z_R = \frac{\pi\omega_0^2}{\lambda}$$

Equation 11

To account for this, it is necessary to calculate the dimensions of the excitation volume and consider the flow rate in the interrogation channel. Some key parameters of the objective lens are given in table 9. The Rayleigh length was calculated according to equation 11 [153], where ω_0 is the Gaussian waist radius and λ the wavelength. Typically a high NA objective is used in confocal spectroscopy as the smaller excitation volume reduces the background noise. However the geometrical limitations of positioning the beam waist at the centre of a 5µm by 20µm channel are such that a 0.25NA objective is the highest that can be used. The spot size was calculated from equation 12 [169] and the excitation volume is calculated by assuming a cylinder of length twice the Rayleigh length.

$$2\omega_0 = \left(\frac{4\lambda}{\pi}\right)\left(\frac{F}{D}\right)$$

Equation 12

To calculate how long a DNA strand takes to pass through the excitation volume, the flow speed in the interrogation channel was modelled using Comsol Multiphysics. The interrogation channel is etched in the same step as the 30µm deep

preconditioning channels. However, due to a width of only 5µm, the DRIE-lag effect causes a reduced etch rate in this region and the depth of the interrogation channel is 20µm. The model of the interrogation channel (figure 103) is therefore 5µm wide and 20µm deep, with an overall length of 200µm.

	10x objective	
Clear aperture (mm)	9.19	
Effective focal length (mm)	18	
NA	0.25	
Wavelength (nm)	**543**	**633**
Gaussian waist (µm)	1.35	1.58
Channel occupancy [20µm * 5µm] (%)	54	63
Rayleigh length (µm)	10.6	12.4
Excitation volume (m^3)	$1.2x10^{-16}$	$1.9x10^{-16}$

Table 9, characteristics of the objective lens and estimation of the excitation volume for each wavelength used.

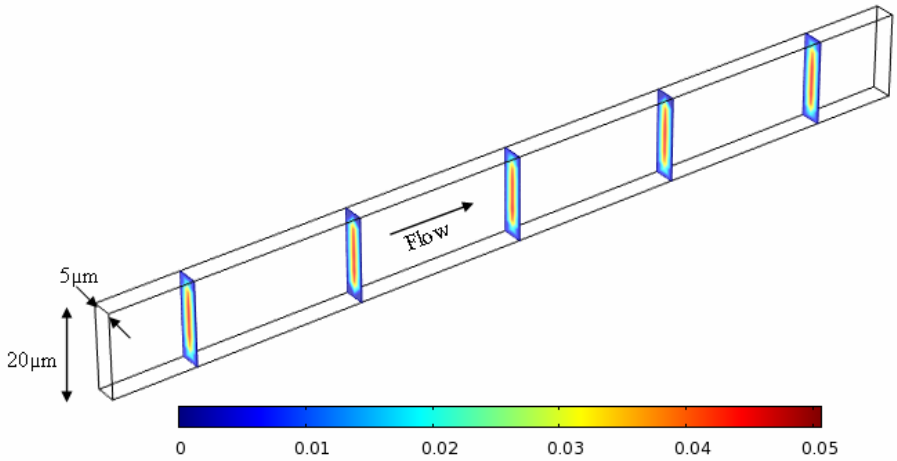

Figure 103, 3D Comsol model of the interrogation channel with colour bar showing the flow velocity for a pump rate of 12µLh^{-1}. This channel is downstream of the preconditioning channel, immediately after the in-plane taper in which the elongational flow extends the DNA.

The model is solved for input pressures corresponding to pump rates of 3-15µLh^{-1} in 1µLh^{-1} increments and an average flow speed and thus spot transit time is calculated in each case. The detection volume is assumed to be a cylinder defined by the

Gaussian beam waist radius and of length twice the Rayleigh length. The average x-velocity of the flow through a rectangle defined by these dimensions positioned at the centre of the channel is therefore used to calculate the average flow speed. Only the x-component of the fluid velocity is used because this is the value on which the calculation of the DNA strand length is later based. It is assumed that the beam is vertically aligned with the channel. This mean velocity through the detection region is used to estimate DNA lengths as well as adjust for the spot transit time; for reference the values are given in table 10.

Pump rate (μLh^{-1})	**Mean velocity in detection volume (ms^{-1})**	
	543nm	633nm
3	0.0087	0.0081
4	0.0116	0.0108
5	0.0145	0.0136
6	0.0175	0.0163
7	0.0203	0.0189
8	0.0232	0.0216
9	0.0262	0.0244
10	0.0291	0.0271
11	0.032	0.0298
12	0.0348	0.0325
13	0.0378	0.0352
14	0.0407	0.0379

Table 10, modelling parameters for the spot transit time correction calculation.

To verify the adequacy of the average values in table 10, the inferred length of a molecule travelling through the centre of the laser spot was compared to the inferred length of a molecule transiting through some other lateral position, up to the extreme case close to the very edge of the spot. It should be noted that as the intensity will be greatest at the centre of the spot, molecules travelling through the centre are more likely to be detected and hence this calculation will tend to overestimate the variation. The figures quoted in the following paragraph relate to the 633nm

excitation/detection volume; being the larger of the two, this gives the maximum value for the error. The point close to the edge of the spot was chosen as 1.5µm from the centre (radius 1.58µm) and the error thus calculated is the maximum value for 95% of the spot. Assuming no lateral movement of the molecule occurs as it transits the detection volume, the error due to which part of the spot the molecule passes through is the same for all strand lengths.

At an input flow rate of $12\mu Lh^{-1}$, a point source transiting the centre of the detection volume would provide a 65µs signal (spot diameter divided by modelled flow speed on a streamline = $3.16\mu m/0.0485ms^{-1}$). The same point source transiting close to the edge of the excitation volume (chord length divided by modelled speed = $0.99\mu m/0.0310ms^{-1}$) would provide a 32µs signal. Thus the same source could produce a signal anywhere in the range 32µs to 65µs. Converting these times into an implied molecular length using the data from table 10 gives a range of 1.04µm to 2.11µm, i.e. a maximum error of 1.07µm. Repeating the calculation for flow rates of $3\mu Lh^{-1}$ and $15\mu Lh^{-1}$ yields a maximum error of 1.07µm to three significant figures, indicating that whilst there is variation in the error calculation due to the change in flow rate due to the steeper laminar flow profile at higher flow rates, it is not significant on this scale.

Although the higher intensity increases the chance of detecting a molecule transiting the centre of the detection volume, it is assumed that the distribution of DNA strands across the volume is uniform in the time-averaged case. Simulated and experimental results of other authors for channels of similar size [77, 78] suggest this will be the case. As stated in section 3.1.3, the non-uniformity of DNA across the section of the channel is due to hydrodynamic interactions with the channel surfaces [79, 80]. Hence although there is a probability of a depletion region where DNA migrates away from the wall in shearing flow, the results of other authors (e.g. [77], reproduced in figure 19, for a channel of comparable dimensions and a stronger shearing flow) demonstrate an almost uniform distribution across the centre of the channel.

The results referenced in the preceding paragraph relate most directly to channels of similar size to the preconditioning channels described in the thesis. These are

considered to be the most relevant since there is a significant time dependence (order seconds or greater) to establish a depletion region. Given that the excitation/detection volume is immediately downstream of the taper where the channel width reduces, there is insufficient time for a different distribution to be established. (The transit time from the preconditioning channel to the detection volume is of the order of milliseconds.) The streamlines for flow through the taper shown in figure 35 suggest that if there is no time for the shearing flow in the narrow channel to alter the distribution then it will be maintained through the point of detection.

The binning time for photon counts was fixed at 0.1ms because this value had been demonstrated to be adequate for measuring λ-DNA molecular extension in comparable systems [19] and could be inexpensively implemented in electronic hardware. The relatively large detection volume causes the signal to noise ratio to be relatively high and hence a longer integration time helps to identify weak signals from passing molecules. As the flow rate increases, each bin therefore represents a larger section of the molecule, so at $3\mu Lh^{-1}$ a one-bin event represents a molecular length of 0.87μm, while at $7\mu Lh^{-1}$ it represents 2.03μm. The flow rate of $3\mu Lh^{-1}$ was the only case in which the bin size was smaller than the error of 1.07μm described above. In the histograms of section 6.7.9 therefore, counts from adjacent bins were combined such that the minimum quantisation was two-bins and hence greater than the maximum error due to where each strand transits the detection volume. To avoid discarding any information about molecular length, this correction was not applied to other calculations such as the plot of mean lengths in figure 129.

6.5.9 Errors in Strand Length Measurement

The fluorescence signal is recorded by counting the photons in discrete time intervals of 0.1ms. The worst-case error induced by this discretisation is illustrated by figure 104 and occurs when a strand is just entering the detection volume at the end of the first time period, t_0, and is leaving the volume at the start of the last time period, t_6. This error has a maximum limit of two time bins (0.2ms) although it can never reach this value exactly. The total length of the signal ($t_0 + t_1 + \ldots t_6$) is multiplied by the average flow rate through the detection volume to calculate a nominal strand length.

This strand length is therefore overestimated by a maximum amount defined by two time bins. Note that the length of the strand cannot be underestimated due to this discretisation error. However, it is possible that the length of the strand is underestimated by up to two time bins in the pulse detection process, as the low signal in bins t_0 and t_6 becomes indistinguishable from the background.

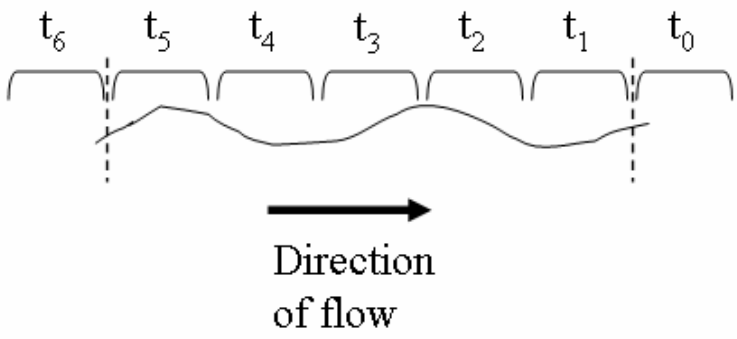

Figure 104, discrete-time measurement of strand length: as the strand moves in flow from left to right it passes the detection point, the fluorescence signal is recorded in time bins $t_0 \ldots t_6$.

The nominal strand length calculated from the number of time bins occupied by the detection pulse is adjusted for the time taken to transit the detection volume. A signal is potentially detected from the point at which the leading end of the strand enters the detection volume to the point at which the trailing end leaves the detection volume. As the three dimensional path of the strand through the detection volume is unknown, the correction is performed in two dimensions and is therefore assumed to be the time taken for the strand to cross the detection volume laterally, the width of the detection volume being defined by the beam waist.

Pump rate (μLh^{-1})	Length represented by one 0.1ms bin 633nm source (µm)	Length represented by one 0.1ms bin 543nm source (µm)
3	0.81	0.87
4	1.08	1.16
5	1.36	1.45
6	1.63	1.75
7	1.89	2.03
8	2.16	2.32
9	2.44	2.62
10	2.71	2.91
11	2.98	3.20
12	3.25	3.48
13	3.52	3.78
14	3.79	4.07
15	4.07	4.36

Table 11, length represented by the fixed-length time bin used for photon counting. The values are calculated from the modelled flow velocity through the excitation volume and the spot size of 3.16µm (633nm excitation source) or 2.7µm (543nm excitation source).

To estimate the error in the strand length measurement, a normal distribution was generated for each pump rate and spot size, the limits of which were defined by the measurement uncertainty. Table 11 shows the nominal length of DNA strand inferred from each time bin. As discussed above, the upper limit for overestimation of strand length is two bins as each end of the strand partially occupies a time slot. The maximum underestimation also tends to two bins as each end of the pulse in the photon count may be obscured by the background, especially in the case where the end of the strand is only in the observation volume for a small proportion of the bin time. The normal distribution is therefore generated such that 95% of the area under the curve is between ± two time bins [170], as illustrated by the vertical dashed lines in figure 105. The strand length implied by two time bins is calculated using the mean velocity through the excitation volume.

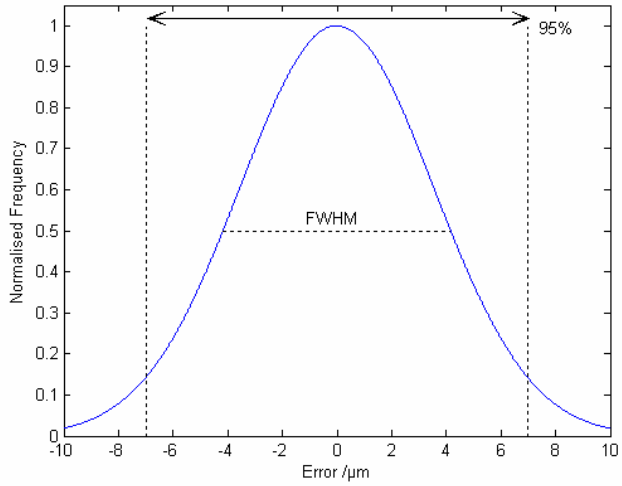

Figure 105, example normal distribution plot used to estimate the error in length measurement using the 543nm excitation source, plotted for 12µLh^{-1}.

The distribution was generated from one million random values which were fitted with a Gaussian curve having an R^2 value of at least 99%. The full width at half maximum height (FWHM) was then calculated and used to represent the error interval: in the example from figure 105, FWHM=8.34µm, giving an error in the nominal strand length of ±4.17µm. Figure 106 shows the corresponding errors for the various flow rates used experimentally, for both the 633nm and 543nm sources. The difference between the two traces stems from the fact that the average velocity through the excitation volume is used to convert the signal length in time to the strand length in distance; this mean velocity is higher in the smaller excitation volume associated with the 543nm source.

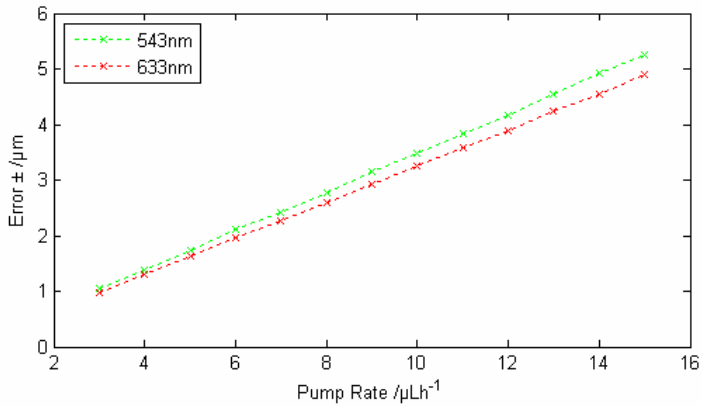

Figure 106, error half-interval for all pump rates used experimentally.

6.5.10 Skew-Normal Data Fitting

To interpret the histograms such as those shown in the results presented in section 6.7, skew normal distributions [171, 172] were fitted to the data using least-squares fitting. This is based on the principle that a continuous random variable X has a probability density function of the form shown in equation 13.

$$f(x) = 2\phi(x)\Phi(\alpha x)$$

Equation 13

where

$$\phi(x) = \exp(-x^2/2)/\sqrt{2\pi}$$

Equation 14

and

$$\Phi(\alpha x) = \int_{-\infty}^{\alpha x} \phi(t)dt = \frac{1}{2}\left[1 + erf\left(\frac{\alpha x}{\sqrt{2}}\right)\right]$$

Equation 15

Equation 14 is the standard normal density function and equation 15 is its distribution function, evaluated at αx. For numerical work the location (ζ) and scale (ω) parameters are added *via* the transformation of equation 16 and combined with the shape parameter (α) they may be used to describe the shape of a skew-normal distribution.

$$Y = \zeta + \omega X$$

Equation 16

The mean (μ_x) and variance (σ_X^2) of X may then be used to calculated the skew of the distribution, γ_1 as shown in equation 17.

$$\gamma_1 = \frac{4-\pi}{2}\frac{\mu_X^3}{(\sigma_X^2)^{3/2}}$$

Equation 17

Figure 107 and figure 108 show some example skew-normal distributions to demonstrate how the key characteristics of these curves change with the location (ζ), scale (ω) and shape (α) parameters. Where the shape parameter is zero, the skew-normal distribution produces a typical normal distribution as shown by the solid line in figure 107; in this case the location parameter gives the x-position of the peak. Varying the shape parameter skews the distribution to the left (dashed line, positive α) or right (dotted line, negative α).

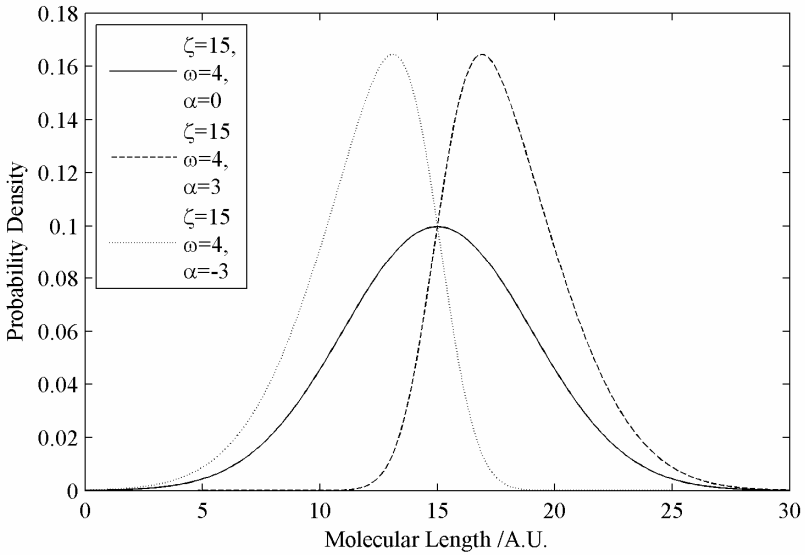

Figure 107, example skew-normal plots showing the effect of changing the shape parameter, α. A normal distribution is achieved with α=0, in which case the distribution is centred on the location parameter, ζ.

The skew parameter (γ_1) has a maximum of around 0.995 which corresponds with the half-normal case (occurring as $\alpha \rightarrow \infty$) [171], an approximation of such a fit is shown in figure 108 for α=100 (dashed line). The scale parameter (ω) describes the width and height of the distribution; as shown in figure 108 (dotted line), reducing the scale parameter from 4 to 2 doubles the peak height of the normal distribution.

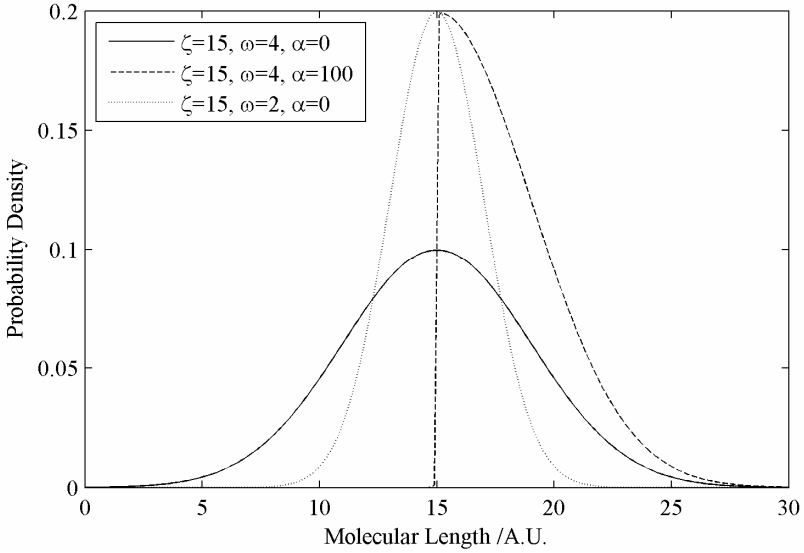

Figure 108, example skew-normal plots showing a fit to highly-skewed data (α=100) and the effect of changing the scale parameter, ω.

6.6 World-to-Chip Connection Efficiency Results

As described above, the efficiency of the world-to-chip connection was assessed by loading a dilute sample of λ-DNA, collecting the output and measuring the difference in input and output concentration by qPCR. Using this method, a comparison was made between a microfluidic device with a sloping connection and one with a stepped connection. In each case a 130µm deep capillary-housing trench is connected to a 30µm deep microfluidic channel. In the stepped device there is a vertical step of 100µm between these two trenches; in the sloped connection the lower glass wall of the capillary butts-up to a step at the base of the capillary trench and the fluid path is smoothed by an out-of-plane slope connecting this step to the 30µm trench. In addition to testing each type of device, the experiment was repeated with a simple glass capillary of equivalent length but no device connected to check for sample loss occurring elsewhere in the system.

For each device tested (and for the control experiment with no device), the mean of four samples injected, collected and quantified by qPCR was calculated as shown in table 12. A standard curve was produced in each experiment using a serial dilution to improve accuracy. The standard curve is produced by finding the second derivative maximum of the fluorescence curves and plotting the cycle number at that

point (interpolated to 2 decimal places) against the $\log_{10}$ of the concentration. A linear regression fit to these points is used to determine unknown concentrations. Template concentrations for the standard curve were: $10ngmL^{-1}$, $1ngmL^{-1}$, $100pgmL^{-1}$, $10pgmL^{-1}$ and $1pgmL^{-1}$. Each measurement consisted of up to 50 cycles of PCR, although typically samples containing template reached a plateau after approximately 30 cycles. No amplification of the no-template control (NTC) was observed over 30 cycles.

Connection Design	**Recovery of input DNA (with standard error)**
Slope	95±7%
Step	56±16%
No Chip	99±13%

Table 12, DNA recovery through each of the different connection designs.

To verify that sufficient output volume had been collected, a sample taken after the experimental volume of 500µL had been collected was included and was found to be indistinguishable from the NTC sample. The Lightcycler software calculates PCR efficiency from the slope of the standard curve according to $gradient = -1/\log_{10}(E)$; typical efficiency was ~1.8. The mean squared error of the standard curve was checked for each experiment to highlight the variation between capillaries (most commonly due to operator inconsistency). All experiments included in the mean recovery calculation had an error of less than 0.1 as recommended by the Lightcycler manufacturer (Roche).

The almost complete recovery of DNA pumped through a capillary rather than a microfluidic device indicates that sample loss in the injection valve and connecting tubing is minimal and was not a limiting factor. The sloped interconnect design also had a high efficiency and the striking difference between the sloped and stepped connections demonstrates how critical the sample loading stage is to successful experiments with microfluidic devices. The sloped interconnect therefore represents a significant improvement for any microfluidic DNA analysis system.

6.7 DNA Stretching Results

Having established that the sloped connection was substantially more efficient than the stepped connection, only devices with sloped connections were used to measure DNA extension in the subsequent confocal spectroscopy experiments, the results of which are described here. For each preconditioning channel design that was tested, a microfluidic device was assembled, primed, and connected to the fluid handling system as described in sections 6.4.1 and 6.5.1. The fluidic system of pressure driven flow provided by a syringe pump and sample injection through a six-port valve with 100µL sample loop was unchanged from the interconnect testing experiments. Once a device was connected to the fluidic system it was typically used for several experiments. After a device was primed with buffer it was aligned to the optical detection system using the small reflected signal from the excitation source. The distance of the laser spot from the extension funnel (x-position) was minimised during this alignment. The reflected signal at the glass-silicon interface adjacent to the channel differs significantly from the glass-buffer interface at the channel. The chip was mounted on a translation stage which allowed measurement of the distance that the channel was moved relative to the excitation volume, which allowed the excitation volume to be located initially in the funnel and then shifted a few micrometres into the interrogation channel. At $12\mu Lh^{-1}$ the average flow speed through the excitation volume is of the order $40\mu mms^{-1}$; the relaxation time of λ-DNA in buffer is estimated as 94ms and hence in one relaxation time a strand could travel 3.8mm. After the initial positioning had taken place, the alignment was improved by loading fluorescent dye into the device and locating the excitation volume at the centre of the interrogation channel (in the y and z directions).

Once the system was aligned and the fluorescent dye flushed out, a sample of stained λ-DNA was injected and data collection initiated. To minimise background light, the area around the chip and optical system was enclosed and all other light sources in the room were extinguished. A networked PC was used to monitor the data acquisition to avoid disturbing the ongoing experiment with unnecessary vibration or background light. Extensive data collection before and after the fluorescently stained DNA sample was introduced revealed a negligible number of peaks above the background photon count. Sections 6.7.1 - 6.7.4 show a representative selection

of results for the preconditioning designs that were tested; a full set of graphs is available in appendix B.

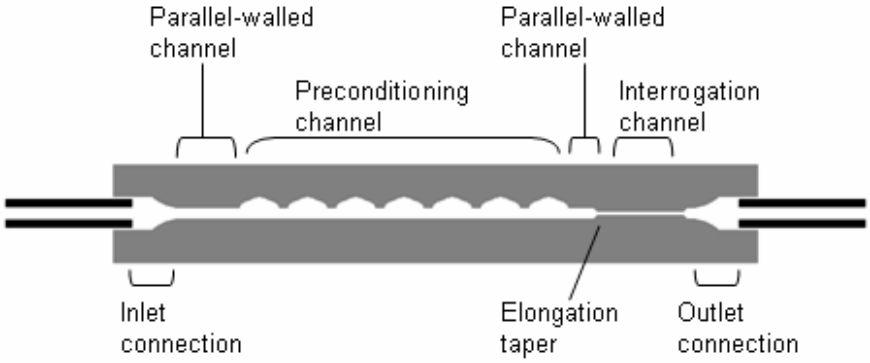

Figure 109, sketch showing the various microfluidic elements present in each device. The inlet and outlet connections are sloped as previously described; at the inner end of each slope the depth is equal to that of the other features on the chip at 30µm. A short section of parallel-walled channel bounds either end of the preconditioning channel, ensuring the channel width reduction at the elongation taper is the same in all devices. Optical interrogation takes place in the interrogation channel immediately after the elongation taper.

Figure 109 shows the features that are common to all the microfluidic devices with the different preconditioning channel designs, fluid flow in normal operation is from left to right. In the parallel-walled sections the channel is 30µm deep and 30µm wide; in the control channel the preconditioning section has the same dimensions. In the preconditioning channel the width can reach 62µm depending on the design. At the elongation taper, the channel width reduces from 30µm to 5µm over a distance of 5µm; the optical excitation volume is positioned immediately downstream of the taper.

6.7.1 Control Preconditioning Channel

Figure 110 shows a section of the control channel in bright-field; at this point the channel is 30µm wide and 30µm deep. Downstream it tapers to 5µm wide and 20µm deep in the detection channel. The geometry of the taper is shown in chapter 3, section 3.5.

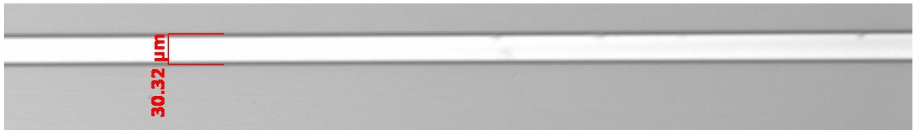

Figure 110, microscope image of a section of the control preconditioning channel.

The probability distributions for nominal DNA strand length at flow rates of 8-14µLh^{-1} for the experiments using TOTO-3 to stain the backbone are shown in figure 111 – figure 114 below along with a legend showing the total number of strands detected in each experiment; each graph represents one experiment. As the flow rate increases, the peak in the distribution moves from less than 5µm to almost 10µm and the proportion of strands stretched to the contour length increases dramatically.

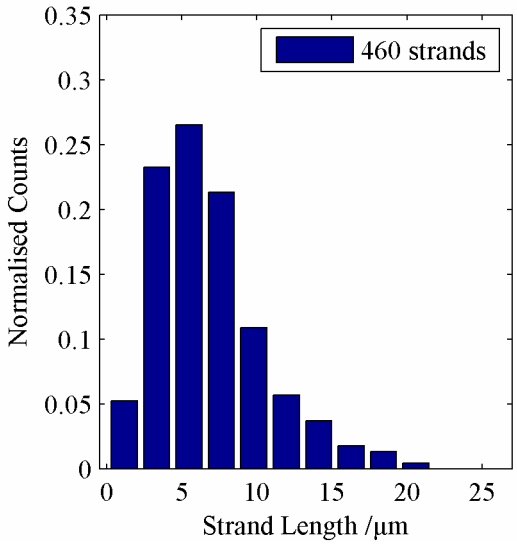

Figure 111, probability distribution of nominal DNA length in the control channel, pump rate 8µLh^{-1}.

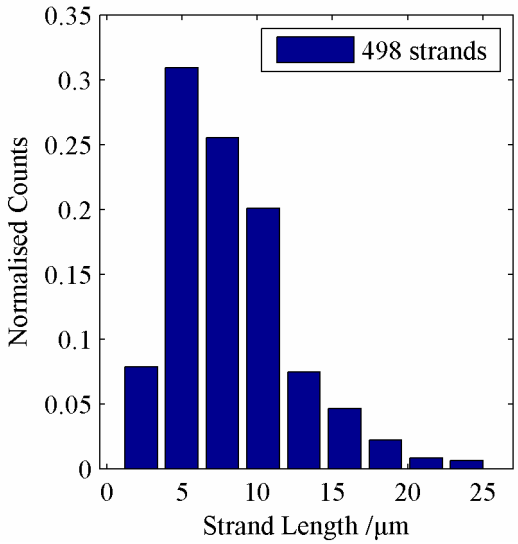

Figure 112, probability distribution of nominal DNA length in the control channel, pump rate 10µLh^{-1}.

The contour length of unstained λ-DNA is 16.5µm, although intercalation with dimeric cyanine dyes can increase the contour length to up to 22µm as discussed in section 6.3. Strands with nominal lengths longer than 25µm are therefore not shown in the histograms in this section. (Complete plots are available in Appendix B.) These data may arise from (a) noise blurring the edges of the signal pulse, (b) multiple strands passing through the observation volume concurrently, (c) overstretched strands or possibly (d) dimers. Data which equate to a strand length of less than zero after accounting for the transit time through the excitation volume are excluded. Such signals could result from noise, however due to the separate threshold levels used for pulse detection and pulse length calculation it is more likely they are the result of strands that only partially enter the excitation volume.

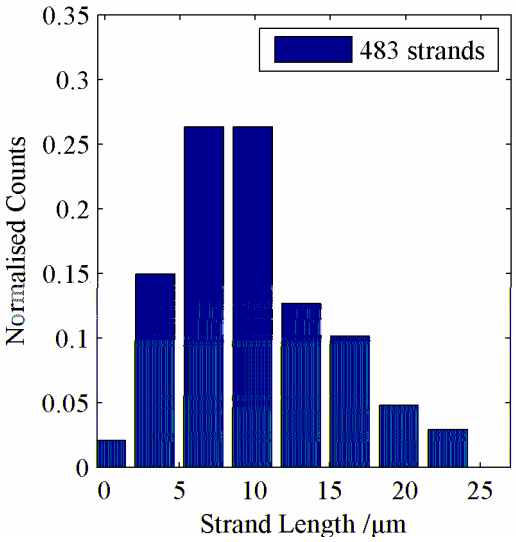

Figure 113, probability distribution of nominal DNA length in the control channel, pump rate 12µLh^{-1}.

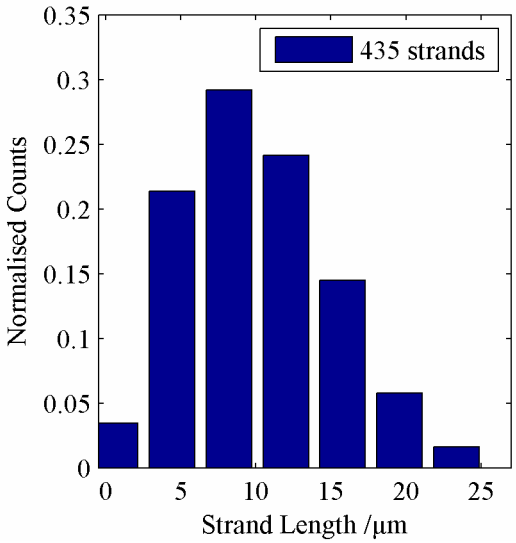

Figure 114, probability distribution of nominal DNA length in the control channel, pump rate 14µLh^{-1}.

The increased flow rate has two effects on DNA strand length; in the preconditioning channel, the shearing flow is stronger due to the no slip condition at the channel wall (*cf.* figure 29, chapter 3), while the fluid acceleration through the downstream elongation funnel is also greater. As the polymer relaxation time is unchanged, the Weissenberg (Wi) and Deborah (De) numbers are therefore increased, indicating an increased likelihood of polymer extension, as described in chapter 3. This is

reflected in the proportion of strands that are stretched close to contour length. The proportion of observed DNA strands with length >15µm was just 3.5% at a flow rate of 8µLh^{-1}, reaching 21.8% at a flow rate of 14µLh^{-1}.

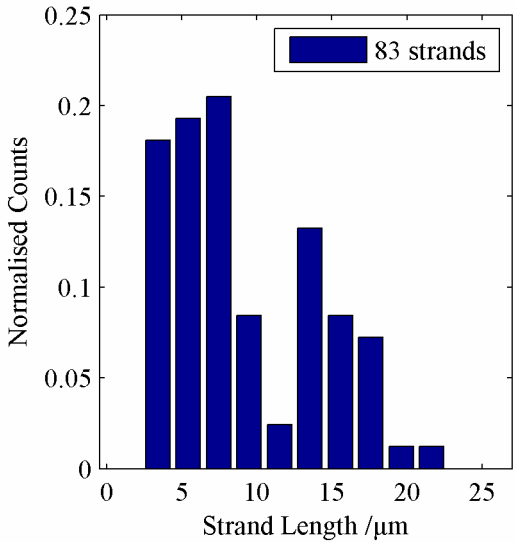

Figure 115, probability distribution of nominal DNA length in the control channel measured using POPO-3, pump rate 7µLh^{-1}.

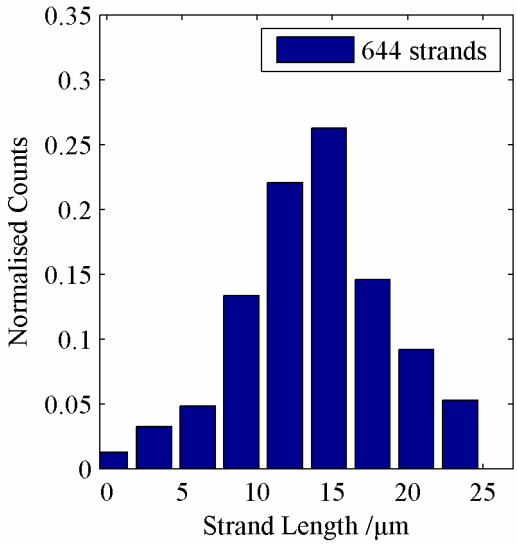

Figure 116, probability distribution of nominal DNA length in the control channel measured using POPO-3, pump rate 10µLh^{-1}.

Similar results were produced for equivalent flow rates when using POPO-3 as the DNA stain and these may be found in their entirety in Appendix B. Figure 115 shows the distribution for this experiment at a pump rate of 7µLh^{-1} and figure 116 at a pump rate of 10µLh^{-1}. The same trend of increasing probability of extension around the unstained contour length may be seen in these graphs. In both experimental variations the peak of the distribution seems to be around the unstained contour length, although a significant proportion of strands are stretched beyond this. For POPO-3 stained λ-DNA, the proportion of strands with length greater than 15µm was calculated as 18.1% for a flow rate of 7µLh^{-1} and 29% for 10µLh^{-1}. It is difficult to make quantitative comparisons between the experiments with different stains due to the difference in the size of the excitation volume and the uncertainty of the position of a strand within that volume. However the signal to background ratio of the TOTO-3 experiments was generally superior, which improved the efficiency of the pulse detection software. The staining ratio of 1:5 (dye molecules to base pairs) is considered to account for molecular lengths of 16.5-22µm as the contour length

may be extended by intercalation but would be expected to be less than the 22µm seen for a molecule saturated with dye (staining ratio 1:4).

6.7.2 Narrowing Serpentine Preconditioning Channel

A brightfield image of the narrowing serpentine preconditioning design is shown in figure 117. The section immediately downstream of the inlet connection is identical to the control channel, the first sidewall feature is 300µm from the in-plane taper of the connection. Each feature in the sidewall of the channel is 102µm in length by design and the preconditioning part of the channel extends for 1cm. At the end of the preconditioning part of the channel there is a 500µm parallel-walled section which is again identical to the control channel, prior to the extension funnel and observation channel.

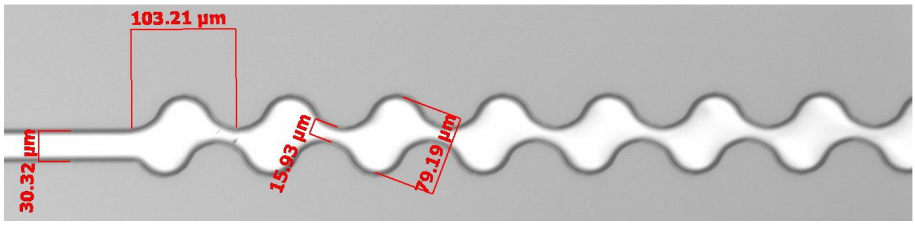

Figure 117, microscope image of a section of the narrowing serpentine preconditioning channel. The pitch of the repeating curve in the side wall is 102µm by design, the depth is 30µm and the total length of the preconditioning part of the channel is 1cm.

The probability distributions in figure 120 – figure 119 show the performance of the narrowing serpentine channel stretching λ-DNA stained with TOTO-3. As with the control channel described in section 6.7.1, an increased flow rate causes the peak of the distribution to shift right and a greater proportion of strands are stretched to the unstained contour length or beyond. At all flow rates however the narrowing serpentine design outperforms the control channel using this measurement: at 8µLh^{-1} 4.7% of strands have nominal lengths of 15µm or more; at 14µLh^{-1} the proportion is 48.1%.

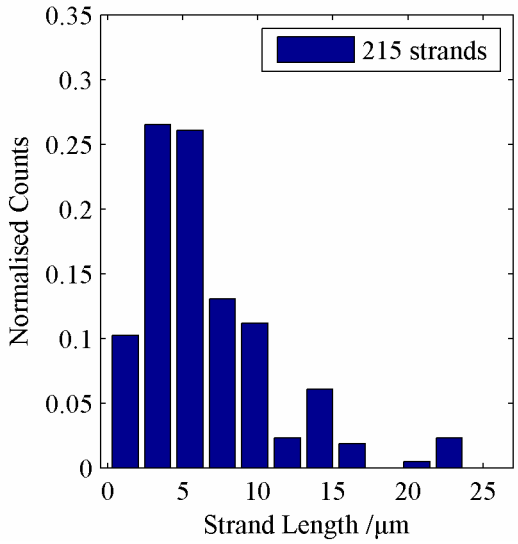

Figure 120, probability distribution of nominal DNA length in the narrowing serpentine channel, pump rate 8µLh^{-1}.

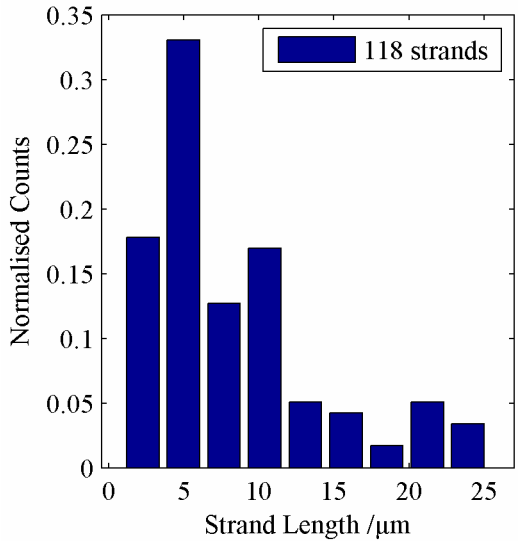

Figure 121, probability distribution of nominal DNA length in the narrowing serpentine channel, pump rate 10µLh-1.

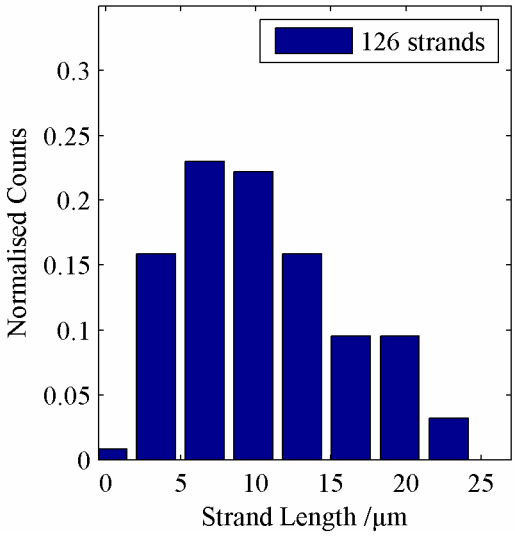

Figure 118, probability distribution of nominal DNA length in the narrowing serpentine channel, pump rate 12µLh^{-1}.

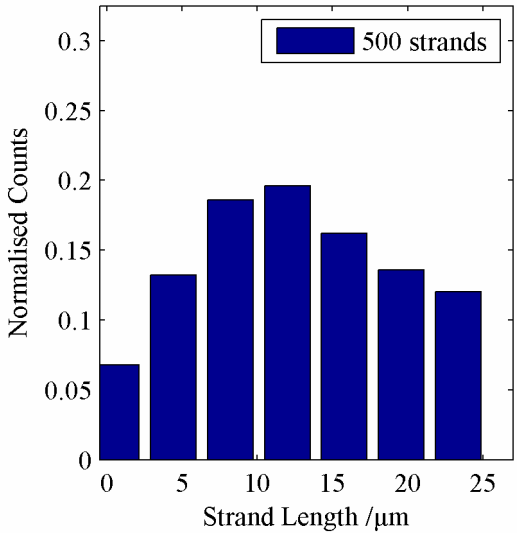

Figure 119, probability distribution of nominal DNA length in the narrowing serpentine channel, pump rate 14µLh^{-1}.

6.7.3 Serpentine Preconditioning Channel

A brightfield image of the serpentine preconditioning channel is shown in figure 122. In common with the other preconditioning channel designs the inlet connection is followed by 400µm of parallel-walled channel prior to the preconditioning section which itself is 1cm long and is upstream of the stretching taper and interrogation channel.

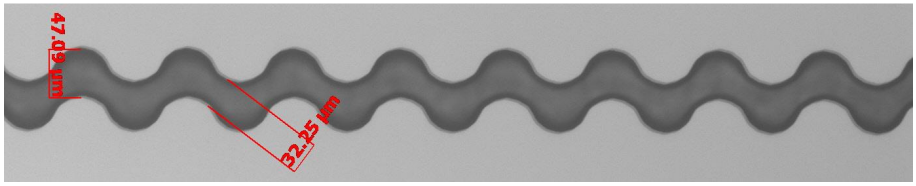

Figure 122, microscope image of a section of the serpentine preconditioning channel. The pitch of the repeating unit is 204µm and the total length of the preconditioning channel is 1cm.

The results of two experiments for POPO-3 labelled λ-DNA are shown in figure 123 and figure 124; the complete set of results is available in Appendix B. As with the other preconditioning channels and the control case, increasing the pump rate increases the Weissenberg (Wi) and Deborah (De) numbers and therefore DNA stretching. The serpentine channel is wider in places (as shown in figure 122) than the control channel and hence for a given pump rate Wi would be lower if measured across the channel at any one such point. However as discussed in chapter 3, it is the variation in Wi as well as the disruption of the position of the Wi minimum that is proposed to assist DNA stretching. The proportion of DNA strands stretched to 15µm or more by the serpentine preconditioning channel is greater than that of the control channel for flow rates of 7-12µLh^{-1}; at 12µLh^{-1} the proportion for the serpentine channel is 60.4% against 33.0% for the control channel

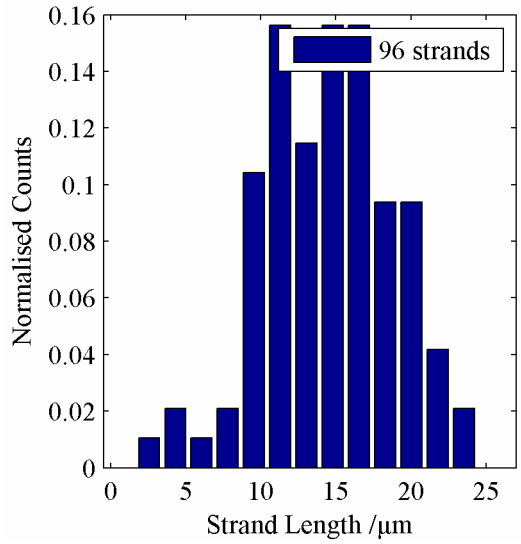

Figure 123, probability distribution of nominal DNA length in the serpentine channel, pump rate 6µLh^{-1}.

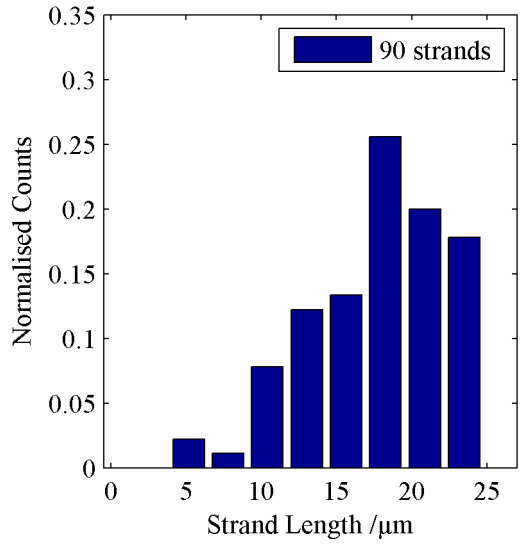

Figure 124, probability distribution of nominal DNA length in the serpentine channel, pump rate 9µLh^{-1}.

It should be noted that in all the preconditioning channel designs there is a 500µm section of 30µm-width parallel-walled channel prior to the stretching funnel, so the flow acceleration due to the taper is the same for each pump rate regardless of channel design.

6.7.4 2:1 Preconditioning Channel

A brightfield image of the 2:1 preconditioning channel is shown in figure 125. A blockage to this channel limited data collection but the results that were collected are shown in figure 126 and figure 127. The distributions appear to again show an increased probability of longer strands being detected as the pump rate increases, although it is difficult to say for certain from this limited sample. In general, laboratory equipment was extensively cleaned and sterilised and solutions were filtered wherever possible. The dimensions of these devices however are still such that they are extremely sensitive to contamination and a bubble or dust particle in the buffer solution can easily cause a device to become inoperable.

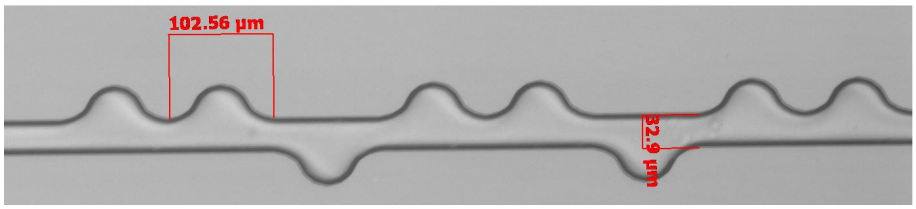

Figure 125 microscope image of a section of the 2:1 preconditioning channel. The design repeats axially every 306µm and the total length of the preconditioning channel is 1cm.

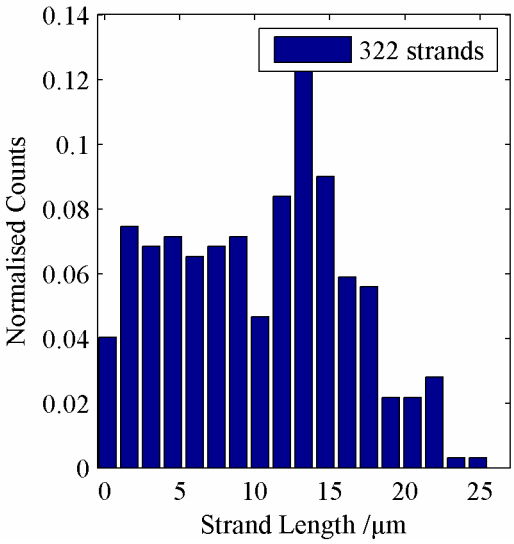

Figure 126, probability distribution of nominal DNA length in the 2:1 channel, pump rate 5µLh^{-1}.

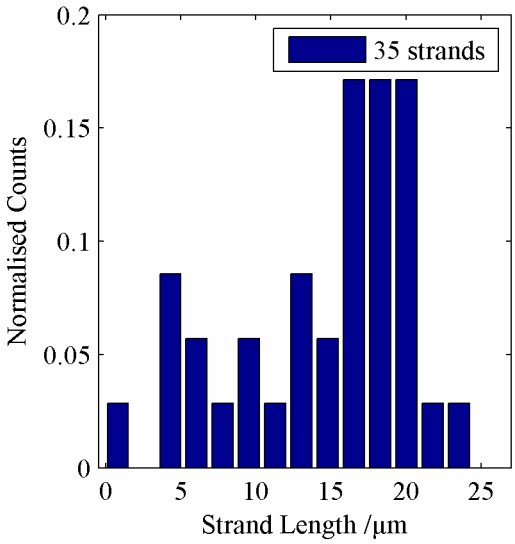

Figure 127, probability distribution of nominal DNA length in the 2:1 channel, pump rate 6µLh^{-1}.

6.7.5 Nominal Strand Length Comparison

To highlight the differences in stretching performance of the different preconditioning channel types, figure 128 and figure 129 show the mean nominal strand length as a function of pump rate for the TOTO-3 and POPO-3 experiments respectively. At higher flow rates, the control preconditioning channel consistently had the worst performance, while the serpentine channel appears to offer a greater

performance improvement than the narrowing serpentine. For all channels the mean strand length tends to increase with pump rate which is a consequence of the higher average shear rate in the preconditioning region. At the higher flow rates the mean strand length approaches the unstained contour length of the λ-DNA molecule (16.49µm). As discussed above, the contour length for a λ-DNA saturated with the intercalator TOTO-1 has been reported as 22µm [51]. The difference is attributed to the sub-saturation staining ratio used [19] although the contour length of a strand saturated with TOTO-3 or POPO-3 may not be exactly equivalent to the TOTO-1 case.

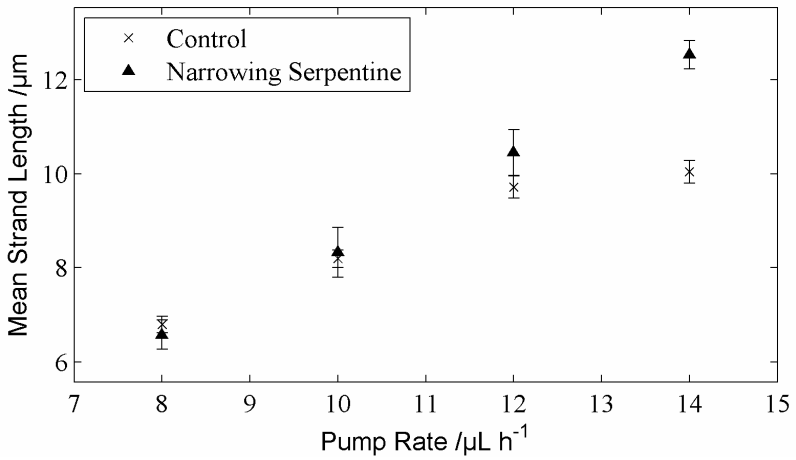

Figure 128, mean nominal DNA strand length for narrowing serpentine preconditioning channel and control channel as a function of pump rate for experiments using TOTO-3 stained DNA. Error bars show the standard error.

The plots of mean length allow a basic comparison of the whole dataset from each experiment, but in practice there will always be a distribution of measured molecular lengths. An alternative figure of merit that can be used to make comparisons between preconditioning channel designs is the proportion of strands stretched to the unstained contour length or greater. For genomic analysis applications, repeatable stretching to approximately the contour length can be sufficient for reproducible detection of abnormalities. Figure 130 shows the percentage of strands with nominal length greater than 15µm for the TOTO-3 stained molecules. The narrowing serpentine preconditioning channel can be seen to outperform the control across the whole measured range of pump rates; the highest measured proportion reaching

41.8%. Similar results are shown for the experiments using POPO-3 stained λ-DNA in figure 131; flow rates of 9μLh^{-1} and greater have more than 60% 'fully' extended molecules. Again from flow rates of 7μLh^{-1} and greater, the control channel is always the worst performer.

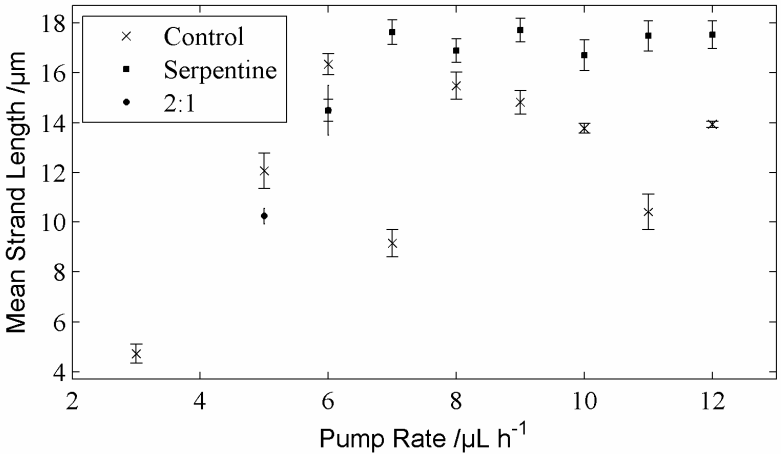

Figure 129, mean nominal DNA strand length for serpentine preconditioning channel, 2:1 channel and control channel as a function of pump rate for experiments using POPO-3 stained DNA. Error bars show the standard error.

The signal to background ratio (SBR) varied between approximately 5 and 25 across all experiments as measured by the average pulse height against the average background, but was typically slightly higher for the TOTO-3 experiments. This difference is attributed to the background reduction due to rejection of out-of-focus light by the pinhole. It is important to note that the aim of these experiments is not high accuracy DNA length measurement, for which there are more appropriate methodologies. The primary aim is to identify if there is any difference between preconditioning of DNA strands in shearing flow in a straight, parallel walled (control) channel compared to a channel of varying geometrical proportions or with frequent changes in flow direction. For future applications it is necessary to have to a high proportion of molecules stretched to approximately the contour length. Figure 130 and figure 131 show that this is more readily achieved using a serpentine channel design.

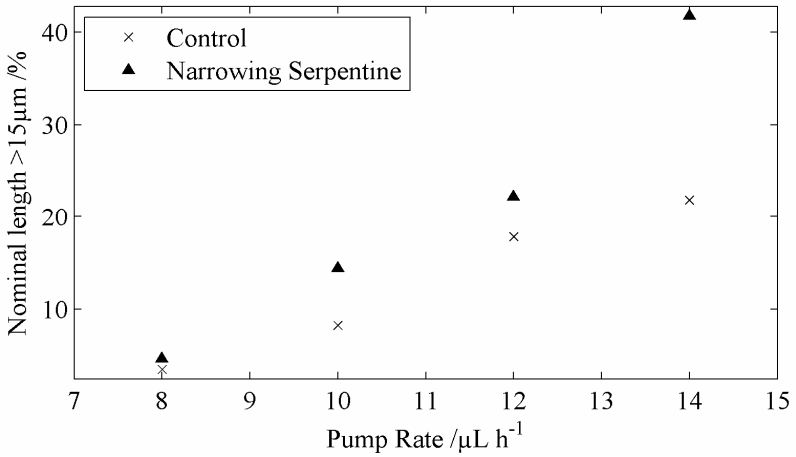

Figure 130, proportion of strands with nominal length greater than 15µm as a function of pump rate (TOTO-3 experiments).

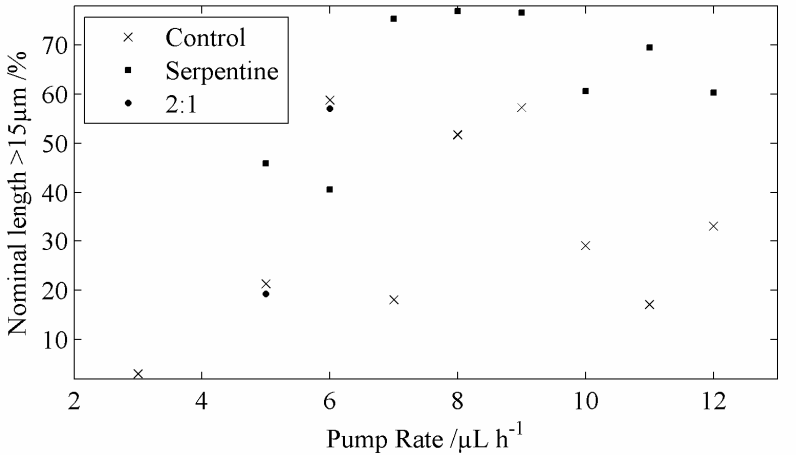

Figure 131, proportion of strands with nominal length greater than 15µm as a function of pump rate (POPO-3 experiments).

6.7.6 Comparison of Control and Serpentine Channels

Three dimensional histograms of the photon count per unit length for each detected strand as a function of its nominal length are shown below for comparison of the control and serpentine preconditioning channels for experiments with POPO-3 labelled DNA. Each row is labelled with the pump rate (PR, in μLh^{-1}) and all the x-axes are equally scaled; the greyscale at each point indicates the number of strands.

To generate these graphs, strand lengths were rounded to the nearest micrometre and burst sizes to the nearest ten photons.

PR	Control	Serpentine
3	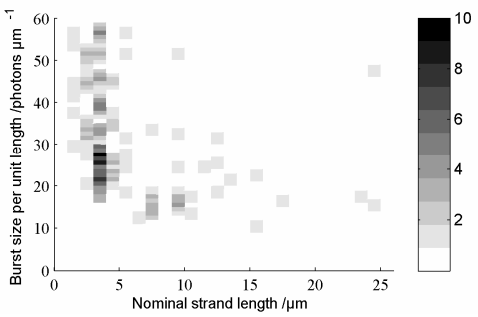	
5	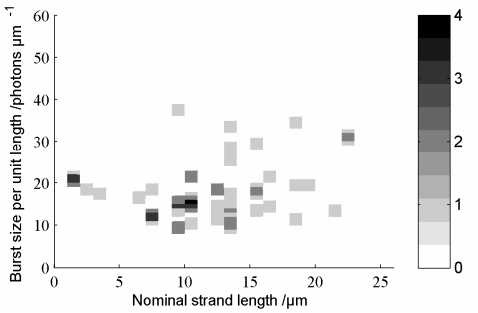	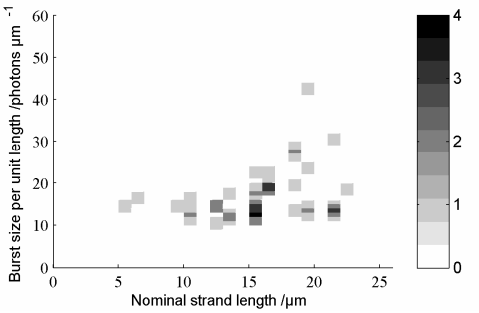
6	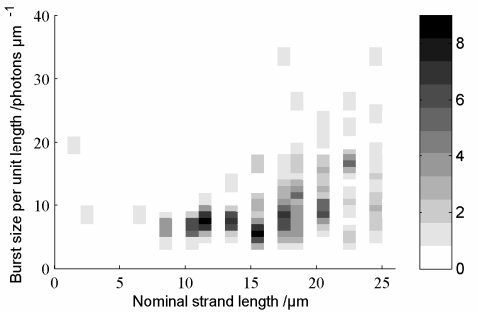	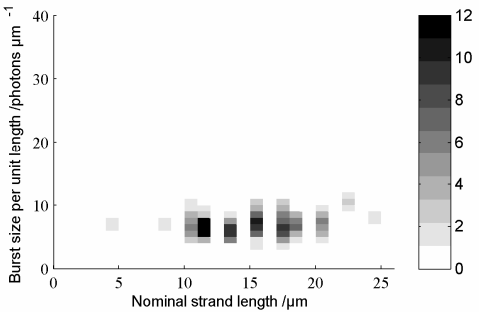
7	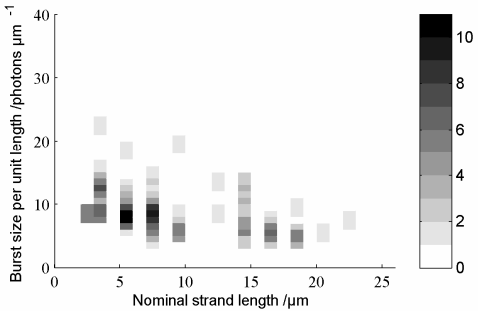	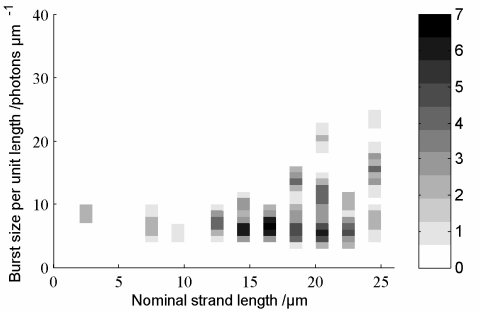

8

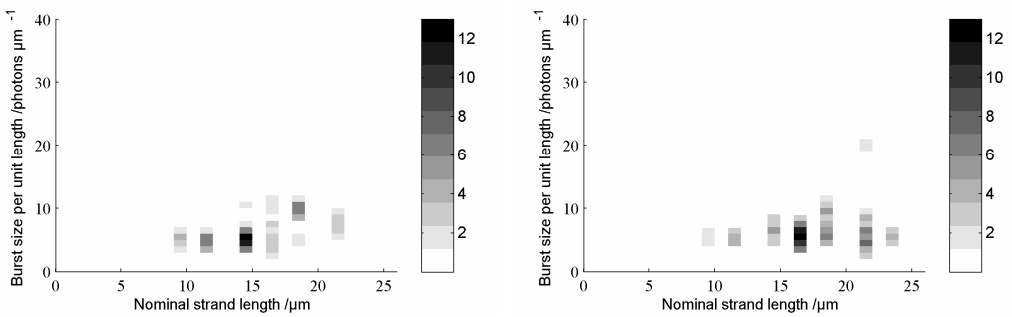
Burst size per unit length /photons µm -1
Nominal strand length /µm
0 5 10 15 20 25
0 10 20 30 40
2 4 6 8 10 12

9

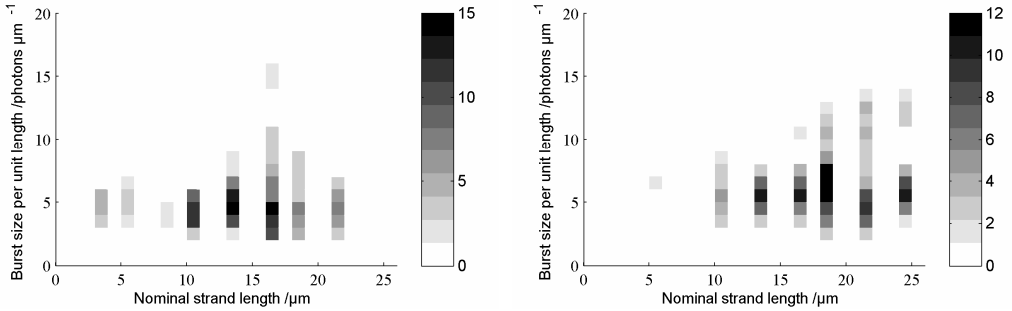
Burst size per unit length /photons µm -1
Nominal strand length /µm
0 5 10 15 20 25
0 5 10 15 20
0 5 10 15
0 2 4 6 8 10 12

10

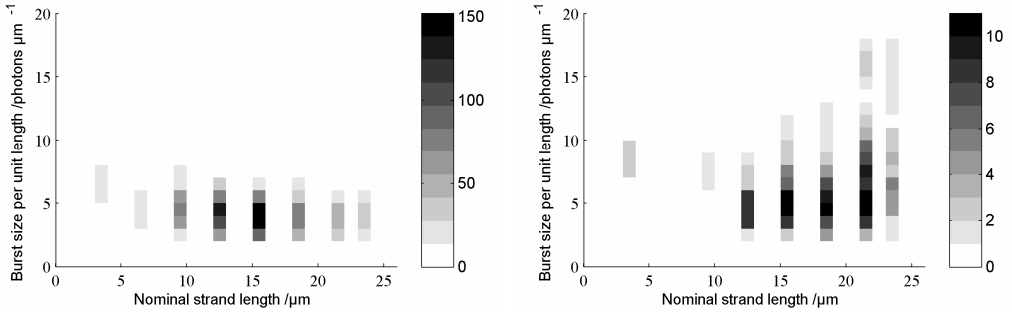
Burst size per unit length /photons µm -1
Nominal strand length /µm
0 5 10 15 20 25
0 5 10 15 20
0 50 100 150
0 2 4 6 8 10

11

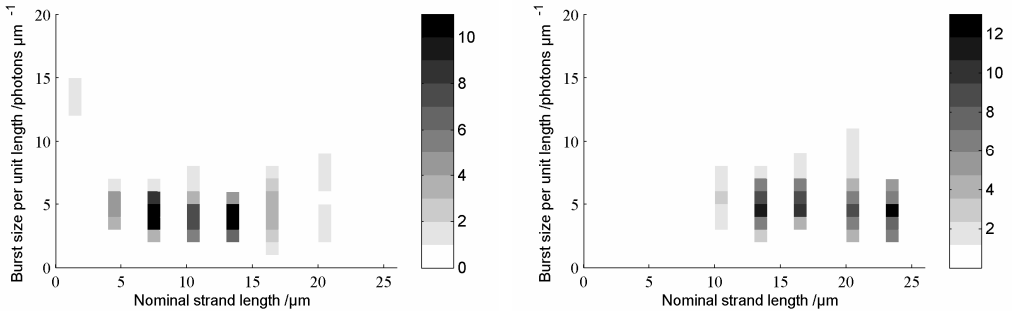
Burst size per unit length /photons µm -1
Nominal strand length /µm
0 5 10 15 20 25
0 5 10 15 20
0 2 4 6 8 10
0 2 4 6 8 10 12

12

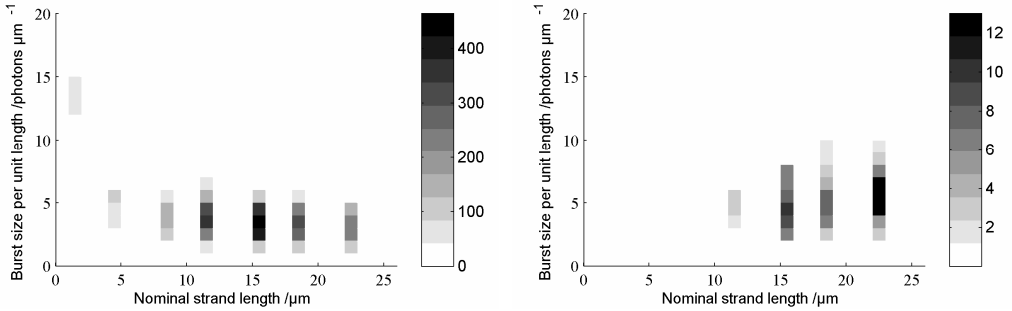
Burst size per unit length /photons µm -1
Nominal strand length /µm
0 5 10 15 20 25
0 5 10 15 20
0 100 200 300 400
0 2 4 6 8 10 12

These plots are analogous to the 'comet plots' showing count rate as a function of length reported by other authors [22, 157] as described in section 6.3, however the lower fidelity of the optical measurement system used in the experiments described here means that the plots reveal less information about the underlying molecular characteristics. Nonetheless, the trend of increased DNA stretching at higher flow rates is again observable, as is the improved performance of the serpentine channel.

The high count rate per unit length seen for short molecules in the control channel at $3\mu Lh^{-1}$ would appear to suggest that whole, intact molecules were detected but that the flow rate was insufficient to cause significant deformation from the RMS coil size. Considering the plots for $5\text{-}8\mu Lh^{-1}$ and comparing the control to the serpentine channel in each case, it is apparent that the counts per unit length are comparable which suggests that the detected molecules were approximately the same size. However over these four pairs of plots, the nominal lengths are generally greater for the serpentine channel and the distribution of sizes and count rates appears a little tighter.

For flow rates of $9\text{-}12\mu Lh^{-1}$, the tendency of the serpentine channel to cause greater molecular extension (which is also observed in figure 129) may be seen in these plots. The plot for the serpentine channel at $12\mu Lh^{-1}$ has the tightest distribution of both nominal lengths and photon counts per unit length. This suggests that this channel and flow rate generated the most reproducible molecular extension and most consistent detection.

The control channel for flow rates of $11\text{-}12\mu Lh^{-1}$ has a small cluster of detected molecules with short lengths and relatively high photon counts per unit length. These are potentially strands which have been detected in their entirety but underwent the most minor of deformations. The absence of these clusters in the plots for the serpentine channel suggests the possibility that fewer molecules are left 'un-stretched' after passing through such devices.

6.7.7 Conformation Classification

To aid the interpretation of the molecular length data, a classification scheme was devised. Strands with a nominal length of 19.5µm or greater were considered to be *stretched* and it is this category which is considered to be useful for genomic analysis applications. While the contour length of an unstained molecule of λ-DNA is 16.49µm when saturated with intercalating dye this can increase to 22µm [51]. The molecules in this study are not saturated with dye by design (1:5 ratio of dye molecules to base pairs rather than the 1:4 required for saturation [26]) so the average contour length is likely somewhere in the range 16.49-22µm. As DNA strands tend to stretch in a stem and flowers configuration [173] a molecule that is slightly below its contour length is in any case still useful for analysis provided that the probed regions are not close to the ends. Strands with a nominal length greater than 30µm were not considered for this analysis, in order to include fully stretched strands with overestimated lengths but exclude dimers and anomalous signals. *Coiled* strands were considered to be those with a nominal length of 7.3µm or less; this is less than a third of the contour length (assuming 22µm) and these molecules are unlikely to be of any use for analysis. Those strands falling between these upper and lower limits were defined as *folded*. This scheme is summarised in table 13.

Limit (L=22µm)	Category	Sketch
Nominal length < 7.3µm (L/3)	Coiled	
7.3µm <= Nominal length < 19.5µm	Folded	
Nominal length > 19.5µm	Stretched	

Table 13, three-part conformation classification scheme: molecules with a length close to L are considered sufficiently stretched to be useful for analysis; shorter strands with a nominal length greater than L/3 are classified as folded, with shorter strands classified as coiled.

Strands with a nominal length greater than 30µm typically constitute less than 5% of detected signals and this upper limit is chosen to focus the analysis on those strands which are suitably stretched to be of use for genomic analysis applications. The most credible explanations for signals with a nominal strand length greater than 30µm are multiple strands in the observation volume or optical noise at the edges of

the signal pulse. It is possible however that some of these signals are representations of real strands. An overstretched DNA molecule extends to approximately 1.7 times its contour length [62] and, assuming the maximum contour length of 22µm, this gives an upper limit on strand length of 37.4µm. (If the maximum measurement error in overstating the nominal length is assumed this value could be greater than 40µm.) Since the transition to S-form implies a structural change in the DNA double helix it cannot be assumed that the intercalating dye will remain bound. Furthermore, there is no trend towards an increasing count of signals with nominal length greater than 30µm as the pump rate is increased for any of the channels described in this chapter, implying that these signals do not originate from overstretched DNA strands. For these reasons, although signals with a large nominal may represent real data, they cannot be used to assess the performance of the different channel types.

6.7.7.1 Control Channel Conformation Classification Results

The results of this classification scheme are presented in figure 132 (543nm source, POPO-3) and figure 133 (633nm source, TOTO-3) below. In the control channel, the axially constant shear rate causes the deformation by extensional flow in the funnel to be the dominant factor affecting the conformation at the point of detection. The Deborah number for a strand transiting through the centre of the channel is therefore plotted against pump rate on a secondary y-axis. At the lowest flow rate, $3\mu Lh^{-1}$, the proportion of coiled molecules is greater than 80% while it is significantly lower for all higher flow rates. This suggests that a Deborah number in excess of approximately 100 is required to generate stretching in this system. Although this value is well above the theoretical minimum of 0.4 for a coil-stretch transition [76], the strongly deforming flow is required due to the short residence time of the DNA molecules in the funnel.

The proportion of strands allocated to each conformation as observed in figure 132 is relatively consistent for flow rates above $5\mu Lh^{-1}$. With the exception of the result for $11\mu Lh^{-1}$ it appears coiled molecules are relatively uncommon at a sufficiently high flow rate. Other than this, the performance of the control channel in producing DNA

strands sufficiently stretched for genomic analysis applications is not significantly improved by increasing the flow rate over the range studied.

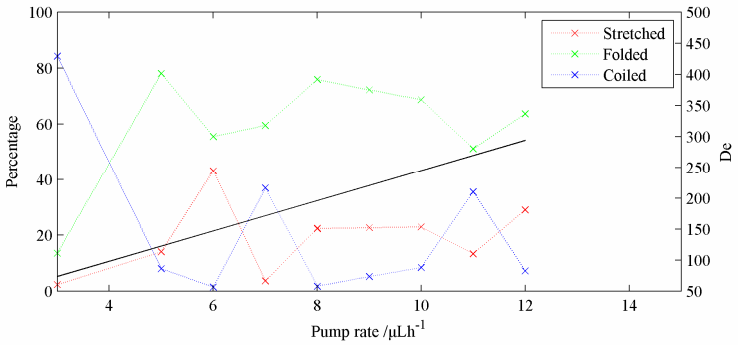

Figure 132, proportion of each class of strand conformation for the control channel with POPO-3 stained DNA (543nm excitation source); the solid black line shows the maximum De in the funnel.

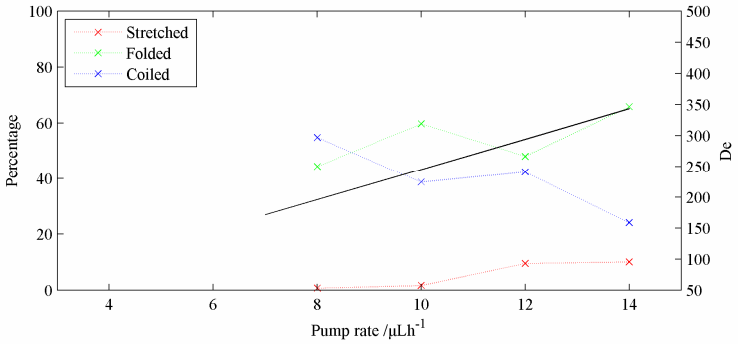

Figure 133, proportion of each class of strand conformation for the control channel with TOTO-3 stained DNA (633nm excitation source); the solid black line shows the maximum De in the funnel.

Figure 133 shows the results for the TOTO-3 stained DNA with the 633nm excitation source. The lower proportion of stretched strands (relative to figure 132) could be attributable to the lower quantum efficiency of the dye in these experiments (0.06) as a fully stretched strand has the lowest possibly quantity of fluorophores in the excitation volume in each time bin. There is some improvement in control channel performance at higher flow rates in this experiment as the proportion of folded molecules is greater than that of stretched molecules for flow rates greater than 8µLh^{-1}. However the proportion of stretched strands remains low even where

the Deborah number exceeds 300, indicating that the control device is unlikely to be useful for practical genomic applications.

To assess whether the three-part conformation scheme was sufficient to assess changes in the population of strands observed in each experiment, an extra category was introduced by splitting the folded molecules into two sub-categories. As illustrated in table 14, this separates strands with an overall length short enough that they must contain at least two folds from those long enough to potentially contain only a single fold. An increase in the proportion of strands classified as having a single fold (as a function of, say, the pump rate) would suggest an underlying improvement in stretching performance that was not identified by the three-part classification scheme.

Limit (L=22µm)	Category	Sketch
Nominal length < 7.3µm	Coiled	
7.3µm <= Nominal length < 11µm	Two Folds	
11µm <= Nominal length < 19.5µm	One Fold	
Nominal length > 19.5µm	Stretched	

Table 14, four-part conformation classification scheme. This is an extension of the three-part scheme in which strands with a nominal length from L/3 to L/2 are classified as having two folds, those with length L/2 to almost L are classified as having one fold.

Figure 134 shows the four part classification results for the POPO-3 experiments; the traces for coiled and stretched molecules are unchanged from the three part scheme seen in figure 132. At the lowest flow rate ($3\mu Lh^{-1}$) there are more molecules with two folds than with one. For higher flow rates the molecules with a single fold are more common, with the proportion of molecules with two folds stabilising at fewer than 20% for pump rates of $8\mu Lh^{-1}$ and greater. An underlying improvement in stretching performance appears to be discernible from these data, considering the difference between strands with one fold and strands with two folds. Excluding the points with spikes in the proportion of coiled molecules (at 7 and $11\mu Lh^{-1}$) there is a

weak correlation (R^2 of 63%) between this difference and the pump rate. This indicates that the increasing pump rate is a causal factor in stretching strands into a one-fold rather than two-folded conformation. (Note that that exact nature of the conformation is not implied from this correlation, merely the categorisation under the scheme of table 14.) The result at 11μLh^{-1} highlights that although there can be a high proportion of coiled strands present in the control devices even at high flow rates, the stretching performance of the funnel at higher De remains intact as of the non-coiled molecules there are still more stretched to a one-fold class than to a two-fold.

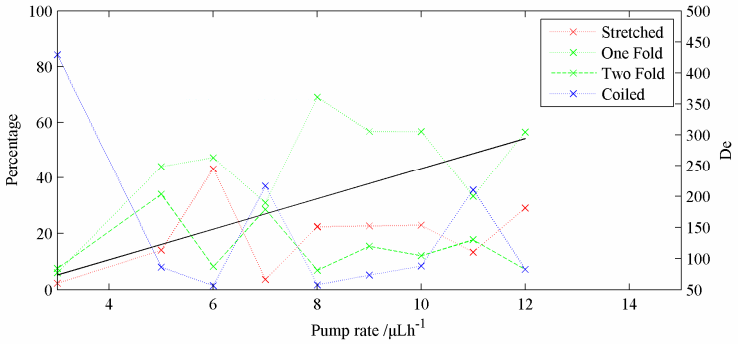

Figure 134, proportions of strands in a four-part conformation classification for the control channel with POPO-3 stained DNA (543nm excitation source); the solid black line shows the maximum De in the funnel.

Figure 135 shows the four part classification results for the POPO-3 experiments. In general the proportion of coiled molecules is higher than in the TOTO-3 experiments and the proportion of stretched molecules is lower. Similarly the performance measured by the folded molecules is poor, with the proportion of one-fold strands only greater than the proportion of two-fold strands at the highest flow rate of 14μLh^{-1}.

Although the four-part classification scheme is of some use to probe the underlying stretching performance of each device, the key indicator for genomic analysis applications remains the proportion of strands stretched sufficiently close to the contour length. For this reason the three-part classification scheme was used to assess the results from the serpentine and narrowing-serpentine channel designs.

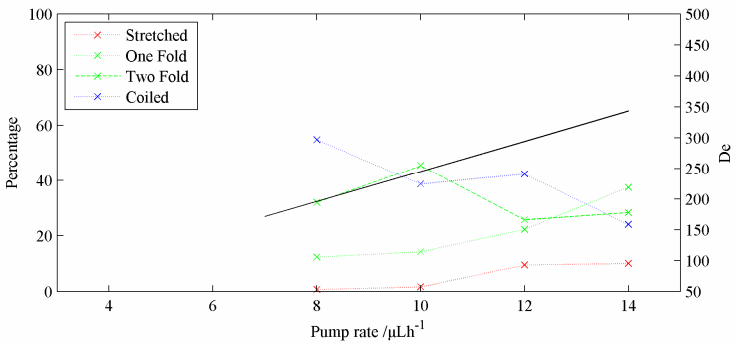

Figure 135, proportions of strands in a four-part conformation classification for the control channel with TOTO-3 stained DNA (633nm excitation source); the solid black line shows the maximum De in the funnel.

6.7.7.2 Serpentine and Narrowing-Serpentine Channel Conformation Classification Results

Figure 136 shows the results of the three-part conformation classification for the serpentine channel based on the results of the experiments with POPO-3 stained DNA and the 543nm excitation source. The maximum value of Wi measured 50nm from a central streamline was calculated from the Comsol model of the channel and is plotted on a secondary y-axis.

The choice of the point at which Wi is measured is somewhat arbitrary. In practice the DNA strands will occupy most of the width and depth of the channel although the population may be depleted close to the channel walls. Also, while measuring Wi over 50nm gives a reasonable estimate of the minimum value experienced by a DNA strand at that point, a strand occupying a greater proportion of the channel width (e.g. a coiled strand) is subject to a higher instantaneous average value of Wi. Both of these factors affect all the types of preconditioning channel, hence a suitable method of computing a comparable value of Wi must be chosen. Using Wi measured 50nm from a central streamline gives a minimum value for each channel and allows different designs to be evaluated according to the methods described in chapter 3.

At 5 and 6µLh^{-1}, the dominant conformation type is folded molecules which represent over 70% of observed strands. Even at these low flow rates, close to 20%

of the strands are stretched close to the contour length. For all flow rates measured the proportion of coiled molecules was less than 6%: at 5μLh^{-1} the minimum value of Wi in the channel is modelled as 7.3, indicating that the flow is sufficient to perturb the coiled strand which explains the low count of coiled molecules. At higher flow rates, the proportion of stretched molecules increases as the proportion of folded molecules decreases; there is a crossover point around 8μLh^{-1} (Wi_{min} = 12) where the proportion of stretched and folded molecules is approximately equal. At flow rates of 10μLh^{-1} (Wi_{min} = 15) and greater, the proportion of stretched molecules is consistently greater than either of the other conformations with stretched molecules representing more than 55% of all observed strands at the highest flow rates.

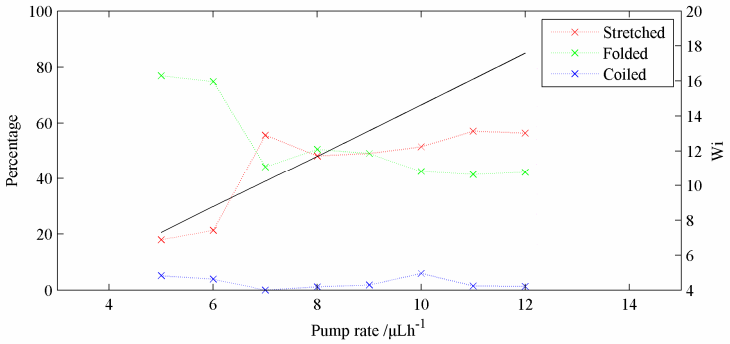

Figure 136, proportions of each apparent conformation for the serpentine channel based on data from the POPO-3 experiments (543nm source). The black line shows the maximum value of Wi measured 50nm from the central streamline.

Comparing figure 136 to figure 132, the proportion of each conformation is more stable and the trends as the pump rate is increased are more consistent. This is in agreement with the hypothesis that strands in the control channel stretch and tumble towards the funnel entrance in a way that is weakly affected by the shear rate in the parallel-walled preconditioning part of the channel, while for the serpentine channel the higher shear rate in the preconditioning section presents a higher proportion of elongated and/or axially aligned strands to the funnel.

Figure 137 shows the proportions of each conformation in the three-part classification for the narrowing-serpentine preconditioning channel design as

measured from the TOTO-3 (633nm excitation source) experiments. As the pump rate increases from 8-12μLh^{-1} the proportion of coiled molecules steadily decreases although the minimum of around 15% is much greater than that observed in the serpentine channel. Between 10 and 14μLh^{-1}, the proportions of stretched and folded molecules are similar. At these flow rates the modelled value of Wi is between 7 and 10: the approximately equal proportion of stretched and folded molecules is therefore comparable with the serpentine channel when the deforming strength of the flow is similar (although the proportion of coiled molecules is less in the serpentine case). In light of this comparison, is appears that the lower minimum width of the narrowing-serpentine channel is not capable of improving overall stretching performance by reducing tumbling in one plane. Indeed, the narrower regions which increase the flow velocity and thereby reduce the minimum Wi appear to limit stretching performance. In comparison to the corresponding control channel experiments however, the narrowing-serpentine channel clearly shows an improvement in both the proportion of stretched molecules detected and in the reduction of coiled molecules detected.

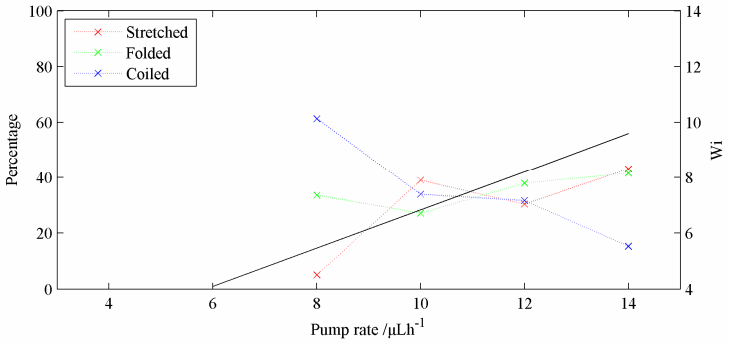

Figure 137, proportions of each apparent conformation for the narrowing-serpentine channel based on data from the TOTO-3 experiments (633nm source). The black line shows the maximum value of Wi measured 50nm from the central streamline.

The serpentine preconditioning channel produces a minimum value of Wi which is capable of favourably deforming the DNA conformation at higher flow rates and as such significantly outperformed the narrowing-serpentine channel as well as the control case. The importance of a suitable preconditioning channel in these devices is illustrated by figure 138: the increased value of De at higher flow rates is of

limited use in production a high proportion of stretched molecules and the main increase in stretching performance is expected to come from the increased shear rate as the pump rate is increased. Figure 138 shows the proportion of stretched molecules observed in the control devices (red traces) and serpentine channels (blue traces) as a function of De. Although the control devices show some improvement in performance as De increases, changes of De ±100 can have little effect. The same is true of each type of serpentine device, although the overall performance is better due to the preconditioning stage.

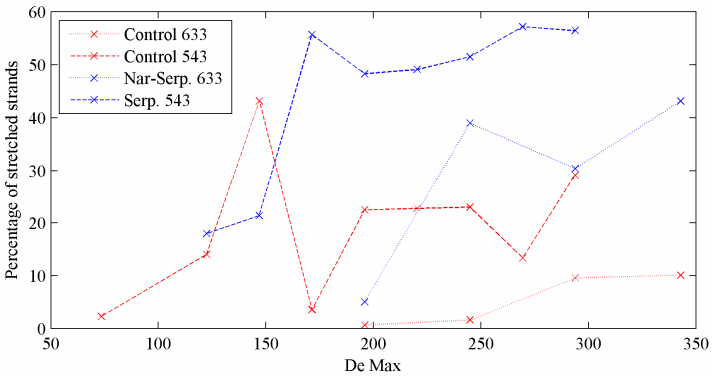

Figure 138, proportion of stretched molecules as a function of the peak De in the funnel; the results from control devices are shown in red, the results from the serpentine and narrowing-serpentine in blue. The results using TOTO-3 (633nm source) are shown with dotted lines; those using POPO-r (543nm source) are shown with dashed lines.

The critical dependence of stretching on the Weissenberg number may be observed from figure 139 and figure 140. Despite the differences between the experiments using TOTO-3 as the DNA stain and those using POPO-3, the trends on these two figures are broadly comparably between the two sets of results. The main difference between the two experiments using control chips (figure 139) is that the TOTO-3 results (dotted lines) show a higher proportion of coiled molecules and a lower proportion of stretched molecules at the corresponding shear rates.

Figure 140 highlights the fact that although the TOTO-3 experiments (narrowing-serpentine channel) included a higher flow rate (of 14μLh^{-1}), the Weissenberg number for these experiments was at the low end of the range applied in the POPO-3 experiments using the serpentine channel. For the way that the Weissenberg number

is generated in the modelling described in section 3.4, there appear to be two critical values for the preconditioning channels. Around *Wi*=10 the proportion of coiled molecules is significantly low and the proportion of stretched and folded molecules appears to be similar. Above *Wi*=14 there is a clear separation between the folded and stretched molecules, with the stretched molecules the most common.

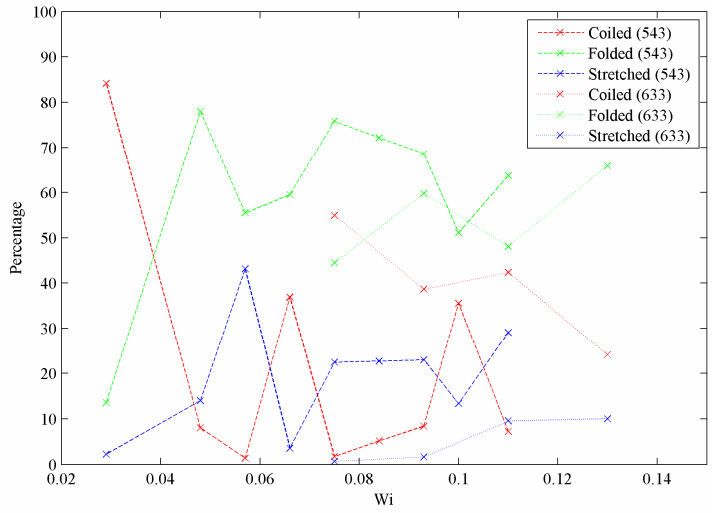

Figure 139, percentage of each conformation type as a function of maximum Wi on the central streamline for the control channels. The results for the experiments with each dye are shown separately: TOTO-3 (633nm excitation source) results are shown with dotted lines; POPO-3 (543nm source) results are shown with dashed lines.

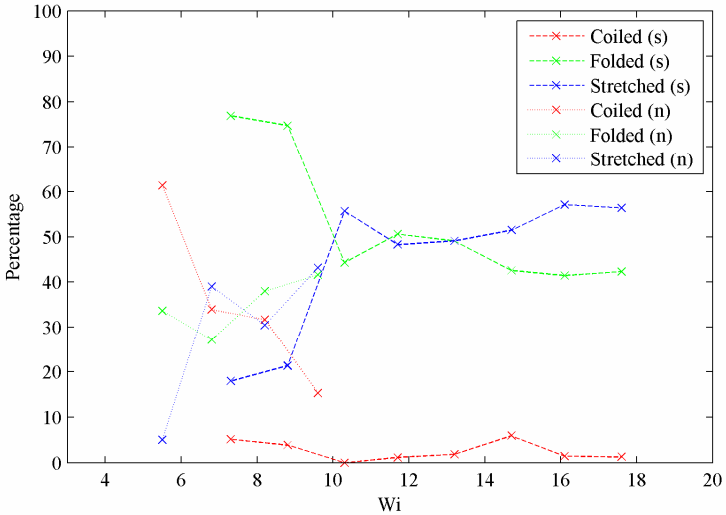

Figure 140, percentage of each conformation as a function of maximum Wi on a central streamline for the serpentine (dashed lines) and narrowing-serpentine (dotted lines) channels.

6.7.8 Conformation Classification by Intensity

An alternative method of investigating the apparent observed conformations would be to use the intensity data to search for regions of the detected molecules which were more folded. It is known, for example, that there are several typical conformations which occur for DNA molecules partially stretched by an extensional flow as described in section 2.3, figure 10 [24].

Some calculations were made to investigate the possibility of such an alternative classification scheme; however the fidelity of the photon burst data was not sufficient for such analysis. For example, to identify folded molecules corresponding to the half-dumbbell conformation, burst data were extracted in which the mean photon count for one half of the strand was different to the mean count for the other half by more than one standard deviation. However, the population of strands thus extracted did not correspond to the proportion measured by strand length. Also, the proportion of 'folded' molecules measured by this method did not show any correlation to changes in flow rate. Finally, at the flow rates showing the most promising results, molecules occupy relatively few time bins and thus the intensity-representation of each strand is coarse, which makes identifying individual features on a strand challenging. In order to pursue this investigation therefore, any future work would need to improve the temporal resolution of the measurement system. This is possible by using higher NA objectives for a more tightly focussed observation volume; the two spot detection system described in section 6.7.9.5 would also aid in improving length measurements.

6.7.9 Molecular Length Analysis using Skew-Normal Fits

6.7.9.1 POPO-3 Stained λ-DNA Experiments

Histograms fitted with skew-normal probability density functions – as described in section 6.5.10 – for results from the POPO-3 stained DNA experiments are shown below to allow a direct visual comparison (ordered by pump rate, PR, in μLh^{-1}). The parameters obtained from the fits are subsequently discussed and are listed in table 15 (control) and table 16 (serpentine). In general a skew-normal fit was readily obtained, however the coarse discretisation of the length data can present a challenge

when fitting a continuous-type distribution. This is more often a problem at the higher flow rates where the discretisation is most coarse-grained, as seen in section 6.7.9.2.

PR	Control	Serpentine
3	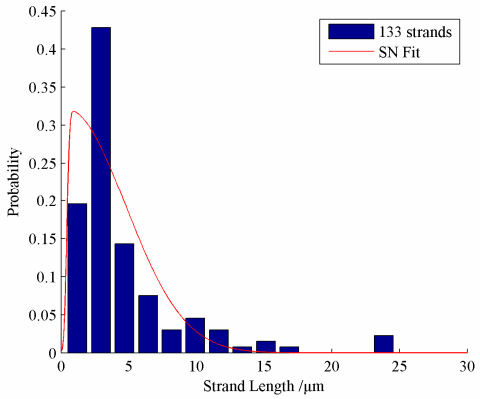	
5	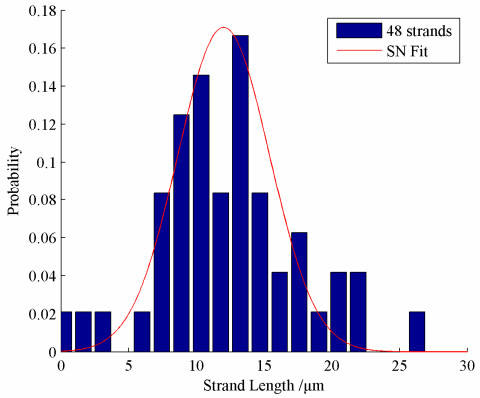	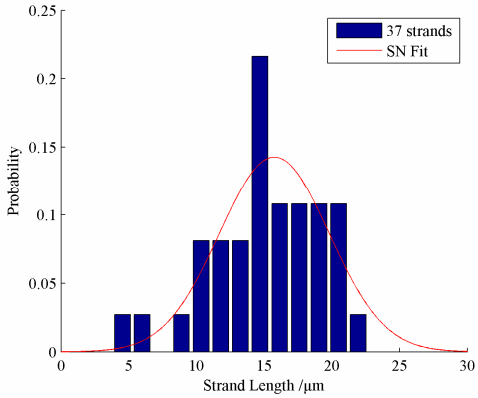
6	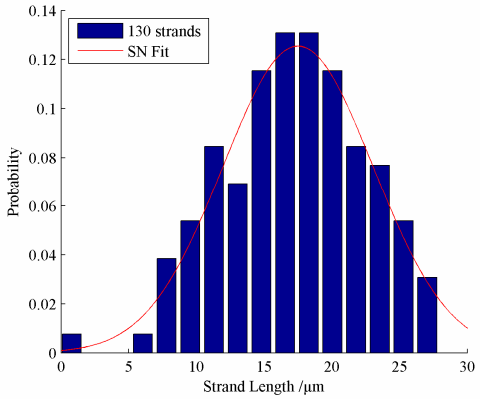	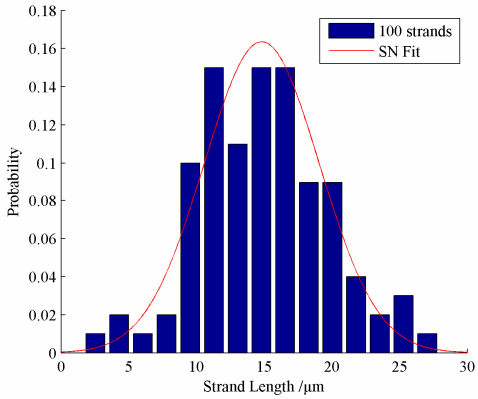

7

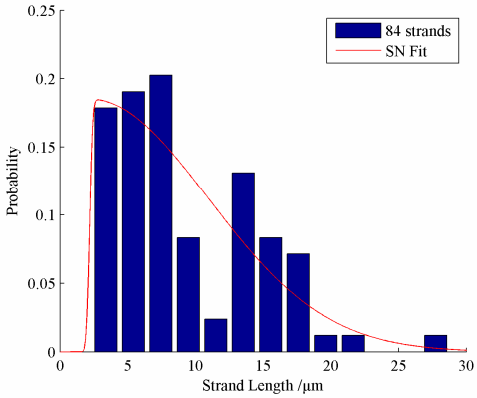
84 strands
SN Fit
Probability
Strand Length /µm

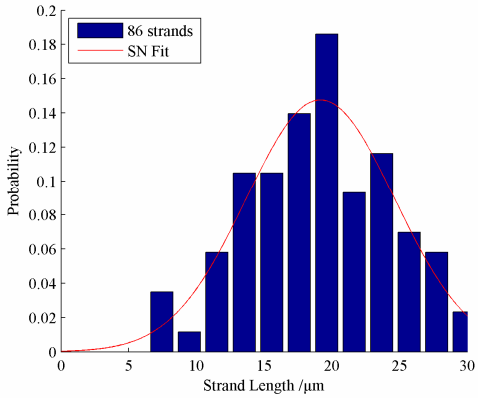
86 strands
SN Fit
Probability
Strand Length /µm

8

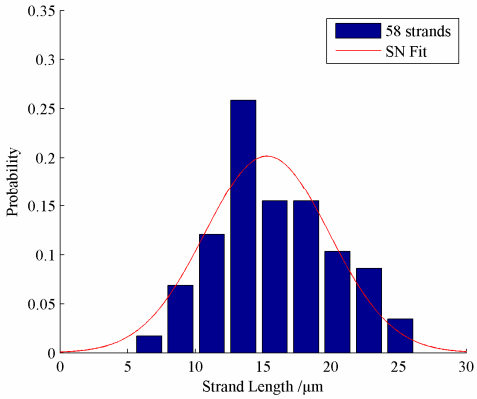
58 strands
SN Fit
Probability
Strand Length /µm

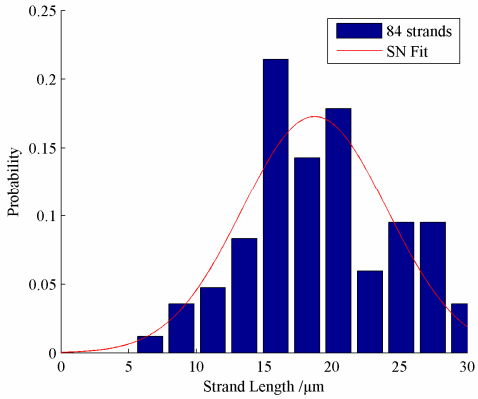
84 strands
SN Fit
Probability
Strand Length /µm

9

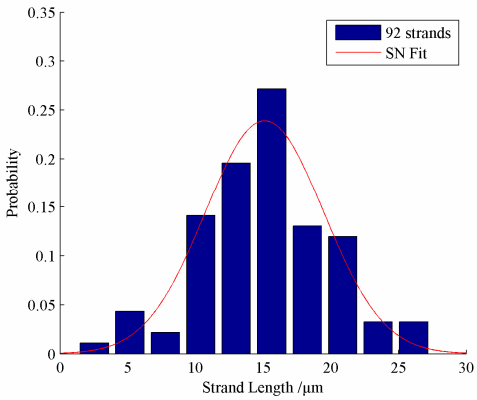
92 strands
SN Fit
Probability
Strand Length /µm

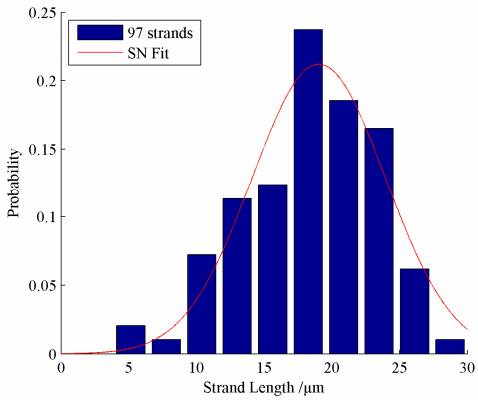
97 strands
SN Fit
Probability
Strand Length /µm

10

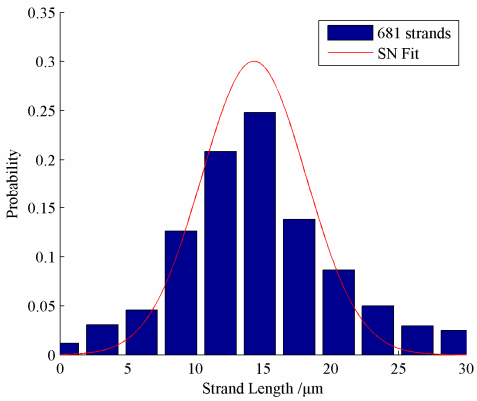
681 strands
SN Fit
Probability
Strand Length /µm

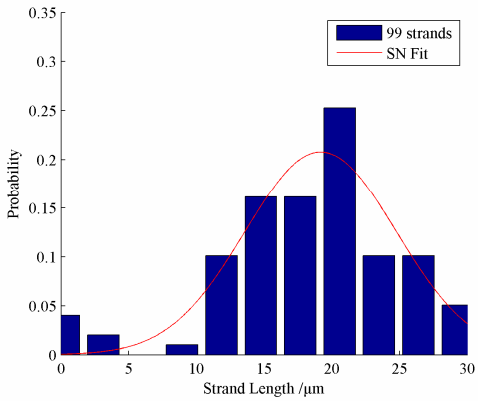
99 strands
SN Fit
Probability
Strand Length /µm

11

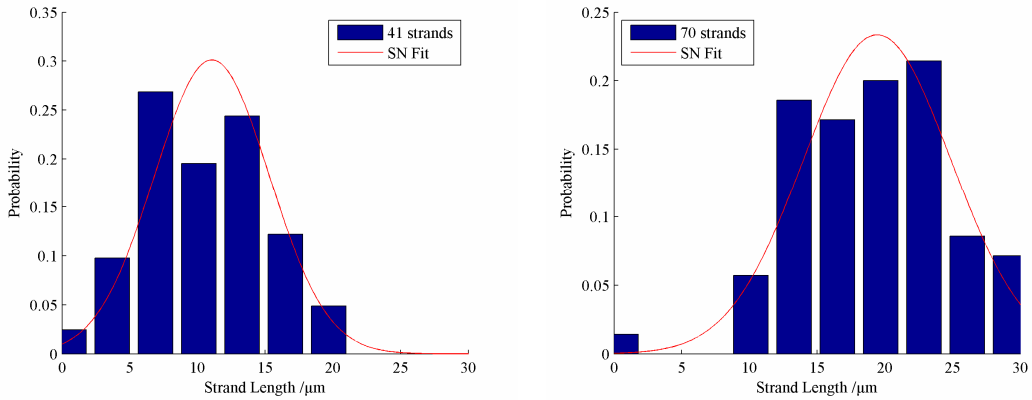

12

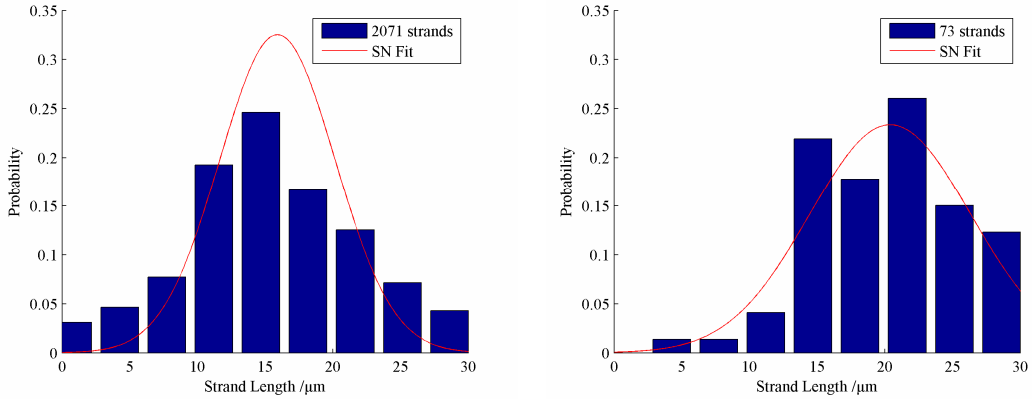

The confidence estimate ('Conf.') given in table 9 and table 10 is based on three factors that indicate a poor fit or low quality data: (i) a skew of greater than 0.95, (ii) a total error of greater than 0.011 in the least-squares fitting process and (iii) a total number of detected strands less than fifty. If two or three of these conditions are met the confidence is given as 'Low', if one of the conditions is met the confidence is 'Medium' and if none of the conditions are met the confidence is 'High'.

Skew (γ_1) has a maximum of around ±0.995; the skew evaluates to zero where the shape parameter (α) is also zero, i.e. the distribution is normal. As the skew tends to zero, the mean and location variables tend to coincide. For normal distributions, the mean and standard deviation of the data are sufficient for analysis – the former corresponds to the location parameter in this case (see, for example, table 15). For a skewed-normal, the location parameter does not correspond to the mean and both the location and skew of the fit must be considered to understand the distribution. However, the plots showing a skewed fit to experimental data show extreme values of skew, which is one of the factors that lead to the low confidence in their

reliability. In the general case a Gaussian distribution would be expected around some underlying mean molecular extension and hence the very low values of skew in most cases give confidence that the fitted curve is adequate.

Pump Rate (μLh^{-1})	Location	Scale	Shape	Mean (µm)	Std. Dev. (µm)	Skew	Conf.
3	0.43	4.33	27.42	3.88	2.61	0.9898	Low
5	11.98	3.38	0.0089	12.01	3.38	$1.52x10^{-7}$	Low
6	17.46	5.57	0.0089	17.50	5.57	$1.53x10^{-7}$	High
7	2.19	8.75	48.69	9.17	5.28	0.9935	Low
8	15.25	4.59	0.0089	15.28	4.59	$1.53x10^{-7}$	Med
9	15.07	4.37	0.0089	15.10	4.37	$1.53x10^{-7}$	High
10	14.29	3.87	0.0089	14.32	3.87	$1.51x10^{-7}$	High
11	11.03	4.24	0.0088	11.06	4.24	$1.50x10^{-7}$	Med
12	15.87	4.27	0.0088	15.90	4.27	$1.51x10^{-7}$	High

Table 15, skew-normal fit parameters for control channel experiments (POPO-3 stained DNA). The parameters for 3, 5 and 7μLh^{-1} are greyed out as the extreme values resulting from the fitting process makes confidence in these values low.

Pump Rate (μLh^{-1})	Location	Scale	Shape	Mean (µm)	Std. Dev. (µm)	Skew	Conf.
5	15.72	4.06	0.0089	15.75	4.06	$1.53x10^{-7}$	Low
6	14.79	4.27	0.0089	14.82	4.27	$1.53x10^{-7}$	High
7	19.11	5.49	0.0089	19.15	5.49	$1.53x10^{-7}$	High
8	18.69	5.36	0.0089	18.72	5.36	$1.53x10^{-07}$	Med
9	19.00	4.93	0.0089	19.03	4.93	$1.53x10^{-7}$	High
10	19.13	5.59	0.0089	19.17	5.59	$1.53x10^{-7}$	High
11	19.39	5.47	0.0089	19.43	5.47	$1.53x10^{-7}$	High
12	20.35	5.94	0.0089	20.34	5.94	$1.53x10^{-7}$	High

Table 16, skew-normal fit parameters for serpentine channel experiments (POPO-3 stained DNA). The parameters for 5μLh^{-1} are greyed out due to low confidence.

The mean nominal strand length for the POPO-3 experiments is plotted in figure 141. The serpentine channel gives a more stable trace which reaches a maximum of 20µm at 12µLh^{-1}. The 3µLh^{-1} point for the control channel could indicate that this flow rate was too low to generate significant stretching in the elongational flow funnel, although this cannot be implied solely from the fit parameters due to the low confidence in the highly skewed fit in this case.

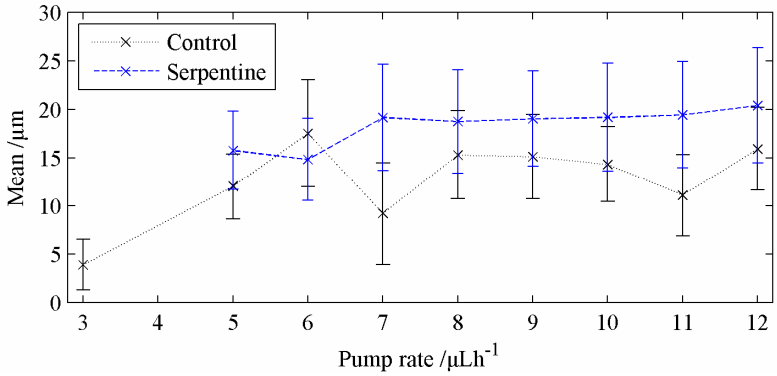

Figure 141, mean strand lengths for POPO-3 experiments with error bars showing the standard deviation.

At 8µLh^{-1} and above, the mean nominal strand length generated by the control channel appears to stabilise at around 15µm. The small sample size (41 strands) seems the most likely explanation for the dip observed at 11µLh^{-1}, although more experimental data would be required to confirm this hypothesis. At 12µLh^{-1} – which appears to be the flow rate which generated the best performance in the serpentine channel – the mean length in the serpentine channel was 4.5µm greater than that in the control channel. The standard deviation at this point is 5.9µm for the serpentine experiment. Although the performance of the serpentine channel is never a whole standard deviation better than the control channel, the serpentine is consistently the best performing channel of the two above 7µLh^{-1}. Additional data could therefore potentially increase the accuracy of these measurements and the serpentine channel may generate a mean strand length that is greater than that of the control channel by more than one standard deviation.

6.7.9.2 TOTO-3 Stained λ-DNA Experiments

Histograms fitted with skew-normal probability density functions for results from the TOTO-3 stained DNA experiments are shown below to allow a direct visual comparison (ordered by pump rate, PR, in μLh^{-1}).

PR	Control	Narrowing Serpentine
8	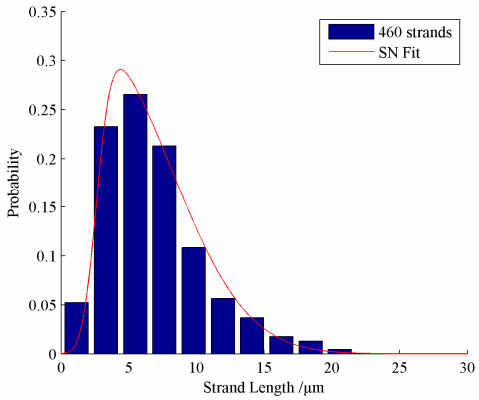	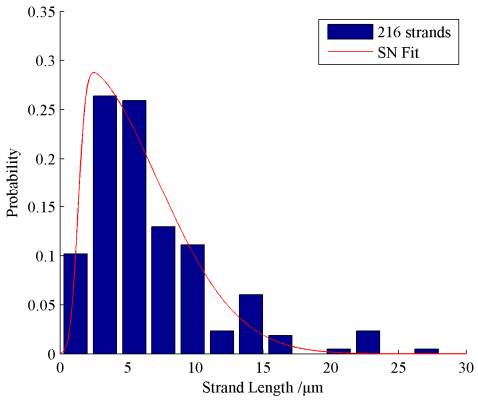
10	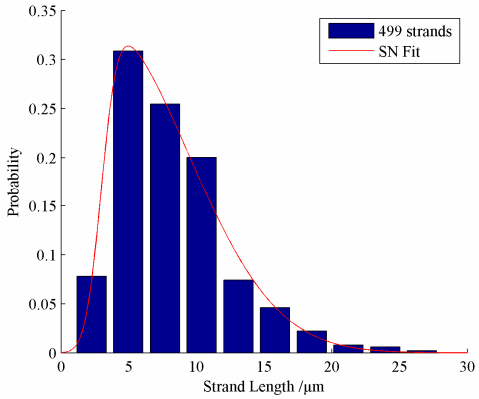	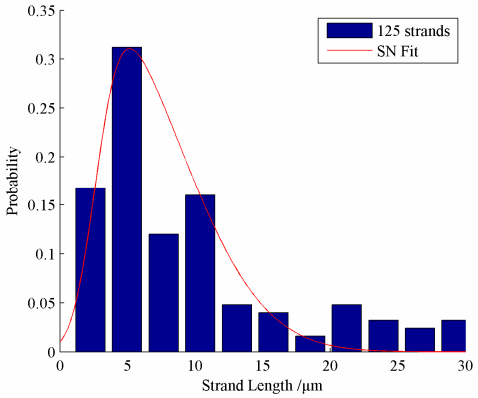
12	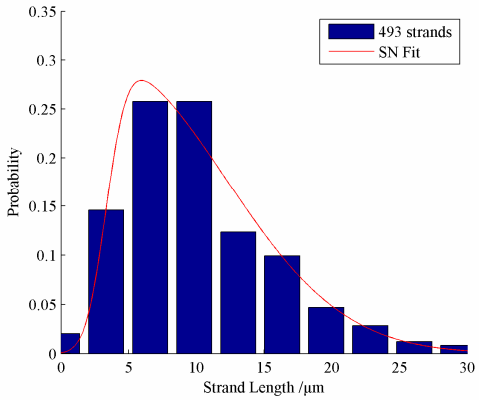	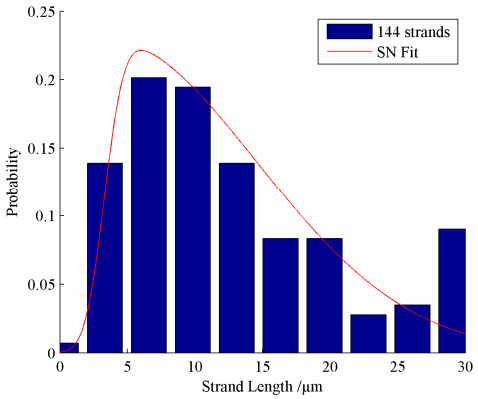

14

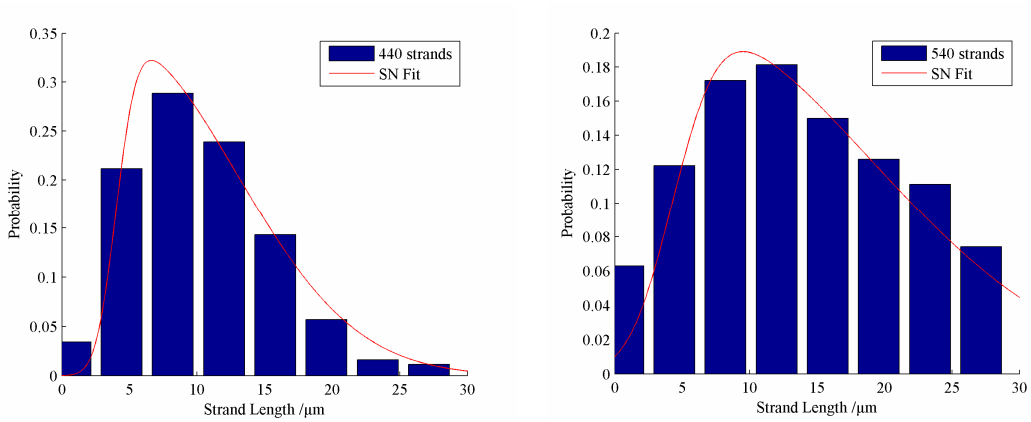

These fits are all more skewed than those obtained for the POPO-3 experiments, although with the exception of the narrowing-serpentine channel at 10 and 12µLh^{-1} they appear to follow the data adequately. As seen in table 17, the mean strand lengths measured in these experiments were generally lower than those of the POPO-3 experiments; hence the control channel experiments were repeated to provide a comparable baseline.

Pump Rate (µLh^{-1})	Location	Scale	Shape	Mean (µm)	Std. Dev. (µm)	Skew	Conf.
Control							
8	2.62	5.53	6.57	6.99	3.40	0.9071	High
10	2.97	6.46	6.86	8.07	3.96	0.9139	High
12	3.34	8.74	7.20	10.25	5.36	0.9209	High
14	4.03	8.86	7.41	11.03	5.42	0.9249	High
N-Serp.							
8	1.33	5.84	12.80	5.98	3.54	0.9707	Med
10	2.67	6.15	4.28	7.45	3.87	0.8071	High
12	3.30	11.27	9.83	12.25	6.86	0.9542	High
14	4.36	14.63	5.50	15.85	9.06	0.8732	High

Table 17, skew-normal fit parameters for control channel experiments (first four rows) and narrowing-serpentine channel experiments (last four rows) using TOTO-3 stained DNA.

While the control channel appears to produce results that area consistently skewed toward shorter strand lengths, the narrowing-serpentine channel shows more variation in such fitting parameters. This is apparent not least in the more steeply increasing mean strand length as is highlighted in figure 142. However, in the case of the TOTO-3 experiments, the large standard deviation in the fitted skew-normal distribution makes the performance difference between the control channel and the narrowing-serpentine channel more difficult to identify. Nevertheless it appears that the narrowing-serpentine does not offer a significant improvement in molecular extension performance over the control channel in the way that the serpentine channel does. This supports the hypothesis developed in chapter 3 that the Weissenberg number is the key design criterion in predicting preconditioning channel performance.

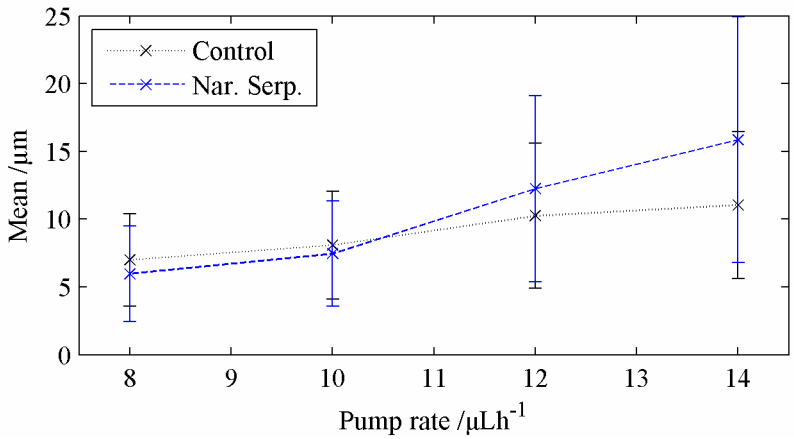

Figure 142, mean strand lengths for TOTO-3 experiments with error bars showing the standard deviation.

6.7.9.3 Comparison of TOTO-3 and POPO-3 Results by Weissenberg Number

The Weissenberg number (Wi) is simply the shear rate scaled by the characteristic relaxation time of the polymer in question (in this case λ-DNA) to produce a dimensionless quantity that describes the deforming strength of the flow on the scale of the molecule of interest. Thus measured, the serpentine channel produces a (modelled) deforming flow of twice the strength of the narrowing-serpentine channel at the equivalent flow rate. In a parallel-walled channel, the Weissenberg number can be increased by increasing the flow rate and hence the fractional molecular extension increases (*cf.*, [22] figure 4). However, with the serpentine channel, the

Weissenberg number and hence molecular extension are larger than the parallel walled case for the same flow rate.

Although a separation of approximately one standard deviation emerges between the serpentine and control channels in figure 141, the same is not true for the narrowing serpentine and the control as observed in figure 142. Two explanations for this are: (i) the larger variation in the Weissenberg number in the serpentine channel makes its benefits over the control more apparent and, (ii) the larger standard deviations seen for the narrowing serpentine. The control channel in the TOTO-3 experiments did not exhibit similarly large standard deviations and the photon count binning and pulse detection was the same for both the POPO-3 and TOTO-3 experiments, suggesting the performance of the narrowing serpentine channel was genuinely worse than the serpentine channel.

Having fitted (in most cases) a normal distribution to the data, the plots of figure 139 and figure 140 may be re-examined. The fitting process suggests that the results at $5\mu Lh^{-1}$ are questionable for the POPO-3 experiments and hence these points should not be relied upon. However, the conclusion that above $Wi=14$ the serpentine channel shows an increase in the proportion of molecules classified as stretched remains valid. Considering figure 140, given that the results from the narrowing serpentine channel show no discernible difference in folded and stretched conformations and that the $5\mu Lh^{-1}$ points for the serpentine channel are questionable, it appears safer to conclude that the difference in the population of folded and stretched molecules can only be identified for $Wi>14$.

Similarly for the control channel in figure 139, if the points representing $3\mu Lh^{-1}$ and $5\mu Lh^{-1}$ are discounted (at $Wi\sim0.03$ and $Wi\sim0.05$), it appears that for the POPO-3 experiments, there is a distribution around a length classified as folded, with some fluctuation around the edges of the distribution causing molecules to be classified as coiled or stretched. For the TOTO-3 experiments, similar results are seen for the proportion of folded molecules but the count of coiled molecules is much higher than that of stretched. This is at least in part due to the fact that the lengths measured in the TOTO-3 experiments were distributed around a lower mean (*cf.* table 15 and

table 17) and since the limits of the classification scheme are fixed, more strands are classified as coiled.

The results of figure 139 and figure 140 are therefore in agreement with the results of the data-fitting; that there is a distribution around some mean value in the control channels and that by the application of a high Weissenberg number preconditioning channel, this distribution may be shifted to a higher mean value. This higher mean allows a majority of detected molecules to be classified as stretched and therefore useful for further analysis.

6.7.9.4 Evaluation of Fitting Results

The skew-normal distributions fitted to the molecular length data support two main conclusions. Firstly the serpentine channel, which is arguably the best design whether considering the modelling results of section 3.4 or looking more simplistically at the length data, is shown to outperform the control case by almost one standard deviation. Secondly, despite the application of higher flow rates in the narrowing serpentine device, this channel did not exhibit similar performance advantages to those seen using the standard serpentine channel. The higher Weissenberg numbers generated by the serpentine channel therefore appear to be the factor most likely to indicate that a channel will extend passing DNA strands.

In some cases, skew-normal fitting produced poor results. While the expectation of an underlying Gaussian distribution around some mean value of nominal length remains unchanged, it is possible that another fit may reveal some other distribution within the data. Since some of the histograms discussed in previous sections appear to have a second peak, the possibility of a two-Gaussian curve fitting the data was investigated. The following histograms demonstrate how in some cases this mixture of two Gaussians appears a much better fit to the experimental data, particularly in the case of the POPO-3 experiments with the control channel for pump rates of 3 and $7\mu Lh^{-1}$ which showed the poorest results when fitting with a skew-normal.

PR	Control	Serpentine
3	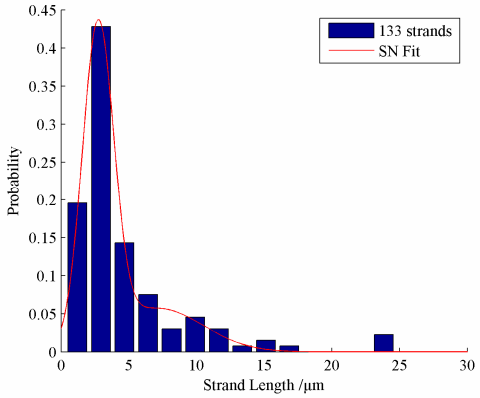	
7	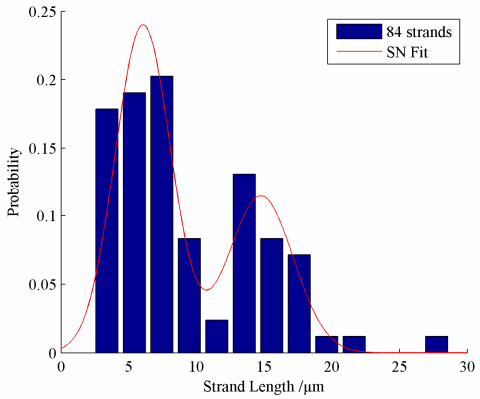	
11	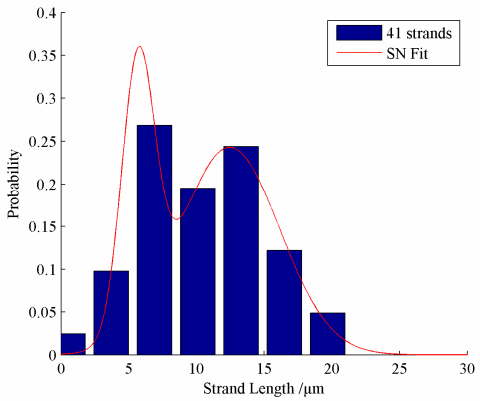	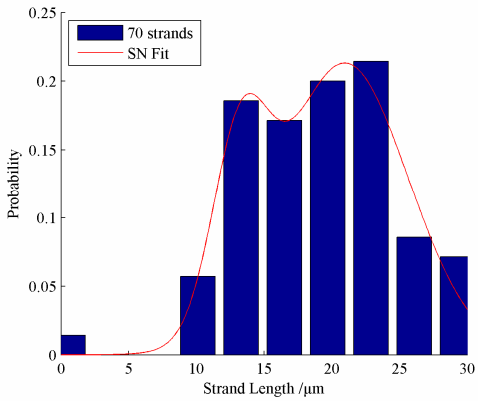
12	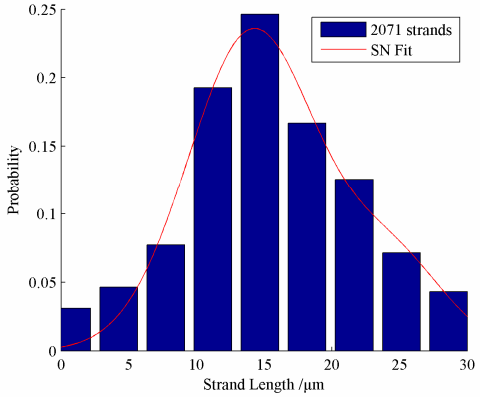	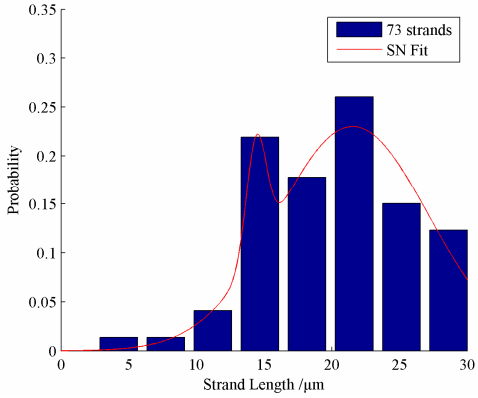

The different means of each two-Gaussian fit are given in table 18. Judging by the sum of the least-squares errors used in the fitting process, the two-Gaussian fit is a much better match to the data for the control channel at 3 and 7μLh^{-1}. Although a visual inspection confirms the quality of the fit, it may not be valid in all cases. The fit for the control channel at 12μLh^{-1} for example, appears to be an over-complication of a simple Gaussian distribution. For the serpentine channel at the same flow rate it is difficult to distinguish between whether the data has an underlying single or double Gaussian distribution due to the coarseness of the histogram binning (which itself is a necessary consequence of the measurement setup).

Channel	**Pump Rate (μLh^{-1})**	**Mean 1 (μm)**	**Mean 2 (μm)**
Control	3	2.73	7.14
Control	7	6.05	14.75
Control	11	5.68	12.45
Control	12	14.17	24.58
Serpentine	11	13.18	20.96
Serpentine	12	14.42	21.54

Table 18, mean values for two-Gaussian fits for control and serpentine channel experiments using POPO-3 stained DNA.

Table 18 appears to suggest that at the higher flow rates there could be a mixed distribution of molecules with a nominal length close to the unstained contour length (16.49μm) and those with a length close to the stained contour length (22μm). However, only three histogram bins cover this range so from the data presented here is it not possible to establish whether this conclusion would be accurate.

6.7.9.5 Evaluation of Measurement System

The limitations of the measurement system used here are apparent for example in figure 114. As the pump rate increases each strand is in the excitation volume for less time and because the binning time is fixed (at 0.1ms) therefore appears in fewer

bins. The total length measurement is made up of segments inferred from each bin and therefore the accuracy decreases as the pump rate increases. However, the adequacy of the measurement is apparent from two features of the results obtained. Firstly, the threshold detection system means that although a short one-bin strand and a longer one bin strand would be reported as being the same length, they are both still captured as valid strands. Therefore if there were a great many short strands in a high pump rate sample, this would show up as a high probability at the shortest discernible length. Considering the high pump rate graphs such as figure 118 this does not appear to be the case. Secondly, the fixed width serpentine preconditioning channel consistently outperforms the control case at pump rates of $7\mu Lh^{-1}$ and greater; this consistency would be masked if the measurement inaccuracy was significant.

While the methodology described in this chapter was sufficient to describe the improved preconditioning offered by the serpentine channel, there are options available to improve these measurements in future work. Simply repeating some of the higher flow rate experiments for the serpentine channel would add confidence to the above conclusions. Also, while the data quality was sufficient in most cases to generate a continuous skew-normal fit, the discretisation of length data could be improved. A modestly improved FPGA would provide the opportunity to decrease the size of the time bins and hence increase the available data quality and the applicability of the fitting process. Ultimately, for a practical application it is necessary to detect a greater proportion of the input DNA in each sample. Hence while small improvements to the experiments described here can be made for differential analysis between channel designs, an improvement in the overall detection rate would be a more valuable direction for further work.

The fidelity of the measurement system (as illustrated by the calculations in sections 6.5.8 and 6.5.9) is the limiting factor in drawing further conclusions about the DNA conformation/orientation from the data presented in this chapter. While this system (as described in section 6.5.2) could be improved by the use of a superior FPGA and a shorter binning time, more advanced detection systems have been reported such as that described by Larson *et al.* [22]. The Larson system (as illustrated in figure 89) uses two smaller detection volumes, defined by a high-N.A. objective, separated

axially within the detection channel by a short distance (e.g. 28μm). Using this method, more information is collected about each detection event. Two traces are collected for each DNA strand since it emits a photon burst as it travels through each detection volume. As the separation between the detection volumes is known, the time difference between the centre of each burst may be used to calculate the speed at which the molecule is travelling. The length estimate is therefore directly calibrated rather than relying on an average velocity through a single detection volume.

The smaller detection volumes defined by the higher-N.A. objective also give the system a superior signal to noise ratio. This allows the use of shorter time bins for photon counting and hence increased fidelity in length measurement, but also allows the possibility of assessing molecular conformation by the variation in burst size along the length of each strand. Hence by 'comet plots' (e.g. figure 91) the degree of folding in a strand can be identified. A further benefit is that single error events can be removed by only analysing data from bursts that apparently show the same strand passing through both detection volumes. The main drawback of this system is that the small confocal detection volumes cannot be easily scaled up and the design of the microfluidic detection channel (and thereby to some extent the rest of the device) is thus restricted if they are to sample a reasonable proportion of the passing molecules.

6.8 Discussion

The results presented in this chapter demonstrate the efficacy of both the sloped world-to-chip interconnects and the preconditioning channel designs. The fabricated interconnects were shown to have an efficiency of 95±7% for loading and unloading λ-DNA molecules to and from a microfluidic device, much greater than the 56±16% of the control interconnect with a step change in channel depth. Indeed, the sloped interconnects performed comparably with the control setup featuring no microfluidic device. The preconditioning channel designs demonstrate a new method of DNA extension in mixed shear and elongational flow. This method provides a material improvement in the efficiency of microfluidic DNA stretching.

6.8.1 Interconnect Performance

Lambda-phage DNA of contour length 16.5µm was successfully loaded into a microfluidic device, passed through a channel of 5µm width and collected at the outlet. Efficient loading of long biopolymers to microfluidic systems is not trivial but was achieved by connecting from world-to-chip in the plane of the microfluidic channels and using a slope rather than a large vertical step to accomplish the necessary change in channel depth.

The loss of DNA relative to the no-chip control experiment is assumed to be primarily a result of non-specific adsorption of DNA to the interior channel surfaces. Damage to the DNA strands due to the higher fluid acceleration in the stepped connection is assumed to be negligible relative to the accuracy of the qPCR method. This is because the PCR amplicon represents ~1% of the length of each λ-DNA strand and a break would have to occur in this region to affect the PCR results. As it is necessary for the capillary groove to be wider than the capillary itself, there is typically some fluid around the outside of the capillary which is assumed to be dead volume, however it is possible that some strands could reach this area and not be collected at the output. Although the error in the qPCR measurements is large, they proved to be sufficient to observe the benefits of the sloped connection. For any practical application the intention would be to use a low concentration of input DNA and not to stain the entire length of each molecule. qPCR therefore represents a suitable compromise for measuring low concentrations of unstained DNA.

Overall the sloped connection performed well, but improvements could be made with further refinement of the fabrication process. The least reliable fabrication step is the vertical alignment of each section of the chip. Adding a capillary-housing recess to the borosilicate wafer would complicate fabrication in that it would require alignment at the wafer bonding stage. However this would allow further reduction of dead volume and could eliminate the need for a two-step slope fabrication process as the depth change required in the silicon channel would be smaller.

6.8.2 Preconditioning Channel Performance

Preconditioning of strands is a key factor in effective microfluidic DNA extension of molecules free in solution [25]. The devices described above demonstrate preconditioning of individual molecules in microfluidic channels that are relatively large and are thus less liable to biofouling and more suitable for high throughput applications than channels with smaller dimensions. Two different channel designs of serpentine-like geometry were shown to consistently deliver a higher proportion of DNA strands stretched to at least the unstained contour length and therefore suitable for genomic analysis applications. The serpentine channel was found to have the most positive effect on DNA preconditioning, with both the highest measured mean strand length and a normal distribution of molecules close to the stained contour length at higher flow rates.

The fluidic taper is sufficient to demonstrate DNA stretching in the control case, in which the only preconditioning comes from the shearing effect of the laminar flow profile. Where the flow rate is high enough for the taper to generate significant DNA stretching, the preconditioning channel designs (upstream of the taper) offer consistently improved stretching efficiencies. The proportion of strands reaching contour length is increased by the application of a serpentine preconditioning channel which would allow greater efficiency in DNA mapping applications.

The device with the serpentine preconditioning channel generated 57% stretched molecules (considered to be useful for genomic analysis applications) at $11\mu Lh^{-1}$ and 56% at $12\mu Lh^{-1}$. Devices reported elsewhere with similar funnels in the elongational flow region have generated 55% stretched molecules (also using λ-DNA), although these channels had a depth of just 1μm [19]. Such devices have already been demonstrated in practical genomic mapping applications [23]. Matching this result with a larger channel allows realisation of the benefits of both DNA elongation and the world-to-chip connectivity in a single device and hence the designs demonstrated in this chapter are directly applicable to genomic analysis applications.

The Weissenberg number proved to be an adequate figure of merit for assessing different designs at the simulation stage and the device with the highest simulated

Weissenberg number (serpentine channel) demonstrated the best preconditioning performance. Using the method described in this chapter, a critical value of Wi=14 appears to be sufficient to generate a majority of stretched molecules. This value has little physical significance as it represents only a simplistic sampling of the flow in the channel; however as the method aims to measure the minimum value of Wi within the channel it does provide some guidance for channel design. The Deborah number is retrospectively useful to aid the design of similar systems, although at the simulation stage the short residence time in the funnel makes it difficult to define a critical value [70].

Overall the system exhibited low loss of DNA, was sensitive enough to detect single strands at low input concentrations and improvements to the preconditioning of DNA strands for stretching by fluid acceleration in a taper were demonstrated.

Chapter 7 Conclusions and Future Work

7.1 Conclusions

The design and fabrication of both a high efficiency connection from world to chip and microfluidic channels provides a new method of preparing DNA molecules for fluidic elongation. This combination offers the potential to help realise some of the key benefits of miniaturised molecular DNA analysis.

Interconnects are of critical importance to lab on a chip applications because loss of sample not only reduces experimental efficiency but also limits device reuse. The sensitivity gains that are offered by reduced device dimensions can only be fully realised with robust and efficient sample loading. As such, the sloped interconnect that has been developed in this work is a key piece of enabling technology for rare-molecule detection. Loading a long polymer into a microfluidic system is more challenging than loading a small molecule and factors such as 90º turns become significant. Connecting to a microfluidic system with an in-plane capillary allows the fluid path to be smoother. The connection described here integrates a 125µm outer diameter capillary with a 30µm microfluidic channel for loading a DNA strand of at least 16µm contour length. The smallest dimension of the fluid path (which necessarily increases to house the outer diameter of the capillary) goes from 75µm, to 90µm, to 30µm over a distance of 800µm with a slope that is 560µm in length. This gradual change (average slope 7.6º) ensures there are no sharp turns or edges in the fluid path and is the critical factor in a DNA transit efficiency of 95±7% which is almost indistinguishable from the capillary control of 99±13% and much better than the stepped channel of 56±16%. Although the DRIE-lag method can produce additional surface roughness in some areas, no DNA strands were observed to adsorb to the sloped region of the interconnects where the roughness is greatest.

Despite being acknowledged as a limiting factor in microfluidic DNA stretching, little progress has been made in improving the preconditioning of molecules prior to stretching in elongational flow. It has been demonstrated in this thesis that improved preconditioning is possible using only fluidic interaction in channels that are much

larger than the DNA strands themselves. The preconditioning channels are 30µm deep and up to 60µm wide; the λ-DNA strands used in this study have a contour length of 16.5µm, width of 2nm, persistence length of 50nm and radius of gyration 0.7µm. In general, the risk of breaking DNA strands increases with any additional interaction with the surfaces of a device and as such it is beneficial to exploit the fluid interaction rather than relying on a solid structure such as a post array. Furthermore, as device dimensions decrease the difficulty of keeping them free of unwanted particles often increases. In genomic DNA analysis, the emphasis is often more on high throughput at sufficient resolution rather than absolute sensitivity. For these reasons a microfluidic, rather than nanofluidic, solution may be preferred for a given application.

Another advantage of a microfluidic system is that pressure-driven flow may be used, which simplifies device fabrication and allows reproducible flows to be generated using a standard laboratory syringe pump. As the devices described in this thesis are based on a continuous flow of buffer and temporally separated sample plugs, they are inherently applicable to high throughput applications. By contrast in a nanochannel, the DNA is typically loaded first into a microchannel and then a separate process is used to load the nanochannels, before immobilising the DNA for imaging (*cf.* [21]). There is a potential for sample loss at the nanochannel loading stage and typically only part of the DNA solution that is loaded into the microchannels is sampled by the nanochannels. The use of a microfluidic channel to load a nanochannel device also limits the savings in reagent use that could be made by the smaller device.

The stretching of free DNA molecules rather than those attached to microspheres or surfaces brings significant benefits because the reduced complexity both increases throughput and reduces the cost of each experiment. A microfluidic system which offers continuous operation on free strands of DNA is also more readily integrated into a micro total analysis system (µTAS). In this work, the smallest channel is 5µm wide and 20µm deep; the detection volume is $9.7 \times 10^{-17} m^3$. Detection of DNA flowing through a small, fixed detection volume has the advantage of not inherently generating any scalability issues for detection of longer molecules.

The final devices that were produced in this work have high-pressure tolerant world to chip connections for operation under continuous, pressure-driven flow that minimise loss of DNA at the interface. They contain innovative preconditioning channels as a complement to established methods of DNA stretching in elongational flow. Elongation of λ-DNA to its unstained contour length has been demonstrated using these devices and further optimisation of the channel geometry is available without compromising the benefits of a microfluidic system as described above.

World-to-chip interconnects designed specifically for loading long polymers to microfluidic systems are rarely reported and few solutions to the DNA preconditioning problem have been produced. As such this work represents a valuable contribution to microfluidic devices for the study of DNA and is of immediate utility to practical applications of direct linear analysis.

7.2 Proposed Future Work

Refinements to the devices described in this thesis should focus on integrating other elements of the experimental system. The silicon substrate gives the possibility of integrating a photodiode directly into the analysis channel and the glass capping layer is available for an upper capillary-housing recess or the integration of optical elements. Another option would be to combine the preconditioning channels with a hydrodynamic focussing device. This gives potentially improved confinement and positional control of the DNA at the point of optical interrogation. Further, since this removes the size constraint from the interrogation channel, components such as gold dish reflectors could be added to the channel base to improve collection of light emitted from fluorescent markers.

The resolution limits of the system described in this thesis stem from the size of the optical observation volume (and hence the number of base pairs that are observed in any single measurement) and the temporal resolution of variations in the photon count. A smaller interrogation channel and thinner capping layer would enable a higher NA lens to be used in the epi-fluorescent optical setup. This would enable an improvement in the signal to background ratio to be made as well as reducing the number of base pairs that are simultaneously in the detection region. The improved

signal to background ratio would also make shortening the time bins used for data collection feasible, thus improving resolution and permitting operation at higher flow rates.

The successful demonstration of DRIE-lag slopes in microfluidics means that they may be considered for a variety of other applications. One example would be gradient generators which are of interest for the study of cellular responses to chemical gradients and typically have some small features fabricated within a larger microfluidic channel [174].

An investigation into genomic mapping applications is of immediate interest and could be performed using the devices described here in their current form. An example application is detection of the chromosomal translocation t(14;18) which affects expression of the bcl-2 (B-cell lymphoma 2) gene, which in turn disrupts apoptotic activity. The bcl-2 gene normally exists on chromosome 18 (18q21) and produces a membrane protein, BCL-2 which is involved in the regulation of apoptosis [175]. The balance of heterodimers and homodimers of BCL-2 and a second protein, BAX (BCL-2 associated X protein), affects cell survival via a rheostat model – an excess of BAX homodimers promotes cell death while an excess of BCL-2 homodimers promotes cell survival [176]. The translocation t(14;18)(q32;q21) transfers all three exons of bcl-2 to the immunoglobulin heavy chain (IgH) locus on chromosome 14, resulting in over expression of BCL-2 and inhibition of programmed cell death [175, 177].

The BCL-2 / IgH rearrangement provides a good marker for follicular non-Hodgkin's lymphoma although it is present in a significant proportion of normal individuals [178]. Detection has been demonstrated by a variety of methods including PCR [179, 180] and FISH [181, 182]. The translocation is a good candidate for detection by direct linear DNA analysis because the breakpoint occurs in two well-defined regions around the bcl-2 gene. In 79% of cases the break occurs in the 'major breakpoint region', a 150bp section in an untranslated section of bcl-2; in many of the remaining cases the break occurs in the 'minor cluster region', a 500bp section 20kbp downstream of bcl-2 [175, 177]. The devices produced in this study could be applied to t(14;18) detection by extending the optical system for the

detection of two fluorescent dyes which would be used to mark each chromosome and thus identify single pieces of DNA containing genetic material from both chromosomes.

Appendix A Calibration Mask Design

Prior to producing the mask set for production of the final devices, it was necessary to make a thorough characterisation of the DRIE-lag effect for the system in use. Etch rates in DRIE are very sensitive to the machine conditions and can vary with time as well as due to the effects of previous samples. The STS ICP used for this work was used exclusively for silicon and silicon dioxide etching and therefore exhibited reasonable stability in etch rates from month to month. A machine-specific characterisation is still required however, for the basic etch rates and profiles as well as for the magnitude of the DRIE-lag effect.

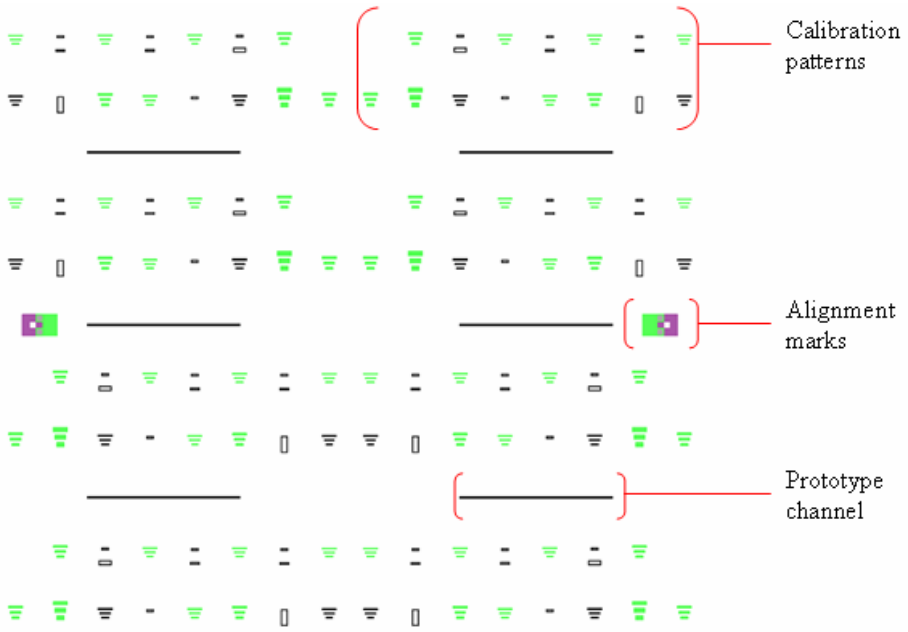

Figure 143, layout of the three layer mask design for DRIE-lag calibration patterns and prototype channels. The coloured regions indicate uncovered glass in the physical mask while the white areas indicate chrome.

The mask design for the characterisation processing is shown in figure 143. There are three layers to produce three physical masks; layer 1 is shown in blue, layer 2 in green and layer 3 in purple. There are three main elements in the design, alignment marks and windows, patterns for DRIE-lag calibration and prototype channels. Calibration wafers were produced using only the layer 2 mask; all three masks were then used to produce device wafers with entire prototype chips. Layer 1 consists of

only alignment marks and saw marks. Layer 2 contains calibration patterns and the mask for the deep part of the device connection channel as well as the DRIE-lag slope. Layer 3 contains the mask for the prototype channel itself between the connections, this is etched last as it will contain the critical dimensions in later processing.

Calibration patterns

A set of several different calibration patterns was designed and an example of each pattern placed into a group on the mask as indicated by the bracketed section in figure 143. This group of patterns is reproduced across the mask eight times; a single group is shown in figure 144. Each individual pattern consists of several narrow rectangles of decreasing width separated by different distances. The rectangles are interchangeably referred to as trenches because they represent the open parts of the mask where the photoresist is removed and a trench is later etched. Similarly the lines separating the rectangles are referred to as walls since the resist from these regions is not removed and walls are formed between the trenches.

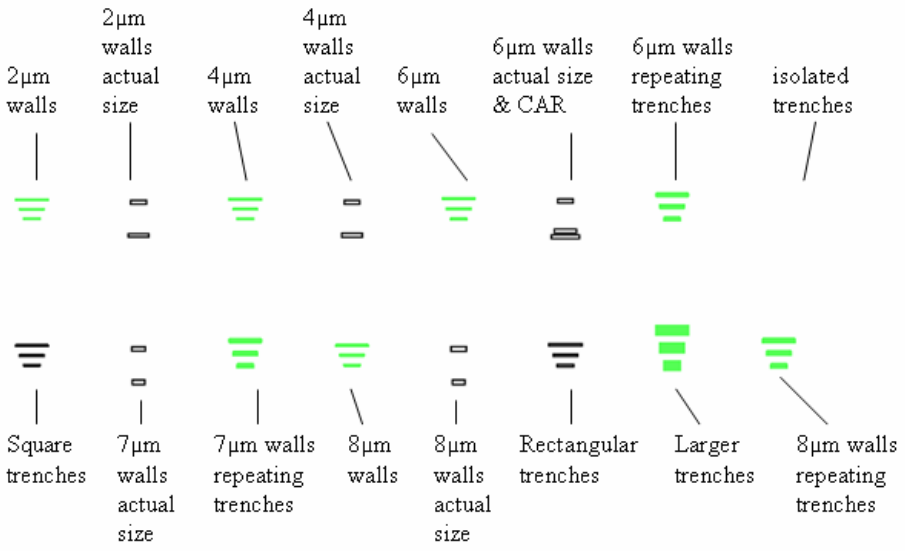

Figure 144, layout of the group of mask patterns used for DRIE-lag calibration; CAR refers to trenches of constant aspect ratio. Some patterns or parts of patterns are not visible at this zoom level.

A higher magnification version of the '8µm walls' pattern is shown in figure 145. In order to measure the etch depths, the wafers are cleaved and the cross section imaged by scanning electron microscope (SEM). For the example of figure 145 the ideal cleave would be vertically down the centre crossing all the trenches. Accurate cleaving of silicon wafers can be challenging practically and therefore longer trenches are produced for ease of analysis. Although the DRIE-lag effect is dominated by the smallest dimension of the mask feature, a series of lengths was fabricated in order that any variation in etch depth due to trench length could be identified.

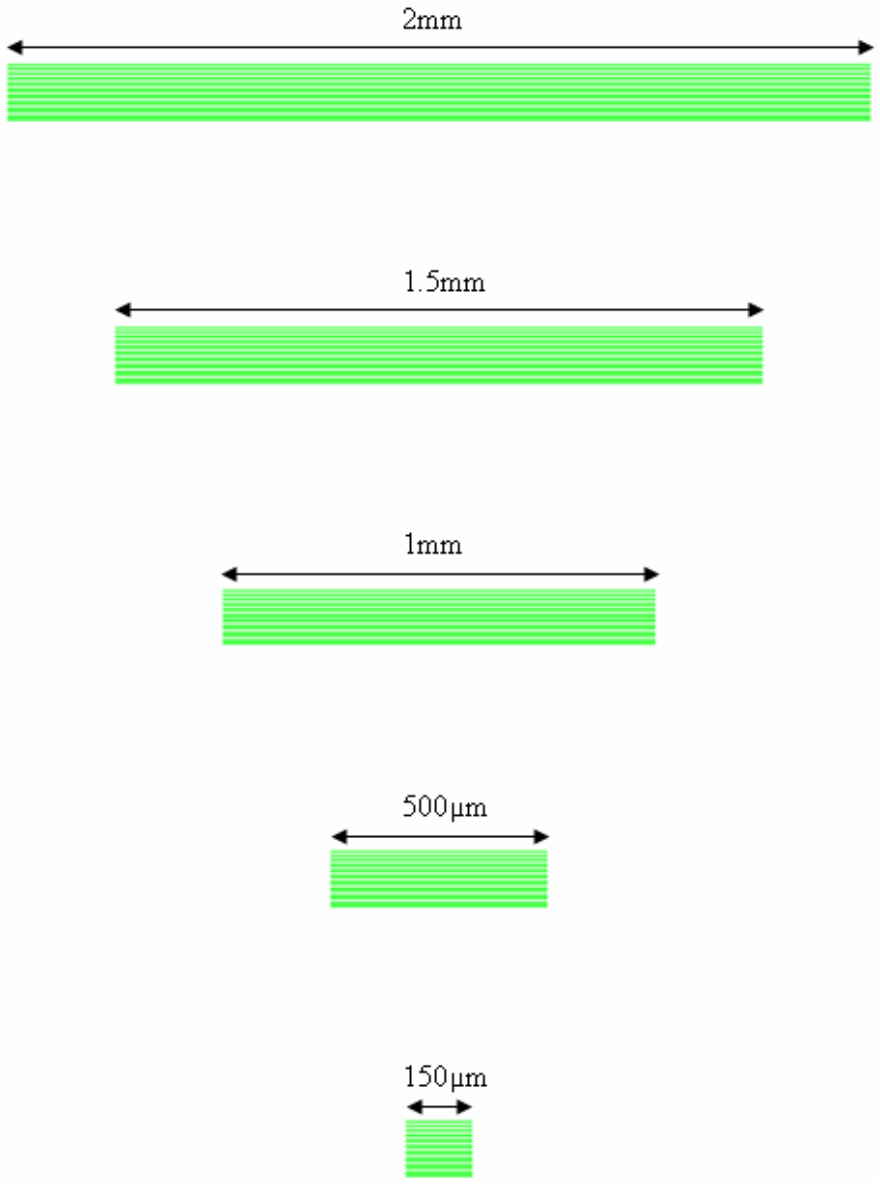

Figure 145, layout of a standard pattern for a set of trenches 1-10µm in width and 0.15-2mm in length (to scale).

The patterns in figure 144 labelled '2µm walls', '4µm walls' and '6µm walls' are similar to the pattern in figure 145, the only difference is that the spacing between the small trenches which is 2, 4 and 6µm respectively. A further magnified image of the 150µm length trenches is shown in figure 146. Measurements of the etch depths in the narrow trenches after anisotropic etching allow calibration of the DRIE-lag effect, which is expected to be similar for all trenches of the same dimensions regardless of the wall size.

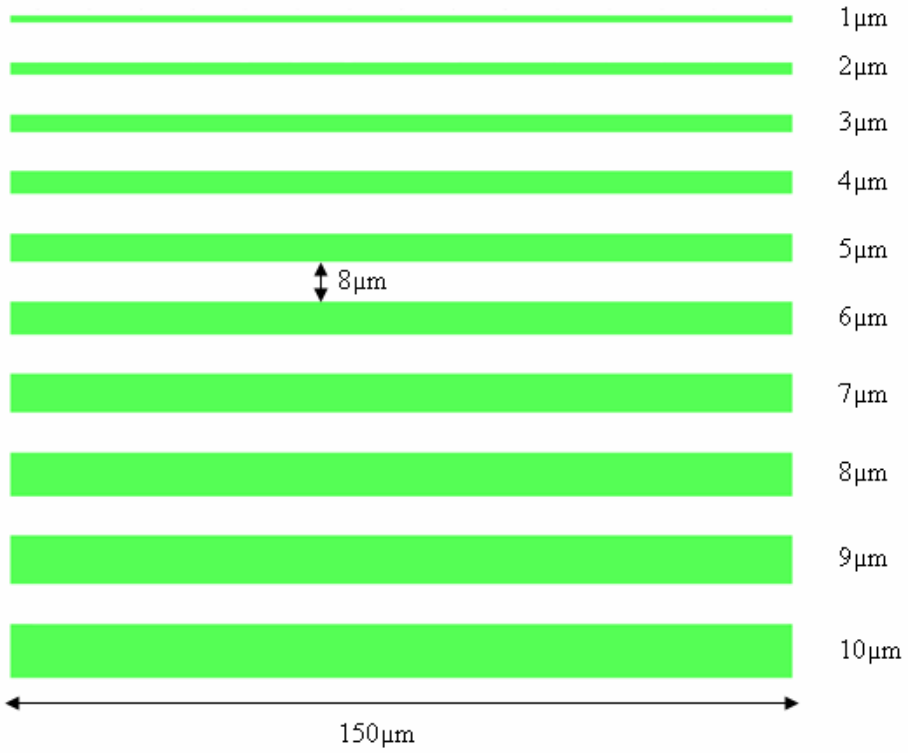

Figure 146, high magnification image of the mask layout for one set of trenches from the 8µm wall pattern set. The separation is 8µm in each case, the trench width varies from 1-10µm and the length is fixed at 150µm.

The variation in the size of the walls between the trenches allows calibration of the isotropic etching parameters required for wall removal. Although true isotropic etching is attainable at the wafer surface, it is challenging to obtain at the bottom of high aspect ratio trenches as the ion angular distribution is limited by the trench opening. The ideal case is to have the highest lateral etch rate at the base of the walls (bottom of the trenches) although in practice it is likely to occur at the top of

the trench. However, any process variation that allows increased etching at the trench base is potentially beneficial in that walls may be released from the substrate and may not have to be etched away in their entirety. This potentially reduces the length of the isotropic etching step which is helpful to maintain the profile produced by DRIE-lag. It is also useful to have a selection of wall widths as this gives further flexibility in later slope design as the distance over which a slope can be fabricated depends on both the trench widths and the wall widths.

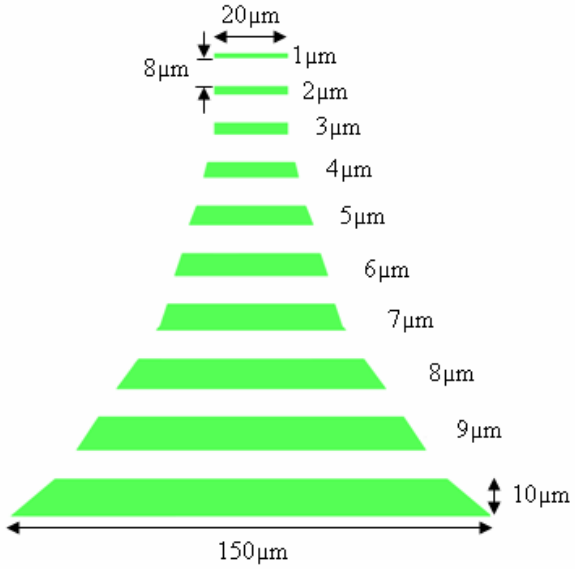

Figure 147, mask layout for a channel-sized calibration pattern. The gap between each trench is 8µm, the trench length tapers from 150µm (the connecting capillary outer diameter) to 20µm (prototype analysis channel diameter) as the width decreases from 10µm to 1µm.

Along with these fixed width calibration patterns, smaller, tapering patterns such as that shown in figure 147 were fabricated in the geometry initially proposed for making the slope at the channel entrance. Cleaving wafers to get a cross-sectional image of the etched trenches proved to be challenging for features with shorter lengths. While the 1-2mm length features are quite accessible, cleaving the wafer through the centre of a 150µm length pattern is challenging. Cleaving through 20µm features with the facilities available during process characterisation as not possible. Specifically in the case of designs such as that in figure 147, which were also produced for 2, 4, 6 and 7µm walls, the wafer tended to cleave at the edge of the trenches and frequently only one or two trenches was exposed for analysis by SEM.

While the DRIE-lag effect is most pronounced in features with a smallest dimension less than approximately ten micrometres, it is also present in larger trenches. Mask patterns were therefore included for trenches with a width of 25-150µm such that these could also be calibrated for possible use in the final slope design. An example of one set of larger trenches is shown in figure 148, for a length of 1mm with widths of 25-150µm and 8µm walls. This individual pattern exists on the mask as part of a set with lengths 150µm, 500µm, 1mm, 1.5mm and 2mm, laid out in the same way as shown in figure 145.

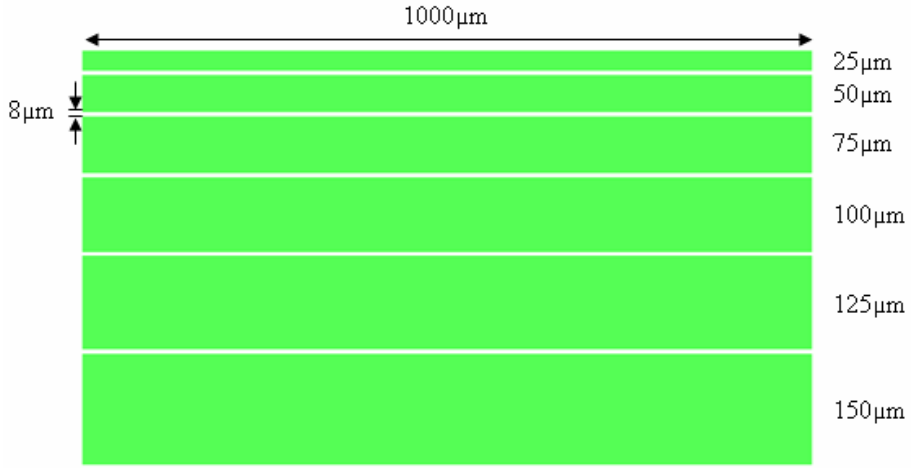

Figure 148, example of a mask layout pattern with larger trenches, separated by 8µm walls for calibration of DRIE-lag in larger features.

Some further mask patterns were added that produced results of little or no interest or produced insubstantial results due to difficulties in the wafer cleaving step. These included breaking up the basic slope design of figure 146 into arrays of squares of side 1-10µm and a series of isolated trenches of 20µm length, width 1-10µm. The latter proved impractical to cleave and analyse, while breaking up the slope designs into more, smaller trenches simply served to make the isotropic etching step more problematic. Finally, trenches of decreasing width and length with constant aspect ratio were fabricated but produced insufficient data for a meaningful analysis.

Prototype channels

To test the proposed process in its entirety during the calibration processing, mask space was reserved for a few prototype channel designs. These consisted of a deep trench for capillary connection and a sloped and tapered region to connect this to a shallow (20µm deep, square cross section) analysis channel. A control was included

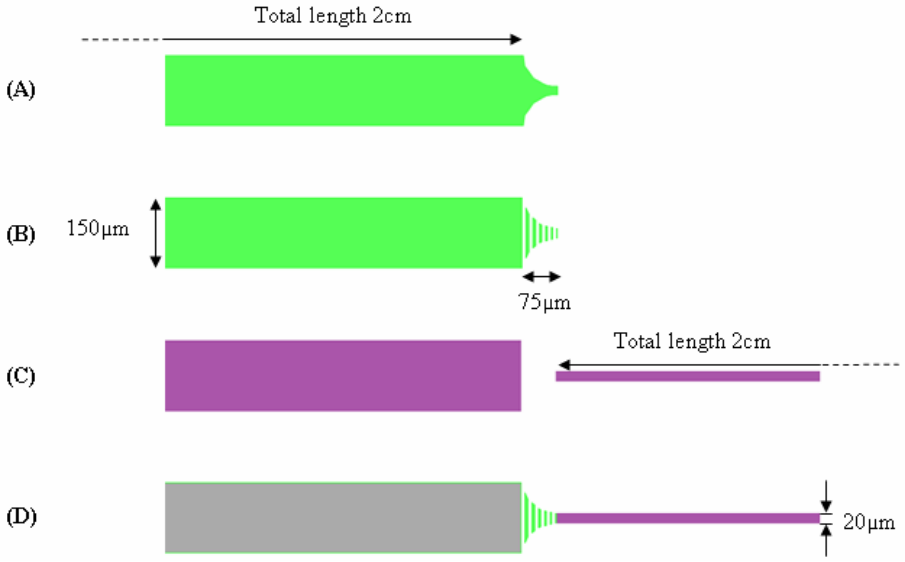

Figure 149, mask layout designs for prototype channels: layer 2 in green layer 3 in purple. (A) Control channel for connection capillary. (B) Channel for connection capillary with DRIE-lag trenches. (C) Mask for the second etch adding depth to the capillary connection region (left) and adding the 20µm analysis channel (right). (D) An example of layers 2 and 3 overlaid to show alignment.

with an in-plane taper from the 150µm channel to the 20µm channel but no out-of-plane slope. The mask features for these channels are shown in figure 149: layouts (A) and (B) are used for a deep etch which produces a slope in the case of (B). The tapered region is then covered in photoresist during the layer 3 etching process which increases the depth of the capillary connection region and adds the analysis channel. The alignment of the layers in the multilayer mask design is shown in (D): the sections are flush with each other in the mask but connection between them is assured due to the isotropic etch step.

Alignment marks

Simple marks are etched into the wafer to keep the three layers aligned and to provide guidance for the saw blade during the dicing process. The saw marks are simple arrows approximately 100µm in size close to the edge of the wafer which allows the saw blade to be aligned at the wafer edge then cut across the wafer in a straight line in order to separate the individual devices into chips. The wafer alignment marks are etched in layer one and consist of a pair of crosses at either side of the wafer.

There are also alignment windows in the masks for layers 2 and 3: the chrome is removed in these areas allowing the alignment mark on the wafer to be located. The marks themselves are shown in figure 150; one such pair exists at either side of the

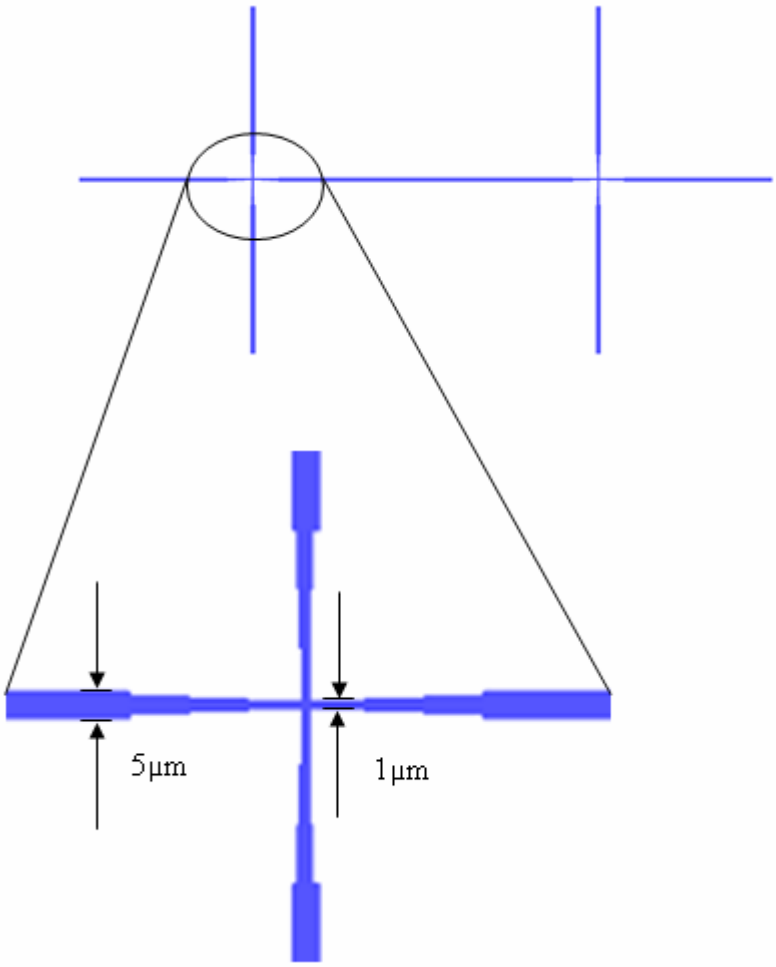

Figure 150, image of the alignment marks in mask layer 1. A pair of crosses (top) is etched at either side of the wafer. The crosses taper to a width of 1µm at the centre providing fine alignment.

mask (see figure 143 for location). Each cross is 5µm wide but tapers to 1µm at the centre; a brief anisotropic etch gives the marks a depth of 2µm on the wafer. Thus coarse x-y alignment is provided by aligning the etched crosses to the chrome crosses in the alignment windows in later layers, while the fine alignment can be checked with the wafer in contact with the mask using the narrow part of the cross. Rotational alignment is provided by ensuring the marks at either side of the wafer are simultaneously aligned.

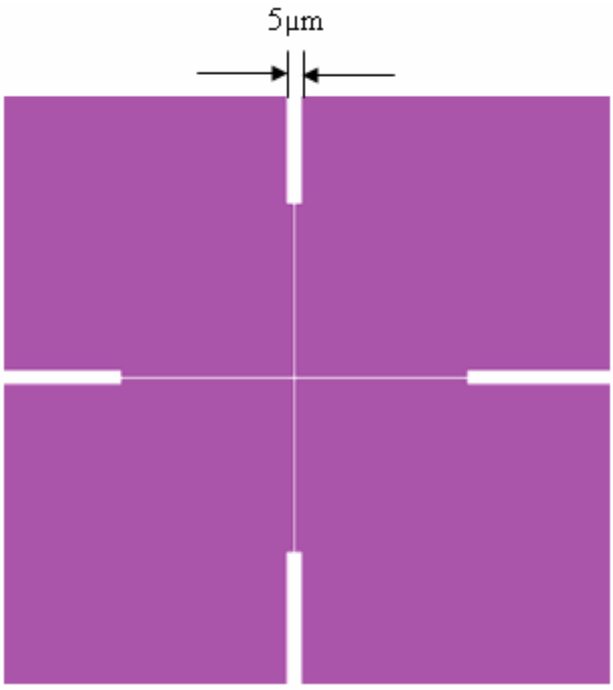

Figure 151, image of the alignment window from mask layer 3. Chrome is removed from the purple areas and remains in the white areas, the effect on the physical mask is to have a small glass window with a chrome cross in it.

The centre of an alignment window is shown in figure 151, in the physical mask this pattern produces a small chrome cross surrounded by a window of glass. The actual extent of the window is much larger as seen in figure 152. These larger windows make it easier to find the alignment marks on the wafer before trying to fully align it to the mask. The outer alignment mark is used for the final layer since this layer contains the most critical dimensions and the rotational alignment is slightly better using the outer mark. Both alignment marks are visible through the layer 3 window and the marks themselves will therefore be rendered useless after the final etch.

Microscope images of the alignment marks in layer 1 and 2 are shown in figure 153. In layer 1 the cross is glass and the surround is chrome, thus a small cross is etched using a positive photoresist. In layer 2 the cross is chrome and appears in a larger glass window which can be used to locate the cross that is etched into the wafer. The chrome cross on the mask is then aligned to the etched cross on the wafer.

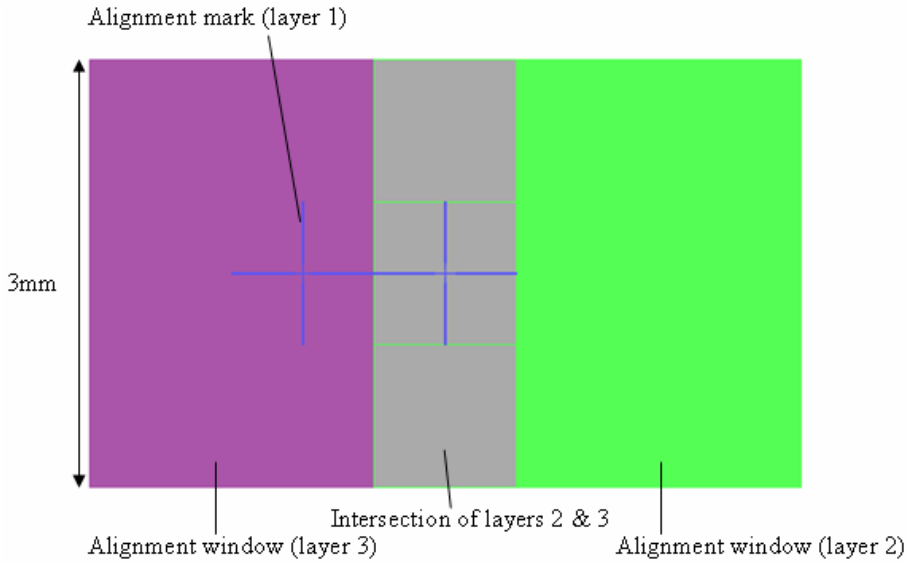

Figure 152, image of the alignment marks and windows from the photomask design shown as an overlay of all three layers.

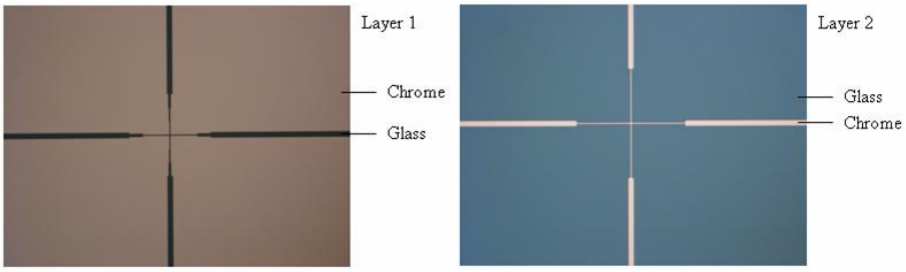

Figure 153, microscope image of the alignment marks on the photomask.

Appendix B Preconditioning Channel Results

Nominal POPO-3 Stained λ-DNA Length Distributions for Control Preconditioning Channel

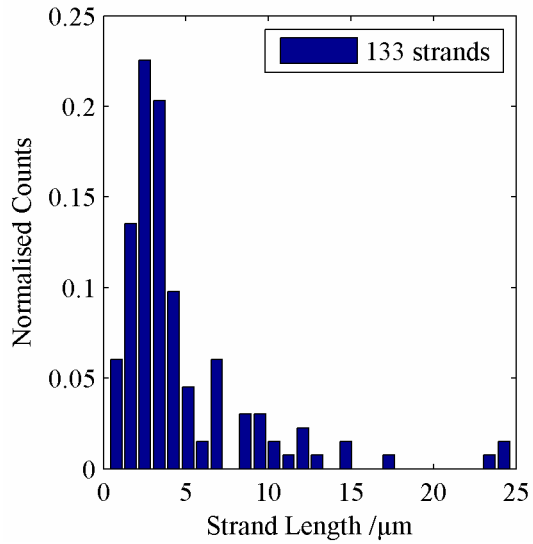

Figure 154, probability distribution of nominal strand lengths for POPO-3~DNA in the control channel, pump rate 3µLh^{-1}.

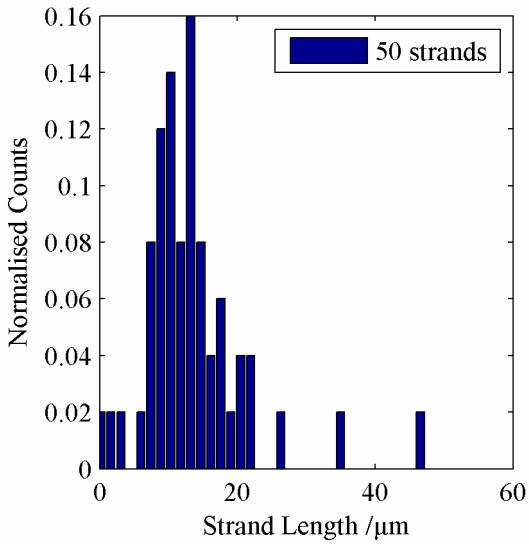

Figure 155, probability distribution of nominal strand lengths for POPO-3~DNA in the control channel, pump rate 5µLh^{-1}.

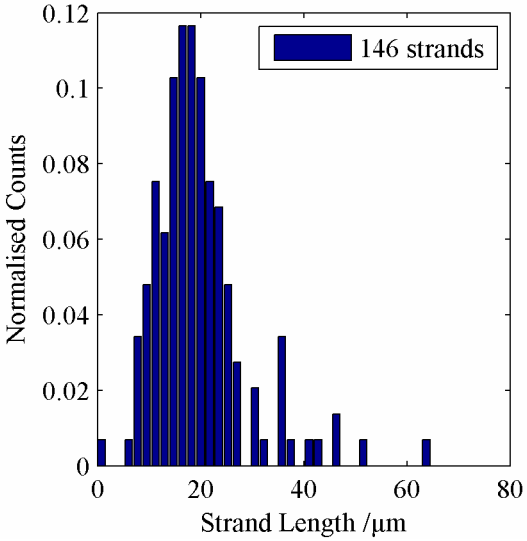

Figure 156, probability distribution of nominal strand lengths for POPO-3~DNA in the control channel, pump rate 6µLh^{-1}.

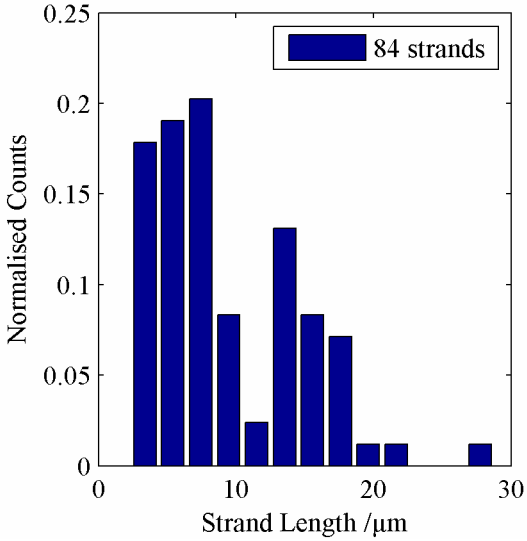

Figure 157, probability distribution of nominal strand lengths for POPO-3~DNA in the control channel, pump rate 7µLh^{-1}.

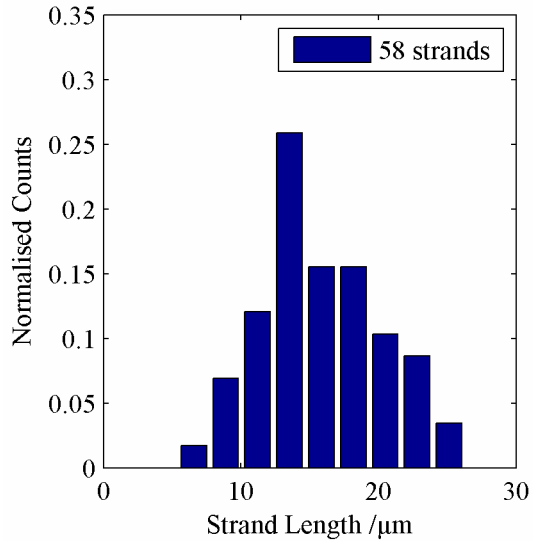

Figure 158, probability distribution of nominal strand lengths for POPO-3~DNA in the control channel, pump rate 8µLh^{-1}.

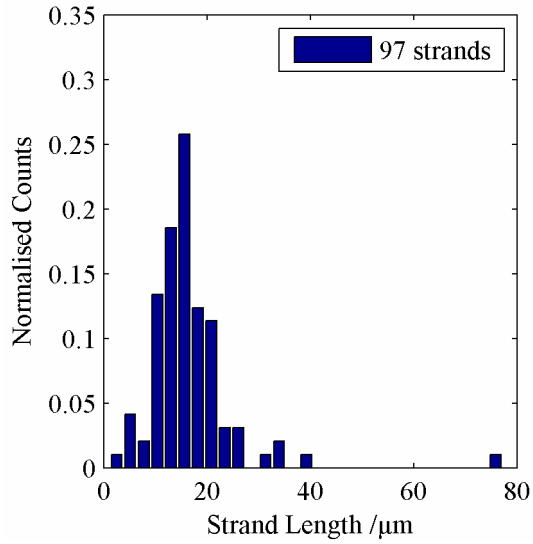

Figure 159, probability distribution of nominal strand lengths for POPO-3~DNA in the control channel, pump rate 9µLh^{-1}.

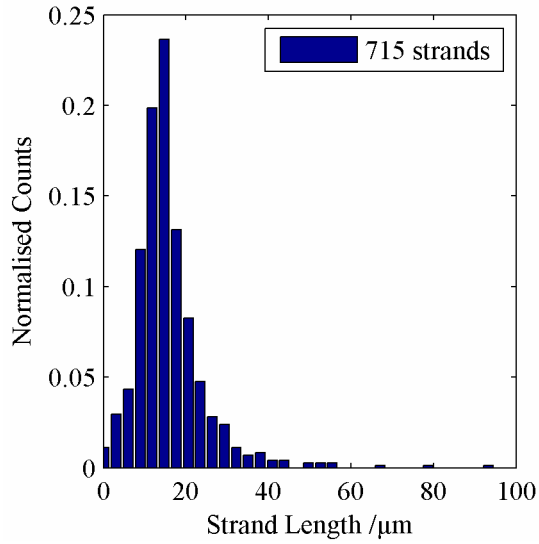

Figure 160, probability distribution of nominal strand lengths for POPO-3~DNA in the control channel, pump rate 10µLh^{-1}.

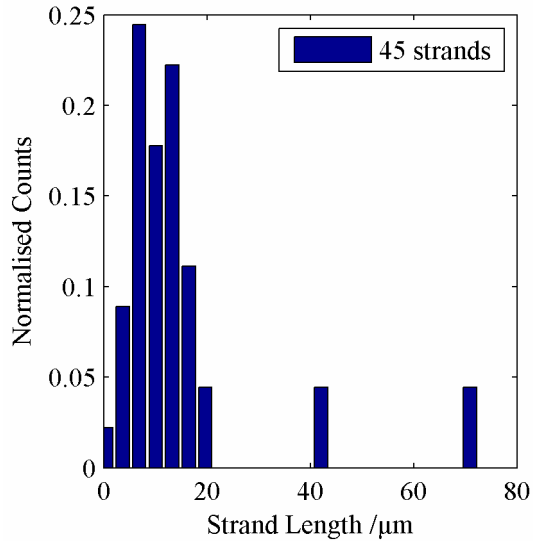

Figure 161, probability distribution of nominal strand lengths for POPO-3~DNA in the control channel, pump rate 11µLh^{-1}.

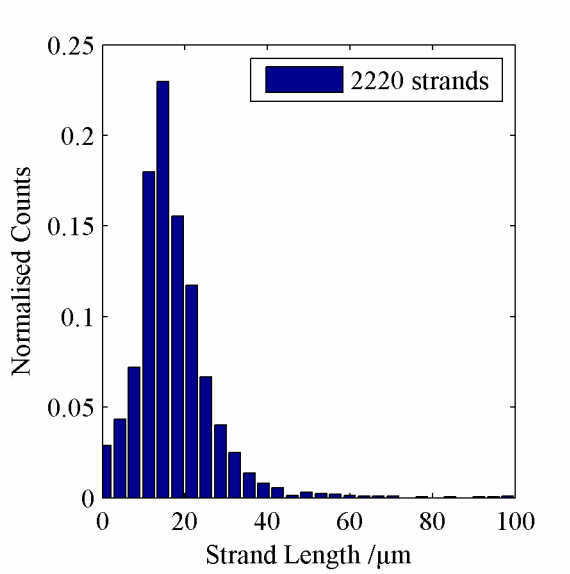

Figure 162, probability distribution of nominal strand lengths for POPO-3~DNA in the control channel, pump rate 12µLh^{-1}.

Nominal POPO-3 Stained λ-DNA Length Distributions for Serpentine Preconditioning Channel

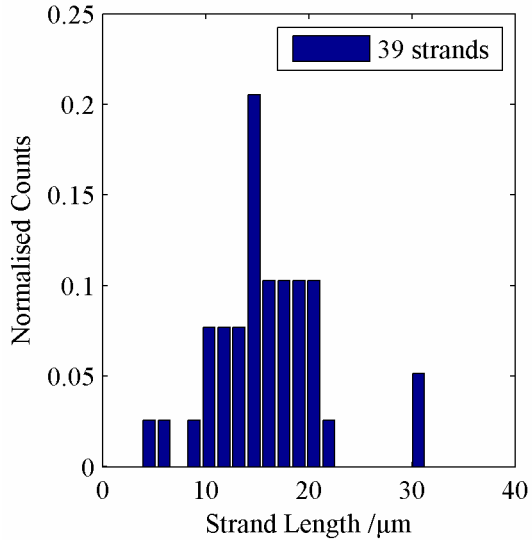

Figure 163, probability distribution of nominal strand lengths for POPO-3~DNA in the serpentine channel, pump rate 5µLh^{-1}.

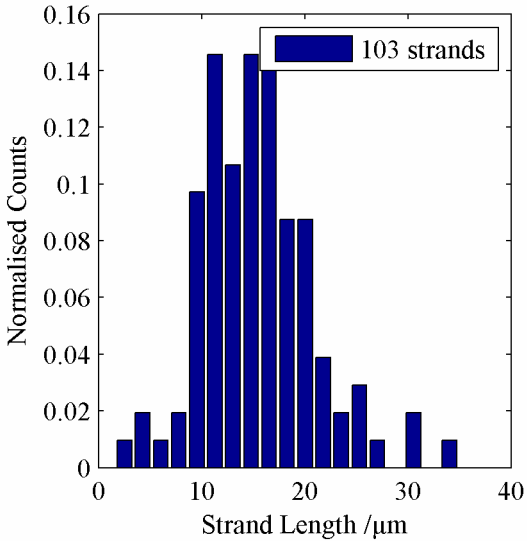

Figure 164, probability distribution of nominal strand lengths for POPO-3~DNA in the serpentine channel, pump rate 6µLh^{-1}.

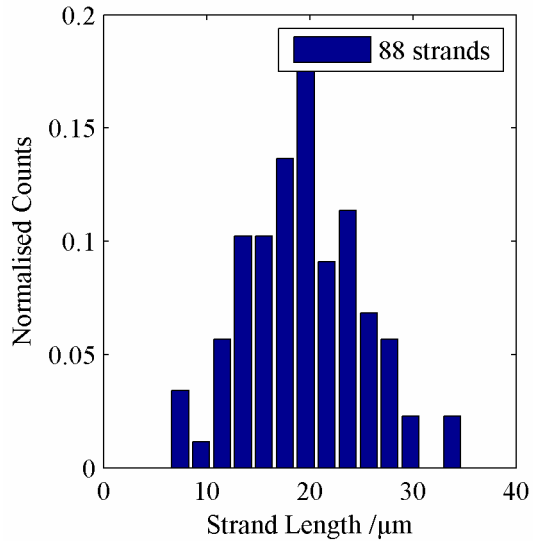

Figure 165, probability distribution of nominal strand lengths for POPO-3~DNA in the serpentine channel, pump rate 7µLh^{-1}.

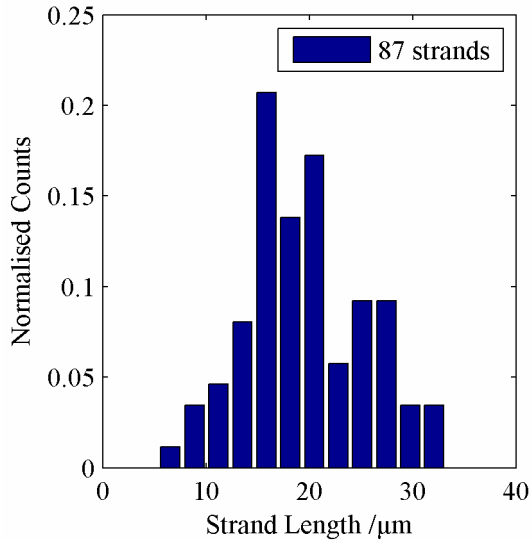

Figure 166, probability distribution of nominal strand lengths for POPO-3~DNA in the serpentine channel, pump rate 8µLh^{-1}.

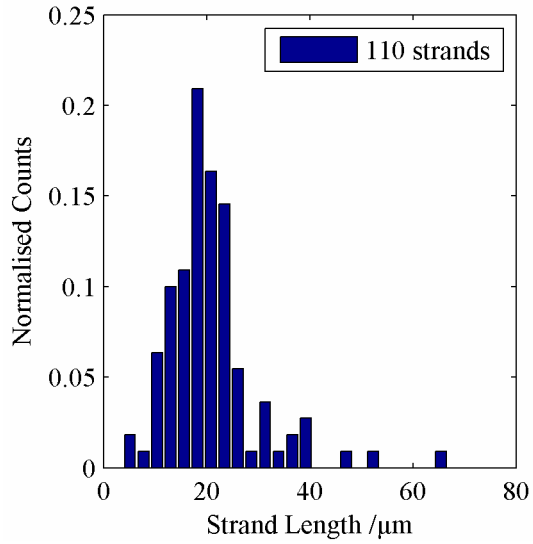

Figure 167, probability distribution of nominal strand lengths for POPO-3~DNA in the serpentine channel, pump rate 9µLh^{-1}.

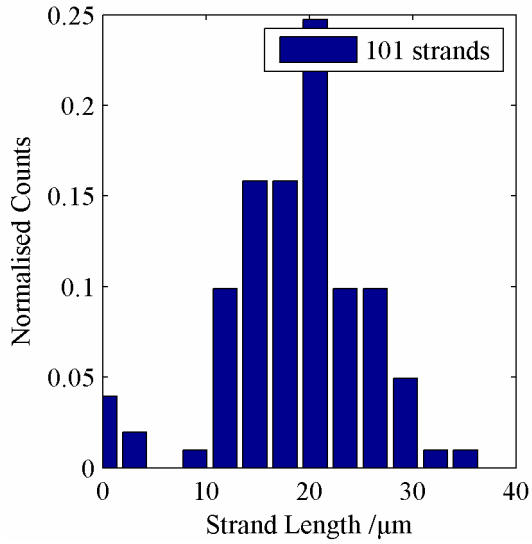

Figure 168, probability distribution of nominal strand lengths for POPO-3~DNA in the serpentine channel, pump rate 10µLh^{-1}.

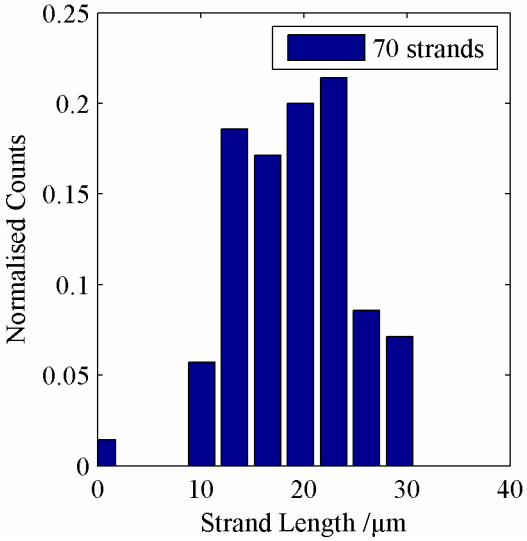

Figure 169, probability distribution of nominal strand lengths for POPO-3~DNA in the serpentine channel, pump rate 11µLh^{-1}.

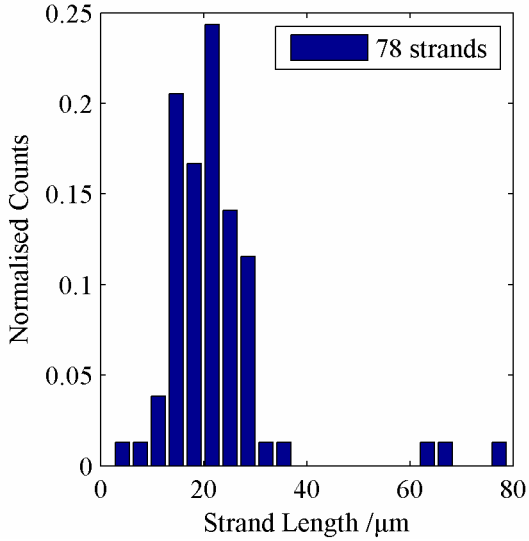

Figure 170, probability distribution of nominal strand lengths for POPO-3~DNA in the serpentine channel, pump rate 12µLh^{-1}.

Nominal TOTO-3 Stained λ-DNA Length Distributions for Control Preconditioning Channel

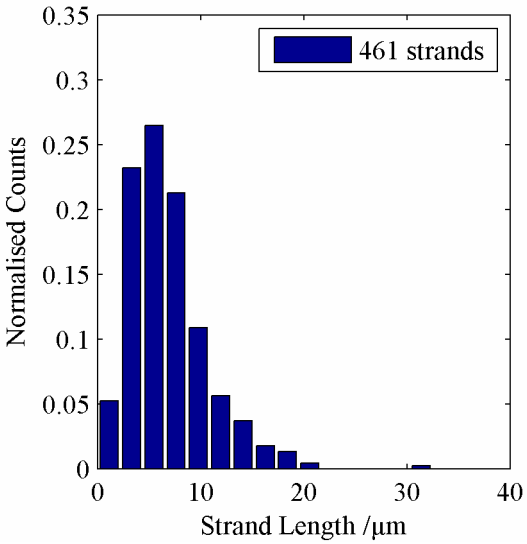

Figure 171, probability distribution of nominal strand lengths for TOTO-3~DNA in the control channel, pump rate 8µLh-1.

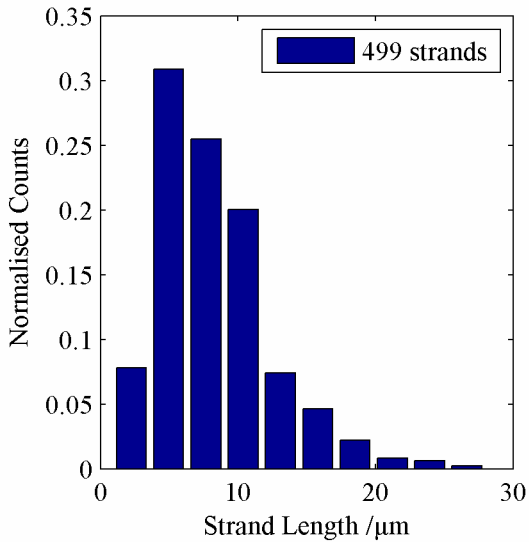

Figure 172, probability distribution of nominal strand lengths for TOTO-3~DNA in the control channel, pump rate 10µLh-1.

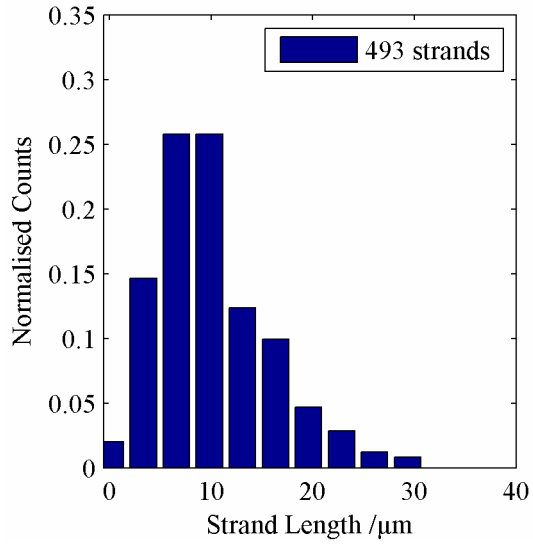

Figure 173, probability distribution of nominal strand lengths for TOTO-3~DNA in the control channel, pump rate 12µLh-1.

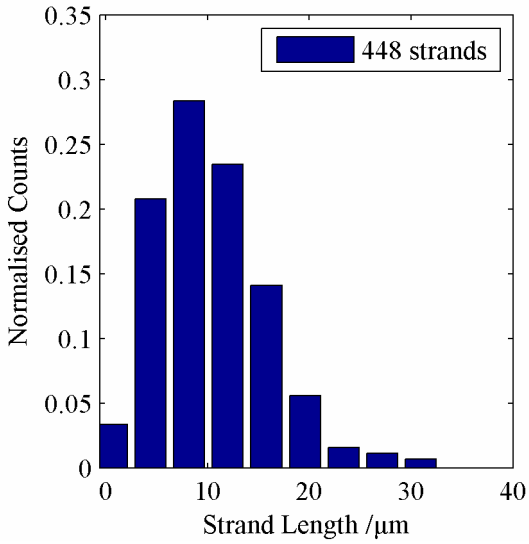

Figure 174, probability distribution of nominal strand lengths for TOTO-3~DNA in the control channel, pump rate 14µLh-1.

Nominal TOTO-3 Stained λ-DNA Length Distributions for Narrowing-Serpentine Preconditioning Channel

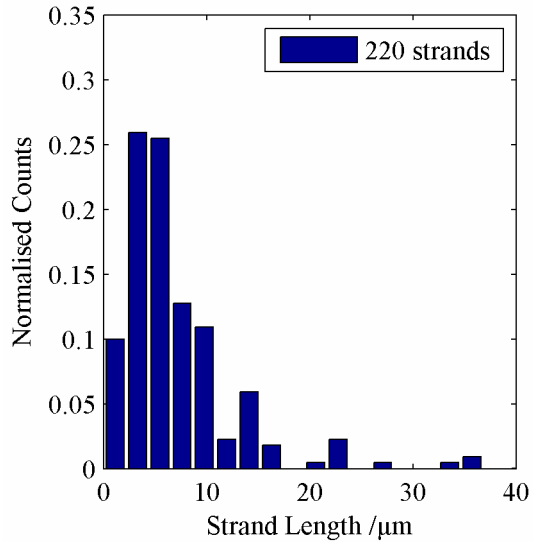

Figure 175, probability distribution of nominal strand lengths for TOTO-3~DNA in the narrowing-serpentine channel, pump rate 8µLh-1.

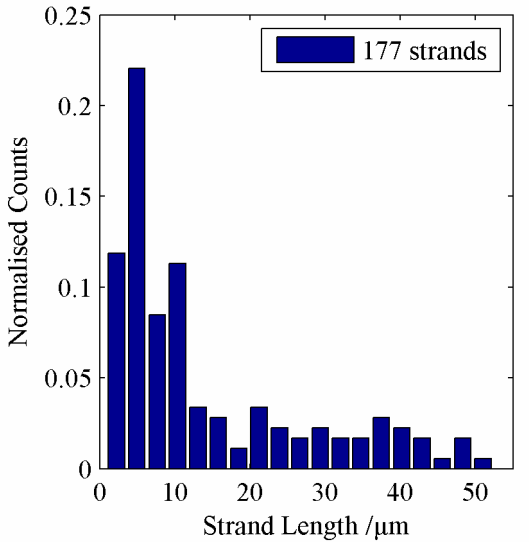

Figure 176, probability distribution of nominal strand lengths for TOTO-3~DNA in the narrowing-serpentine channel, pump rate 10Lh-1.

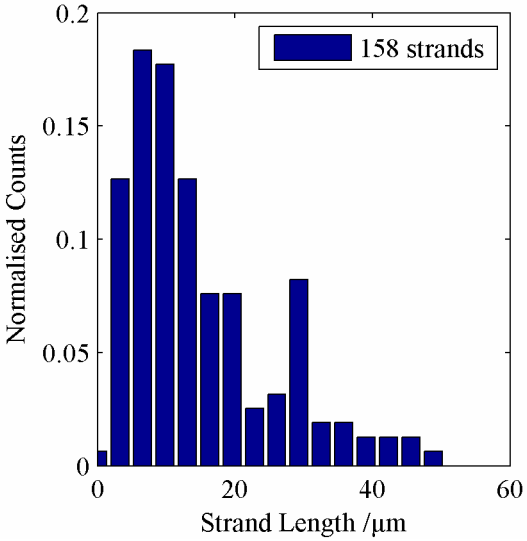

Figure 177, probability distribution of nominal strand lengths for TOTO-3~DNA in the narrowing-serpentine channel, pump rate 12µLh-1.

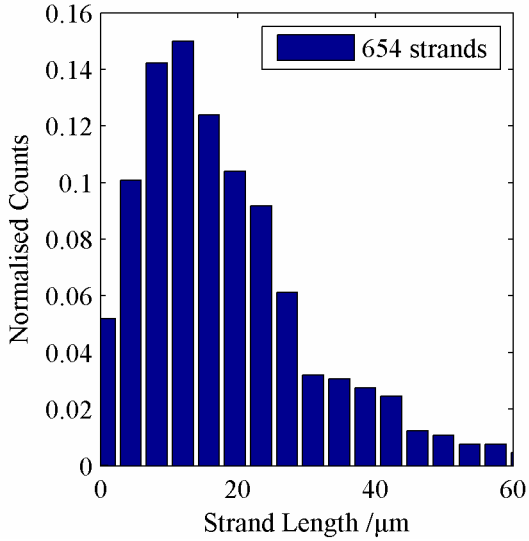

Figure 178, probability distribution of nominal strand lengths for TOTO-3~DNA in the narrowing-serpentine channel, pump rate 14µLh-1.

Appendix C C Programme Code

USB Interface C Programme

```
/*

============================================================================
========
 Name        : captureUSB_fullSpeed.c
 Author      : Tim Humphreys
 Description : Application of Digilent's USB comms API for photon
counter

============================================================================
========
 */
#include <windows.h>
#include <stdio.h>
#include <stdlib.h>
#include "L:\TIM\data\eclipse\captureUSB\inc\dpcdefs.h" /* holds
error codes and data types for dpcutil */
#include "L:\TIM\data\eclipse\captureUSB\inc\dpcutil.h" /* holds
declaration of DPCUTIL API calls */
#include "conio.h"
#include "time.h"

#define rCONTROL  0         // address of control register - it's
the first one...
#define FPGABUFFERLENGTH 255 // 255 8-bit registers, one control,
then 127 2-byte values

int initialise(char *device);
int readRegister(char * device, unsigned char registerAddress,
unsigned char * registerData, HANDLE hif);
int readRegisterGroup(char * device, unsigned char * regAddrs,
unsigned char * regData, HANDLE hif, int numBytes);
int writeRegister(char * device, unsigned char registerAddress,
unsigned char * registerData, HANDLE hif);
int restartUSB(HANDLE hif, char * defDev);
void timeLeader(void);
void ercLookup(ERC code);
void wait(int ms); // delay in seconds

int main(int argc, _TCHAR* argv[]) {

 /*
  * vars
  */
 char defaultDevice[17];
 unsigned char fpgaBuffAddr[FPGABUFFERLENGTH],
fpgaBuffContents[FPGABUFFERLENGTH], resetControl=0, FF=255;
 unsigned int i, doOnce = 1;
 FILE *fptr;
 HANDLE hif;
 ERC erc;

 // fill address array, it's just 1,2,3...32
 for(i=0; i<FPGABUFFERLENGTH; i++)
 {
```

```
  fpgaBuffAddr[i] = i;
 }

 /*
  * setup
  */
 if (initialise(defaultDevice) != 0)
  return 1; // function handles error messages by itself

 /* Default device selected: doesn't guarantee it's connected and
switched on */
 printf("\nDefault device %s selected.\n", defaultDevice);

 /* get interface handle, NULL makes it a blocking call*/
 if (!DpcOpenData(&hif, defaultDevice, &erc, NULL))
 {
  printf("DpcOpenData failed, tried switching the dev board on?\n");
  return 1;
 }

 switch (argc)
 {
 case 1:
  fptr = fopen("out.dat", "wb"); // no file specified
  if (fptr == NULL)
  {
   DpcCloseData(hif, &erc);
   DpcTerm();
   return 1;
  }
  printf("\nWriting to out.dat, use syntax capture <filename> to
specify output file name.\n");
  break;

 case 2:
  fptr = fopen(argv[1], "wb"); // user file specified
  if (fptr == NULL)
  {
   DpcCloseData(hif, &erc);
   DpcTerm();
   return 1;
  }
  break;

 default:
  printf("\nUnrecognised option.\n");
  DpcCloseData(hif, &erc);
  DpcTerm();
  return 1;
 }


 printf("\n");
 timeLeader();
 printf("Waiting to receive data.\n");

 /*
  * data acquisition
  * everything is in the same buffer, pole buffer, reading position
0 until data[0] goes 0->FF
  */
```

```
 while(!_kbhit())
 {
  if (readRegisterGroup(defaultDevice, fpgaBuffAddr,
fpgaBuffContents, hif, FPGABUFFERLENGTH) == 0)
  {
   if (fpgaBuffContents[0] == 255)
   {   // FF is the 'data ready' signal
    if(doOnce)
    {
     timeLeader();
     printf("Receiving data.\n");
     doOnce = 0;
    }

    // write data to file - data starts at fpgaBuffContents[1]
    fwrite(&fpgaBuffContents[1], FPGABUFFERLENGTH-1, 1, fptr); //
write bytes (and assume fwrite works)
    // write 00 to control register to allow next data to be written
    if (writeRegister(defaultDevice, rCONTROL, &resetControl, hif)
!= 0)
    {   // failed to write control register - try again incase it's
just a usb conflict
     printf("Failed to reset control register, restarting USB
interface...");
     if (restartUSB(hif, defaultDevice) == 0)
     {
      printf("succeeded.\n");
      // there will be a delay from restarting so write an error to
the file
      // to prevent timing misunderstandings
      fwrite(&FF, 1, 1, fptr); // writes FF
      fwrite(&FF, 1, 1, fptr); // need two bytes (high and low) to
give an error
      // don't re-read the same frame, need to make sure CTRL gets
set
      if (writeRegister(defaultDevice, rCONTROL, &resetControl, hif)
!= 0)
      {
       printf("Still can't write control register!\n");
       timeLeader();
       printf("Capture error.\n");
       fclose(fptr);
       DpcCloseData(hif, &erc);
       DpcTerm();
       return 1;
      }
     }
     else
     {
      printf("failed.\n");
      timeLeader();
      printf("Capture error.\n");
      fclose(fptr);
      DpcCloseData(hif, &erc);
      DpcTerm();
      return 1;
     }
    }
   }
  }
  else
```

```
  {   // first read failed
   printf("Failed to read FPGA buffer, restarting USB
interface...");
   if (restartUSB(hif, defaultDevice) == 0)
   {
    printf("succeeded.\n");
    // just go back and check control as usual
    // - it still says if there is a valid frame we just don't know
which one it is
    // hence write FFFF
    fwrite(&FF, 1, 1, fptr);
    fwrite(&FF, 1, 1, fptr);
   }
   else
   {
    printf("failed.\n");
    timeLeader();
    printf("Capture error.\n");
    fclose(fptr);
    DpcCloseData(hif, &erc);
    DpcTerm();
    return 1;
   }
  }
 }

 /*
  * clearup
  */
 fclose(fptr);
 timeLeader();
 printf("Capture complete.\n");
 DpcCloseData(hif, &erc);
 DpcTerm();
 return 0;
}

/* initialisation function */
int initialise(char *device)
{
 ERC erc;
 int idDvc;

 /* DpcInit initialises and attaches the dll */
 if (!DpcInit(&erc))
 {
  printf("DpcInit failed, error code %d.  Innit.\n", erc);
  return 1;
 }

 idDvc = DvmgGetDefaultDev(&erc); // get default device
 if (idDvc == -1)
 {
  printf("No default device, ");
  /* but we don't have to give up! */
  printf("opening communication modules dialog box, please select
device.\n");
  /* bring up the dialog box which is the only way in which a
default device may be selected */
  DvmgStartConfigureDevices(NULL, &erc);
```

```
  /* when the dialog box is closed, check again for a default device
*/
  idDvc = DvmgGetDefaultDev(&erc);
  if (idDvc == -1)
  {
   printf("Still no default device selected.\n");
   return 1;
  }
  else
  {
   /* get the device name */
   DvmgGetDevName(idDvc, device, &erc);
  }
 }
 else
 {
  /* get the device name */
  DvmgGetDevName(idDvc, device, &erc);
 }

 return 0;
}

/* read a register once */
int readRegister(char * device, unsigned char registerAddress,
unsigned char * registerData, HANDLE hif)
{
 ERC  erc;

 if (!DpcGetReg(hif, registerAddress, registerData, &erc, NULL))
 {
  printf("DpcGetReg failed.\n");
 }

 /* use error code to check if read was successful */
 erc = DpcGetFirstError(hif);
 if (erc != ercNoError)
 {
  printf("Register read error,\nERC: %d - ", erc);
  ercLookup(erc);
  return 1;
 }

 return 0;
}

int readRegisterGroup(char * device, unsigned char * regAddrs,
unsigned char * regData, HANDLE hif, int numBytes)
{
 ERC  erc;

 if (!DpcGetRegSet(hif, regAddrs, regData, numBytes, &erc, NULL))
 {
  printf("DpcGetRegSet failed.\n");
 }

 /* use error code to check if read was successful */
 erc = DpcGetFirstError(hif);
 if (erc != ercNoError)
 {
  printf("Group register read error,\nERC: %d - ", erc);
```

```
  ercLookup(erc);
  return 1;
 }
 return 0;
}

int writeRegister(char * device, unsigned char registerAddress,
unsigned char * registerData, HANDLE hif)
{
 ERC  erc;

 if (!DpcPutReg(hif, registerAddress, *registerData, &erc, NULL))
 {
  printf("DpcPutReg failed.\n");
 }

 /* use error code to check if write was successful */
 erc = DpcGetFirstError(hif);
 if (erc != ercNoError)
 {
  printf("Register write error,\nERC: %d - ", erc);
  ercLookup(erc);
  return 1;
 }

 return 0;
}

void timeLeader(void)
{
 time_t rawtime;
 struct tm * timeinfo;
 time(&rawtime);
 timeinfo = localtime(&rawtime);
 printf("%02d:%02d:%02d  ", timeinfo->tm_hour, timeinfo->tm_min,
timeinfo->tm_sec);
}

void ercLookup(ERC code)
{
 switch(code)
 {
 case 0:
  printf("No error occurred in transaction.\n");
  break;
 case 3004:
  printf("Invalid parameter sent in API call.\n");
  break;
 case 3005:
  printf("Internal error.  Please report occurrence as a bug.\n");
  break;
 case 3006:
  printf("Internal error.  Please report occurrence as a bug.\n");
  break;
 case 3009:
  printf("Not enough memory to carry out transaction.\n");
  break;
 case 3102:
  printf("Communication device not initialized.\n");
  break;
 case 3103:
```

```
  printf("Can't connect to communication module.\n");
  break;
 case 3104:
  printf("Already connected to communication device.\n");
  break;
 case 3105:
  printf("Error occurred while sending data to communication
device.\n");
  break;
 case 3106:
  printf("Error occurred while receiving data from communication
device.\n");
  break;
 case 3107:
  printf("Error occurred while trying to abort transaction(s).\n");
  break;
 case 3109:
  printf("Completion out of order.\n");
  break;
 case 3110:
  printf("Too much data received from communication device.\n");
  break;
 case 3111:
  printf("Nothing to send or data/address mismatched pairs.\n");
  break;
 case 3201:
  printf("Unable to find matching TRID in transaction queue.\n");
  break;
 case 3202:
  printf("Transaction being cleared is not complete.\n");
  break;
 case 3203:
  printf("Not connected to communication device.\n");
  break;
 case 3204:
  printf("Connected in wrong mode (JTAG or data transfer).\n");
  break;
 case 3205:
  printf("Internal error.  Please report occurrence as a bug.\n");
  break;
 case 3301:
  printf("Device table doesn't exist (an empty one has been
created).\n");
  break;
 case 3302:
  printf("All or part of the device table is corrupted.\n");
  break;
 case 3303:
  printf("Device does not exist in device table.\n");
  break;
 case 3304:
  printf("DpcInit API call failed.\n");
  break;
 case 3306:
  printf("Communications devices dialog box already open.\n");
  break;
 case 3307:
  printf("Error occurred while accessing the registry.\n");
  break;
 default:
  printf("ERC not recognised.\n");
```

```
 }
 return;
}

void wait(int ms)
{
 clock_t endwait;
 endwait = clock() + ms*(CLOCKS_PER_SEC/1000); // division will
truncate but close enough
 while (clock() < endwait);
}

int restartUSB(HANDLE hif, char * defDev)
{ // deliberately silent
 ERC erc;
 // try closing connection and dll
 if (!DpcCloseData(hif, &erc))
   return 1;
 DpcTerm();
 // then starting it all up again, don't need to go thru device
table stuff since
 // that data already exists or execution wouldn't have got this far
 if (!DpcInit(&erc))
  return 1;
 if (!DpcOpenData(&hif, defDev, &erc, NULL))
  return 1;
 return 0;
}
```

DNA Pulse Detection C Programme

```
/*
 * ddpConstantThreshold.c
 *
 *      Author: Tim Humphreys
 */

#include "stdio.h"
#include "malloc.h"
#include "math.h"
#include "string.h"

#define STATISTICS 0
#define SMOOTHING 0
#define VERSION 1.4

unsigned short *movingAverage(unsigned short *data, long
dataLength);
double background(char *fname, double sensitivity);
void getStats(unsigned long int dataLength, unsigned short *data,
double *stdev, double *mean);
unsigned int findPulses(unsigned short *data, unsigned long int
dataLength, double threshold, float maxCounts, float binLength_ms,
FILE *fptrOut, FILE* fptrPulsesOnly);
unsigned int findPulsesStrict(unsigned short *data, unsigned long
int dataLength, double threshold, float maxCounts, float
binLength_ms, FILE *fptrOut, FILE* fptrPulsesOnly);

int main(int argc, char *argv[])
{
 FILE *fptrIn, *fptrOut, *fptrPulsesOnly;
 long int i, endPos, startPos;;
 /* binLength_ms in ms, maxCounts in counts/sec */
 float binLength_ms = 0.1, maxCounts = 25e6; /* anything way above
the specified maximum count rate should be noted as an error */
 double threshold = 0, stdev=0, mean=0;
 unsigned long int dataLength = 0;
 unsigned short *data; // 16-bit data
 double sensitivity = 8; // number of standard deviations above the
mean to set threshold level
 char pfname[255]; /* for the autogenerated pulse file */
 int numPulses = 0;

/*****************************************************************
*****************************************/
/********************************** Initialisation
*************************************************************/

 if (argc < 4)
 {
  printf("\nddp version %.1f\n", VERSION);
  printf("---------------");
  printf("\nPlease use the following syntax:\n\nddp <pulse file>
<output file> <background file> <sensitivity>\n\n");
  printf("This will fill <output file> with intelligible pulse data
and generate p<output file>\ncontaining a column vector of pulse
lengths.\n\n");
  printf("Note that <pulse file> must be a binary file containing
16-bit count values.\nSensitivity is optional.\n\n");
  return 1;
```

```
 }
 if (argc == 5) sensitivity = atof(argv[4]);

 if (*argv[2] == '.')
 {   // not in current directory
  pfname[0] = '\0';
  strcat(pfname, argv[2]);
  char temp[255];
  int j=0;
  for (i=0; pfname[i] != '\0'; i++); // find end of string
  while (pfname[i] != '\\')
  {
   temp[j] = pfname[i];
   i--;
   j++;
  }
  i++; // move to after the '\'
  pfname[i] = 'p';
  while (j>0)
  {
   j--;
   pfname[++i] = temp[j];
  }
 }
 else
 {   // staying in current directory
  pfname[0] = 'p';
  pfname[1] = '\0'; // '\0' is maintained from the first argument of
strcat
  strcat(pfname, argv[2]);
 }

 /*************************************/
 /******* Background Calculation *******/
 threshold = background(argv[3], sensitivity);
 if (threshold == -1)
 {
  printf("Background calculation failed.\n");
  return 1;
 }



/*************************************************************************
*****************************************/
 /*********************************** Read in pulse file
*******************************************************/

 /* Open input file */
 fptrIn = fopen(argv[1], "rb");
 if (fptrIn == NULL)
 {
  printf("Failed to open input file\n");
  return 1;
 }
 else
 {
  /* calculate number of pulses in file */
  fseek(fptrIn,0L,SEEK_END);
  endPos = ftell(fptrIn);
```

```
  fseek(fptrIn,0L,SEEK_SET);  /* might as well see the beginning -
it sets the fptr correctly anyway */
  startPos = ftell(fptrIn);
  dataLength = (endPos-startPos)/2; // 2 bytes in an int
 }

 /* Announce self */
 printf("\nDNA Pulse Detection\n-------------------\n");

 data = malloc((dataLength)*sizeof(unsigned short));
 if (data == NULL)
 {
  printf("malloc() failed.\n");
 }
 else
 {
  printf("Reading %s...", argv[1]);
  fread(data, 2, dataLength, fptrIn);
  printf("done.\n");
 }

 if (STATISTICS) getStats(dataLength, data, &stdev, &mean);

 /* Housekeeping */
 fclose(fptrIn);


/*********************************************************************
*****************************************/
 /*********************************** Find Pulses and Write to
Output ****************************************/

 if (SMOOTHING)
 {   // replace data with five point movingAverage smoothed data
  unsigned short *smoothed;
  smoothed = movingAverage(data, dataLength);
  free(data);
  data = smoothed;
 }


 /* Open output file */
 fptrOut = fopen(argv[2], "w");
 if (fptrOut == NULL)
 {
  printf("Failed to open output file\n");
  return 1;
 }
 else
 {
  // print headers
  if (STATISTICS)
  {
   fprintf(fptrOut, "%lu count values read, mean %3.3lf, standard
deviation %3.3lf, threshold set to %3.3lf\n", dataLength, mean,
stdev, threshold);
  }
  else
  {
   fprintf(fptrOut, "%lu count values read, threshold set to
%3.3lf\n", dataLength, threshold);
```

```
  }
  fprintf(fptrOut, "Input file:      %s\nBackground file: %s
(sensitivity %.1f)\n\n", argv[1], argv[3], sensitivity);
  printf("Finding pulses...");
 }

 maxCounts = 2*maxCounts*(binLength_ms * 1e-3);
 fptrPulsesOnly = fopen(pfname, "w");
 if (fptrPulsesOnly == NULL)
 {
  printf("\nFailed to open pulses only output file %s\n", pfname);
  fclose(fptrOut);
  return 1;
 }
 /* Count data is now stored in data array, fire pulse counter at
will */
 if (VERSION == 1.2)
  numPulses = findPulses(data, dataLength, threshold, maxCounts,
binLength_ms, fptrOut, fptrPulsesOnly);
 if (VERSION >= 1.3)
  numPulses = findPulsesStrict(data, dataLength, threshold,
maxCounts, binLength_ms, fptrOut, fptrPulsesOnly);

 printf("%s.\n%d DNA pulses detected.\n", argv[1], numPulses);

 /* Housekeeping */
 free(data);
 fclose(fptrOut);
 fclose(fptrPulsesOnly);
 return 0;
}
```

Appendix D VHDL Code for Photon Counter Data Acquisition

PhotonCounterSystem.vhd

```
----------------------------------------------------------------------
--------------
-- Company:  ESD Group, School of Electronics, University Of
Southampton
-- Engineer: Julian A Bailey - PhD Research Student
--
-- Create Date:    23/06/2009
-- Design Name:    Photon Counter System
-- Module Name:    Photon Counter System
-- Project Name:   Photon Counter System
-- Target Devices: Xilinx Spartan 3E FPGA Devices w/DLP245BM
-- Tool versions:  Xilinx ISE
--
-- Description:
--
-- Dependencies:
--    XilinxSpartan3EPLL.vhd - Xilinx Digital Clock Manager (DCM)
--                             for Spartan 3E Device.
--    PhotonCounter.vhd - State Machine for Counting Pulses and
Maintaining
--                        Dead Time Specifications.
--    Timer.vhd - 1 Millisecond Timer for Counting Bins.
--    USB.vhd - USB interface to DLP Design DLP245BM Module.
--
-- Revision:
--
----------------------------------------------------------------------
--------------
library IEEE;
use IEEE.STD_LOGIC_1164.ALL;
use IEEE.NUMERIC_STD.ALL;
use IEEE.STD_LOGIC_UNSIGNED.ALL;


entity PhotonCounterSystem is
    generic( TimerPeriod : unsigned(11 downto 0) := x"7D0";
             DeadTime : unsigned(7 downto 0) := x"04"); -- Maximum
16 Bit Counter Length
    port (-- Control Signals
          signal Clock : in std_logic;  -- System Clock
          signal Reset : in std_logic; -- System Reset
          signal Enable : in std_logic; -- System Enable

          -- Signal Line From PhotoDetector
          signal PhotonDetector1 : in std_logic;
          signal PhotonDetector2 : in std_logic;

          -- Control Signals for the USB Device
          signal usbdb         : inout std_logic_vector(7 downto 0);
          signal usbastb  : in std_logic;
          signal usbdstb  : in std_logic;
          signal usbwr  : in std_logic;
```

```
          signal usbwait  : out std_logic

          );
end PhotonCounterSystem;

architecture Behavioural of PhotonCounterSystem is

-- signal SampleClock : std_logic;
signal HighSpeedClock : std_logic;
signal LowSpeedClock : std_logic;


signal SystemReset : std_logic;
signal CounterOutput1 : std_logic_vector(15 downto 0);
signal CounterOutput2 : std_logic_vector(15 downto 0);
signal CapturePeriodFinish : std_logic;

signal PLL_LOCK : std_logic;

begin

SystemReset <= Reset OR NOT(PLL_LOCK) OR NOT(Enable);


PLL1: entity WORK.XilinxSpartan3EPLL
      port map( CLKIN_IN   => Clock,
              RST_IN     => Reset,
              CLKFX_OUT  => HighSpeedClock,
      CLK0_OUT => LowSpeedClock,
              LOCKED_OUT => PLL_LOCK);

PhotonCounter1: entity WORK.PhotonCounter
        generic map (DeadTime => x"04")
        port map(-- Control Signals
                 Clock => HighSpeedClock,
                 Reset => SystemReset,
                 -- Signal Line From PhotoDetector
                 PhotonDetector => PhotonDetector1,
                 ResetCount => CapturePeriodFinish,
                 CounterOut => CounterOutput1);

PhotonCounter2: entity WORK.PhotonCounter
        generic map (DeadTime => x"04")
        port map(-- Control Signals
                 Clock => HighSpeedClock,
                 Reset => SystemReset,
                 -- Signal Line From PhotoDetector
                 PhotonDetector => PhotonDetector2,
                 ResetCount => CapturePeriodFinish,
                 CounterOut => CounterOutput2);

PeriodTimer1: entity WORK.Timer
        generic map (TimerBits => 16)
        port map(Clock => LowSpeedClock,
                 Reset =>  SystemReset,
                TimerPeriod => x"1388",
                TimerLimit => CapturePeriodFinish);


USBIF1: entity WORK.Basys2USB
        generic map(BufferSize => 126)
```

```
        port map (-- Control Signals
                  Clock => LowSpeedClock,
                  Reset => SystemReset,
                -- Photon Counter Module Interface Signals
                SaveData   => CapturePeriodFinish,
                Photon1Data => CounterOutput1,
                Photon2Data => CounterOutput2,
                -- USB Interface Signals
                  pdb => usbdb,
                  astb => usbastb,
                  dstb => usbdstb,
                  pwr => usbwr,
                  pwait => usbwait);

end architecture Behavioural;
```

PhotonCounter.vhd

```
----------------------------------------------------------------------
--------------
-- Company:  ESD Group, School of Electronics, University Of
Southampton
-- Engineer: Julian A Bailey - PhD Research Student
--
-- Create Date:    23/06/2009
-- Design Name:    Photon Counter
-- Module Name:    Photon Counter
-- Project Name:   Photon Counter System
-- Target Devices: Xilinx Spartan 3E FPGA Devices w/DLP245BM
-- Tool versions:  Xilinx ISE
--
-- Description:
--
-- Dependencies: None
--
--
-- Revision:
--
----------------------------------------------------------------------
--------------
library IEEE;
use IEEE.STD_LOGIC_1164.ALL;
use IEEE.NUMERIC_STD.ALL;
use IEEE.STD_LOGIC_UNSIGNED.ALL;


entity PhotonCounter is
    generic (DeadTime : unsigned := x"01");
    port (-- Control Signals
          signal Clock : in std_logic;  -- System Clock
          signal Reset : in std_logic; -- System Reset

          -- Signal Line From PhotoDetector
          signal PhotonDetector : in std_logic;
          signal ResetCount : in std_logic;
          signal CounterOut : out std_logic_vector(15 downto 0));
end PhotonCounter;

architecture Behavioural of PhotonCounter is
```

```
signal PhotonDetector1, PhotonDetector2 : std_logic;
signal PhotonPulse : std_logic;
signal SampleEn : std_logic;
signal LastResetCount : std_logic;

signal CaptureCountQ : unsigned(15 downto 0);
signal CaptureCountD : unsigned(15 downto 0);

signal DeadTimerQ : unsigned(7 downto 0);
signal DeadTimerD : unsigned(7 downto 0);



begin

 PhotonPulse <= PhotonDetector1 AND (NOT PhotonDetector2);

 DATA_SAMPLE: process (Clock, Reset)
 begin
     if (Reset = '1') then
       PhotonDetector1 <= '0';
       PhotonDetector2 <= '0';
       LastResetCount <= '0';
     elsif rising_edge(Clock) then

  LastResetCount<= ResetCount;

      if (SampleEn = '0') then
          PhotonDetector1 <= '0';
          PhotonDetector2 <= '0';
      else
          PhotonDetector1 <= PhotonDetector;
          PhotonDetector2 <= PhotonDetector1;
      end if;
     end if;
 end process DATA_SAMPLE;

COUNTER_SEQ: process (Clock, Reset) is
  begin
    if (Reset = '1') then
      CaptureCountQ <= (others => '0');
      CounterOut <= (others => '0');
    elsif rising_edge(Clock) then

    if ((ResetCount = '1') AND (LastResetCount = '0')) then
         CaptureCountQ <= (others => '0');
      else
         CaptureCountQ <= CaptureCountD;
      end if;


      if ((ResetCount = '1') AND (LastResetCount = '0')) then
        CounterOut <= std_logic_vector(CaptureCountQ);
      end if;

    end if;
  end process COUNTER_SEQ;

COUNTER_COM: process (CaptureCountQ, PhotonPulse) is
  begin
```

```
    if ((PhotonPulse = '1') AND (CaptureCountQ(15) = '0')) then
       CaptureCountD <= CaptureCountQ + 1;
    else
       CaptureCountD <= CaptureCountQ;
    end if;
 end process COUNTER_COM;


 DEAD_TIMER_SEQ: process (Clock, Reset) is
 begin
   if (Reset = '1') then
     DeadTimerQ <= (others => '0');
   elsif rising_edge(Clock) then
     DeadTimerQ <= DeadTimerD;
   end if;
 end process DEAD_TIMER_SEQ;

 DEAD_TIMER_COM: process (DeadTimerQ, PhotonPulse) is
 variable TimerZero : unsigned(7 downto 0);
 begin
   TimerZero := (Others => '0');

   if (DeadTimerQ = DeadTime) then
     DeadTimerD <= TimerZero;
   elsif (DeadTimerQ /= TimerZero) then
     DeadTimerD <= DeadTimerQ + 1;
   elsif (PhotonPulse = '1') then
     DeadTimerD <= x"01";
   else
     DeadTimerD <= DeadTimerQ;
   end if;

   if (DeadTimerQ = TimerZero) then
     SampleEn <= '1';
   else
     SampleEn <= '0';
   end if;
end process DEAD_TIMER_COM;
end architecture Behavioural;
```

DataBuffer.vhd

```
----------------------------------------------------------------------------
--------------
-- Company:
-- Engineer:
--
-- Create Date:    21:54:59 07/12/2009
-- Design Name:
-- Module Name:    DataBuffer - Behavioral
-- Project Name:
-- Target Devices:
-- Tool versions:
-- Description:
--
-- Dependencies:
--
-- Revision:
-- Revision 0.01 - File Created
-- Additional Comments:
```

```
--
----------------------------------------------------------------------
--------------
library IEEE;
use IEEE.STD_LOGIC_1164.ALL;
use IEEE.STD_LOGIC_ARITH.ALL;
use IEEE.STD_LOGIC_UNSIGNED.ALL;

---- Uncomment the following library declaration if instantiating
---- any Xilinx primitives in this code.
--library UNISIM;
--use UNISIM.VComponents.all;

entity DataBuffer is
    generic (BufferSize : integer := 32);
    Port ( Clock : in  STD_LOGIC;
           Address : in  STD_LOGIC_VECTOR (7 downto 0);
           DataIn : in  STD_LOGIC_VECTOR (7 downto 0);
     DataOut : out STD_LOGIC_VECTOR (7 downto 0);
           WR : in  STD_LOGIC);
end DataBuffer;

architecture Behavioral of DataBuffer is

type MemArray is array(BufferSize-1 downto 0) of std_logic_vector(7
downto 0);
signal Memory : MemArray;

begin

process (Clock, Address, WR, Memory, DataIn) is
variable IntAddress : integer;
begin
  IntAddress := conv_integer(unsigned(Address));

  if rising_edge(Clock) then
    if (WR = '1') then
   Memory(IntAddress) <= DataIn;
      end if;
 end if;

   DataOut <= Memory(IntAddress);

end process;

end Behavioral;
```

Timer.vhd

```
----------------------------------------------------------------------
--------------
-- Company:  ESD Group, School of Electronics, University Of
Southampton
-- Engineer: Julian A Bailey - PhD Research Student
--
-- Create Date:    23/06/2009
-- Design Name:    Photon Counter System
-- Module Name:    Timer
-- Project Name:   Photon Counter System
-- Target Devices: Xilinx Spartan 3E FPGA Devices w/DLP245BM
```

```
-- Tool versions:  Xilinx ISE
--
-- Description:
--
-- Dependencies: None
--
--
-- Revision:
--
----------------------------------------------------------------------
--------------
library IEEE;
use IEEE.STD_LOGIC_1164.ALL;
use IEEE.NUMERIC_STD.ALL;
use IEEE.STD_LOGIC_UNSIGNED.ALL;

entity Timer is
    generic( TimerBits : natural := 16); -- Maximum 16 Bit Counter
Length
    port (-- Control Signals
          signal Clock : in std_logic;  -- System Clock
          signal Reset : in std_logic; -- System Reset

          signal TimerPeriod : in unsigned(TimerBits-1 downto 0);
          signal TimerLimit  : out std_logic
          );
end Timer;

architecture Behavioural of Timer is

signal TimeD : unsigned(TimerBits - 1 downto 0);
signal TimeQ : unsigned(TimerBits - 1 downto 0);

begin

SEQ: process (Clock, Reset) is
begin
  if (Reset = '1') then
    TimeQ <= (Others => '0');
  elsif rising_edge(Clock) then
    TimeQ <= TimeD;
  end if;
end process SEQ;

COM: process (TimerPeriod, TimeQ)
begin

      if (TimeQ = TimerPeriod) then
        TimerLimit <= '1';
        TimeD <= (others => '0');
        TimeD(0) <= '1';
      else
        TimerLimit <= '0';
        TimeD <= TimeQ + 1;
      end if;


end process COM;
end architecture Behavioural;
```

References

[1] R. Dahm, "Friedrich Miescher and the discovery of DNA," *Developmental Biology,* vol. 278, pp. 274-288, 2005.

[2] J. D. Watson and F. H. C. Crick, "Molecular Structure of the Nucleic Acids: A Structure for Deoxyribose Nucleic Acid," *Nature,* vol. 171, pp. 737-738, 1953.

[3] F. Sanger, S. Nicklen, and A. R. Coulson, "DNA Sequencing with Chain-Terminating Inhibitors," *Proceedings of the National Academy of Sciences,* vol. 74, pp. 5463-5467, 1977.

[4] J. C. Venter et al., "The Sequence of the Human Genome," *Science,* vol. 291, pp. 1304-1351, 2001.

[5] L. D. Stein, "Human genome: End of the beginning," *Nature,* vol. 431, pp. 915-916, 2004.

[6] K. V. Voelkerding, S. A. Dames, and J. D. Durtschi, "Next-Generation Sequencing: From Basic Research to Diagnostics," *Clinical Chemistry,* vol. 55, pp. 641-658, 2009.

[7] T. Sjöblom, S. Jones, L. D. Wood, D. W. Parsons, J. Lin, T. D. Barber, D. Mandelker, R. J. Leary, J. Ptak, N. Silliman, S. Szabo, P. Buckhaults, C. Farrell, P. Meeh, S. D. Markowitz, J. Willis, D. Dawson, J. K. V. Willson, A. F. Gazdar, J. Hartigan, L. Wu, C. Liu, G. Parmigiani, B. H. Park, K. E. Bachman, N. Papadopoulos, B. Vogelstein, K. W. Kinzler, and V. E. Velculescu, "The Consensus Coding Sequences of Human Breast and Colorectal Cancers," *Science,* vol. 314, pp. 268-274, 2006.

[8] E. Bailo and V. Deckert, "Tip-Enhanced Raman Spectroscopy of Single RNA Strands: Towards a Novel Direct-Sequencing Method," *Angewandte Chemie International Edition,* vol. 47, pp. 1658-1661, 2008.

[9] D. Branton, D. W. Deamer, A. Marziali, H. Bayley, S. A. Benner, T. Butler, M. Di Ventra, S. Garaj, A. Hibbs, X. Huang, S. B. Jovanovich, P. S. Krstic, S. Lindsay, X. S. Ling, C. H. Mastrangelo, A. Meller, J. S. Oliver, Y. V. Pershin, J. M. Ramsey, R. Riehn, G. V. Soni, V. Tabard-Cossa, M. Wanunu, M. Wiggin, and J. A. Schloss, "The potential and challenges of nanopore sequencing," *Nat Biotech,* vol. 26, pp. 1146-1153, 2008.

[10] J. Kasianowicz, J., E. Brandin, D. Branton, and D. Deamer, W., "Characterization of individual polynucleotide molecules using a membrane channel," *Proceedings of the National Academy of Sciences,* vol. 93, pp. 13770-13773, 1996.

[11] J. Li, D. Stein, C. McMullan, D. Branton, M. J. Aziz, and J. A. Golovchenko, "Ion-beam sculpting at nanometre length scales," *Nature,* vol. 412, pp. 166-169, 2001.

[12] P. Lichter, C.-J. C. Tang, K. Call, G. Hermanson, G. A. Evans, D. Housman, and D. C. Ward, "High-Resolution Mapping of Human Chromosome 11 by in Situ Hybridization with Cosmid Clones," *Science,* vol. 247, pp. 64-69, 1990.

[13] J. Herrick, X. Michalet, C. Conti, C. Schurra, and A. Bensimon, "Quantifying single gene copy number by measuring fluorescent probe lengths on combed genomic DNA," *Proceedings of the National Academy of Sciences,* vol. 97, pp. 222-227, 2000.

[14] D. A. Norwood Jr and J. A. Sands, "Physical map of the Clostridium difficile chromosome," *Gene,* vol. 201, pp. 159-168, 1997.

[15] D. M. Olive and P. Bean, "Principles and Applications of Methods for DNA-Based Typing of Microbial Organisms," *J. Clin. Microbiol.,* vol. 37, pp. 1661-1669, 1999.

[16] M. Heiskanen, O. Kallioniemi, and A. Palotie, "Fiber-FISH: Experiences and a Refined Protocol," *Genetic Analysis: Biomolecular Engineering,* vol. 12, pp. 179-184, 1996.

[17] A. Bensimon, A. Simon, A. Chiffaudel, V. Croquette, F. Heslot, and D. Bensimon, "Alignment and Sensitive Detection of DNA by a Moving Interface," *Science,* vol. 265, pp. 2096-2098, 1994.

[18] F. Persson and J. O. Tegenfeldt, "DNA in nanochannels - directly visualizing genomic information," *Chemical Society Reviews,* vol. 39, pp. 985-999, 2010.

[19] E. Y. Chan, N. M. Goncalves, R. A. Haeusler, A. J. Hatch, J. W. Larson, A. M. Maletta, G. R. Yantz, E. D. Carstea, M. Fuchs, G. G. Wong, S. R. Gullans, and R. Gilmanshin, "DNA Mapping Using Microfluidic Stretching and Single-Molecule Detection of Fluorescent Site-Specific Tags," *Genome Research,* vol. 14, pp. 1137-1146, 2004.

[20] K. Jo, D. M. Dhingra, T. Odijk, J. J. de Pablo, M. D. Graham, R. Runnheim, D. Forrest, and D. C. Schwartz, "A single-molecule barcoding system using nanoslits for DNA analysis," *Proceedings of the National Academy of Sciences,* vol. 104, pp. 2673-2678, 2007.

[21] R. Riehn, M. Lu, Y.-M. Wang, S. F. Lim, E. C. Cox, and R. H. Austin, "Restriction mapping in nanofluidic devices," *Proceedings of the National Academy of Sciences of the United States of America,* vol. 102, pp. 10012-10016, 2005.

[22] J. W. Larson, G. R. Yantz, Q. Zhong, R. Charnas, C. M. DAntoni, M. V. Gallo, K. A. Gillis, L. A. Neely, K. M. Phillips, G. G. Wong, S. R. Gullans, and R. Gilmanshin, "Single DNA molecule stretching in sudden mixed shear and elongational microflows," *Lab on a Chip,* vol. 6, pp. 1187 - 1199, 2006.

[23] E. Protozanova, M. Zhang, E. J. White, E. T. Mollova, D. T. Broeck, S. V. Fridrikh, D. B. Cameron, and R. Gilmanshin, "Fast high-resolution mapping of long fragments of genomic DNA based on single-molecule detection," *Analytical Biochemistry,* vol. 402, pp. 83-90, 2010.

[24] D. E. Smith and S. Chu, "Response of Flexible Polymers to a Sudden Elongational Flow," *Science,* vol. 281, pp. 1335-1340, 1998.

[25] R. G. Larson, "The role of molecular folds and 'pre-conditioning' in the unraveling of polymer molecules during extensional flow," *Journal of Non-Newtonian Fluid Mechanics,* vol. 94, pp. 37-45, 2000.

[26] H. S. Rye, S. Yue, D. E. Wemmer, M. A. Quesada, R. P. Haugland, R. A. Mathies, and A. N. Glazer, "Stable fluorescent complexes of double-stranded DNA with bis-intercalating asymmetric cyanine dyes: properties and applications," *Nucleic Acids Research,* vol. 20, pp. 2803-2812, 1992.

[27] J. Shaughnessy, E. Tian, J. Sawyer, K. Bumm, R. Landes, A. Badros, C. Morris, G. Tricot, J. Epstein, and B. Barlogie, "High incidence of chromosome 13 deletion in multiple myeloma detected by multiprobe interphase FISH," *Blood,* vol. 96, pp. 1505-1511, 2000.

[28] R. J. Florijn, A. J. Bonden, H. Vrolijk, J. Wiegant, J.-W. Vaandrager, F. Bass, J. T. den Dunnen, H. J. Tanke, G.-J. B. van Ommen, and A. K. Raap, "High-resolution DNA Fiber-FISH for genomic DNA mapping and colour

bar-coding of large genes," *Human Molecular Genetics,* vol. 4, pp. 831-836, 1995.

[29] P. S. Bernard and C. T. Wittwer, "Real-Time PCR Technology for Cancer Diagnostics," *Clinical Chemistry,* vol. 48, pp. 1178-1185, 2002.

[30] D. Botstein, R. L. White, M. Skolnick, and R. W. Davis, "Construction of a genetic linkage map in man using restriction fragment length polymorphisms," *American Journal of Human Genetics,* vol. 32, pp. 314-331, 1980.

[31] G. W. Dewald, T. Therneau, D. Larson, Y. K. Lee, S. Fink, S. Smoley, S. Paternoster, A. Adeyinka, R. Ketterling, D. L. Van Dyke, R. Fonseca, and R. Kyle, "Relationship of patient survival and chromosome anomalies detected in metaphase and/or interphase cells at diagnosis of myeloma," *Blood,* vol. 106, pp. 3553-3558, 2005.

[32] S. Y. Chou, P. R. Krauss, and P. J. Renstrom, "Imprint of sub-25 nm vias and trenches in polymers," *Applied Physics Letters,* vol. 67, pp. 3114-3116, 1995.

[33] M. Harmening, W. Bacher, P. Bley, A. El-Kholi, H. Kalb, B. Kowanz, W. Menz, A. Michel, and J. Mohr, "Molding of three dimensional microstructures by the LIGA process," in *Micro Electro Mechanical Systems, 1992, MEMS '92, Proceedings. An Investigation of Micro Structures, Sensors, Actuators, Machines and Robot. IEEE*, 1992, pp. 202-207.

[34] C. Lee, E.-H. Yang, N. V. Myung, and T. George, "A Nanochannel Fabrication Technique without Nanolithography," *Nano Letters,* vol. 3, pp. 1339-1340, 2003.

[35] J. T. Mannion, C. H. Reccius, J. D. Cross, and H. G. Craighead, "Conformational Analysis of Single DNA Molecules Undergoing Entropically Induced Motion in Nanochannels," *Biophysical Journal,* vol. 90, pp. 4538-4545, 2006.

[36] A. Balducci, P. Mao, J. Han, and P. S. Doyle, "Double-Stranded DNA Diffusion in Slitlike Nanochannels," *Macromolecules,* vol. 39, pp. 6273-6281, 2006.

[37] S. S. Verbridge, J. B. Edel, S. M. Stavis, J. M. Moran-Mirabal, S. D. Allen, G. Coates, and H. G. Craighead, "Suspended glass nanochannels coupled with microstructures for single molecule detection," *Journal of Applied Physics,* vol. 97, pp. 124317-4, 2005.

[38] H. Cao, Z. Yu, J. Wang, J. O. Tegenfeldt, R. H. Austin, E. Chen, W. Wu, and S. Y. Chou, "Fabrication of 10 nm enclosed nanofluidic channels," *Applied Physics Letters,* vol. 81, pp. 174-176, 2002.

[39] F. Brochard and P. G. de Gennes, "Dynamics of confined polymer chains," *Journal of Chemical Physics,* vol. 61, pp. 52-56, 1977.

[40] T. Odijk, "The statistics and dynamics of confined or entangled stiff polymers," *Macromolecules,* vol. 16, pp. 1340-1344, 1983.

[41] J. D. Cross, E. A. Strychalski, and H. G. Craighead, "Size-dependent DNA mobility in nanochannels," *Journal of Applied Physics,* vol. 102, pp. 024701-5, 2007.

[42] W. Reisner, K. J. Morton, R. Riehn, Y. M. Wang, Z. Yu, M. Rosen, J. C. Sturm, S. Y. Chou, E. Frey, and R. H. Austin, "Statics and Dynamics of Single DNA Molecules Confined in Nanochannels," *Physical Review Letters,* vol. 94, p. 196101, 2005.

[43] R. Verma, J. C. Crocker, T. C. Lubensky, and A. G. Yodh, "Entropic Colloidal Interactions in Concentrated DNA Solutions," *Physical Review Letters,* vol. 81, p. 4004, 1998.

[44] J. O. Tegenfeldt, C. Prinz, H. Cao, S. Chou, W. W. Reisner, R. Riehn, Y. M. Wang, E. C. Cox, J. C. Sturm, P. Silberzan, and R. H. Austin, "The dynamics of genomic-length DNA molecules in 100-nm channels," *Proceedings of the National Academy of Sciences of the United States of America,* vol. 101, pp. 10979-10983, 2004.

[45] X. Liang and S. Y. Chou, "Nanogap Detector Inside Nanofluidic Channel for Fast Real-Time Label-Free DNA Analysis," *Nano Letters,* vol. 8, pp. 1472-1476, 2008.

[46] P. Chen, J. Gu, E. Brandin, Y.-R. Kim, Q. Wang, and D. Branton, "Probing Single DNA Molecule Transport Using Fabricated Nanopores," *Nano Letters,* vol. 4, pp. 2293-2298, 2004.

[47] T. T. Perkins, S. R. Quake, D. E. Smith, and S. Chu, "Relaxation of a single DNA molecule observed by optical microscopy," *Science,* vol. 264, pp. 822-826, 1994.

[48] E. T. Dimalanta, A. Lim, R. Runnheim, C. Lamers, C. Churas, D. K. Forrest, J. J. de Pablo, M. D. Graham, S. N. Coppersmith, S. Goldstein, and D. C. Schwartz, "A Microfluidic System for Large DNA Molecule Arrays," *Analytical Chemistry,* vol. 76, pp. 5293-5301, 2004.

[49] P. K. Wong, Y.-K. Lee, and C.-M. Ho, "Deformation of DNA molecules by hydrodynamic focusing," *Journal of Fluid Mechanics,* vol. 497, pp. 55-65, 2003.

[50] D. Bensimon, A. J. Simon, V. Croquette, and A. Bensimon, "Stretching DNA with a Receding Meniscus: Experiments and Models," *Physical Review Letters,* vol. 74, pp. 4754-4757, 1995.

[51] T. T. Perkins, D. E. Smith, R. G. Larson, and S. Chu, "Stretching of a single tethered polymer in a uniform flow," *Science,* vol. 268, pp. 83-87, 1995.

[52] Y. S. Fan, L. M. Davis, and T. B. Shows, "Mapping small DNA sequences by fluorescence in situ hybridization directly on banded metaphase chromosomes," *Proceedings of the National Academy of Sciences,* vol. 87, pp. 6223-6227, 1990.

[53] G. Senger, T. A.Jones, H. Fldlerová, P. Sanséau, J. Trowsdale, M. Duff, and D. Sheer, "Released chromatin: linearized DNA for high resolution fluorescence in situ hybridization," *Human Molecular Genetics,* vol. 3, pp. 1275-1280, 1994.

[54] M. Heiskanen, E. Hellsten, O. P. Kallioniemi, T. P. Makela, K. Alitalo, L. Peltonen, and A. Palotie, "Visual Mapping by Fiber-FISH," *Genomics,* vol. 30, pp. 31-36, 1995.

[55] A. K. Raap, R. J. Florijn, L. A. J. Blonden, J. Wiegant, J.-W. Vaandrager, H. Vrolijk, J. den Dunnen, H. J. Tanke, and G.-J. van Ommen, "Fiber FISH as a DNA Mapping Tool," *Methods in Enzymology,* vol. 9, pp. 67-73, 1996.

[56] S. Röttger, P. H. Yen, and W. Schempp, "A fiber-FISH contig spanning the non-recombining region of the human Y chromosome," *Chromosome Research,* vol. 10, pp. 621-635, 2002.

[57] C. Aston, B. Mishra, and D. C. Schwartz, "Optical mapping and its potential for large-scale sequencing projects," *Trends in Biotechnology,* vol. 17, pp. 297-302, 1999.

[58] J. A. Ferguson, F. J. Steemers, and D. R. Walt, "High-Density Fiber-Optic DNA Random Microsphere Array," *Analytical Chemistry,* vol. 72, pp. 5618-5624, 2000.
[59] T. R. Strick, J.-F. Allemand, D. Bensimon, A. Bensimon, and V. Croquette, "The Elasticity of a Single Supercoiled DNA Molecule," *Science,* vol. 271, pp. 1835-1837, 1996.
[60] S. B. Smith, L. Finzi, and C. Bustamante, "Direct Mechanical Measurements of the Elasticity of Single DNA Molecules by Using Magnetic Beads," *Science,* vol. 258, pp. 1122-1126, 1992.
[61] P. Cluzel, A. Lebrun, C. Heller, R. Lavery, J.-L. Viovy, D. Chatenay, and F. Caron, "DNA: An Extensible Molecule," *Science,* vol. 271, pp. 792-794, 1996.
[62] S. B. Smith, Y. Cui, and C. Bustamante, "Overstretching B-DNA: The Elastic Response of Individual Double-Stranded and Single-Stranded DNA Molecules," *Science,* vol. 271, pp. 795-799, 1996.
[63] C. Bustamante, S. B. Smith, J. Liphardt, and D. Smith, "Single-Molecule Studies of DNA Mechanics," *Current Opinion in Structural Biology,* vol. 10, pp. 279-285, 2000.
[64] W. Saenger, *Principles of Nucleic Acid Structure*. New York: Spinger-Verlag, 1984.
[65] A. Lebrun and R. Lavery, "Modelling extreme stretching of DNA," *Nucleic Acids Research,* vol. 24, pp. 2260-2267, 1996.
[66] M. W. Konrad and J. I. Bolonick, "Molecular Dynamics Simulation of DNA Stretching Is Consistent with the Tension Observed for Extension and Strand Separation and Predicts a Novel Ladder Structure," *Journal of the American Chemical Society,* vol. 118, pp. 10989-10994, 1996.
[67] A. Agronskaia, J. M. Schins, B. G. de Grooth, and J. Greve, "Two-Color Fluorescence in Flow Cytometry DNA Sizing: Identification of Single-Molecule Fluorescent Probes," *Analytical Chemistry,* vol. 71, pp. 4684-4689, 1999.
[68] D. E. Smith, H. P. Babcock, and S. Chu, "Single-Polymer Dynamics in Steady Shear Flow," *Science,* vol. 283, pp. 1724-1727, 1999.
[69] A. Keller and J. A. Odell, "The extensibility of macromolecules in solution; A new focus for macromolecular science," *Colloid and Polymer Science,* vol. 263, pp. 181-201, 1985.
[70] P. G. De Gennes, *Scaling Concepts in Polymer Physics*: Cornell University Press, 1979.
[71] T. R. Strick, J.-F. Allemand, D. Bensimon, and V. Croquette, "Stress-Induced Structural Transitions In DNA and Proteins," *Annual Review of Biophysics and Biomolecular Structure,* vol. 29, pp. 523-543, 2000.
[72] D. E. Smith, T. T. Perkins, and S. Chu, "Dynamical Scaling of DNA Diffusion Coefficients," *Macromolecules,* vol. 29, pp. 1372-1373, 1996.
[73] K. Yamashita, Y. Yamaguchi, M. Miyazaki, H. Nakamura, H. Shimizu, and H. Maeda, "Direct Observation of Long-Strand DNA Conformational Changing in Microchannel Flow and Microfluidic Hybridization Assay," *Analytical Biochemistry,* vol. 332, pp. 274-279, 2004.
[74] K. Yamashita, Y. Yamaguchi, M. Miyazaki, H. Nakamura, H. Shimizu, and H. Maeda, "Direct Observation of Long-strand DNA Stretching in Microchannel Flow," *Chemistry Letters,* vol. 33, pp. 628-629, 2004.

[75] S. Gerashchenko and V. Steinberg, "Critical slowing down in polymer dynamics near the coil-stretch transition in elongation flow," *Physical Review E,* vol. 78, p. 040801, 2008.
[76] T. T. Perkins, D. E. Smith, and S. Chu, "Single polymer dynamics in an elongational flow," *Science,* vol. 276, pp. 2016-2021, 1997.
[77] Y. L. Chen, M. D. Graham, J. J. de Pablo, K. Jo, and D. C. Schwartz, "DNA Molecules in Microfluidic Oscillatory Flow," *Macromolecules,* vol. 38, pp. 6680-6687, 2005.
[78] K. Jo, Y. L. Chen, J. J. Pablo, and D. C. Schwartz, "Elongation and migration of single DNA molecules in microchannels using oscillatory shear flows," *Lab on a Chip,* vol. 9, pp. 2348-2355, 2009.
[79] R. M. Jendrejack, E. T. Dimalanta, D. C. Schwartz, M. D. Graham, and J. J. de Pablo, "DNA Dynamics in a Microchannel," *Physical Review Letters,* vol. 91, p. 038102, 2003.
[80] H. Ma and M. D. Graham, "Theory of shear-induced migration in dilute polymer solutions near solid boundaries," *Physics of Fluids,* vol. 17, pp. 083103-13, 2005.
[81] L. Fang, H. Hu, and R. G. Larson, "DNA Configurations and Concentration in Shearing Flow Near a Glass Surface in a Microchannel," *Journal of Rheology,* vol. 49, pp. 127-138, 2005.
[82] L. Fang and R. G. Larson, "Concentration Dependence of Shear-Induced Polymer Migration in DNA Solutions near a Surface," *Macromolecules,* vol. 40, pp. 8784-8787, 2007.
[83] R. M. Jendrejack, J. J. de Pablo, and M. D. Graham, "Stochastic simulations of DNA in flow: Dynamics and the effects of hydrodynamic interactions," *Journal of Chemical Physics,* vol. 116, pp. 7752-7759, 2002.
[84] M. Doi and S. F. Edwards, *The theory of polymer dynamics*: Oxford University Press, 1986.
[85] R. Duggal and M. Pasquali, "Visualization of individual DNA molecules in a small-scale coating flow," *Journal of Rheology,* vol. 48, pp. 745-764, 2004.
[86] F. E. H. Tay, *Microfluidics and BioMEMS Applications*: Kluwer Academic Publishers, 2002.
[87] T. M. Squires and S. R. Quake, "Microfluidics : Fluid Physics at the Nanoliter Scale," *Reviews of Modern Physics,* vol. 77, pp. 977-1026, 2005.
[88] C. Bustamante, Z. Bryant, and S. B. Smith, "Ten years of tension: single-molecule DNA mechanics," *Nature,* vol. 421, pp. 423-427, 2003.
[89] H. P. Babcock, D. E. Smith, J. S. Hur, E. S. G. Shaqfeh, and S. Chu, "Relating the Microscopic and Macroscopic Response of a Polymeric Fluid in a Shearing Flow," *Physical Review Letters,* vol. 85, p. 2018, 2000.
[90] J. Shinohara, M. Suda, K. Furuta, and T. Sakuhara, "A high pressure-resistance micropump using active and normally-closed valves," in *Micro Electro Mechanical Systems, 2000. MEMS 2000. The Thirteenth Annual International Conference on*, 2000, pp. 86-91.
[91] Y. Sun, C. S. Lim, A. Q. Liu, T. C. Ayi, and P. H. Yap, "Design, simulation and experiment of electroosmotic microfluidic chip for cell sorting," *Sensors and Actuators A: Physical,* vol. 133, pp. 340-348, 2007.
[92] D. Erickson, X. Liu, U. Krull, and D. Li, "Electrokinetically Controlled DNA Hybridization Microfluidic Chip Enabling Rapid Target Analysis," *Analytical Chemistry,* vol. 76, pp. 7269-7277, 2004.

[93] A. V. Pattekar and M. V. Kothare, "Novel microfluidic interconnectors for high temperature and pressure applications," *Journal of Micromechanics and Microengineering,* p. 337, 2003.

[94] T. Honegger, K. Berton, T. Pinedo-Rivera, and D. Peyrade, "Design and realization of a microfluidic system for dielectrophoretic colloidal handling," *Microelectronic Engineering,* vol. 86, pp. 1401-1403.

[95] P. Aniruddha and H. A. Chong, "Self-aligning microfluidic interconnects for glass- and plastic-based microfluidic systems," *Journal of Micromechanics and Microengineering,* p. 35, 2002.

[96] E. Meng, S. Wu, and Y.-C. Tai, "Silicon couplers for microfluidic applications," *Fresenius' Journal of Analytical Chemistry,* vol. 371, pp. 270-275, 2001.

[97] C. Chi-Han and L. Gwo-Bin, "Minimal dead-volume connectors for microfluidics using PDMS casting techniques," *Journal of Micromechanics and Microengineering,* p. 1484, 2004.

[98] A. M. Christensen, D. A. Chang-Yen, and B. K. Gale, "Characterization of interconnects used in PDMS microfluidic systems," *Journal of Micromechanics and Microengineering,* p. 928, 2005.

[99] B. L. Gray, D. Jaeggi, N. J. Mourlas, B. P. van Drieenhuizen, K. R. Williams, N. I. Maluf, and G. T. A. Kovacs, "Novel interconnection technologies for integrated microfluidic systems," *Sensors and Actuators A: Physical,* vol. 77, pp. 57-65, 1999.

[100] F. Lärmer and A. Schilp, "Method for Anisotropically Etching Silicon," German Patent DE4241045 Patent, 1992.

[101] S. A. McAuley, H. Ashraf, L. Atabo, A. Chambers, S. Hall, J. Hopkins, and G. Nicholls, "Silicon micromachining using a high-density plasma source," *Journal of Physics D: Applied Physics,* vol. 34, pp. 2769-2774, 2001.

[102] J. Hopkins, H. Ashraf, K. Bhardwaj, A. M. Hynes, I. Johnston, and J. N. Shepherd, "The Benefits of Process Parameter Ramping During The Plasma Etching of High Aspect Ratio Silicon Structures," in *Proceedings of the Materials Research Society Fall Meeting*, Boston, Massachusetts, USA, 1998.

[103] A. A. Ayon, R. Braff, C. C. Lin, H. H. Sawin, and M. A. Schmidt, "Characterization of a Time Multiplexed Inductively Coupled Plasma Etcher," *Journal of The Electrochemical Society,* vol. 146, pp. 339-349, 1999.

[104] N. Roxhed, P. Griss, and G. Stemme, "A method for tapered deep reactive ion etching using a modified Bosch process," *Journal of Micromechanics and Microengineering,* vol. 17, p. 1087, 2007.

[105] H. T. M. Pham, W. Jia, C. R. de Boer, and P. M. Sarro, "In-Situ Isotropic and Anisotropic DRIE Sequence for Massive Parallel Multistage Brownian Ratchets," in *Solid-State Sensors, Actuators and Microsystems Conference. Transducers 2007*, 2007, pp. 497-500.

[106] E. H. Klaassen, K. Petersen, J. M. Noworolski, J. Logan, N. I. Maluf, J. Brown, C. Storment, W. McCulley, and G. T. A. Kovacs, "Silicon fusion bonding and deep reactive ion etching: a new technology for microstructures," *Sensors and Actuators A: Physical,* vol. 52, pp. 132-139, 1996.

[107] B. Stoeber and D. Liepmann, "Arrays of hollow out-of-plane microneedles for drug delivery," *Microelectromechanical Systems, Journal of,* vol. 14, pp. 472-479, 2005.
[108] E. V. Mukerjee, S. D. Collins, R. R. Isseroff, and R. L. Smith, "Microneedle array for transdermal biological fluid extraction and in situ analysis," *Sensors and Actuators A: Physical,* vol. 114, pp. 267-275, 2004.
[109] C. Chen-Kuei, "Geometrical pattern effect on silicon deep etching by an inductively coupled plasma system," *Journal of Micromechanics and Microengineering,* vol. 14, p. 656, 2004.
[110] J. Kiihamaki, H. Kattelus, J. Karttunen, and S. Franssila, "Depth and profile control in plasma etched MEMS structures," *Sensors and Actuators A: Physical,* vol. 82, pp. 234-238, 2000.
[111] R. A. Gottscho, C. W. Jurgensen, and D. J. Vitkavage, "Microscopic uniformity in plasma etching," *Journal of Vacuum Science & Technology B: Microelectronics and Nanometer Structures,* vol. 10, pp. 2133-2147, 1992.
[112] H. Jansen, M. de Boer, R. Wiegerink, N. Tas, E. Smulders, C. Neagu, and M. Elwenspoek, "RIE lag in high aspect ratio trench etching of silicon," *Microelectronic Engineering,* vol. 35, pp. 45-50, 1997.
[113] A. A. Ayon, R. A. Braff, R. Bayt, H. H. Sawin, and M. A. Schmidt, "Influence of Coil Power on the Etching Characteristics in a High Density Plasma Etcher," *Journal of The Electrochemical Society,* vol. 146, pp. 2730-2736, 1999.
[114] M. Chabloz, Y. Sakai, T. Matsuura, and K. Tsutsumi, "Improvement of sidewall roughness in deep silicon etching," *Microsystem Technologies,* vol. 6, pp. 86-89, 2000.
[115] D. Pradeep and M. Jianmin, "Effect of SF6 flow rate on the etched surface profile and bottom grass formation in deep reactive ion etching process," *Journal of Physics: Conference Series,* p. 577, 2006.
[116] J. Kiihamaki and S. Franssila, "Pattern shape effects and artefacts in deep silicon etching," in *Papers from the 45th National Symposium of the American Vacuum Society*, Baltimore, Maryland (USA), 1999, pp. 2280-2285.
[117] F. Laermer and A. Urban, "Challenges, developments and applications of silicon deep reactive ion etching," *Microelectronic Engineering,* vol. 67-68, pp. 349-355, 2003.
[118] P. T. Docker, P. K. Kinnell, and M. C. L. Ward, "Development of the one-step DRIE dry process for unconstrained fabrication of released MEMS devices," *Journal of Micromechanics and Microengineering,* vol. 14, pp. 941-944, 2004.
[119] T. K. A. Chou and K. Najafi, "Fabrication of out-of-plane curved surfaces in Si by utilizing RIE lag," in *Micro Electro Mechanical Systems, The Fifteenth IEEE International Conference on*, 2002, pp. 145-148.
[120] T. Bourouina, T. Bourouina, T. Masuzawa, and H. Fujita, "The MEMSNAS process: microloading effect for micromachining 3-D structures of nearly all shapes
The MEMSNAS process: microloading effect for micromachining 3-D structures of nearly all shapes," *Microelectromechanical Systems, Journal of,* vol. 13, pp. 190-199, 2004.
[121] M. P. Rao, M. F. Aimi, and N. C. MacDonald, "Single-mask, three-dimensional microfabrication of high-aspect-ratio structures in bulk silicon

using reactive ion etching lag and sacrificial oxidation," *Applied Physics Letters,* vol. 85, pp. 6281-6283, 2004.

[122] V. Nock and R. J. Blaikie, "Fabrication of optical grayscale masks for tapered microfluidic devices," *Microelectronic Engineering,* vol. 85, pp. 1077-1082.

[123] H. Cao, J. O. Tegenfeldt, R. H. Austin, and S. Y. Chou, "Gradient Nanostructures for Interfacing Microfluidics and Nanofluidics," *Applied Physics Letters,* vol. 81, pp. 3058-3060, 2002.

[124] H. Henmi, S. Shoji, Y. Shoji, K. Yoshimi, and M. Esashi, "Vacuum packaging for microsensors by glass-silicon anodic bonding," *Sensors and Actuators A: Physical,* vol. 43, pp. 243-248, 1994.

[125] T. Rogers and J. Kowal, "Selection of glass, anodic bonding conditions and material compatibility for silicon-glass capacitive sensors," *Sensors and Actuators A: Physical,* vol. 46, pp. 113-120.

[126] N. R. Harris, M. Hill, S. Beeby, Y. Shen, N. M. White, J. J. Hawkes, and W. T. Coakley, "A silicon microfluidic ultrasonic separator," *Sensors and Actuators B: Chemical,* vol. 95, pp. 425-434, 2003.

[127] C. G. J. Schabmueller and et al., "Design and fabrication of a microfluidic circuitboard," *Journal of Micromechanics and Microengineering,* vol. 9, p. 176, 1999.

[128] J. Sambrook and D. W. Russell, *Molecular cloning: a laboratory manual*: Cold Spring Harbour Laboratory Press.

[129] I. M. Mackay, K. E. Arden, and A. Nitsche, "Real-time PCR in virology," *Nucleic Acids Research,* vol. 30, pp. 1292-1305, 2002.

[130] G. Taylor, "Dispersion of Soluble Matter in Solvent Flowing Slowly through a Tube," *Proceedings of the Royal Society of London. Series A, Mathematical and Physical Sciences (1934-1990),* vol. 219, pp. 186-203, 1953.

[131] R. Aris, "On the Dispersion of a Solute in a Fluid Flowing through a Tube," *Proceedings of the Royal Society of London. Series A, Mathematical and Physical Sciences (1934-1990),* vol. 235, pp. 67-77, 1956.

[132] K. B. Mullis, "The unusual origin of the polymerase chain reaction," *Scientific American,* vol. 262, 1990.

[133] Y. Li, S. Korolev, and G. Waksman, "Crystal structures of open and closed forms of binary and ternary complexes of the large fragment of Thermus aquaticus DNA polymerase I: structural basis for nucleotide incorporation," *EMBO,* vol. 17, pp. 7514-7525, 1998.

[134] W. S. J. Freeman W.M., Vrana, K.E., "Quantitative RT-PCR: pitfalls and potential," *Biotechniques,* vol. 26, pp. 112-122,124-125, 1999.

[135] T. B. Morrison, J. J. Weis, and C. T. Wittwer, "Quantification of Low-Copy Transcripts by Continuous SYBR® Green I Monitoring during Amplification," *Biotechniques,* vol. 24, pp. 954-962, 1998.

[136] S. Giglio, P. T. Monis, and C. P. Saint, "Demonstration of preferential binding of SYBR Green I to specific DNA fragments in real-time multiplex PCR," *Nucleic Acids Research,* vol. 31, p. e136, 2003.

[137] H. Zipper, Brunner, H., Bernhagen, J., Vitzthum, F., "Investigations on DNA intercalation and surface binding by SYBR Green I, its structure determination and methodological implications," *Nucleic Acids Research,* vol. 32, 2004.

[138] C. A. Heid, J. Stevens, K. J. Livak, and P. M. Williams, "Real time quantitative PCR," *Genome Research,* vol. 6, pp. 986-994, 1996 1996.

[139] A. Tichopad, A. Didier, and M. W. Pfaffl, "Inhibition of real-time RT-PCR quantification due to tissue-specific contaminants," *Molecular and Cellular Probes,* vol. 18, pp. 45-50, 2004.
[140] S. Bustin, "Quantification of mRNA using real-time reverse transcription PCR (RT-PCR): trends and problems," *J Mol Endocrinol,* vol. 29, pp. 23-39, 2002.
[141] S. Weiss, "Fluorescence Spectroscopy of Single Biomolecules," *Science,* vol. 283, pp. 1676-1683, 1999.
[142] F. Kulzer and M. Orrit, "Single-molecule optics," *Annual Review of Physical Chemistry,* vol. 55, pp. 585-611, 2004.
[143] J. van Mameren, E. J. G. Peterman, and G. J. L. Wuite, "See me, feel me: methods to concurrently visualize and manipulate single DNA molecules and associated proteins," *Nucleic Acids Research,* vol. 36, pp. 4381-4389, 2008.
[144] S. Nie and R. N. Zare, "Optical detecion of single molecules," *Annual Review of Biophysics and Biomolecular Structure,* vol. 26, pp. 567-596, 1997.
[145] X. S. Xie, P. J. Choi, G.-W. Li, N. K. Lee, and G. Lia, "Single-Molecule Approach to Molecular Biology in Living Bacterial Cells," *Annual Review of Biophysics,* vol. 37, pp. 417-444, 2008.
[146] X. Michalet and S. Weiss, "Single-molecule spectroscopy and microscopy," *Comptes Rendus Physique,* vol. 3, pp. 619-644, 2002.
[147] M. L. Chabinyc, D. T. Chiu, J. C. McDonald, A. D. Stroock, J. F. Christian, A. M. Karger, and G. M. Whitesides, "An Integrated Fluorescence Detection System in Poly(dimethylsiloxane) for Microfluidic Applications," *Analytical Chemistry,* vol. 73, pp. 4491-4498, 2001.
[148] S. Cova, M. Ghioni, A. Lotito, I. Rech, and F. Zappa, "Evolution and prospects for single-photon avalanche diodes and quenching circuits," *Journal of Modern Optics,* vol. 51, pp. 1267 - 1288, 2004.
[149] S. Cova, A. Longoni, and A. Andreoni, "Towards picosecond resolution with single-photon avalanche diodes," *Review of Scientific Instruments,* vol. 52, pp. 408-412, 1981.
[150] S. Cova, A. Lacaita, M. Ghioni, G. Ripamonti, and T. A. Louis, "20-ps timing resolution with single-photon avalanche diodes," vol. 60, pp. 1104-1110, 1989.
[151] S. Cova, M. Ghioni, A. Lacaita, C. Samori, and F. Zappa, "Avalanche photodiodes and quenching circuits for single-photon detection," *Appl. Opt.,* vol. 35, pp. 1956-1976, 1996.
[152] M. Brinkmeier, K. Dörre, K. Riebeseel, and R. Rigler, "Confocal spectroscopy in microstructures," *Biophysical Chemistry,* vol. 66, pp. 229-239, 1997.
[153] C. Zander, J. Enderlein, and R. A. Keller, *Single Molecule Detection in Solution - Methods and Applications*, 1 ed.: Wiley-VCH, 2002.
[154] B. B. Haab and R. A. Mathies, "Single molecule fluorescence burst detection of DNA fragments separated by capillary electrophoresis," *Analytical Chemistry,* vol. 67, pp. 3253-3260, 1995.
[155] S. M. F. W. S. J. B. S. A. S. Musundi B. Wabuyele, "Single molecule detection of double-stranded DNA in poly(methylmethacrylate) and polycarbonate microfluidic devices," *Electrophoresis,* vol. 22, pp. 3939-3948, 2001.
[156] B. B. Haab and R. A. Mathies, "Single-Molecule Detection of DNA Separations in Microfabricated Capillary Electrophoresis Chips Employing

Focused Molecular Streams," *Analytical Chemistry,* vol. 71, pp. 5137-5145, 1999.

[157] J. R. Krogmeier, I. Schaefer, G. Seward, G. R. Yantz, and J. W. Larson, "An integrated optics microfluidic device for detecting single DNA molecules," *Lab on a Chip,* vol. 7, pp. 1767-1774, 2007.

[158] S.-K. Hsiung, G.-B. Lee, C.-H. Lin, and C.-H. Lee, "Microcapillary Electrophoresis Chip Device Integrated with Micro Focusing Lens Structures and Its Biomedical Applications," vol. 1, pp. 11-20, 2009.

[159] K. M. Phillips, J. W. Larson, G. R. Yantz, C. M. D'Antoni, M. V. Gallo, K. A. Gillis, N. M. Goncalves, L. A. Neely, S. R. Gullans, and R. Gilmanshin, "Application of single molecule technology to rapidly map long DNA and study the conformation of stretched DNA," *Nucleic Acids Research,* vol. 33, pp. 5829-5837, 2005.

[160] S. Taylor, S. Smith, B. Windle, and A. Guiseppi-Elie, "Impact of surface chemistry and blocking strategies on DNA microarrays," *Nucleic Acids Research,* vol. 31, p. e87, 2003.

[161] A. Untergasser, H. Nijveen, X. Rao, T. Bisseling, R. Geurts, and J. A. M. Leunissen, "Primer3Plus, an enhanced web interface to Primer3," *Nucleic Acids Research,* vol. 35, pp. W71-W74, 2007.

[162] C. W. Dieffenbach, T. M. Lowe, and T. M. Dveksler, "General Concepts for PCR Primer Design," *Genome Research,* vol. 3, pp. S30-37, 1993.

[163] K. R. Tindall and T. A. Kunkel, "Fidelity of DNA synthesis by the Thermus aquaticus DNA polymerase," *Biochemistry,* vol. 27, pp. 6008-6013, 1988.

[164] J. T. Petty, M. E. Johnson, P. M. Goodwin, J. C. Martin, J. H. Jett, and R. A. Keller, "Characterization of DNA Size Determination of Small Fragments by Flow Cytometry," *Analytical Chemistry,* vol. 67, pp. 1755-1761, 1995.

[165] T. L. Netzel, K. Nafisi, M. Zhao, J. R. Lenhard, and I. Johnson, "Base-Content Dependence of Emission Enhancements, Quantum Yields, and Lifetimes for Cyanine Dyes Bound to Double-Strand DNA: Photophysical Properties of Monomeric and Bichromomphoric DNA Stains," *The Journal of Physical Chemistry,* vol. 99, pp. 17936-17947, 1995.

[166] M. Müller, *Confocal Fluorescence Microscopy*: SPIE Press, 2006.

[167] J. R. Lakowicz, *Principles of Fluorescence Spectroscopy*: Springer Science+Business Media, 2006.

[168] R. M. Wadkins, J. P. Golden, and F. S. Ligler, "Calibration of Biosensor Response Using Simultaneous Evanescent Wave Excitation of Cyanine-Labeled Capture Antibodies and Antigens," *Analytical Biochemistry,* vol. 232, pp. 73-78, 1995.

[169] W. T. Silfvast, *Laser Fundamentals*, 2 ed.: Cambridge University Press, 2004.

[170] J. A. Rice, *Mathematical Statistics and Data Analysis*, 2nd ed.: Duxbury Press, 1995.

[171] A. Azzalini, "A Class of Distributions which Includes the Normal Ones," *Scandinavian Journal of Statistics,* vol. 12, pp. 171-178, 1985.

[172] A. Azzalini and A. Capitanio, "Statistical applications of the multivariate skew normal distribution," *Journal of the Royal Statistical Society: Series B (Statistical Methodology),* vol. 61, pp. 579-602, 1999.

[173] F. Brochard-Wyart, "Polymer Chains Under Strong Flows: Stems and Flowers," *EPL (Europhysics Letters),* vol. 30, p. 387, 1995.

[174] D. Irimia, D. A. Geba, and M. Toner, "Universal Microfluidic Gradient Generator," *Analytical Chemistry,* vol. 78, pp. 3472-3477, 2006.
[175] J. P. P. Meijerink, "t(14;18), a journey to eternity," *Leukemia,* vol. 11, pp. 2175-2187, 1997.
[176] Z. N. Oltval, C. L. Milliman, and S. J. Korsmeyer, "Bcl-2 heterodimerizes in vivo with a conserved homolog, Bax, that accelerates programed cell death," *Cell,* vol. 74, pp. 609-619, 1993.
[177] A. Lopez-Guillermo, F. Cabanillas, T. I. McDonnell, P. McLaughlin, T. Smith, W. Pugh, F. Hagemeister, M. A. Rodriguez, J. E. Romaguera, A. Younes, A. H. Sarris, H. A. Preti, and M.-S. Lee, "Correlation of Bcl-2 Rearrangement With Clinical Characteristics and Outcome in Indolent Follicular Lymphoma," *Blood,* vol. 93, pp. 3081-3087, 1999.
[178] K. E. Summers, L. K. Goff, A. G. Wilson, R. K. Gupta, T. A. Lister, and J. Fitzgibbon, "Frequency of the Bcl-2/IgH Rearrangement in Normal Individuals: Implications for the Monitoring of Disease in Patients With Follicular Lymphoma," *J Clin Oncol,* vol. 19, pp. 420-424, 2001.
[179] G. Buchonnet, P. Lenain, P. Ruminy, S. Lepretre, A. Stamatoullas, F. Parmentier, F. Jardin, C. Duval, H. Tilly, and C. Bastard, "Characterisation of BCL2-JH rearrangements in follicular lymphoma: PCR detection of 3' BCL2 breakpoints and evidence of a new cluster," *Leukemia,* vol. 14, pp. 1563-1569, 2000.
[180] A. Rambaldi, E. Carlotti, E. Oldani, I. D. Starza, M. Baccarani, S. Cortelazzo, F. Lauria, L. Arcaini, E. Morra, A. Pulsoni, L. Rigacci, M. Rupolo, F. Zaja, P. L. Zinzani, T. Barbui, and R. Foa, "Quantitative PCR of bone marrow BCL2/IgH+ cells at diagnosis predicts treatment response and long-term outcome in follicular non-Hodgkin lymphoma," *Blood,* vol. 105, pp. 3428-3433, 2005.
[181] A. Godon, A. Moreau, P. Talmant, L. Baranger-Papot, F. Genevieve, N. Milpied, M. Zandecki, and H. Avet-Loiseau, "Is t(14;18)(q32;q21) a constant finding in follicular lymphoma? An interphase FISH study on 63 patients," *Leukemia,* vol. 17, pp. 255-259, 2003.
[182] B. Espinet, B. Bellosillo, C. Melero, M. C. Vela, C. Pedro, M. Salido, L. Pijuan, L. Florensa, C. Besses, S. Serrano, and F. Solé, "FISH is better than BIOMED-2 PCR to detect IgH/BCL2 translocation in follicular lymphoma at diagnosis using paraffin-embedded tissue sections," *Leukemia Research,* vol. 32, pp. 737-742, 2008.